MODELLING OF THE EFFECTS OF ENTRAINMENT DEFECTS ON MECHANICAL PROPERTIES IN AL-SI-MG ALLOY CASTINGS

By

YANG YUE

A dissertation submitted to
University of Birmingham
for the degree of
DOCTOR OF PHILOSOPHY

School of Metallurgy and Materials
University of Birmingham
June 2014

Abstract

Liquid aluminium alloy is highly reactive with the surrounding atmosphere and therefore, surface films, predominantly surface oxide films, easily form on the free surface of the melt. Previous researches have highlighted that surface turbulence in liquid aluminium during the mould-filling process could result in the fold-in of the surface oxide films into the bulk liquid, and this would consequently generate entrainment defects, such as double oxide films and entrapped bubbles in the solidified casting. The formation mechanisms of these defects and their detrimental effects on both mechanical properties and reproducibility of properties of casting have been studied over the past two decades. However, the behaviour of entrainment defects in the liquid metal and their evolution during the casting process are still unclear, and the distribution of these defects in casting remains difficult to predict. An algorithm developed by Reilly, named the oxide film entrainment model (OFEM), could be used to predict the formation and distribution of entrainment defects in castings. The model was integrated into the computational fluid dynamics (CFD) software *FLOW-3D*, and applied face normals of free surface and their interaction to capture the entrainment of surface films.

In this research, validation and development of the OFEM were carried out. Preliminary simulations were run to investigate the entrainment criteria defined in the OFEM and to understand the capability of the model. The initial validation of OFEM used previous reported experimental data on the fatigue and tensile properties of castings, but did not succeed owing to the quality of the data. Then modelling of three common entrainment mechanisms in fluid flow, namely plunging jet, return wave and rising jet, were conducted, and the predicted defect quantities in the samples were compared with the bending strengths of the castings from the Al-7Si-0.4Mg alloy. Directly observation of transient flows in moulds by real-time X-ray radiography showed good correlation between real filling scenario and simulation results. However, the attempt to establish a quantitative relationship between the predicted quantities of the entrainment defects and the mechanical properties of the real castings, were adversely affected by shrinkage porosity found in the castings. A further validation eliminated the influence of shrinkage porosity on the casting properties. The tensile strength of the cast test bars from this validation was compared with either the number of defects, or the defect concentration within the bars

obtained from the simulation. A general relationship between the mechanical strength of the cast test bars and the quantity of estimated defects was apparent.

The validation test for OFEM algorithm has been conducted, but strong correlation between the modelling prediction and the experimental results have not been achieved yet. A series of modelling work undertaken in this research highlighted the potential of the method as an indicator of the entrainment severity in different mould designs. Comparison of the Weibull moduli obtained from the modelling and experimental results also showed that the model had the potential to predicted the reliability of castings. The effects of different modelling conditions on the modelling results were discussed, and some useful courses were suggested, such as proper settings of the particle properties should be used, to increase the accuracy of future simulations.

This research also assessed the behaviour of entrainment defects in the liquid state and during solidification. The samples that contained entrainment defects were scanned using ultra-fast synchrotron X-ray radiography. The defects were directly viewed at both room temperature before melting and in a fully liquid state. The reconstructed images showed three different pore morphologies, namely entrained pores, tangled double oxide films and closed cracks. The morphology evolution of the entrainment defects were studied, which showed that the oxidation of the internal atmosphere was the main driving force of the pore shape changes, but has less effect on the morphology change of tangled double oxide films. The reconstructed three-dimensional images gave direct evidence of the mechanism of morphological change of defect and the interaction between entrainment defects and microporosity.

To my family

Acknowledgements

I would like to express my sincere gratitude to both my supervisors, Prof. Nick Green, for his kind guidance and encouragement in the first two year of my research, and Dr. Bill Griffiths, for his constructive criticisms and continuous support throughout the course of this work. Although they only shared a fraction of their wisdom, I benefited a great deal from their insight and knowledge. Without their help and great patience, this work could not have been accomplished.

I thank the financial support from the School of Metallurgy and Materials at University of Birmingham for my program, without which I would never start my PhD here.

I wish to acknowledge Dr. Carl Reilly, who initiated the modelling method used in this study and introduced it to me, and Dr. Jean-Christophe Gebelin, who offered technical assistance for the modelling work; the technicians, Adrian Caden and Peter Craemer in the Foundry, and David Price in the Mechanical Testing Lab, who provided a wealth of experience to facilitate the experimental work contained within this thesis. Their assistance is critical to this work. I thank Julie Fife in Swiss Light Source (SLS) at Paul Scherrer Institut (PSI) in Switzerland for her help on conducting synchrotron X-ray experiments.

I am also grateful to my colleagues in School of Metallurgy and Materials, especially, Dr. Hang Wang and Dr. Jianglin Huang, for their continuously support both in academics and after-hour life, and friends at University of Birmingham, Mofei Guo, Xi Liu, Guangxiong Wang, Yang Yang and others, their "distractions" made my PhD life in Birmingham varied and colourful.

The last mention must go to my family: my father YUE Zhihong and my mother ZHANG Huiping. Their unconditional support and love in this as with every endeavour are what made my success possible. Now and always, they are everything to me.

Preface

This dissertation is submitted for the degree of the Doctor of Philosophy at the University of Birmingham. It describes research carried out in School of Metallurgy and Material Science between October 2009 and September 2013, under the supervision of Dr. W.D. Griffiths and Prof. N.R. Green. Except where appropriately referenced, this work is original and has not been submitted for any other degree, diploma and other qualification. It does not exceed 50,000 words in length.

Parts of this dissertation have been published or submitted for publication in:

- Y. Yue, W.D. Griffiths and N.R. Green, "Modelling of the effects of entrainment defects on mechanical properties in Al-Si-Mg alloy", in *Materials Science Forum*, Vol.765, pp.225-229, 2013.

- Y. Yue, W.D. Griffiths, J.L. Fife, and N.R. Green, "In-Situ Characterization of Entrainment Defects in Liquid Al-Si-Mg Alloy," in *1 International Conference on 3D Materials Science*, 2012, pp.131–136.

- Y. Yue and N.R. Green, "Modelling of Different Entrainment Mechanisms and Their Influences on the Mechanical Reliability of Al-Si Castings," in *IOP Conference Series: Materials Science and Engineering*, 2012, vol. 33, paper No.012072

Yang Yue

September 2013

Contents

List of Figures

List of Tables

Chapter 1

Introduction

Aluminium is the second most used metal in the world following iron, and more aluminium is produced than all other non-ferrous metals combined [1]. According to their composition, aluminium alloys are conventionally divided into two major categories: wrought and casting alloys [2]. Typical wrought products include plate or sheet, household foil, extruded frames and forged components. Although currently more aluminium is produced by wrought processes, aluminium castings are increasingly used in the automotive and aviation industries primarily because of their high strength-to-weight ratio, compared with steel and other structural materials, for vehicle weight reduction compared to steel and other structural materials, to improve fuel economy and reduce CO_2 emission and achieve ecological sustainability [3, 4].

Despite the great castability, low melting point and negligible solubility for gases (except hydrogen) of aluminium alloy [2, 5], aluminium castings are vulnerable to oxide related defects due to the high affinity of aluminium with oxygen [6]. Once an aluminium oxide film forms on the free surface of the liquid alloy, surface turbulence due to delivery or pouring during casting process can easily fold the oxide film upon itself, creating a double oxide film defect- a kind of entrainment defect. This partly explains why the mechanical properties and reliability of aluminium castings are highly sensitive to the manner in which the liquid alloy is treated and also the way in which it is subsequently transferred into the mould. The entrained double oxides films (bifilms)

constitute cracks within the liquid that are subsequently frozen into the component, and are believed by some researchers to be associated with the formation of void defects, *e.g.* shrinkage porosity and gas porosity, resulting in unreliability of the castings [6, 7].

Although the concept of oxide entrainment defects in the aluminium casting has been gradually accepted in the past two decades and studies of their behaviour and effects in castings have been conducted, there is still lack of fundamental evidence for their behaviour in liquid and solid alloys, and it remains difficult to identify the specific locations at which free surface entrainment occurs, or even predict the final distribution of these defects in solidified casting.

To understand the entrainment location and to track the distribution of entrainment defects during a casting process, a numerical algorithm named the Oxide Film Entrainment Model (OFEM), which is able to locate entrainment events in complex 3D flows, has been developed by Reilly at University of Birmingham as a customised subroutine within the commercial software *FLOW-3D*, and preliminary studies conducted to validate the outputs [8]. The model makes assumptions about the physical characteristics (size and density) and behaviour of the entrainment defects within the liquid. The defects are also treated as sites for heterogeneous nucleation of microporosity. Previous study has demonstrated the potential of the algorithm in predicting surface turbulence and entrainment defect formation [8], but further experimental validation is still required to assess the accuracy of the algorithm.

1.1 Objectives of This Work

The objectives of this project are:

- To validate the OFEM algorithm for tracking entrainment defects in castings.
- To develop a quantitative assessment based on OFEM for predicting mechanical properties of aluminium castings.

- To characterise the behaviour of entrainment defects in the liquid state and during solidification.

Working with high purity and automotive aluminium alloys, experimental investigations were conducted using real-time radiographic imaging of the fluid flow to resolve defect formation and possible transport. Both numerical modelling approaches and experimental work have been conducted and used to establish probabilistic distributions of defects formed by different entrainment mechanisms. Individual defects were characterised using synchrotron X-ray microtomography techniques and changes in defect morphology characterised further as a function of time within the liquid alloy. Critical casting experiments have been developed to verify the predicted defect formation and consequent distributions.

It is hoped that increased understanding of the behaviour of entrainment defects will provide more information to improve the model, and further development of the model can resolve the formation of entrainment defects and track the final locations of the defects, eventually developing a model as a tool for casting process optimisation.

1.2 Thesis Layout

The thesis is constructed in the following way: A literature review is given in Chapter 2 including: the formation and evolution of entrainment defects and their influences on mechanical properties of aluminium castings, the computational modelling methods used for studying entrainment defects, and X-ray microtomography of materials and defects. In Chapter 3, modelling methods are introduced, and the boundary conditions of models for validation of previous experimental study, three entrainment mechanisms experiments, the heating profile in the X-ray microtomography study, and tensile bar mould models are detailed. The contents in Chapter 4 correspond to those in Chapter 3, and explain the experimental procedures followed in the practical work, giving the moulding and pattern work, heat treatment and mechancial testing details for three

entrainment mechanisms and tensile bar mould experiments and synchrotron X-ray microtomography work. Chapter 5 reports the useful experimental and modelling results obtained from the four parts of the work in chronological sequence as the project was conducted. In the modelling results, interpretation focuses on the quantitative comparison between the predicted quantity of defects and the experimentally obtained tensile strength of castings. Characterisation of entrainment defects was concentrated on their morphology. The X-ray microtomography results are detailed with explanation of the categorisation and morphology evolution of entrainment defects. In Chapter 6, the entrainment mechanisms in the casting and the OFEM algorithm, the influence of different modelling conditions on the modelling results, the limitation of the OFEM model *per se.* and the characteristics of entrainment defects are discussed. Finally, principal conclusions and potential future work are given in Chapter 7 and Chapter 8 respectively.

Chapter 2

Literature Review

The Literature Review begins with a description of the formation of entrainment defects during the casting process and their influence on casting properties, followed by a detailed review of the modelling methods of the defects and associated validation approaches. The principles of microtomography for characterisation of materials, especially for small defects are reviewed afterwards.

2.1 Entrainment Defects

At room temperature, the exposed surface of aluminium reacts with oxygen in the surrounding atmosphere and forms an inert aluminium oxide film of the thickness of tens of nanometres. This thin oxide film does not flake off to expose fresh surface and behaves as a barrier between the metallic surface and atmosphere to hinder further oxidation of aluminium [2]. At temperatures above the melting point of aluminium, an amorphous alumina film forms at the surface of the melt initially, but after a few minutes incubation time, the film transforms to γ-Al_2O_3, and then can transform to α-Al_2O_3 after approximately five hours depending on the holding temperature [9–12]. Studies reported alloy elements can alter the oxidation products. For instance, the addition of magnesium in aluminium results in three different oxides in melt, *i.e.* Al_2O_3, MgO and $MgAl_2O_4$, depending on the magnesium content [9, 10, 12]. The alloying elements in the molten aluminium also affect the oxidation rate. Silicon, copper, zinc and

iron have little effect on the oxidation behaviour, whilst magnesium, sodium, selenium and calcium increase the rate of oxidation [13], and strontium decreases the rate [14]. Studies also pointed out that higher temperature and relative movement between oxygen and the melt increase the oxidation rate [12, 15–17]. Although most research on oxidation of aluminium and its alloy concern the growth rate and transformation of oxides at a long time scale, investigation of the characteristics of oxide films in aluminium alloys in short time scale showed that the thickness of the oxide film can be 150 nm after an exposure time of 0.1 s, or even thicker in dynamic conditions [18–21]. In the casting process of aluminium alloys, oxide film can either form when the alloy is being melted or when the alloy is being poured. The oxide films created in the former scenario have had a longer time to react with the atmosphere, and hence are thicker and stronger, and are normally named "old" films; the latter have relatively limited time to grow and consequently thinner and weaker, and are called "young" or "new" films [22,23]. But the sizes of "young" and "old" oxide films that found on the fracture can be similar, as both of them can be broken into small debris during casting. It should be noted that "young" and "old" are only descriptive for the morphology of oxide film in casting, and should not be treated as two different oxides or defects.

Due to the high affinity of aluminium for oxygen, the free surface of liquid aluminium is almost inevitably covered by a layer of oxide film all the time, during transfer or pouring in the casting process. Considering the high melting point of the oxides in aluminium, *e.g.* 2051 °C for Al_2O_3, 2800 °C for MgO [24], the oxide film would always be a solid in the melt once they form in the casting process. The oxide films remaining on the surface of the casting can be machined off, and fine oxide particles can act as potent sites for nucleation of aluminium and grain refinement, and hence, increase the strength of castings [25]. However, once the surface oxide films are folded and entrain into the bulk liquid flow, forming entrainment defects (defined below), the submerged oxide film can be extremely harmful to the casting properties or "dominate the strength

distribution of any set of castings" as concluded by Campbell and Green [22].

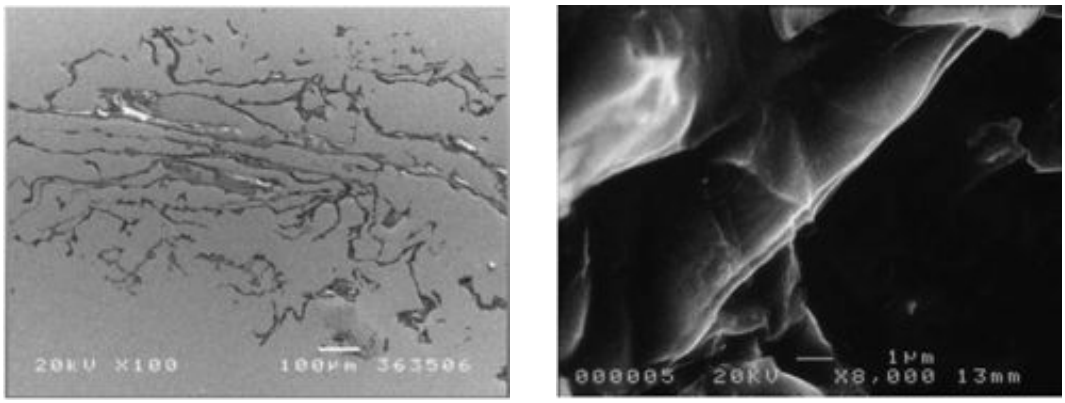

(a) **(b)**

Figure 2.1: Examples of the morphology of oxide film defects examined by microscopes [7]. (a). tangled double oxide film; (b). folded thin film.

Entrainment defects, principally entrained bubbles and bubble trails, doubled-over oxide films and entrained debris [7], are very common in castings, but it seems they have been overlooked in earlier research, especially the doubled young oxide films. This was mainly due to the difficulty in detecting the thin, convoluted films. However, metallographic and fractographic analyses have confirmed the existence of entrainment defects in the casting [7,26–28]. For instance, Figure 2.1a shows a relatively thick double oxide film on a polished sample. Figure 2.1b shows a thinner folded oxide film on a fracture surface. Microscopic observation can only detect defects and reveal the morphology of individual defect in very small volumes of material, and hence double oxide films in other areas of a casting would be easily missed. Based on the hypothesis that double oxide films trap a thin layer of gas between their two halves, Fox and Campbell carried out a reduced pressure test (RPT) and successfully visualised entrained double oxide films in the casting. In their tests, the liquid alloy was allowed to solidify in a chamber in which the pressure was lower than the atmosphere pressure, consequently the trapped air expanded in the casting and the morphology of the defects was captured [29]. Figure 2.2 shows the results from Fox and Campbell, which compares the

morphology of the defects within the castings that were solidified at different pressures, revealing the locations of defects and the unbonded nature of double oxide films. These efforts have provided direct evidence that entrainment defects exist in castings, which also inspired researchers to explore more about entrainment defects.

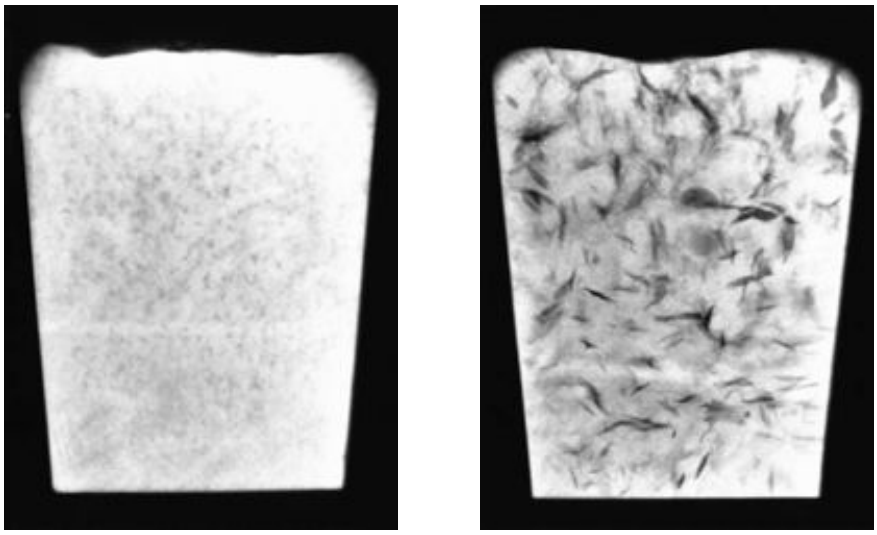

(a) **(b)**

Figure 2.2: X-ray images of Al-7Si-0.4Mg alloy subjected to solidification under two different pressures [29]. Images were taken at same time after pouring from (a). 1 atmosphere; (b). 0.01 atmosphere.

2.1.1 Formation of Entrainment Defects

Formation of entrainment defects requires surface turbulence of the flow. The Weber number (We), which is the ratio of the inertial force to the surface tension of the liquid, determines if surface turbulence would occur. Equation 2.1 gives the definition of Weber number, where l is the characteristic length (m), v is the characteristic velocity ($\mathrm{m \cdot s^{-1}}$), ρ is the density of the liquid ($\mathrm{kg \cdot m^{-3}}$) and γ is the surface tension ($\mathrm{N \cdot m^{-1}}$) [30]. When We is greater than 1, the inertial force exceeds the surface tension and sufficient to disturb the liquid surface, but only when We reaches the critical value, the surface turbulence can then generate in the fluid flow. Various critical We values has been reported in different casting processes. Campbell suggested a general value of 100,

at which surface turbulence would generate with jumping and splashing to a height, folding the surface film into the liquid, and consequently forming doubled over oxide film (bifilm) defects [6]. These defects constitute cracks, or enfolds some air forming micro bubbles, or even contain inclusions, as the schematic shown in Figure 2.3.

$$We = \frac{lv^2\rho}{\gamma} \tag{2.1}$$

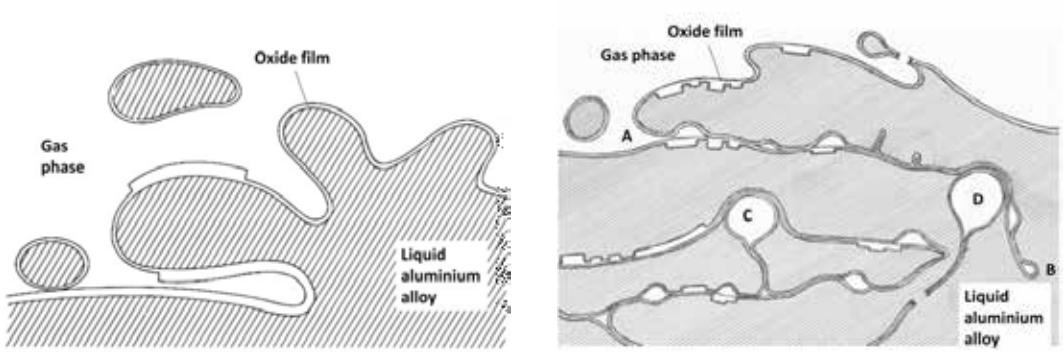

(a) **(b)**

Figure 2.3: Schematic representations of surface turbulence causing the entrainment of surface films forming defects: a folded-over film (A to B) and bubbles with trails (C and D).(a). surface turbulence [6]; (b). entrainment defects [7].

Poorly designed running systems always cause the development of surface turbulence during filling. For instance, incorrectly tapered downsprue would generate a persistent plunging jet near the exit of the sprue. There are several commonly seen entrainment mechanisms in the casting process, *e.g.* *a*). plunging jet, *b*). rising jet, *c*). returning wave, and *d*). colliding fronts [6], as shown schematically in Figure 2.4. Although the directions of flow are different in these entrainment mechanisms, all of them involve folding and breaking up of the surface oxide films and subsequently entrainment of the folded-over double oxide films and debris into the melt. Besides, surface turbulence not only entrains surface films, but also directly entrains air to form micro-bubbles, which if not eliminated would later exist as pores in the solidified casting. It should be noted that the terms of different entrainment mechanisms here are

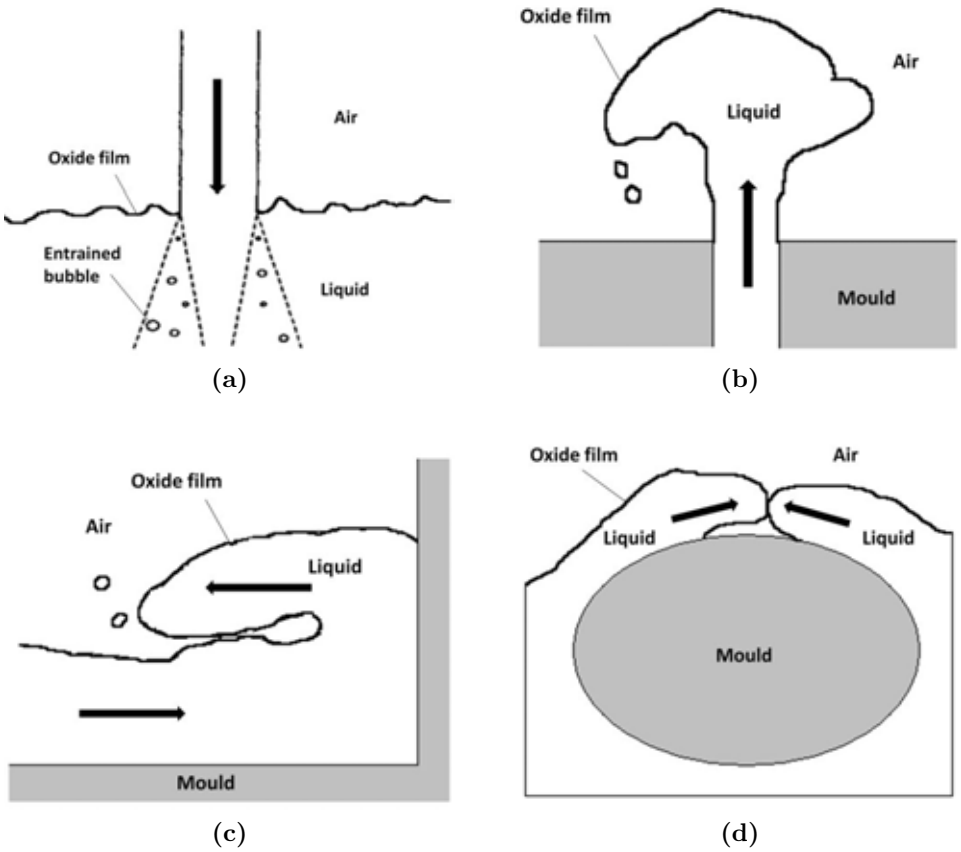

Figure 2.4: Schematics of commonly seen entrainment mechanisms during filling in casting. (a). plunging jet; (b). rising jet; (c). return wave; (d). colliding fronts.

descriptive, and do not necessarily agree with the definition of those terms used in fluid mechanics. For example, in fluid mechanics plunging jet flow describes the flow condition that the fast moving liquid jet impacting on the slower moving bulk liquid. Plunging jet and return wave in Figure 2.4(a and c) both involve fast incoming flow impinging on the bulk flow. Therefore, they could be plunging jet type of flows in different manifestations [31].

2.1.2 Evolution of Entrainment Defects

2.1.2.1 Furling and Unfurling

Once the double oxide films and debris are entrained in the bulk liquid, they are carried along and deformed by the bulk turbulence of the flow in the mould. Owing to the thinness and low rigidity of the oxide film, it can be convoluted or broken, forming a compact and tangled defect. The surface area of the convoluted oxide film does not necessarily decrease, or even increases during the furling, as new films would form at the ruptured points of the film. Since the two layers of the doubled film cannot bond together in the short period during filling [32, 33], and thus leave a gap or trap gas between the two layers, it can later act as a crack initiator in the solidified casting. Meanwhile, directly entrained bubbles can exist as pores or float up, creating bubble trails.

When the filling of a mould is completed, the bulk turbulence subsides and the casting cools and solidifies. Campbell suggested that during this period the compacted defect would undergo an unfurling transformation, in which the defect could unravel until it forms a planar crack-like defect close to its initial size, and this transformation would determine the properties of the casting [6]. This transformation of entrained defect depends on the original morphology and size of the defect, the thermal properties of the alloy, the hydrogen content in the surrounding liquid alloy, and the solidification time of casting. Campbell proposed several unfurling mechanisms, the driving forces including a). gas precipitation from solution, b). hydrostatic strain due to solidification

contraction, c). uniaxial strain due to linear contraction in the solid state, d). dendrite pushing, and e). nucleation and growth of intermetallics [7].

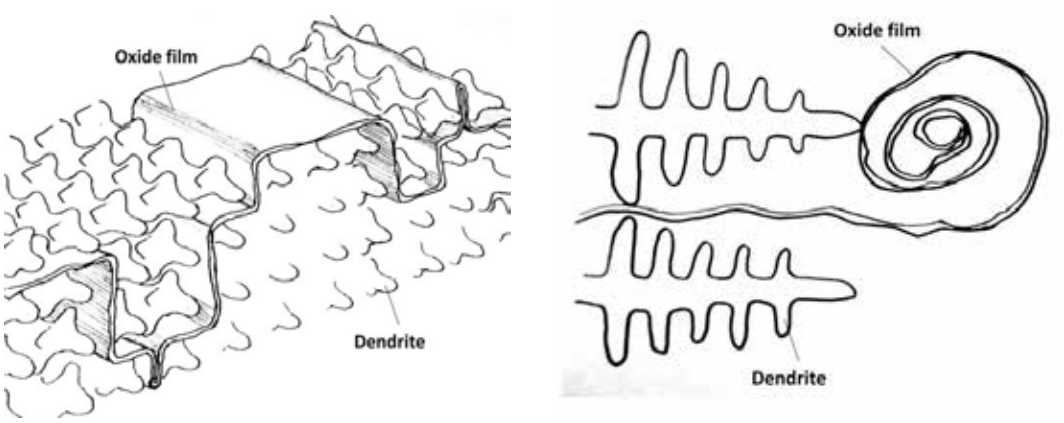

(a) **(b)**

Figure 2.5: Schematic of advancing dendrites to straighten convoluted surface film. (a). film flattened [6]; (b). film unrolled.

The first mechanism is detailed in the next section. The two contraction related mechanisms (b and c) are easy to accept, as the negative pressure caused by shrinkage during solidification can expand the volume of entrained double oxide films to offset the volume loss, and the isotropic contraction of the casting in solid state would readily increase the space between the two layers of the unbonded or weakly-bonded double oxide films. In regard to dendrite pushing (mechanism d), since the growing dendrite fronts cannot penetrate oxide films, Campbell speculated and gave an example that the advancing dendrites pushed the debris of films into the interdendritic spaces and flattened the convoluted films, as shown in Figure 2.5 [7]. He argued that when one end of the film was attached to the mould wall or fixed by the root of the dendrites, the growth of the dendrite tips might mechanically iron out the furled films, as illustrated in Figure 2.5b. However, no experimental evidence provided for this mechanism. However, Cao and Campbell observed the nucleation of Fe-rich phase in the aluminium casting, providing direct evidence that primary α-Fe particles prefer to nucleate and grow on the wetted exterior sides of doubled oxide films [27]. Campbell supposed that

this progressive growth of the crystal could force the tangled films to straighten [7] and corresponded to mechanism *e*. Bangyikhan further added that the hydrogen could penetrate into the trapped films, forcing the double film to inflate along the platelets of the Fe-rich phase, forming crack-like double oxide film defects [34].

2.1.2.2 Relationship between Entrainment Defects and Porosity

Porosity in aluminium is mostly caused by the precipitation of hydrogen from liquid solution (*i.e.* gas porosity) or by shrinkage during solidification (*i.e.* shrinkage porosity), and more commonly by a combination of the two [35]. In terms of gas porosity, hydrogen is the only gas that has appreciable solubility in aluminium and its alloys. The hydrogen solubility is significantly greater in liquid aluminium than in the solid state, and increases dramatically with increasing temperature above the liquidus, as shown in Figure 2.6. Therefore, conventional nucleation theory of gas porosity in aluminium castings refers to precipitation of the excessive dissolved hydrogen in the form of gas molecules, which must be thermodynamically stable and can initiate pore growth [35,36]. The driving force for nucleation is the thermal fluctuation that provides the energy required to overcome the nucleation energy barrier in the system. The nucleation of a pore in liquid reduces the bulk free energy and increases the energy related to the formation of the interface, which can be described by Equation 2.2,

$$\Delta G = -V\Delta P + A\gamma \tag{2.2}$$

where V (m^3) is the volume of the pore, ΔP ($\mathrm{N\cdot m^{-2}}$) is the pressure difference between the exterior and the interior of the pore, A (m^2) is the surface area of the pore and γ ($\mathrm{N\cdot m^{-1}}$) is the surface tension of the interface between the gas and liquid phases. Considering the formation of a spherical pore with a radius of r (m), the work required for homogeneous nucleation of the pore in the liquid can then be expressed as [6]:

$$\Delta G = -\frac{4}{3}\pi r^3 \Delta P + 4\pi r^2 \gamma \tag{2.3}$$

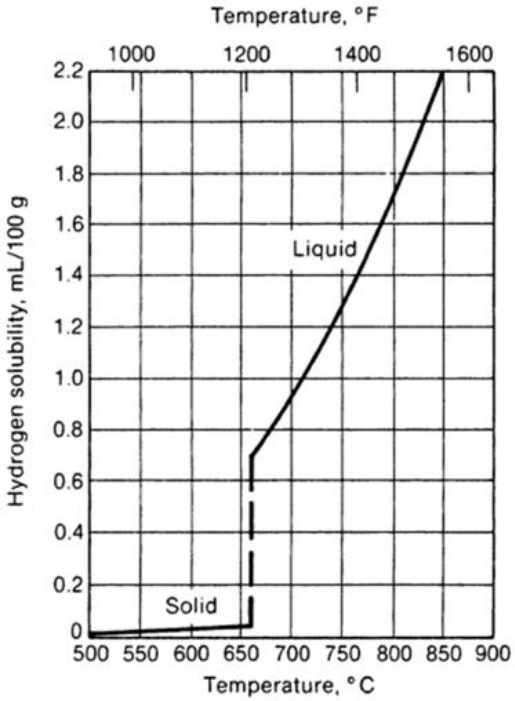

Figure 2.6: Solubility of hydrogen in aluminium at 1 atm hydrogen pressure [35].

The first part at the right of the equal sign describes the bulk free energy decrease during the process, and the second part describes the increase in the energy related to the formation of the liquid/gas interface in the system. The maximum work ΔG_{max}, *i.e.* the energy barrier needed to be overcome for pore nucleation, is achieved when the radius of the pore reaches $r_c = 2\gamma/\Delta P$, and hence, $\Delta G_{max} = 16\pi\gamma^3/3\Delta P^2$. For liquid aluminium alloy, the critical pressure difference (ΔP) for homogeneous pore nucleation is as high as 30 000 atm [6, 37], which makes the homogeneous nucleation of pores in the liquid aluminium alloy in normal atmospheres extremely difficult.

Conventional heterogeneous nucleation theory of pores considers the inclusions and other substrates in the liquid as the nucleation sites. The contact between the liquid phase and the solid substrate reduces the energy barrier for pore nucleation significantly, and the reduction closely relates to the contact angle, which depends on the balance of surface tension forces at the junction where the solid, liquid and gas phases meet. With a small contact angle, the pressure difference estimated from Equation 2.3

is 10 to 100 atm [37], suggesting heterogeneous nucleation of a pore is more realistic in the casting process. However, Campbell compared the homogeneous and heterogeneous nucleation theories, and pointed out that the heterogeneous nucleation of a pore in aluminium alloy was still impractical, as the minimum contact angle (approximately 20°) between the liquid/pore interface and the substrate in reality still requires a high pressure difference, (although it is about 5% of that in homogeneous nucleation), and thus, the energy barrier for pore nucleation is still difficult to overcome [6].

Instead, Campbell proposed a nucleation-free mechanism for porosity formation in the casting based on the unfurling of entrainment defects in the liquid alloy [6, 7]. He suggested entrainment defect, containing residual entrained gas, as the easiest initiating feature, because the unbonded layers can be separated with minimum effort. In his theory, the entrainment defect exists as pre-formed porosity, while excessive hydrogen in the liquid can precipitate into the gap of the entrainment defect and unfold the compact double oxide films, as illustrated in Figure 2.7. Therefore, hydrogen precipitation can assist the growth of porosity, but the initial shape of entrainment defects, the hydrogen content and the solidification times of castings would determine the morphology of the porosity. For example, spherical pores form only when the double oxide films are simply folded and there is sufficient hydrogen to inflate the porosity as shown in Figure 2.7a through to Figure2.7c. Shrinkage during solidification can open the porosity further. However, Campbell did not mention the extra work that need to be applied to displace the liquid around the defect, which might be significant, because the calculation of the homogeneous nucleation of pore has showed the difficulty to displace the liquid and expand the interface between the liquid and the gas. So the unfurling and inflation mechanisms shown in Figure 2.7 still need further investigation.

Because of the size of entrainment defects and their unpredictable locations, the unfurling mechanisms of gas precipitation are difficult to be directly observed. Raiszadeh and Griffiths conducted an experiment which mimicked the behaviour of a trapped air

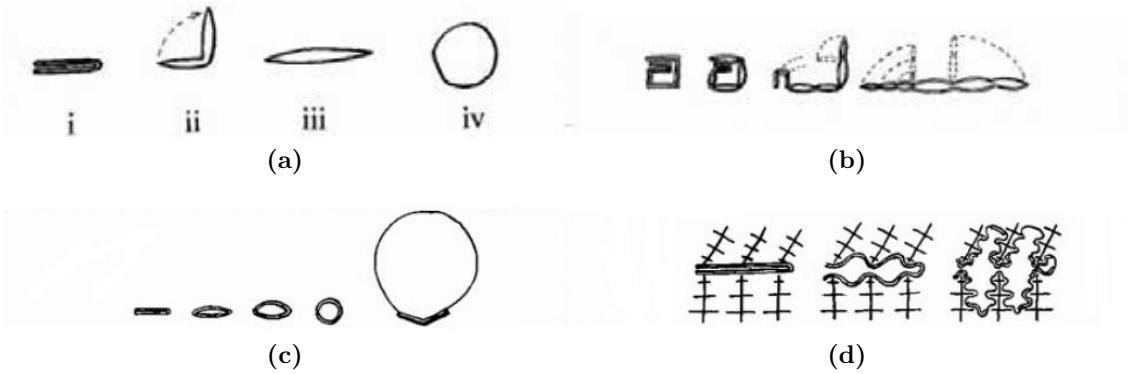

Figure 2.7: Schematic of unfurling and inflating of doubled films [7].(a). simply folded double film ; (b). tangled convoluted double film; (c). over-inflation of double film; (d). the over-inflation of a folded film resulting in an interdendritic pore.

bubble with a known amount of air within the melt. They continuously monitored the volume change of the air and examined the reaction products on the interface between the air and the melt. The results showed that if the initial hydrogen content of the melt was higher than the equilibrium amount associated with the ambient atmosphere, hydrogen diffused into the trapped air bubble and caused its expansion [28]. The experiment proved that double oxide films in aluminium alloy melts could act as initiators of hydrogen porosity. Further study in similar conditions pointed out that the unfurling mechanisms by hydrogen passing into or out of the trapped air in double oxide films should involve physical damage to the oxide films to create a pathway for the gas precipitation [38], because the oxide films hinder the passage of hydrogen.

Campbell claimed that the unfurling mechanism is the major nucleation mechanism of pore in aluminium alloy, if not the only one [6]. However, the unfurling mechanisms is not universal. Felberbaum and Rappaz applied synchrotron-based X-ray tomographical observation to examine the micropores in Al-Cu alloy and found some unconventional pore morphologies, which were suspected to be associated with double oxide films. These micropores only accounted for less than 5% of the total cases in the experiment involving pouring process, especially when the hydrogen content was low, and were not found in the experiment set-up without pouring process [39]. Therefore, the growth of

gas porosity by the double oxide films may be a significant mechanism only when the liquid feeding and/or the filtration systems are not properly designed. Further *in situ* observation of the evolution of entrainment defects is required to verify the unfurling mechanisms on initiating porosity in castings.

2.1.3 Effects on the Mechanical Properties of Castings

The main influences of entrainment defects on the mechanical properties of castings besides acting as porosity growth sites, are that they reduce the load bearing area, and hence lower fracture strength, and/or initiate cracks, and thus, reduce fatigue life of casting. Both decrease the reliability (reproducibility of mechanical properties) of castings.

In an early study of the effects of entrainment defects on the mechanical properties of castings, Green and Campbell studied the relationship between filling conditions and the tensile strength of castings. Their fractographic analysis of the test bars found tangled oxide films on the fracture surfaces. They pointed that poorly designed filling methods would result in high surface turbulence during filling, and consequently, more entrainment defects; and the entrainment defects generated by the surface turbulence would cause premature failure of castings [22, 40]. Dai *et al.* compared different running system designs in experiments and computational models, and demonstrated that the level of entrainment during filling was inversely proportion to the strength of castings [41, 42]. Cáceres and Selling studied the relationship between casting defects and tensile properties of Al-Si-Mg alloy. They showed that the bulk porosity content had little effect on both ductility and tensile strength of castings, but highlighted the significance of dross and oxide films on decreasing the strength of castings [43]. Other researches also confirmed that the presence of structural defects such as porosity and entrained oxide films in aluminium castings has the general effect of reducing elongation in tensile tests [44–46].

With regard to the effects of entrainment defects on the fatigue life of castings, a study of the influence of porosity on fatigue behaviour of Al-Si-Mg alloy by Major pointed out that the quantity of oxide films in the melt was directly linked to the pore size, which in turn determined the fatigue life [47]. Nyahumwa *et al.* conducted detailed research on the effects of oxide films on fatigue life of Al-Si-Mg alloy and found that most of the cracks initiated at oxide films, both "young" and "old" [23]. This was later confirmed by Zhang *et al.* , as they reported the oxide films near the surface of castings initiated cracks regardless of the size of the secondary dendrite arm spacing (SDAS) of the casting, which was believed to be the microstructural effect that controlled the fatigue behaviour of castings [48]. Jiang *et al.* compared the fatigue lives of sand-cast and die-cast Al-Si-Mg alloy, and found that the detrimental effects of oxide films were as important as porosity in sand castings, and oxide films played more important role in controlling fatigue life in die castings, as there were much higher levels of surface turbulence generated during the process, and hence more oxide film defects created [49]. However, Wang *et al.* later studied the effects of defects on fatigue life of a similar alloy and showed porosity was more detrimental to fatigue life, as porosity was always associated with brittle phases such as eutectic silicon and other intermetallic particles in castings, and the three-dimensional morphology of the pore resulted in isotropic impacts on the fatigue properties of casting under different applied stress directions [50]. Although the oxide films always led to sharper cracks, their influences depended on the loading direction. Later a review paper written by Wang *et al.* concluded that oxide films and porosity had a dominant effect on fatigue life that can be rationalised with fracture mechanics. He also highlighted that for defects of the same size (projected area), oxide films are often less detrimental to fatigue life than pores [51].

Currently, the relative importance of oxide film defects and porosity in determining the fracture and fatigue properties of casting is not entirely clear. Campbell claimed

that gas and shrinkage porosity are the secondary defects initiated from oxide film defects [7], but further examination on the porosity and oxide film defects on the mechanical properties of castings is still needed to validate this conclusion as mentioned in Section 2.1.2.2.

The presence of oxide films adversely affects the reproducibility of the mechanical properties of castings, resulting in higher variability of strength or fatigue lives of castings from the same batch. Green and Campbell proposed a quantitative measurement for casting reliability based on the two-parameter Weibull distribution, as summarised in Equation 2.4:

$$F_w = 1 - exp\left[-\left(\frac{x}{\sigma}\right)^{\lambda}\right] \tag{2.4}$$

where F_w is the probability of failure of specimens failing at or below a given value of x, *e.g.* ultimate tensile strength (UTS) or fatigue life, σ is a characteristic value of x, at which 62.8% of the population of specimens have failed, and λ is the Weibull modulus [40]. F_w can be estimated by Equation 2.5, as suggested by Khalili and Kromp [52]:

$$F_w = \frac{n - 0.5}{N} \tag{2.5}$$

where n is the ranking of the specimen when all results are ranked in an ascending order and N is the total number of specimens. A linear relationship of the results can be obtained by plotting $ln(x)$ *vs.* $ln\{ln[1/(1 - F_w)]\}$, making λ the slope of the fitted curve. The greater the value of λ, the narrower is the range of the data, hence the higher reliability or reproducibility of the properties.

Green and Campbell used Weibull distribution to demonstrate that the highly surface turbulent filling of a mould resulted in a low reliability of castings [40]. The Weibull analysis was adopted by many researchers and similar results have been observed by other researchers in different casting techniques, *e.g.* sand casting, investment casting and by different filling methods, such as gravity filling, tilt filling and counter-gravity filling [41, 53–55].

Using the Weibull distribution, Gokhale and Patel found the origins of variability of mechanical properties of Al-Si-Mg alloy were due to the presence of both porosity and oxide films [56, 57], but Eisaabadi *et al.* demonstrated that oxide films led to a larger scatter of properties compared with porosity, as castings containing more oxide films showed a higher standard deviation and lower Weibull modulus in their properties [46]. Since the variability of properties is also linked with the size distribution of defects, the relative importance of porosity and oxide films on influencing the scatter of properties is still debatable. With regard to the method of studying reliability of casting, a "Weibull Mixture" was proposed by Tiryakioğlu and Campbell, which was referred to the three-parameter Weibull analysis [58]. This distribution could reveal the effects of two types of defects that were present in casting structures and impairing properties at different levels. Therefore, it has the potential to be applied in the study of the reliability of castings with different defect types, such as oxide films and porosity.

2.1.4 Healing of Entrainment Defects

Complete healing of entrainment defects requires two processes: closure of the double oxide film and bonding between the two layers. The closure of double oxide films can be achieved either by application of external pressure or by consumption of internal atmosphere [7]. Literature has reported the application of hot isostatic pressing (HIP) increasing the fatigue life of aluminium castings, as the process reduced the size of defects, particularly pores and oxide films [59, 60]. On the other hand, as proposed by Nyahumwa *et al.*, the trapped oxygen and nitrogen in the double oxide films could be consumed by the surrounding liquid alloy during holding and solidification, and once the two oxide layers contacted with each other, the rearrangement of atoms would lead to diffusion bonding at the contact points [60]. The consumption of interior gas phase in the double oxide film has been verified by Raiszadeh and Griffiths, and their observation suggested most of the internal gas phase in the double oxide films could be consumed within three minutes and only residual argon and excess hydrogen would

remain, causing partial contact at some points of the two layers [28, 38, 61]. However, the bonding between the two oxide layers is much more difficult. Since the oxides of aluminium and aluminium alloy are stable, the bonding would form at the contacting points only when the transformation of the oxide occurs, *e.g.* from Al_2O_3 to $MgAl_2O_4$ in Al-Si-Mg alloy or from γ- to α-Al_2O_3 in commercial purity aluminium. Since these transformations take from several tens of minutes (in Al-Si-Mg alloy) to several hours (in commercial purity aluminium) in the liquid state [32, 33], double oxide film defects cannot self-heal in normal casting processes, but holding the liquid metal within the mould at high temperature or HIPping can reduce the adverse influences of oxide film defects on casting properties.

2.2 Computational Modelling of Entrainment Defects

Since the sizes of entrainment defects are usually below the resolution of conventional non-destructive testing (NDT) techniques, detection of the location of these defects in castings is extremely difficult. Observation of the flow conditions that can generate entrainment defects during filling is feasible, for example, by real-time X-ray radiography facility, but determination of the final distribution of the generated defects in solidified castings is challenging. As modelling techniques for casting simulation and performance of computer hardware improve, computational modelling provides solutions for simulating entrainment defect, showing their motion and predicting their final distribution in a casting.

To accurately model the casting process it is necessary to model two stages, the filling process (fluid flow) and solidification (heat transfer). The filling process can be simulated by general purpose computational fluid dynamics (CFD) software, such as *CFX*, *FLUENT*, *FLOW-3D* and *OpenFOAM*. The solidification model of a liquid alloy involves heat transfer and phase transformations. Modelling of shrinkage, gas porosity

and solidification microstructures employ different in-house codes or commercial software packages. Various successes have been achieved in modelling shrinkage related defects in metal castings [62]. Several casting simulation software, including *MAGMAsoft*, *ProCAST*, *THERCAST*, and *PHYSICA*, etc., have successfully integrated these two stages into their package and these optimisation software have been used in the casting industry and research laboratories [63]. However, entrainment defects that form by surface turbulence during the filling process still cannot be modelled by these packages. Modelling the formation and distribution of entrainment defects requires precise modelling of both the motion of the liquid free surface and multiphase interactions as the gas is trapped in the double oxide films. To model the movement of a thin film with a thickness of several micrometer requires a very fine mesh and the solution cannot be obtained within a reasonable simulation time. Therefore, direct modelling of the entire entrainment processes is currently believed as unfeasible considering the complexity of the process and current computational power.

However, a variety of approaches to consider the entrainment and its associated defects in casting process have been developed. In general, these approaches either treat entrainment defects as discrete objects or integrate them into the solution of the bulk fluid flow, but either method requires a robust CFD solver to correctly reproduce the flow field in the mould and accurately model the movement of the free surface of the liquid.

2.2.1 Background

A brief description of the common CFD models and methodologies is given here. Liquid metal can be treated as an incompressible Newtonian fluid. Its motion under gravity can be represented by the Navier-Stokes equations shown below [64] (Equations 2.6 to 2.8):

$$\rho \frac{Dv_x}{D_t} = \rho g_x - \frac{\partial P}{\partial x} + \mu \left(\frac{\partial^2 v_x}{\partial x^2} + \frac{\partial^2 v_x}{\partial y^2} + \frac{\partial^2 v_x}{\partial z^2} \right) \tag{2.6}$$

$$\rho\frac{Dv_y}{D_t} = \rho g_y - \frac{\partial P}{\partial y} + \mu\left(\frac{\partial^2 v_y}{\partial x^2} + \frac{\partial^2 v_y}{\partial y^2} + \frac{\partial^2 v_y}{\partial z^2}\right) \tag{2.7}$$

$$\rho\frac{Dv_z}{D_t} = \rho g_z - \frac{\partial P}{\partial z} + \mu\left(\frac{\partial^2 v_z}{\partial x^2} + \frac{\partial^2 v_z}{\partial y^2} + \frac{\partial^2 v_z}{\partial z^2}\right) \tag{2.8}$$

where v_x, v_y and v_z are the x-, y- and z-components of the velocity respectively, ρ is the liquid density, P is the pressure, μ is the dynamic viscosity and g is the gravitational acceleration. These partial differential equations coupled with other heat transfer equations can be solved by finite element method (FEM), finite volume method (FVM) or finite difference method (FDM). These methods all involve mesh generation, in which the whole domain is divided into simpler subdomains (elements) and an approximate solution obtained. The solvers based on these methods use different structures and types of elements, mainly dependent upon a compromise between the ability to capture the details of a flow field and the ability to define complex geometries, within a reasonable computation time. Several turbulence models have been developed in the CFD field and internal fluid turbulence can also be predicted [65].

Obviously, to accurately predict surface turbulence created entrainment defects, it is necessary to precisely define the free surface movement and capture the entrainment in the model. In casting modelling, two main methods have been applied to predict the free surface in CFD packages, the marker-and-cell (MAC) method, and volume of fluid (VOF) method [66]. The MAC method effectively tracks the free surface evolution as the mould fills with a liquid, but only calculates the value within the meshes in which liquid is present [67]. This approach can be applied in FDM and FEM, but is primarily a two-dimensional approach as it requires considerable memory and computation time. The VOF method was pioneered by Hirt and Nichols and is the most popular approach in casting simulation software for prediction of free surface movement. The method consists of three ingredients: a scheme to locate the surface, an algorithm to track the free surface as a sharp interface moving through a computational grid, and a means of

applying boundary conditions at the free surface [68]. VOF method has been developed and implemented in FDM and FVM codes.

The brief introduction below explains the method in 2D condition as it was initially proposed. The time-dependant step function F to locate the surface element is governed by Equation 2.9 [68], where t is the time, u and v are the velocities in x and y directions respectively. F defines the fluid volume fraction in a mesh element within a range from zero to one. When F in a mesh element is greater than zero but less than one, the element mesh contains a free surface.

$$\frac{\partial F}{\partial t} + u\frac{\partial F}{\partial x} + v\frac{\partial F}{\partial y} = 0 \tag{2.9}$$

Once surface element is located, the surface location and orientation will be determined. The location of the surface in a cell is defined by the single-value function $Y(x)$ or $X(y)$ as shown in Equations 2.10 and 2.11, where i and j are the indices of the mesh elements in x and y directions respectively, δx and δy are the sizes of the elements in x and y directions respectively.

$$Y_i = Y(x_i) = F(i, j-1)\delta y_{j-1} + F(i, j)\delta y_j + F(i, j+1)\delta y_{j+1} \tag{2.10}$$

$$X_j = X(y_j) = F(i-1, j)\delta x_{i-1} + F(i, j)\delta x_i + F(i+1, j)\delta x_{i+1} \tag{2.11}$$

The slope of the surface will be defined by Equation 2.12 and 2.13. If $|dY/dx|$ is smaller than $|dX/dy|$, the surface is more nearly horizontal than vertical and vice versa. If dX/dy is negative, fluid lies below the surface. After the surface slope and side occupied by fluid have been determined, the free surface of the liquid then can be reconstructed. The boundary conditions will be applied to both the computational domain and free surface. The details of the means to apply boundary conditions on the free surface can be found in the report from Hirt *et al.* [69].

$$(\frac{dY}{dx})_i = \frac{2(Y_{i+1} - Y_{i-1})}{\delta x_{i+1} + 2\delta x_i + \delta x_{i-1}} \tag{2.12}$$

$$(\frac{dX}{dy})_i = \frac{2(X_{j+1} - X_{j-1})}{\delta y_{j+1} + 2\delta y_j + \delta y_{j-1}} \tag{2.13}$$

VOF methods lead to a sharp interface, and small time step can be used for a given mesh to overcome the mass conservation problem in the VOF method, to approximate accurate results. Therefore, the VOF method has now been applied in many models [66].

Non-conventional computational fluid dynamics methods, such as the smoothed-particle hydrodynamics (SPH) and the Lattice Boltzmann method (LBM), can also be applied to solve the fluid flow problems in casting processes [70, 71]. Nevertheless, the simulation methods in this review are mostly based on conventional CFD software using the VOF method to track free surface movement.

2.2.2 Integrated Modelling of Entrainment Defects

2.2.2.1 Cumulative Entrained Free Surface Area Method

Sun *et al.* and Lai *et al.* used the area of free surface in the fluid to measure the magnitude of entrainment [72, 73]. The work by Sun *et al.* studied the defect formation in iron castings. They plotted the liquid free surface area against filling fraction of a component with two different running system designs. The results showed lower liquid free surface area in filling led to a reduced oxide defect rate, but no details of the modelling methods were reported [72].

Lai *et al.* determined the instantaneous free surface area in the model and plotted it as a function of time during filling, as shown in Figure 2.8. This was compared to the proposed baseline, which was defined by the instantaneous free surface area of liquid if the mould filling had been perfectly tranquil. The difference of free surface area between the turbulent and tranquil filling was used as a measure of entrainment. The work showed that, in their mould with simple geometries, the largest excess free surface area was gained during pouring the liquid alloy from the crucible into the mould [73]. Although Campbell later argued that using excess free surface area could not correctly

measure the real area of surface oxide film during filling [74], this work still highlighted the significance of the pouring stage to entrainment defects generation.

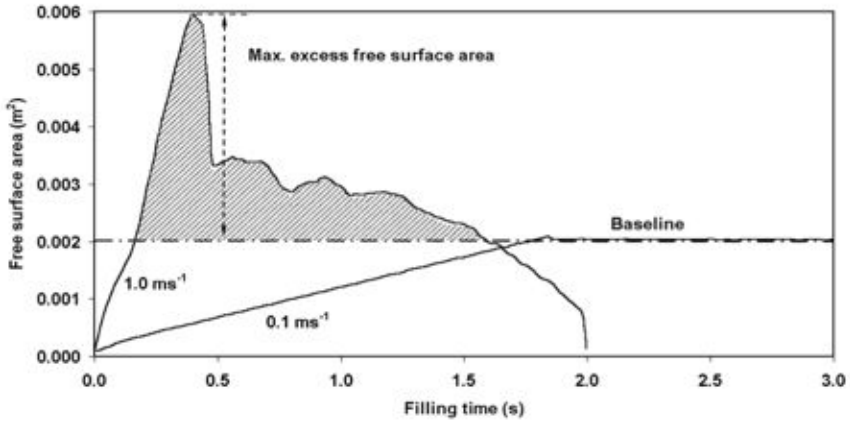

Figure 2.8: Potential surface oxide film entrainment quantified by considering the originated excess free surface area [73].

Measurement of entrained free surface area requires little computational effort, but there are two main drawbacks to Lai's work. Firstly, for a mould with complex geometry, it can be difficult to estimate the instantaneous free surface area of the liquid even in a quiescent manner, and secondly, the method gives no information about the formation and distribution of the entrainment defects. Nevertheless, this cumulative entrained free surface area method provided an informative indicator to illustrate at which stage of mould filling a large number of entrainment defects are likely to be generated.

2.2.2.2 Cumulative Surface Scalar Method

Some commercial software including *MAGMAsoft* and *FLOW-3D* use a cumulative surface scalar technique to track the formation of oxide film on the free surface of liquid metal. The method assumes that oxide film defects cumulate upon the free surface of the metal flow at a constant rate, and the quantity of the oxide films is recorded by a scalar in each mesh element. The scalar is allowed to advect with the bulk fluid, and thus, a final surface defect distribution can be obtained. Although

this approach neglects the folding or turbulence involved in the formation of double oxide film defects, it has shown promising results for the prediction of the location of surface defects, especially the confluence welds, which form when two flow fronts meet [75]. Figure 2.9 shows an example of a filling model using cumulative surface scalar in *FLOW-3D*, where the darker area represents higher defect concentration and the gray scales illustrate the diffusion of the scalar in the liquid.

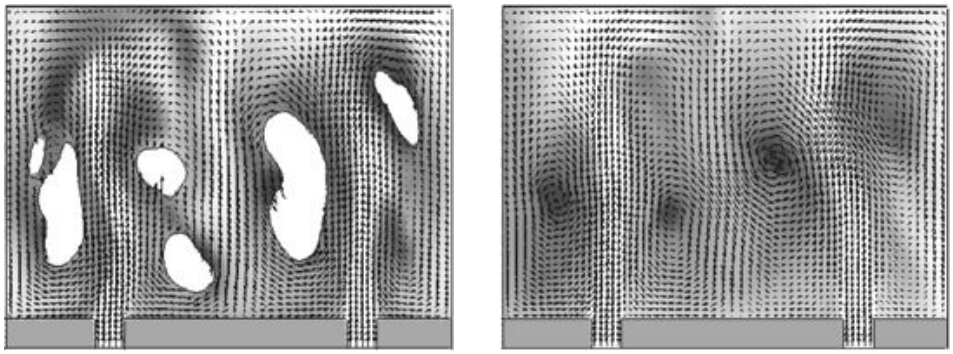

(a) **(b)**

Figure 2.9: Example of scalar distribution and filling pattern during high pressure filling process. The scalar variable represents oxide films and darker area indicates higher defects concentration [75]. (a). 90% full; (b). 100% full cavity.

Since there were no detailed experimental data to establish a relationship between the quantity of actual surface defects and the value of the scalars in the model, currently it is impossible to assign any significance to the absolute values of the scalar used in this technique. Besides, the cumulative surface scalar method does not account for any interaction between the entrainment defects and the fluid, and neglects the physical properties of individual defects.

These drawbacks can be overcome by using the SPH method with a similar cumulative scalar tracking technique, as the information about the surface oxide can be directly assigned to the particles at the interface and the particles can then be entrained into the bulk liquid without loss of history of the surface defects. A simplified linear relationship is used in some research to define the oxide content of any

particles [70, 76–78], as shown in Equation 2.14:

$$\frac{dO_x}{dt} = k_l \tag{2.14}$$

where t is time, O_x is oxide growth and k_l is a rate constant (10.9×10^{-3} kg m^{-2} s was used). Other more complex models for oxide growth rates can be applied in the same way to achieve more accurate results of surface oxidation. But no further development or validation of this method has been reported.

2.2.2.3 Air Entrainment Model

The cumulative surface scalar method can also be used to model the air entrainment at the liquid/air interface, in which the oxidation rate is replaced by the air entrainment rate. In *FLOW-3D* a more accurate algorithm based on a variable density formulation was developed to model the air entrainment by the surface turbulence at a free surface. The liquid splashes above a free surface raised by the turbulent eddies may entrap air and carry it back into the bulk liquid body. Based on this concept, this model assesses whether the turbulent energy at the free surface (P_t) is enough to overcome the surface stabilising forces of surface tension and gravity (P_d) [79]. The disturbance kinetic energy per unit volume (*i.e.* pressure,P_d), can be calculated by considering the height of raise liquid and the surface tension energy that shown in Equation 2.15:

$$P_d = \rho g_n L_t + \frac{\gamma}{L_t} \tag{2.15}$$

where ρ is the liquid density, γ is the coefficient of surface tension, g_n is the component of gravity normal to the free surface and L_t is a characteristic size of turbulence eddies, which is defined in Equation 2.16:

$$L_t = cnu\frac{\sqrt{3/2}Q^{\frac{2}{3}}}{D} \tag{2.16}$$

where cnu is a constant which is also used in the calculation of the turbulent viscosity, Q is the turbulent kinetic energy, and D is a dissipation function. For air entrainment

to occur the turbulent kinetic energy per unit volume, $P_t = \rho Q$, must be larger than P_d. The volume of air entrained per unit time V_a is given by Equation 2.17:

$$V_a = C_{air}\, A_s \sqrt{\left(2\frac{P_t - P_d}{\rho}\right)} \tag{2.17}$$

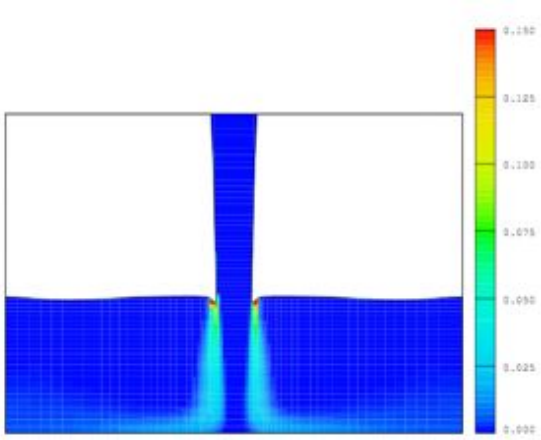

Figure 2.10: Example of a jet plunging into a pool. Colour scale indicates air volume fraction [79].

Figure 2.10 shows the validation example of a jet plunging into the liquid pool. The red spots in the impinging points show high air entrainment in those regions. The model was validated by comparing the volume of entrained air with previous studies on hydraulic jumps, spill ways and plunging jets in hydraulic engineering. Good correlation in predicting the location of entrainment was reported [79]. The drawback to this model is that it cannot model the size and movement of entrained air bubbles. Therefore, in a casting filling simulation, it can only illustrate the entrainment points in the filling system and show a contour map of potential gas distribution in the fluid, but no further information about the distribution of associated individual defects can be obtained. This is a common problem for integrated models for entrainment defects.

2.2.2.4 Dimensionless Number Criterion

Dimensionless numbers are commonly used in fluid mechanics, and several dimensionless number are applied to describe the interfacial conditions in fluid flow [80]. The

Weber number (We), which is a ratio of inertial force to surface tension, and the Froude number (Fr), the ratio of gravitational pressure to inertial pressure, are the two most used in research into the casting process. The Weber number is defined in Equation 2.1 and the Froude number is given in Equation 2.18, where v is a characteristic velocity ($\mathrm{m \cdot s^{-1}}$), l is a characteristic length (m), and g is the gravitational acceleration ($\mathrm{N \cdot kg^{-1}}$).

$$Fr = \frac{v}{\sqrt{gl}} \tag{2.18}$$

Campbell studied the "critical velocity" of liquid alloys entering a vertically oriented ingate of a mould, and defined the condition at which the surface would start to suffer surface turbulence. He then utilised the Weber number to quantify the entrainment of the fluid surface [6]. In theory, when $We = 1$ the inertial and surface forces are in balance, and hence less than 1 would result in no disturbance of the surface occur. However, in the casting industry smaller Weber number is adopted generally for higher casting integrity, with high pressure die casting as an exception, in which the We can reach 10000 [6].

Cuesta *et al.* followed the idea of a critical velocity and studied the effects of ingate geometries on the critical velocity for the surface film entrainment of aluminium and iron using the Weber number [81]. They modelled the liquid metal entering vertical ingates with round or rectangular cross sections using *FLUENT*, and validated the results against previously published data. This work showed that both the size and shape of the ingate had effects on the critical velocity, and round channels were less vulnerable to surface entrainment than the rectangular ones for the same entering velocity and channel area. The authors suggested that instead of using the arbitrary value of 0.5 $\mathrm{m \cdot s^{-1}}$ for the critical velocity that suggested by Runyoro *et al.* [82], the Weber number gave a better quantification of the occurrence and intensity of surface entrainment [81]. Although Cuesta *et al.* proposed several values of the Weber number for assessment of the entrainment, some flaws in the modelling work affected the validity of the conclusions. Figure 2.11 compares the modelling and experimental results of the

molten aluminium entering an open mould through an ingate. It is clear that some mismatch between the model and the experiments occurred. As the modelling was done in 2D, it might not be accurate enough to represent 3D filling conditions, especially when considering the geometric differences in the mould.

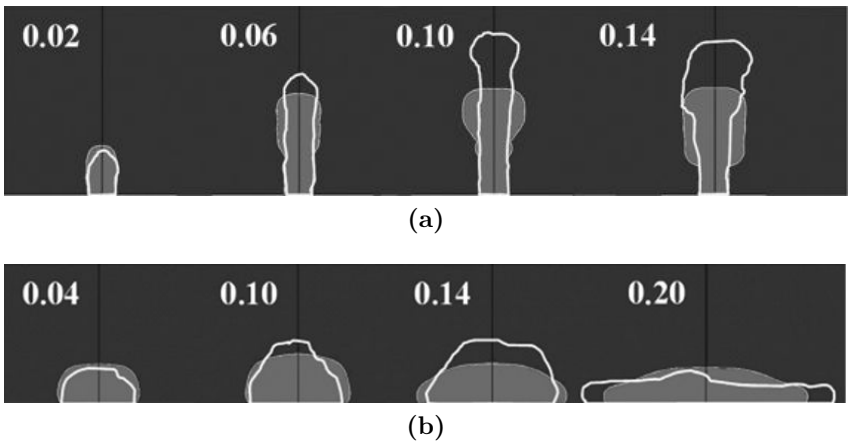

Figure 2.11: A comparison of modelling (shadowed) and experimental results (white-line encircled) for the flow of molten aluminium rising up from a channel, from Cuesta's work [81]. (a). 10 mm thick channel, melt speed of 0.85 m·s^{-1}; (b). 30 mm thick channel, melt speed of 0.34 m·s^{-1}.

In terms of the application of the Froude number, Reilly *et al.* applied the Froude number in a horizontal runner to create a criterion function and integrated this into *FLOW-3D* for quantification of entrainment during filling [83]. The flow regime in the runner bar was first classified as one of the four types, as described in Figure 2.12, then the relevant parameters were derived to calculate Froude number at pre-defined frequencies. The Froude number was then used to calculate a quantitative "total damage" value for each model to quantitatively compare the entrainment level between running systems. Similar techniques were later used for extracting the Weber number and the Hsu number, the latter being a ratio of inertial pressure to gravitational plus surface tension pressure, as defined in Equation 2.19, where H is the fluid depth (m), and the other parameters are the same as those used in the definitions of Weber and

Froude Numbers.

$$Hsu = \frac{\rho v^2}{\rho g H + \frac{4\gamma}{H}} \tag{2.19}$$

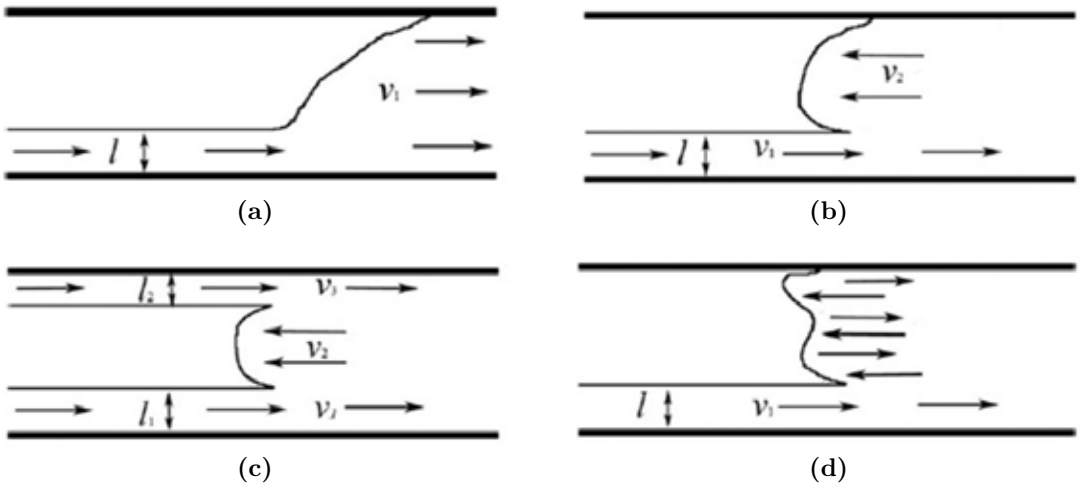

Figure 2.12: Flow type schematics for Fr models, where v is the velocity and l is the length. (a). Type 1; (b). Type 2; (c). Type 3; (d). Type 4.

This method was validated against experimental work, and comparison between experimental and modelling results showed the same flow types. Reilly found that the Froude and Hsu numbers correlated with the experimental data to some extent, whereas the Weber number showed large differences in magnitude between different flow conditions [8]. Reilly then concluded that the Froude number appeared to provide a better representation of entrainment within a horizontal runner bar than the Weber number, as high energy flows within a runner bar often overcome the surface tension forces without generating surface entrainment. The author here questions the conclusion as in the studies of Campbell and Cuesta *et al.* the flow direction was upwards [6, 81], in which the surface tension and gravitational forces were combined together to restrain the breakup and entrainment of surface flow, whereas in runner bar the flow direction intersected with the direction of gravitational forces, meanwhile gravitational forces and surface tension applied in different direction on the flow. Therefore, this may

suggest that Weber number is better for assessing the vertical inlet conditions, while Froude number is better for horizontal flows.

Another combination was made by Hernandez-Ortega *et al.* using the Froude number and the Reynolds number (Re) to characterise the filling structures within a vertical rectangular die, filled using two different pressures [84]. The Reynolds number is the ratio of inertial forces to viscosity, defined in Equation 2.20, where l is the characteristic length and μ is the dynamic viscosity of the fluid.

$$Re = \frac{\rho v l}{\mu} \tag{2.20}$$

Instead of calculating the combination, the authors plotted a flow pattern map, as shown in Figure 2.13, to define four discrete flow patterns, a transition, mound, palm and shell in the order of increasing probability of surface entrainment occurring. Although this work did not directly model surface entrainment, it demonstrated both experimentally and in the model that the Froude and Reynolds numbers could be used to classify the filling structure of flow entering a vertical rectangular mould. Therefore, this technique could potentially be used to assess the likelihood of entrainment in the mould cavity, but clearly further investigation is required to validate this method for liquid metals and more complex mould geometries. Another concern is that the Reynolds number is a measure of bulk turbulence rather than surface turbulence in a flow field, while a flow with high levels of bulk turbulence would not necessarily show a high level of surface entrainment and therefore, would not induce entrainment of oxide film defects.

The above results show that dimensionless numbers have the potential to allow the quantification of entrainment during mould filling. The main advantage of this technique is minimal computational expense. The limitations for the use of dimensionless numbers for quantifying entrainment in casting systems are: firstly, their inability to differentiate between the many types of entrainment mechanisms, namely plunging jet, fountain, bubble trail and colliding fluid fronts, etc.; secondly, they are not able to

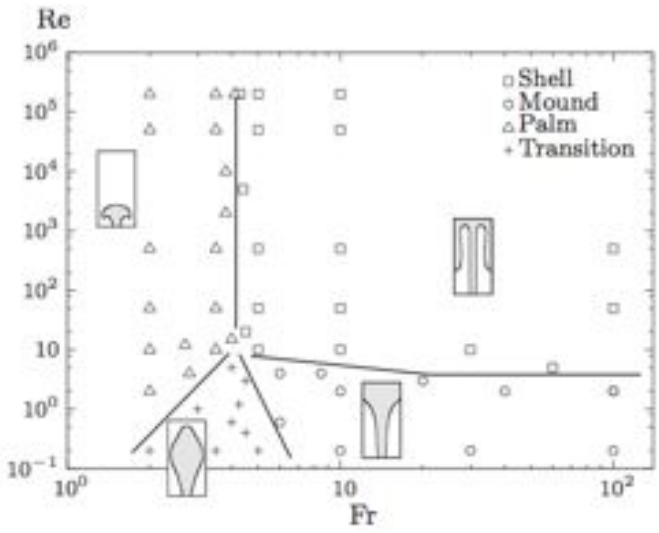

Figure 2.13: Flow pattern map as a function of the Froude and Reynolds numbers [84].

assess entrainment in all regions of a casting, especially in a mould cavity of complex geometry; thirdly, they cannot track the individual defect directly. Further development of these techniques should focus on quantification of the entrainment threshold in liquid metal as opposed to water, and establishment of a relationship between the value of the dimensionless numbers and the degree of oxide entrainment.

2.2.2.5 Bubble Entrainment Model

Bubble entrainment discussed here is different from air entrainment, the former considers the air pockets entrained in the bulk fluid body rather than in the region near the free surface. Air bubbles in the casting can be created by a directly entrained gas phase during filling, or by chemical reaction at a high temperature, perhaps between the liquid metal and the mould materials. The bubbles can float up due to their buoyancy or be moved by the flow, and both will result in bubble trails as the gas phase in the bubble continuously reacts with the surrounding liquid phase [6, 85]. Full physical modelling of bubble entrainment would consider the complicated matters of bubble entrapment and formation, its advection, and bubble agglomeration in multiphase flow, and therefore, is generally avoided due to its complexity.

2.2 Computational Modelling of Entrainment Defects

Modelling of bubble entrainment lies between the continuum and discrete models. Most CFD models used in casting simulation consider a bubble formed by bulk turbulent flow, which can encapsulate volumes of air into the liquid phase. These bubbles are then treated as void regions in the liquid phase and have no effect on the fluid flow. In these scenarios, bubbles can only be considered if their sizes are greater than the size of the mesh. This limits the bubble sizes that can be modelled, and has a huge impact on the result considering the large population of micro-bubbles formed during highly surface turbulent filling. Besides, as the free surface tracking methods do not guarantee the conservation of mass, the modelled sizes of bubbles may not be accurate. In order to track small bubbles, Ohnaka's group developed a model to replace the void region with particles and set the density of particles equal to the gas density, when the size of the bubbles became too small for the mesh element. These particles are then tracked and their final locations defined [86, 87]. However, considering the large density difference between the liquid metal and the gas phase, the result must be extremely sensitive to the particle buoyancy, and solving the movement of these small bubbles (particles) in a turbulent flow requires very small time steps in simulation, which increases computational expense dramatically.

Accurate modelling of bubbles and their entrainment, advection and coalescence requires a multiphase CFD model. By modelling both the bulk fluid and the surrounding gas (two-phase model), modelling of the argon gas injection and bubble transportation in continuous casting processes has been achieved [88]. A multiphase model of shape casting is more complicated, but some preliminary research has been done in relatively simple mould geometries with turbulent filling. Wang *et al.* and McBride *et al.* reported the applications of multiphase flow models in tilt and centrifugal castings [89–91]. Bounds *et al.* and Pang *et al.* provided models for gravity casting [92, 93]. They all reported relatively good agreement between experimental and modelling results. Current developers of two-phase models focus on flow modelling rather than

quantitative prediction of casting defects. The use of any two-phase fluid flow model to quantify or track defects produced by entrained gas has yet to be undertaken.

Modelling of bubble trails is currently facing more difficulties, as the formation of a bubble trail actually involves solid phase formation around the track of the bubble movement in the flow and there is a lack of information about the physical properties of a bubble trail, which in return creates difficulty in estimation of the size and properties in the model. Therefore, direct modelling of the formation of bubble trails using an extremely fine mesh is felt to be unrealistic and other approximations, such as the research done by Reilly (Section 2.2.3.3), which marked the track of bubbles using particles, may give a reasonable solution.

2.2.3 Modelling of Discrete Defects

Discrete modelling of entrainment defects provides considerable advantages over the methods reviewed above, such as the ability to identify different entrainment mechanisms, quantitatively estimating the entrainment level, and particularly, predicting the possible final location of individual entrainment defects in the solidified casting, but obviously requires greater computational efforts than the integrated models of entrainment defects. There are also some issues which baffle the application of these techniques, including a lack of knowledge of: *a*). both physical characteristics of the defects and their behaviour in the liquid and solid state in the alloy, *b*). the critical entrainment threshold in the process, *c*). the interaction between the defects and the mould materials or between each other, and *d*). the evolution of entrainment during cooling and solidification.

Because of the limitation on the modelling techniques currently available, many of the following models use particles to represent the discrete entrainment defect, in which the liquid and particle in the flow are coupled and reasonable accuracy is obtained using current modelling approaches [94, 95]. However, using particle models not only carries with it the problems mentioned earlier, but also carries inherent issues with particle

models, such as the problem that individual unique film-like defects cannot be correctly described by spherical particles with pre-defined identical properties. Therefore, current models are usually semi-empirical or even use assumed properties and behaviour of defects based on intuition. Nevertheless, discrete models have demonstrated their potential to predict the formation and distribution of entrainment defects. Further investigation into the fundamental understanding of entrainment defects will benefit the models significantly.

2.2.3.1 Modelling of Reoxidation Inclusion in Steel

Reoxidation inclusions in steel account for a large portion of the inclusions found in steel castings. The formation mechanisms of the inclusions are similar to those of a surface oxide film during filling of aluminium castings. Carlson and Beckermann applied a particle model to consider the formation, growth, and motion of reoxidation inclusions during the pouring of steel casting and to predict the final size, quantity, distribution and other characteristics of these defects [96]. This model was implemented into *MAGMAsoft*. The inclusions were assumed to be spheres of diameter d and constant density ρ_{incl}. Two formation mechanisms of the inclusions could be modelled: a). the particles could be either generated at the fluid inlet, to represent the large inclusions from the ladle, named the release mechanism, or b). nucleated on the free surface of the melt to represent tiny new inclusions, named the birth mechanism. In the release mechanism, the user could define the initial diameter d_{rel} (cm) and inclusion number density n_{rel} (cm^{-3}), while in the birth mechanism, the user should specify a "nucleation" spacing l_0 (cm) between each nucleus on the free surface or the number of nuclei per unit free surface area $n_0^{''}$ (cm^{-2}), which was used to limit the total number of particles generated in the model to balance the accuracy of the result and the simulation time. The number of inclusions that were nucleated N_{birth}, was determined from Equation 2.21,

$$N_{birth} = n_0^{''} A_{birth} = l_0^{-2} A_{birth} \tag{2.21}$$

where A_{birth} (cm^{-2}) is the free surface area available in the cell, calculated from the cell free surface area minus the free surface area taken up by the existing inclusions, and the growth of inclusions was only considered for those particles on the free surface. The growth rate was defined by Equation 2.22

$$\frac{dV_{incl}}{dt} = A_{FS_incl}\beta \tag{2.22}$$

where V_{incl} is inclusion volume (cm^3), A_{FS_incl} (cm^2)is the area of the melt free surface that is contributing oxide to the growing inclusion, and β is the effective mass transfer coefficient ($cm \cdot s^{-1}$). The diameter of the inclusions after growth was given by Equation 2.23. The model also considered the agglomeration of inclusions, in which once the distance between two separated particles was smaller than the critical distance L_{crit} (cm), the colliding or merging of these small particles would form a single larger particle. Equation 2.24 determines the critical distance between particles.

$$d = \left(\frac{6V_{incl}}{\pi}\right)^{\frac{1}{3}} \tag{2.23}$$

$$L_{crit} = 0.084\sqrt{\frac{d_{max}}{2}} \tag{2.24}$$

Once the formation and size of the particles were defined, their motions were coupled with the fluid solver with consideration of drag and buoyancy applied to the inclusions. The motion of each particle was determined individually and tracked until solidification. The modelling results provided a probabilistic representation of the potential location and size of the reoxidation inclusions being present.

Preliminary validation of this model compared the predicted largest inclusion locations with the inclusions in a steel plate casting, as shown in Figure 2.14. This model was further developed by Melendez *et al.* with more detailed growth and agglomeration models and used in sand casting with complex geometries [97, 98]. Reasonable agreement was achieved.

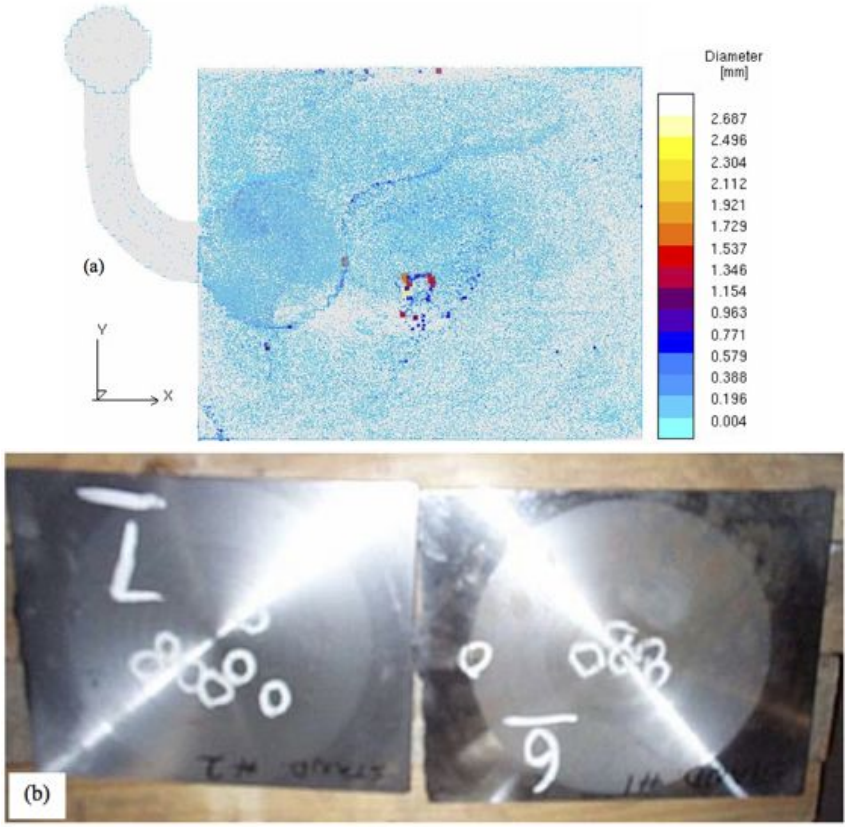

Figure 2.14: Comparison between modelling and experimental results in a casting plate: (a). Top view of predicted inclusion locations; (b). Locations of inclusion on the surface of real cast plates [96].

Carlson and Beckermann's model initially assumed the inclusion would stick to the mould wall once it contacted the mould surface [96], and this was then developed to a partial slip model [98]. However, the properties controlling oxide adhesion to mould walls are not fully understood, as the mould material, impact velocity and inclusion properties would all influence inclusion adherence to the mould wall. This assumption has not got any experimental evidence, but the setting could have a large effect on the final location of defects, if there are thin sections in the mould.

2.2.3.2 Modelling of the Folding Mechanisms

Lin *et al.* and Yang *et al.* separately developed similar models, which placing particles on a fluid free surface to represent the oxide film formed [42, 99, 100]. Once the free

surface was broken or torn apart, new particles were placed on the newly generated free surface to represent "younger" oxide films, and all particles were relabelled. The particles were tracked every time-step to capture the free surface movement.

Lin used the links between neighbouring particles to represent the oxide film, and predicted the strain that the film was under by tracking the movement of these particles in the model. Once the strain exceeded the strength of the film, the film would be torn apart and further particles added immediately to track the new oxide film formed. Once a film was entrained in the bulk liquid the tracking particles were no longer adjusted to fit the free surface of liquid. It was assumed that there was no internal atmosphere for oxidisation within the bulk liquid. The scatter and quantity of these entrained films were tracked [99]. However, there was a lack of experimental information about the strength of the films.

Instead of considering the strength of the film, the method developed by Yang *et al.* assessed the face normals of the films on the liquid free surface. If they pointed towards each other and their velocity vectors obeyed a predefined rule, then the associated film folded upon itself and entrainment was deemed to occur. If the surface normals pointed back on each other and the local inertial pressure exceeded the restraining pressure, then the film was torn up and new particles added [42, 100].

Both models were only implemented in 2D in-house codes, and preliminary validation results reported. As the particles were placed on the free surface and relabelled when new particles were placed, the models were computationally intensive. It should also be noted that placing particles on the free surface is indeed a method to model free surface problems in CFD. To expand this method into three dimensions would be complicated, and further increase the computational effort. Although no further improvement on these techniques has been reported, these methods could model the formation mechanisms of entrainment defects correctly, quantify the amount of defects generated, and predict the motion and location of defects. Further investigation and

development is required to exploit their full potential.

2.2.3.3 Modelling of Oxide Entrainment

To model gas porosity in casting, Ohnaka group further developed their model with consideration of entrainment of oxide films [101]. This model assumed that the free surface of the aluminium melt was covered all the time, but the oxide films are only entrained into the bulk fluid body when the free surfaces collide. If entrainment occurs, marker particles are placed at the centre of the element to represent the entrained oxides, as shown in Figure 2.15. The number and area of the entrained oxides are associated with the alloy composition and colliding velocities of the free surface. The number of broken oxides per unit area, N_{is}, was determined using Equation 2.25,

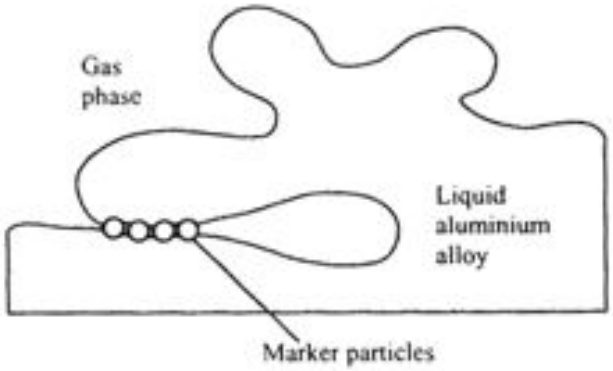

Figure 2.15: Generation of marker particles on the free surface of the melt [101].

$$N_{is} = \alpha_1 |u_{js1} - u_{js2}| + \alpha_2 \tag{2.25}$$

where α_1 and α_2 are parameters depending on the alloy composition, u_{js1} and u_{js2} are the velocities of the colliding free surfaces. The average surface area of the broken oxides (S_M), is estimated using Equation 2.26 , where S is the collision surface area. Equations 2.25 and 2.26 show that a higher colliding velocity will lead to more, but smaller oxides entrained. However, it is unknown from the published work by Ohanka *et al.* what was the method to calculate the α_1 and α_2 values, and no values were

reported for the two parameters either, probably due to a lack of knowledge of the effects of alloy composition on film strength and tearing properties.

$$S_M^{Average} = \frac{\sum S_M}{N_{is} S} = \frac{1}{N_{is}} \tag{2.26}$$

The free surface collisions were classified to three types: collision within the element, collision at the element surface, and collision with a wall. The collision criteria assessed the velocity vectors, distances between particles and the time period, as defined in Equation 2.27,

$$\sum \vec{n} \cdot \vec{u}^{t+\Delta t} \cdot \Delta t \geq \left(1.0 - \beta_{d\_dw}^t - \beta_{d\_up}^t\right) \cdot d \tag{2.27}$$

where $\vec{n}$ is the inward normal of the free surface element, $\vec{u}$ is the velocity vector on the element surface, Δt is the time step, β_{d_dw} and β_{d_up} are dimensionless distances for downwards flow and upwards flow respectively, and d is the element size. The collision surface is defined as the surface vertical to the collision direction, and the collision area is derived by a dimensionless distance of element before melt surface contact, but no details were reported regarding to this value. Figure 2.16 shows the three types of free surface collisions and the definition of β_d in the x and y directions. Once the number and size of the marker particles are defined, the motion of the particles will be tracked in a fully 3D flow until the casting is solidified. Therefore, the final distribution of the oxides can be determined, and later coupled with a porosity growth model, to predict the location and size of gas porosity.

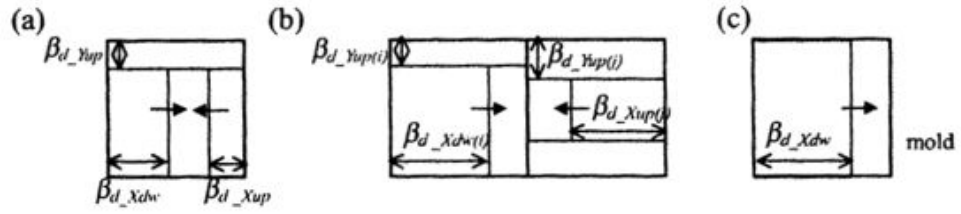

Figure 2.16: Types of free surface collision. (a) within the element, (b) at the element surface, (c) with wall [101].

This model focused on predicting the location of gas porosity, and allows the entrainment caused by different flow conditions to be captured, rather than only folding

mechanisms. The model was further developed for cast iron [102, 103], and now has been implemented into a commercial casting optimisation software *JSCAST*.

Reilly *et al.* developed a *FLOW-3D* customisation, named the oxide film entrainment model (OFEM) [8], which was very similar to that developed by Ohnaka's group. This model used the capability of user-defined subroutines in *FLOW-3D* to identify the surface elements and assess the velocity vectors, the fraction of fluid at both the beginning and end of a time step, the orientation of the free surface normals and the surface area in the different mesh elements, and then defined entraining events by Boolean logic criteria. The model defined 48 entrainment forms and categorised them into three groups, namely Colliding Fronts (Entrainment Forms 1 to 3), Shearing Flows (Entrainment Forms 4 to 36) and Impingements (Entrainment Forms 37 to 48), according to the relative motions of the free surfaces in adjacent mesh cells. Figure 2.17 shows examples of typical relative motions of free surfaces in the three types of entrainment. The entrainment criteria are defined separately for each entrainment form. For examples, to define a shearing flow event as shown in Figure 2.17b, the N_f values, which are the location indicators of the free surface in the cell, are assessed by the subroutines to detect if the orientation of the free surfaces in cells ijk and $ipjpk$ correlate to the defined directions, then the velocities of the liquid (free surface) in the two cells are examined to determine if $u(ijk) > 0$ and $u(ipjpk) < 0$. Here u represents the velocity vector in the x-axis. If the two cells are full at the end of this time step, the free surfaces are considered to shear each other at the boundary, and entrainment is believed have occurred. A particle with determined size and density is then placed at the entraining location to represent the defect. In Figure 2.17b the particle is placed in the top right corner of the grey cell. The motion of the particle is then tracked until solidification. Detailed entrainment criteria and initial particle locations in mesh are listed in Appendix. As the model focuses on the modelling of entrainment of the oxide film, no porosity growth model was coupled in the subroutines. This is also partly due

to limitations on the properties of particles that can be defined.

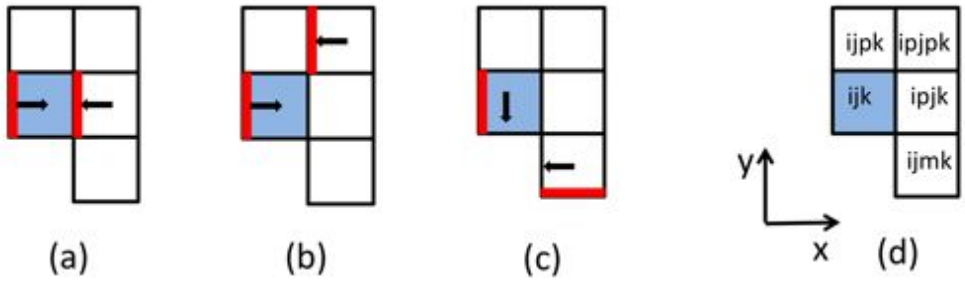

Figure 2.17: Examples of three entrainment groups in 2D. (a). colliding fronts, (b). shearing flows, (c). impingement. The grey cell is the element being assessed at current time step. Red lines within the cells are the profiles of free surface and indicate their position within the cells. Arrows point the moving direction of the free surfaces. (d). the identification of each cell.

The quantity of particles in the whole casting or in a region of interest can be exported to quantitatively study the effects of entrainment defects on the properties of casting. Reilly modelled the experimental work of Green and Campbell with OFEM [22], and higher particle counts in the model were correlated to lower Weibull moduli of the castings, although the difference was not significant [104, 105]. The Weibull modulus of the better castings was two times that of the worse castings in the experiments, while the particle counts in the better casting were only 30% lower than that in the worse casting in the model. A larger data set or different running system designs should be used in further investigations for a conclusive validation of the OFEM algorithm.

It should be noted that the concept of OFEM is quite similar to the model developed by Ohnaka's group, but it provided more comprehensive definitions of the free surface entrainment scenarios, as it considers not only colliding fluid fronts, but also other mechanisms. Besides, Ohnaka's model used marker particles, while the particles employed in OFEM have defined properties, which means that buoyancy and momentum interaction between the defects (particles) and flow can be described, and hence, more accurate results are expected to be obtained.

Based on the assumption that the gas porosity could nucleate and grow on the oxide film defects, Ohnaka and Reilly claimed that their models could potentially predict the location of gas porosity in the castings. But clearly, the initial gas content in the melt affects the nucleation of the gas pores, and the growth of the gas porosity would determine their impacts on the mechanical properties of castings. Jakumeit *et al.* developed a four-phase fully-coupled model, in which the gas, liquid and solid phases were considered during mould filling and solidification, and an extra hydrogen phase was introduced to predict the gas porosity [106]. This model used VOF method to detect the entrainment of oxide films and employed finite volume method to solve the flow field. The entrainment of oxide films was determined by two approaches: *a).* a geometrical approach, which detected if the adjacent free surfaces would collide, and *b).* a Weber number based approach, which detected whether the Weber number in an element was greater than the unity. Once the entrainment of oxide films was deemed to have occurred, the oxide film density in the element was estimated and recorded in a scalar and then traced in the fluid flow. These oxide films, along with dissolved gas concentration and gas pressure, were used to determine the nucleation of pores in the casting. The pore growth model considered the surrounding temperature, pressure and dissolved gas. Jakumeit *et al.* affirmed that the results form their pore growth model agreed with previous published experimental findings. However, the prediction from the fully-coupled model did not correlate the experimental validation. Further development to improve the accuracy of the model is demanded.

2.2.4 Modelling of Oxide Film Deformation

Both integrated models for entrainment and discrete models of entrainment defects do not take into account the film nature of a surface oxide film. This is owing to limitations in our knowledge of oxide films and the capability of current modelling techniques. Pita and Felicelli proposed an immersed element-free Galerkin method to solve the liquid-structure interaction. They demonstrated in 2D the capability of the model to

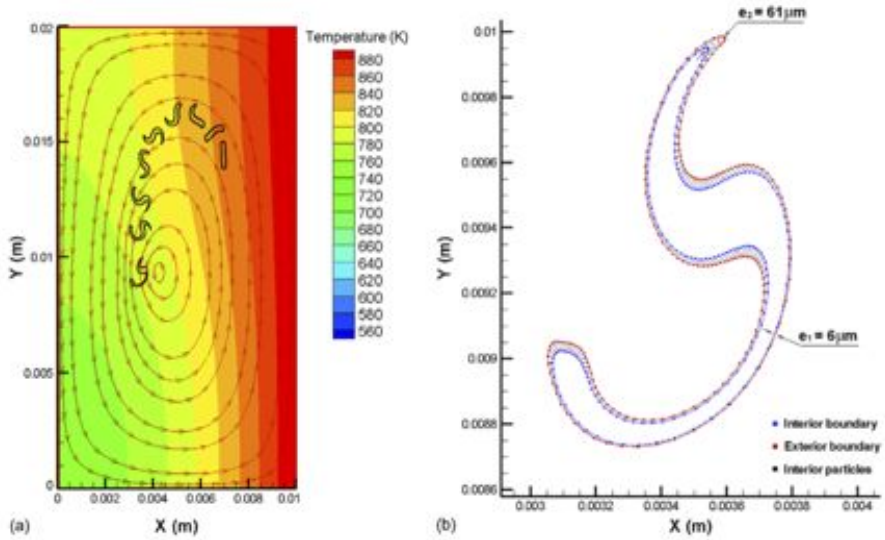

Figure 2.18: Example of the modelled rotation and deformation of oxide film. (a). Position and shape of the solid body at nine different times are shown. From right to left, the corresponding times are increasing. The background corresponds to the temperature distribution and the velocity streamlines within the fluid domain at t = 4.22 s. (b). Final shape of the solid body at time t = 4.2168 s. The red dots indicate the outside boundary, the blue dots represent the inside boundary and the black dots represent the interior particles. The minimum (e_1) and maximum (e_2) thicknesses of the solid are also indicated [107].

capture large rotations, translations and deformations of a solid oxide film, induced by convective a flow, as shown in Figure 2.18 [107]. The result showed good potential for modelling the furling and unfurling of oxide films during the casting process. Pita and Felicelli stated that a more realistic constitutive model with consideration of film fracture, phase change and solute transport during solidification would be developed.

The current model has only been applied to single oxide film inside a relatively small liquid pool. It is difficult to apply this method to a lager scale casting model due to the computational intensity of modelling a large number of oxide films within the fluid flow field and subsequent solidification of casting. However, the technique may play an important role to understand the physical behaviour of oxide films within a casting during cooling and solidification, as so far there is no published experimental evidence to prove or disprove Campbell's theory about evolution of double oxide film. If gas precipitation and the momentum field of a semi-solid melt model can be integrated

into the current model, and the strength of oxide films be considered, the furling and unfurling mechanisms of oxide films can be assessed.

2.2.5 Validation of Modelling

Due to the size of entrainment defects, it is difficult to directly observe the formation of entrainment defects and validate the modelling results. Real-time X-ray radiography has been a widely used technique to observe the filling scenario within the mould cavity and to validate the flow model. Sirrell *et al.* carried out a test using X-ray radiography and thermocouples to set a benchmark for flow and solidification models for aluminium castings [108]. Real-time X-ray observation has since been used by many researchers, either to assess the filling of the mould or validate their models [83,105,109,110], or to quantify the evolution of entrainment defects [28]. The main shortcoming of real-time X-ray radiography is that it cannot be used to visualise the formation and distribution of entrainment defects in castings due to its low resolution.

To validate the distribution of inclusions or entrainment defects, a positron emission particle tracking (PEPT) method, used in medical research, has been examined for use in casting research. Griffiths *et al.* applied this technique to determine the movement of inclusions in a low-melting point alloy, an aluminium alloy and liquid steel during the casting process [111–115]. The traces of the particles, which represent the movement of inclusions in the casting were accurately recorded and available for validation of particle model in CFD software. However, the reproducibility of the PEPT experiment was low and only one particle can be tracked at once, and there is no literature reported using this method to validate a particle model in CFD software.

Mechanical testing to understand the fracture or fatigue behaviours of aluminium castings, and subsequent fractography analysis are easily carried out. Quantitative analysis of defect populations in castings or Weilbull statistics of mechanical properties of castings can reveal the severity of entrainment defects further. This method has been used by many researchers to validate their models. For example, Dai *et al.* used the

Weibull analysis to compare the influences of three different running system designs on the bending strength of the castings [41]. The results showed that the running system, which could generate high surface turbulence, would lead to high population of entrainment defects. Mi *et al.* investigated the tensile strength of the samples from tilt castings, in which various rotation speeds were used. The Weibull analysis of the UTS of samples showed higher rotation speed of the process resulted in lower reliability of the castings [54]. Yang *et al.* quantitatively studied the casting defect area fraction of the castings from different moulds. The results suggested that the bending strength of the castings were mainly decided by the entrainment defects distribution features and the defects morphology [116].

2.3 X-Ray Tomography of Materials and Defects

Previous studies mainly used optical and scanning electron microscopy (SEM) at room temperature to investigate the morphology of entrainment defects on fracture surfaces or on metallographic sections. Novel techniques are required to better understand the physical phenomena that occur within entrainment defects during cooling and solidification at high temperature, especially considering the complex three-dimensional geometries and micro-scale thickness of the convoluted films.

Three-dimensional tomography has been used as a non-invasive and non-destructive technique in the medical research field for decades. Computed tomography (CT scan) and magnetic resonance imaging (MRI) are typical medical imaging techniques that use radiography to visualise internal body structures in detail. In the materials science field, the similar technique as used in CT scans, *i.e.* X-ray computed tomography, can provide an accurate map of the variation of X-ray absorption within an object. High energy X-ray sources can even reveal the interiors of samples with very high spatial and contrast resolution below the scale μm. This gives technical advantages for studying the behaviours of entrainment defects in 3D without destruction of the sample by

deformation or sample preparation [117].

2.3.1 Introduction of X-ray Tomography

2.3.1.1 Principles of X-ray Tomography

In X-ray tomography, an X-ray beam is projected on an object and the transmitted beam is recorded by a detector. The image obtained is a two-dimensional superimposed projection of a volume with different grey scales to represent the different absorption levels or X-ray attenuation in the photon path. The visibility of the features of an object depends on the spatial resolution, which defines how well small details can be imaged, and the contrast, which determines how well a feature can be distinguished from the neighbouring background [117].

The reconstruction of an object in a slice is based on the X-ray attenuation in the projections in different viewing directions. For example, Figure 2.19 shows a low absorption rectangle feature within a slice, in which the various attenuation on the two profiles can be used to depict the general feature of the object. To get a more complex 3D feature, a set of projections must be recorded over the entire cross-section of interest to obtain sufficient definition of the features on a slice, when rotating the sample between 0° and 180°. A stack of these slices then can be used to generate the volume of the 3D feature information, from the filtered back-projection algorithm [118]. Figure 2.20 illustrates the process to obtain 3D features within a sample.

The quality of reconstruction relies on the spatial frequencies in the projection, the number of views, and also the reconstruction method. The spatial frequencies in the projection is generally more important than the number of views, and both are constrained by the detectors of computed tomography [117]. Summarising the variety of reconstruction algorithms falls outside the scope of the present review, but can be found in a series of books and reconstruction software are available commercially or as open license software [120–124].

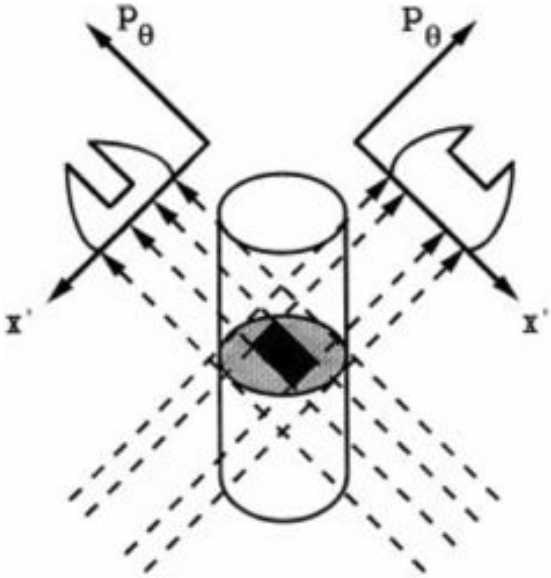

Figure 2.19: Illustration of the method of determining the internal structures from projections. For simplicity only single plane and parallel X-ray are pictured, and rotation axis for collecting views (*i.e.* absorption profile P_θ) along different directions θ is vertical and in centre of cylindrical sample [117].

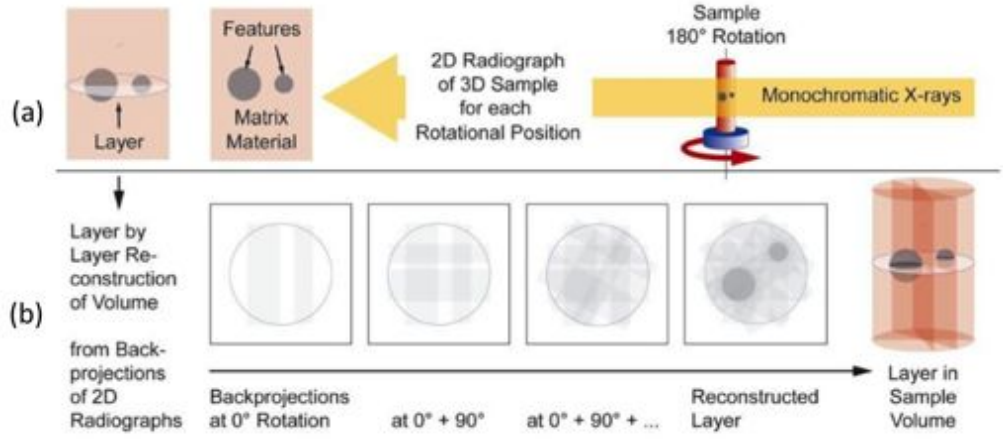

Figure 2.20: General principle of X-ray tomography scanning: (a). data acquisition from top right to top left of image; (b). back projection and reconstruction from bottom left to bottom right of the image [119].

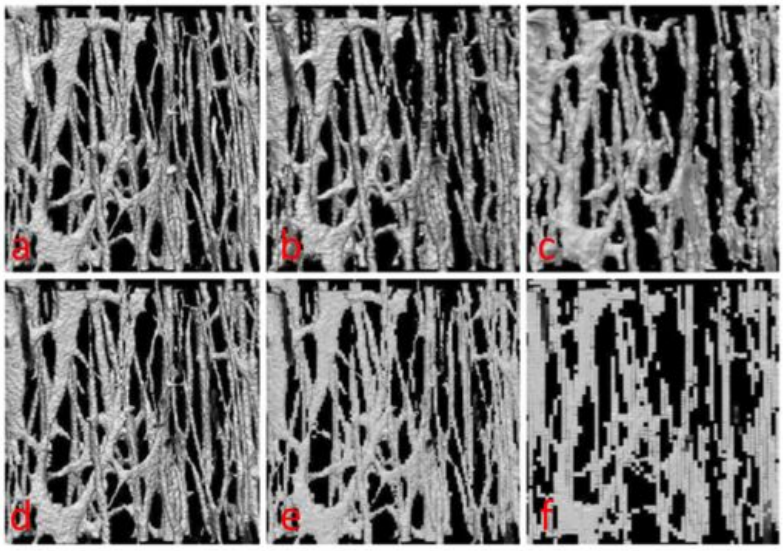

Figure 2.21: 3D images with different voxel values. The scanned images are with: 5 (a), 10 (b) and 15 (c) μm voxels. Artificially degraded images are with: 10 (d), 20 (e) and 40 (f) μm voxels [125].

The spatial resolution affects detail discrimination and the quantitative analysis of volumetric 3D images, as shown in Figure 2.21. The highest possible spatial resolution is always desired in X-ray tomography, but with compensating scanning time and cost. The smallest element in a volumetric image is called a "voxel", which defines the spatial resolution of a reconstructed structure. The voxel size (vox) is related to the field of view (FOV), *i.e.* the width and height of the scanning area of the detector, and the number of X-ray elements that the detector can detect. It can be calculated by the relationship: $vox = \mathrm{FOV}/N$, where N is the number of detections. The specimen needs to be centred and inside the FOV. If the specimen is not inside the FOV, or not centred in the rotator of the specimen holder, some part of the specimen will be in and another out of the scanning area, which can cause mismatched signals during the rotation, as demonstrated in Figure 2.22 [126]. Furthermore, if the specimen is not at the centre of the FOV, specimen wobble and rotation axis misalignment can be generated during the reconstruction.

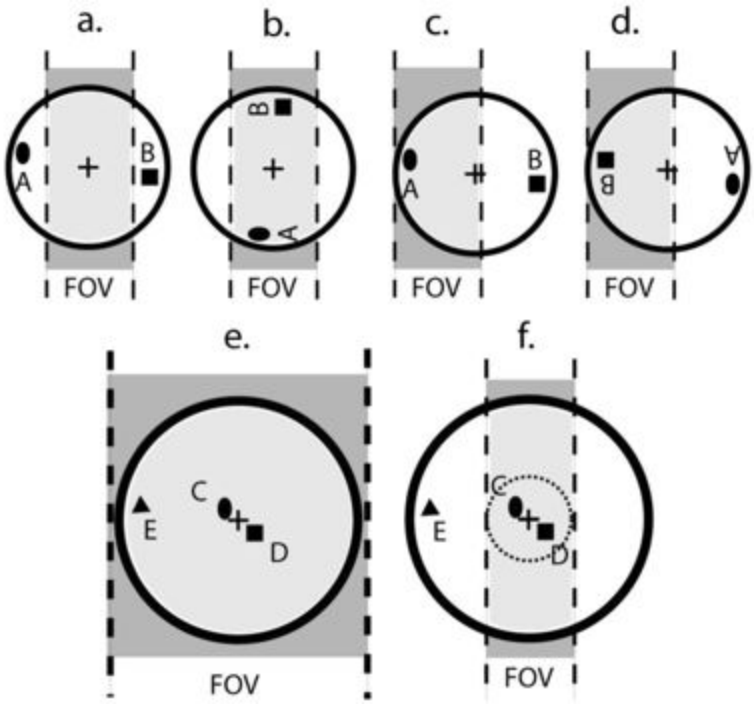

Figure 2.22: Field of view (FOV) and specimen diameter. The X-ray beam illuminates area shaded grey. (a) to (d). Features rotate into and out of FOV; (e). Entire specimen diameter is within FOV, but smallest voxel size is limited; (f). Smaller region of interest in FOV [126].

2.3.1.2 Tomography Mode and Radiation Source

There are three different modes to perform X-ray tomography:

- *The absorption mode*: the contrast is given by the difference between the linear attenuation coefficients, hence essentially based on the density of the element. The larger the difference between elements, the better the contrast can be obtained. This is the conventional mode.

- *The phase contrast mode*: the contrast is observed when the beam is partially coherent. The contrast achieved is higher than that from the absorption contrast and it is efficient for edge detection. But segmentation or further analysis of such images may be difficult [118].

- *The holotomography mode*: this method requires two to four complete scans at various distances, but can get higher contrast than that from the conventional absorption mode. This mode allows quantitative analysis of the density of the material in 3D.

There are four microtomography geometries: pencil beam, fan beam, cone beam and synchrotron-based beam, as shown in Figure 2.23.

In pencil beam systems (Figure 2.23a), a pinhole collimator C from a point source P generates a narrow beam which is scanned across the object O along x_1 to produce each view. Very accurate values of the linear attenuation coefficients can be detected from the point detector D. Successive views can be obtained by rotating the sample about x_2 and repeating the process. But the volumetric data, *i.e.* a set of slices cannot be obtained because of the long scan times required to collect the data from a point X-ray detector.

Fan beam systems (Figure 2.23b) use a flat fan X-rays and rotate the sample during the scan. This detector consists of an array of discrete point detectors, which allows the

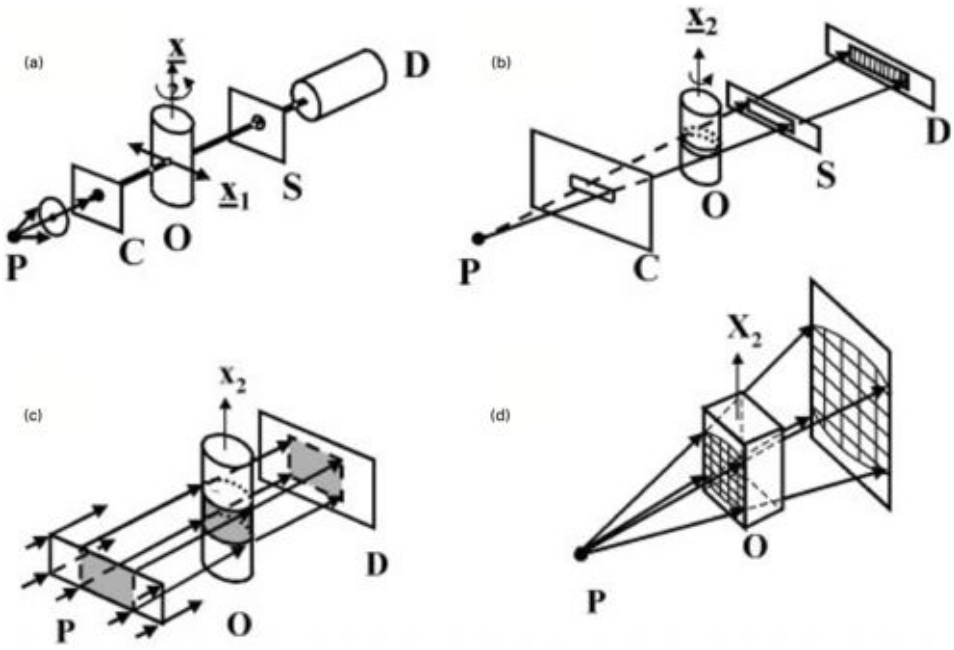

Figure 2.23: Sketch of four experimental methods to X-ray microtomography data collection: (a). pencil, (b). fan, (c). parallel, and (d). cone beam methods. P is X-ray source, C is collimator, O is object being imaged, x_2 is axis about which sample is rotated to produce different views required for reconstruction, S is slit, and D is detector [117].

entire view of the sample to be collected simultaneously. Therefore, data acquisition of fan beam systems is much more rapid than pencil beam systems [117].

The cone beam systems (Figure 2.23d) expand the fan beam arrangement to three-dimensions, and hence, it is suited for volumetric computed tomography. But the cone beam reconstruction algorithm is an approximation, as there is usually some blurring on the edges of the features.

The time for a complete scan using these beam systems is strongly influenced by the resolution required, the size of the CCD camera used and the radiation source. Scanning time can be longer than 30 min. These beam systems normally perform in absorption mode, since the beams are not coherent and cannot use phase contrast modes. There are a wide range of laboratory devices based on these beam systems, and can be customised, such as inserting mechanical devices or a furnace in the set-up [127–129].

In the parallel beam geometry shown in Figure 2.23c, high performance area detectors are used, and the data collection rates increased dramatically, much faster than the systems introduced above. Slices are reconstructed with isotropic voxels, which means the slice thickness is equal to the voxel size. In practice, parallel beam is obtained generally by hard synchrotron X-ray radiation from storage rings.

The advantage of synchrotron source is that it delivers a very high flux from a small source size. Moreover, it generates a partially coherent beam which is necessary for phase contrast mode. Depending on the experimental set-up, a white beam (a beam with the full bandwidth of X-ray wavelengths in the incoming beam) or a monochromatic beam, can be used to make an "exact" and quantitative reconstruction that is free of geometrical and beam hardening artefacts. Synchrotron tomography can be performed at the European Synchrotron Radiation Facility (ESRF) in France, Deutsches Elektronen-Synchrotron (DESY) in Germany, Swiss Light Source (SLS) in Switzerland, Diamond Light Source in the UK, the National Synchrotron Light Source (NSLS) and the Advanced Photon Source (APS) in the US and in other countries [130].

2.3.1.3 Artefacts in X-ray Tomography

The main artefacts in X-ray tomography are noise, beam hardening and ring artefacts. Statistical noise is not normally considered as an artefact. It can be affected by specimen geometry and size, rotation step angle and possibly magnification [126]. The noise is easily identified as small spots without clear pattern or feature. The main effect is that small features are more difficult to identify and, when surface rendering is applied, it introduces rough textures to surfaces [131]. Increasing the exposure scanning time and the number of projects performed during rotation can reduce the noise in the images [117].

Beam hardening is seen in tomography systems using a polychromatic X-ray beam. Hardening means that the lower energy absorption rate increases when the beam passes through a specimen. For example, when the X-ray beam passes through the specimen,

the lower energies in the X-ray spectrum to be preferentially attenuated compared to the higher X-ray energy photons. Consequently, this hardening effect makes the specimen appear to be less dense in the centre, as shown in Figure 2.24b. Beam hardening can be reduced using an attenuation filter, smaller sample size and correction during image reconstruction [131].

(a) (b) (c)

Figure 2.24: Examples of reconstructed images with and without artefacts [131]. (a). perfect reconstruction; (b). with beam hardening;(c). with ring artefact.

Ring artefact, which results from differences in the sensitivity of adjacent detector elements, is usually caused by the local defects in the detector. The differences are emphasised in the reconstruction process and show up as streaks. Since these streaks are in the same position in all projections, ring patterns form as the projections are summed, as shown in Figure 2.24c. There is a trend of increasing ring artefact severity towards the centre. Scanner calibration and time delay integration methods can reduce the severity of the ring artefacts [117, 131, 132],

2.3.2 The Application of X-ray Tomography

X-ray tomography has been applied in many fields of material science. Most of the studies used the conventional absorption mode, with a smaller number using the phase contrast mode and the holotomography mode [118]. X-ray tomography was initially applied to imaging inorganic composites, to the study of pathways for material transport

in porous solids, and to studying fatigue crack closure in metal samples [117, 133]. As the techniques improved, the application of tomography became more diversified, with more studies on the distribution of phases, cellular materials, deformation, fracture, and also on materials processing [126].

2.3.2.1 3D Visualisation and Image Analysis

3D volumetric reconstruction is usually completed in the work stations connected with the control terminal of the beam. After the 3D reconstruction of a series of projections is completed, 3D visualisation is conducted as the second step. Efficient 3D visualisation requires specialised software, both commercial visualisation software, *e.g.* Aphelion [134], Amira [124], VG [135], Avizo [136], etc., and freeware, *e.g.* ImageJ [137], Fiji [138], etc., are available. Image analysis needs segmentation of the volume to differentiate different features in the volume images. General analysis can be done in the software, but some more sophisticated analysis may require special algorithms, sometimes written by the user themselves [118].

2.3.2.2 Quantitative Characterisation

Maire *et al.* reported the application of visualisation of the internal structures of a metallic foam using X-ray tomography before and after compression [139]. Jones *et al.* quantified the 3D macrostructure of tissue scaffolds for cell growth. The results led to new design criteria for the development of biomaterials [128]. Maire *et al.* using synchrotron X-rays compared the size, morphology and spatial distribution of the intermetallic phases in an aluminium alloy under different working conditions with very high resolution achieved (0.3 μm) [140]. Quantitative characterisation was also used in the assessment of deformation-induced damage in a semi-solid aluminium alloy [129], and quantification of the interaction within defect populations on the fatigue behaviour in an Al-Si alloy [141].

2.3.2.3 *In Situ* Experiments

The high energy and the parallel beam set-up of synchrotron-based X-ray allows *in situ* experiments to be conducted with 3D quantitative analysis. The main advantage of *in situ* experiments is that it allows direct observation of physical phenomena as they occur, for example, imaging the microstructural evolution in cavitation processes. But it may be impossible to perform a real *in situ* observation sometimes, as the scanning time to achieve high resolution results is quite long, of the order of the time that the physical transformation is taking. An interrupted *in situ* experiment is usually performed instead. During this kind of experiment, the material is strained, unloaded, set on the tomography set-up, scanned and then strained again and so forth. Similar processes can also be used in thermal cycles. This process obviously introduces artefacts, but the same sample is investigated, and thus, continuous results obtained.

In situ characterisation has been applied to understand the deformation and fatigue behaviour of materials. Buffière *et al.* studied the initiation and development of damage inside an aluminium alloy based composite during mechanical tests [142]. Phillion *et al.* studied the deformation behaviour of aluminium alloys, but during a semi-solid process at higher temperatures [143]. Similar techniques were further applied to study defect evolution during deformation to understand fracture mechanisms [144, 145]. Toda *et al.* utilized synchrotron X-ray tomography to observe fatigue crack opening/closure during load cycles, and reconstructed clear crack images with microstructural features. They highlighted the link between micro-pores and crack tip propagation [146]. Zhang *et al.* further studied the interaction between pores and cracks during fatigue cycles *in situ*. They found the area fraction of micro-pores on the crack surface to be higher than that in other cross sections, and fatigue cracks were generally deflected toward nearby micro-pores [147].

In situ observation has also provided information about porosity evolution inside materials at different temperatures. Felberbaum and Rappaz studied the nucleation

and growth of micro-pores in Al-Cu alloy by X-ray tomography, and showed the effects of hydrogen content and secondary dendrite arm spacing on the curvature of micropores [39]. Chaijaruwanich *et al.* investigated the evolution of porosity in a direct chill (DC) cast Al-Mg alloy during a homogenisation heat treatment and revealed that the intra-pore Ostwald ripening is the key mechanism for the morphological evolution of pores, especially the pores with complex 3D geometries [148, 149].

2.3.2.4 Simulation of Tomography Data

The reconstructed 3D structures can be meshed and imported to software or codes to model the behaviour of materials under different conditions. Youssef *et al.* investigated the initial microstructure and local deformation mechanisms of a polyurethane foam during a compression test using X-ray tomography. The foam was reconstructed and meshed, then a predictive finite element model of the mechanical behaviour of the foam was then implemented, and good correlation between the modelling results and experimental observation found [150]. Watson *et al.* applied X-ray microtomography to generate a 3D representation of actual microstructures of an aluminium-based particulate-reinforced metal matrix composite. They then used a 3D imaging analysis technique to determine the size distribution and extrusion texture of the reinforcement particles and meshed the 3D images for FEA. The elasto-plastic behaviour of the two-phase material with complex microstructure was accurately simulated [151]. The tomographical data have also been employed to assist the validation of models of deformation and fatigue behaviour of materials [127, 141].

2.3.2.5 X-ray Tomographical Study of Entrainment Defects

The X-ray tomography has not been widely used in the study of entrainment defects. Park reported preliminary study of the behaviours of double oxide films in the A356 alloy during solidification, using a desktop-based X-ray tomography technique [152]. In his work, the samples were cast from sand moulds that could generate highly turbulent

filling scenario, and then machined to cylinders of 4 mm in diameters. The oxide film defects were scanned and then remelted at 745 °C, air cooled, and scanned at the room temperature again, to understand the evolution of the defects during cooling and solidification. This work successfully revealed the morphologies of entrainment defects in three dimensions. Figure 2.25 shows four examples of the 3D structures of entrainment defects. Since these were not *in situ* observation, most of the defects were not captured in the scans after the remelting, and hence, could not generate a large dataset to measure the behaviour of entrainment defects. However, Park found that in the limited number of samples studied, the unfurling of double oxide films was not observed [152]. This implied the need of a better technique for studying the behaviours of entrainment defects, probably an *in situ* technique with higher resolution and shorter scanning time.

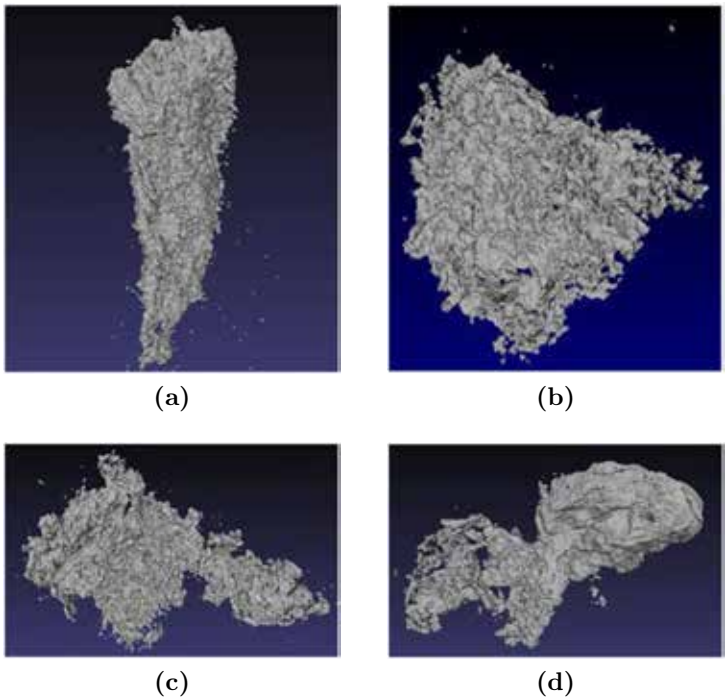

Figure 2.25: Examples of 3D structures of four entrainment defects [152].

2.4 Summary

The concept, formation and evolution of entrainment defects have been introduced. The influences of entrainment defects on the fracture, ductility and fatigue properties of aluminium castings were reviewed. There is no doubt that the existence of entrainment defects significantly reduced the reproducibility of mechanical properties of casting. However, there are some controversies about the relationship between porosity and entrainment defects in casting, *i.e.* whether porosity is a secondary defect from an entrainment defect, and about the relative importance of porosity and entrainment defects in determining the mechanical properties of castings. Further studies area required to resolve these issues.

The modelling methods of entrainment defects have been reviewed. Researchers have clearly demonstrated the capabilities of different models to measure or quantify entrainment defects in casting processes, but there are still complex questions needing to be answered. The nature and behaviour of oxide films themselves in the liquid and during solidification is lack of understand. The size distribution of entrainment defects generated in different entrainment mechanisms or impact velocity still require further study. The method to simulate these factors in the model and meanwhile, to balance computation time with accuracy, must also be considered. Although a "critical" velocity for aluminium casting filling has been proposed, the entrainment thresholds are not known. Besides, the relationship between the discrete particle counts predicted by the model and the real defects quantity in the casting should be linked by experimental validation.

The X-ray tomography techniques used to understand defect morphologies or *in situ* characterisation of materials have been reviewed. The principle of X-ray tomography has been briefly explained and the application of this method introduced. This method could be applied to the fundamental research of entrainment defects in castings.

Chapter 3

Computational Modelling

3.1 Hardware and Software

All computational simulations were conducted on the cluster in the Centre for Partnership for Research in Simulation of Manufacturing and Materials (PRISM2). The node consisted of two 64-bit 2.6 GHz AMD Opteron quad-processors with 16 GB RAM. Post-processing of the simulations was completed on a desktop computer using the 64-bit openSUSE Linux operating system.

Commercial CFD software, *FLOW-3D*, version 9.4 [153], was used in this research. *FLOW-3D* uses a finite difference method (FDM) to model the fluid flow in structured Cartesian meshes, and the main features of the software include:

- Multi-Block gridding with nested and linked blocks;
- The fractional area/volume Obstacle Representation (FAVOR^{TM}) technique for efficient and accurate geometry definition of the structural mesh [154];
- TruVOF Volume-of-Fluid (VOF) method for fluid interfaces;
- Additional customisation potential to meet specific requirements of modelling.

The Oxide Film Entrainment Model (OFEM) [8], proposed and developed by C. Reilly and implemented in *FLOW-3D*, was applied in this research. A general description was introduced in Section 2.2.3.3, and detailed definition of Colliding fronts (Forms

1 to 3), Shear flows (Forms 4 to 35) and Impingement (Forms 37 to 48) are listed in Appendix. The governing equations for the free surface modelling method used in OFEM were expressed in Equations 2.9 to 2.13 in Chapter 2, Section 2.2.1. OFEM uses the mass particle model in *FLOW-3D* to track the predicted defects. The dynamics of the mass particles is governed by Equation 3.1, where u_p and ρ_p are the particle mean velocity and density respectively, g includes gravity and other body forces, u and ρ are the fluid velocity and density respectively and β is a drag coefficient. The particle motion influenced by fluid through the drag force, and hence the drag coefficient β, which is a function of the Reynolds number of flow around the particle, and is calculated by Equation 3.2, where Re is the Reynolds number as defined in Equation 2.20, d is the diameter of the particle. u' is calculated by u_p plus a particle diffusion velocity u_{diff}, which is estimated by Monte Carlo technique. The details of calculation of u_{diff} can be found in the *FLOW-3D* manual, *Theory* section [155]. It should be note OFEM per se does not calculate or predict the free surface location, but uses the capability of *FLOW-3D* to capture the free surface movement and then uses mass particle model of *FLOW-3D* to track subsequent particle movement.

$$\frac{du_p}{dt} = -\frac{1}{\rho_p} \bigtriangledown P + g + \beta(u - u')|u - u'|\frac{\rho}{\rho_p} \tag{3.1}$$

$$\beta = (\frac{24}{Re} + \frac{6}{1 + \sqrt{Re}} + 0.4) \cdot \frac{3}{4d} \tag{3.2}$$

Figure 3.1 shows a flow chart for the OFEM algorithm and the pre-defined three types of entrainment criteria. Appendix details the entrainment criteria and initial particle locations in mesh of the 48 entrainment forms. Further development of the subroutines was mainly focus on defining particle properties and post-processing of the results. These were done in FORTRAN 90 using an Intel FORTRAN Compiler 9.1 on the cluster in PRISM2.

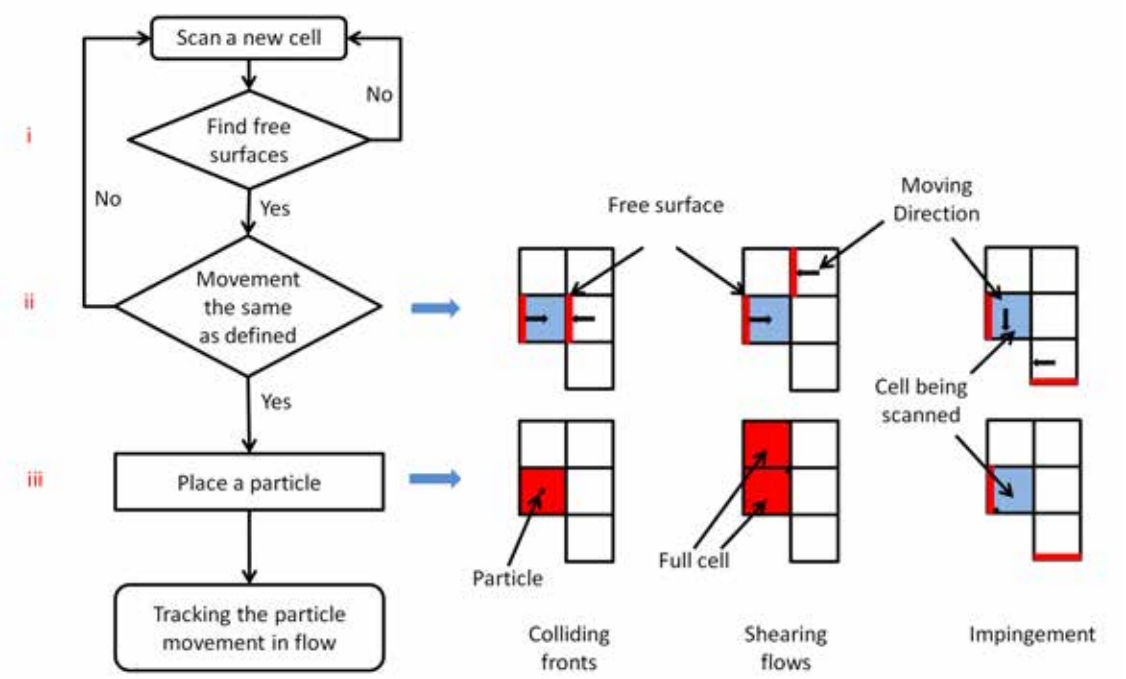

Figure 3.1: Flow chart of OFEM algorithm and three types of entrainment forms.

3.2 Implementation of the OFEM in *FLOW-3D*

The *FLOW-3D* distribution includes a variety of subroutines in FORTRAN source form that allow users to customise *FLOW-3D* to meet their unique requirements. The *qsadd.f* file, which is located in the subdirectory *hydr3d*, is the customisable interface for users to include other subroutines into the main *FLOW-3D* solver, by using **CALL** statement.

In the OFEM codes, the *qsadd.f* was modified to include the main source codes, including:

- *Double_Oxide.f*: defining the entrainment criteria of the 48 entrainment forms.
- *Particle_Placing.f*: defining the initial location and velocity of the predicted particles according to the entrainment form.
- *File_Format.f*: formating the output files resulted from the customised subroutines.

Other source codes to extract the particle count or particle concentration in specified regions in the model were written separately for each model. Variables placed in the *prepin.inp* file (simulation pre-processing file) under the **XPUT** name list, were used to control which code should be called, and to define the modelling conditions, for example, the particle placing frequency in the OFEM. In each simulation, the dummy number **idum25** was set to 1 in the *prepin.inp* to switch on the OFEM codes. The details of the implementation of OFEM and the original source codes can be found in Reilly's work [8].

3.3 The OFEM Algorithm Investigation

Although previous validation of the OFEM algorithm had highlighted the potential of this method for the quantitative measurement of entrainment events in the casting process and the prediction of entrainment defect distribution in solidified castings [8,83, 105], further investigation of the algorithm performance with different running systems and moulds was required to understand the capability of the algorithm.

3.3.1 Preliminary Modelling of Different Entrainment Events

To understand the relationship between the pre-defined entrainment forms in the OFEM and the entrainment mechanisms in modelled flow structure, *e.g.* if the Impingement flow forms in the algorithm link with the plunging jet in a modelled flow structure, simulations were conducted in *FLOW-3D* on three common entrainment mechanisms, namely plunging jet, rising jet and return wave as summarised by Campbell [6]. The OFEM code exported the location and entrainment form of each entrainment event as a text file after each computing cycle of the simulation. These were later analysed to study the relationship. Three moulds used for generating plunging jets were named Plunging_Jet_4, 5, 11; moulds for generating return waves were Return_Wave_1, 5, 6; and moulds for generating rising jets were Rising_Jet_1, 3, 7, 10. The mould shapes

are shown in Figure 3.2 and their dimensions are shown in Tables 3.1 to 3.3. The designation of the dimensions are defined in Figure 3.2. The thickness of all the moulds was 15 mm.

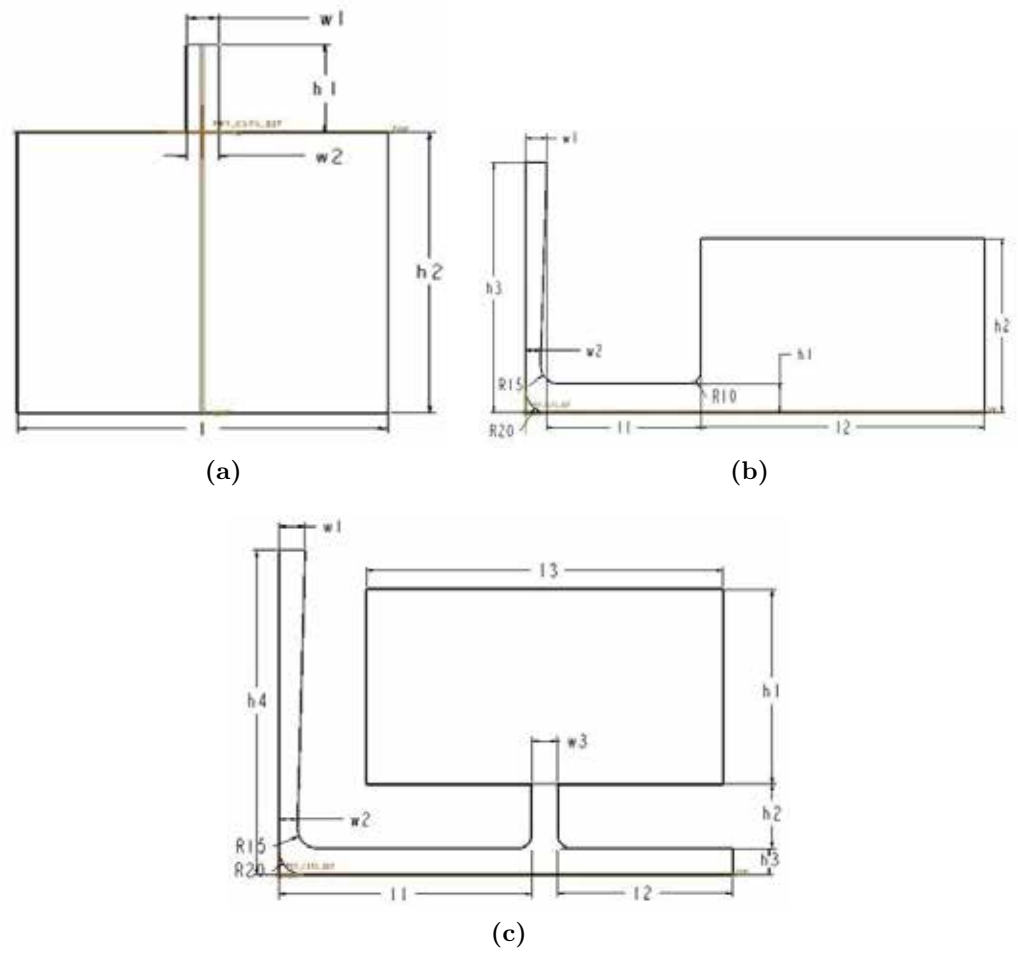

Figure 3.2: The geometric parameter of three types of moulds. (a). Plunging Jet; (b). Return Wave; (c). Rising Jet.

Initially all the moulds were modelled with one mesh block for simplicity and to reduce computing time. The typical layout of the mould inside the mesh block is shown in Figure 3.3. More mesh blocks were then added to the mesh geometries of the simulations of the rising jet and return waves, as shown in Figures 3.3b and 3.3d, to study the location of entrainment and the code sensitivity to the numbers of mesh blocks. The boundary condition was set at the top surface of the mesh block, as shown

Table 3.1: The dimensions of Plunging_Jet moulds. (Unit: mm)

Plunging_Jet	W1	W2	H1	H2	I
4	17	17	65	150	275
5	17	14	65	150	275
11	17	14	65	275	150

Table 3.2: The dimensions of Return_Wave moulds. (Units: mm)

Return_Wave	Fixed dimensions	I1	I2	H1	H2
1	W1=20	150	275	25	150
5	W2=14	150	330	25	125
6	H3=250	150	330	5	125

Table 3.3: The dimensions of Rising_Jet moulds. (Unit: mm)

Rising_jet	Fixed dimensions	W3	I2	H2	H3
1	W1=20 W2=14	20	135	50	20
3	I1=195 I3=275	20	135	25	20
7	H1=150	20	135	25	20
10	H4=250	15	0	50	15

in Figure 3.3d. The size of the mesh cells was set to 5 mm in all three dimensions to reduce computational expense.

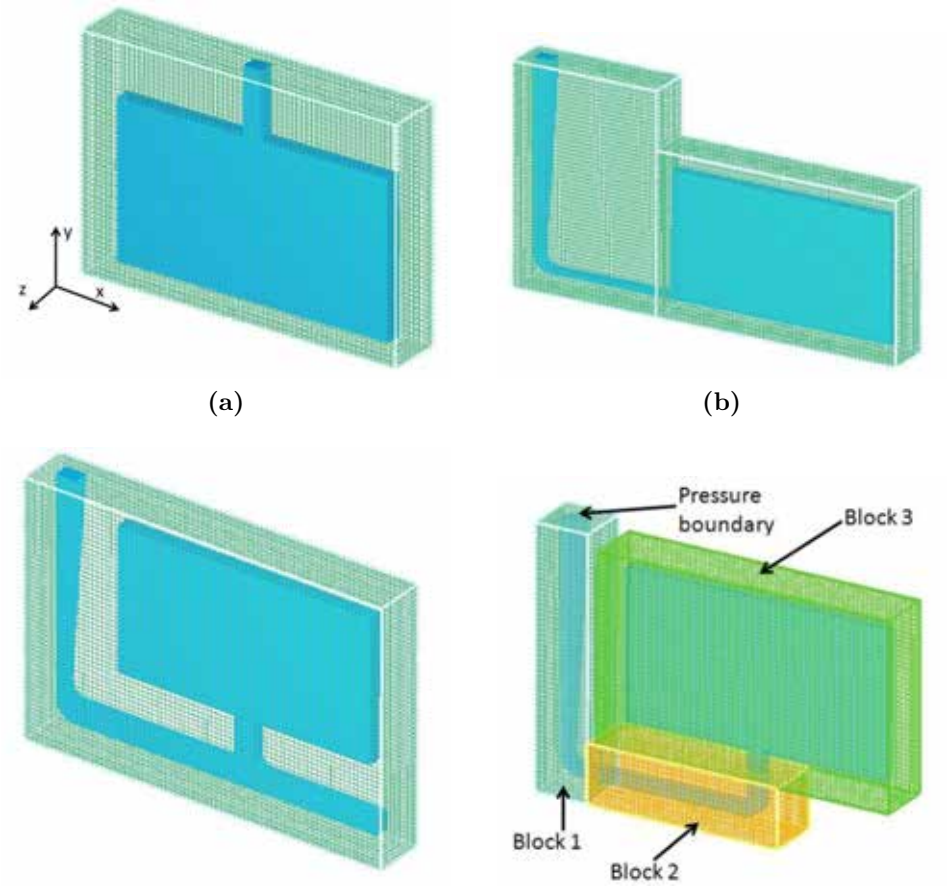

Figure 3.3: The mesh settings of preliminary simulations.(a). Plunging Jet; (b). Return Wave; (c). Rising Jet; (d). Rising Jet (three blocks).

The simulations were modelled as isothermal, assuming that heat transfer and solidification during filling had minimal influence on the entrainment mechanisms and the free surface structure of the fluid flow. The widely used Al-7Si-0.4Mg alloy (A356.0) was used in the simulations and the physical properties of A356 alloy used in these simulations are listed in Table 3.4. The data were from *FLOW-3D* v9.4 liquid materials database. The special factors of the alloy in Table 3.4, *i.e.* the "Coefficient of solidification drag", "Critical solid fraction" and "Coherent solid fraction", are used to model the liquid-to-solid phase change in *FLOW-3D*. When the solid fraction of liquid

reaches the "Coherent solid fraction", the viscosity of the liquid increases and the drag force that will be applied to the region is calculated by a function, which depends on the "Coefficient of solidification drag". Once the solid fraction of the liquid reaches "Critical solid fraction", the liquid in the region will stop moving. The general settings of *FLOW-3D* for these simulations are listed in Table 3.5.

Table 3.4: The physical properties of liquid A356 alloy in *FLOW-3D*.

Properties	**Value**	**Unit**
Density (liquid)	2420	$kg \cdot m^{-3}$
Dynamic viscosity	0.00119	$Pa \cdot s$
Specific heat (liquid)	1194	$J \cdot kg^{-1} \cdot K^{-1}$
Thermal conductivity (liquid)	86.9	$W \cdot m^{-1} \cdot K^{-1}$
Density (solid)	2570	$kg \cdot m^{-3}$
Thermal conductivity (solid)	185	$W \cdot m^{-1} \cdot K^{-1}$
Specific heat (solid)	1265	$J \cdot kg^{-1} \cdot K^{-1}$
Coefficient of solidification drag	500	
Critical solid fraction	0.68	
Coherent solid fraction	0.23	
Liquidus temperature	884	K
Solidus temperature	828	K
Latent heat of fusion	4.29 E+05	$J \cdot kg^{-1}$

3.3.2 Modelling with Gravity along the Different Axis

The preliminary simulations showed that Impingement forms were dominant amongst the three types of entrainment forms. Meanwhile, four Impingement forms, which involved description of the liquid jet dropping down to impact the bulk liquid, created the majority of particles. More simulations were carried out to try to understand if the domination of the four Impingement forms was associated with the entrainment event in fluid flow, *i.e.* plunging jet flow, or was due to potential error in the entrainment criteria of the codes. Since the OFEM algorithm was defined in three dimensions, it was believed that simulations with gravity set along another direction with the mould were

Table 3.5: The global setting for the modelling in *FLOW-3D*.

Gravity	Gravity component in the y-direction	-9.81 N$\cdot$ kg^{-1}
Particles	Mass particles	Variable diameter
	Particle density	2200 kg$\cdot$ m^{-3}
	Maximum number of particles allowed	1.0E+07
	Diffusion coefficient	0
	Inverse Schmidt number	0
	Coefficient of restitution	-1
	Drag coefficient	1
	Free surface interaction	Particles can move in fluid only
	Initialization	By customised code
Surface tension	Surface tension coefficient, σ	1
	Contact angle	160°
	Numerical approximation for surface tension pressure	Explicit
	Viscosity options	Newtonian viscosity
Viscosity and turbulence	Turbulence models	Renormalized group (RNG) model
	Turbulent mixing length	0.001 mm
	Wall shear boundary conditions	No-slip or partial slip
	Friction coefficient	-1
	Vertical viscosity multiplier	1
Boundary condition	Specific pressure	948.64 Pa

rotated accordingly to a different angle, should entrain the same number of particles as those simulations with initial setting, when the simulations have identical boundary condition and mesh definition. The only difference between these two types of models should be the entrainment form of the particles. For example, there are four dominant Impingement forms in terms of placing particles in the mould shown in Figure 3.3c (the gravity was along y negative direction). If the mould rotates 90° anti-clockwise around z-axis, and the gravity direction is set to along x positive direction, with the same initial modelling conditions, the same amount of particles should be placed. In this case, there should be another four dominant Impingement forms, of which the velocity vector of the free surface defined in the code is rotated clockwise 90°, the forms will be the same as those that have y negative gravity.

Two moulds used in the preliminary modelling were used again in the simulation, but with different mesh layout. The moulds and meshes were rotated 90° anti-clockwise

around z-axis, as shown in Figure 3.4. The pressure boundary then altered to x-min with the same value listed in Table 3.5. Using the "Gravity" module in *FLOW-3D*, the gravity direction was changed to the x-direction with the value of 9.81 $\mathrm{N \cdot kg^{-1}}$.

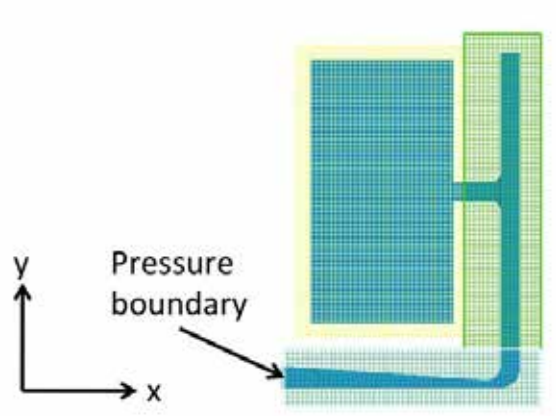

Figure 3.4: Mesh settings for model with gravity along x-direction.

3.3.3 Colliding Fronts and Shear Flows

Since the Colliding Fronts and Shear Flows forms seemed very rare in placing particles in the simulations, to study their mechanism of placement and to find the reason they were unusual, modelling of typical colliding fluid fronts and shear flows was conducted, using a bar with pressure boundaries at the two ends of the mould, as shown in Figure 3.5. The arrows indicate the location and inlet directions at the pressure boundary. Models of Colliding Fronts were set with and without gravity, while models of shear flows were set to have no gravity effect, which was believed could create some flow conditions that meet the entrainment criteria defined in the subroutines in the OFEM. Models were also setup with different surface tension and finer mesh size (0.002 mm).

3.3.4 Mesh Sensitivity of OFEM Algorithm

To understand the mesh sensitivity of the OFEM codes, a series of simulations of filling the three moulds shown in Figure 3.6 were conducted. The models using the parameters shown in Table 3.5 with a pressure boundary of 948.64 MPa (equal to a

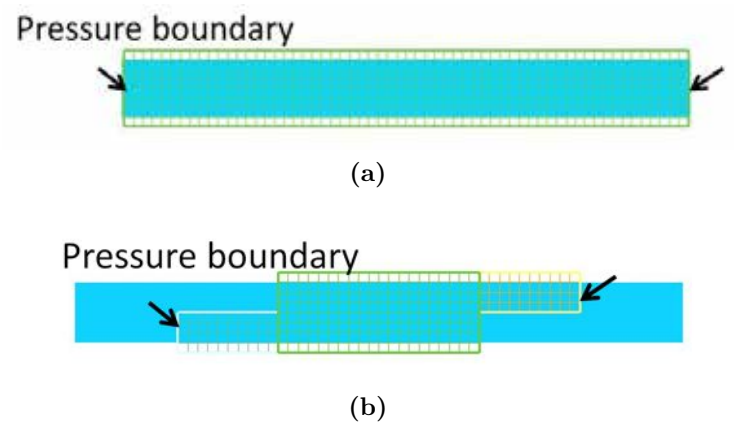

Figure 3.5: Mesh settings for colliding fronts and shear flows models. (a). colliding fronts model; (b). shear flow model.

pressure head of 40 mm liquid A356 alloy) applied at the inlet of the downsprue. The mesh size of the blocks containing the mould cavity were adjusted to 2, 2.5, 3, 4 and 5 mm in different simulations, to test the mesh sensitivity of the particle distribution.

3.4 Validation of OFEM by Previous Experiments

3.4.1 Fatigue Life Validation Model

Nyahumwa studied the influence of double oxide films on the fatigue life of cast Al-7Si-Mg alloy and pointed out that 90% of fatigue failures in his experiment were initiated from double oxide film defects [156]. The experimental results were used in the study, intended validate the OFEM algorithm.

3.4.1.1 Experimental Procedure and Fatigue Test Results

In Nyahumwa's research, two batches of test bars were cast in a resin-bonded silica sand mould with and without 20 ppi (pores per inch) ceramic foam filters. The experiment details are documented in Nyahumwa's thesis [156]. Figure 3.7 shows the estimated geometries of the crucible and pouring basin used in the experiments, as there was no drawing provided in Nyahumwa's report. The geometries of the mould used in the experiments are shown in Figure 3.8. The filter print region was at the junction of the

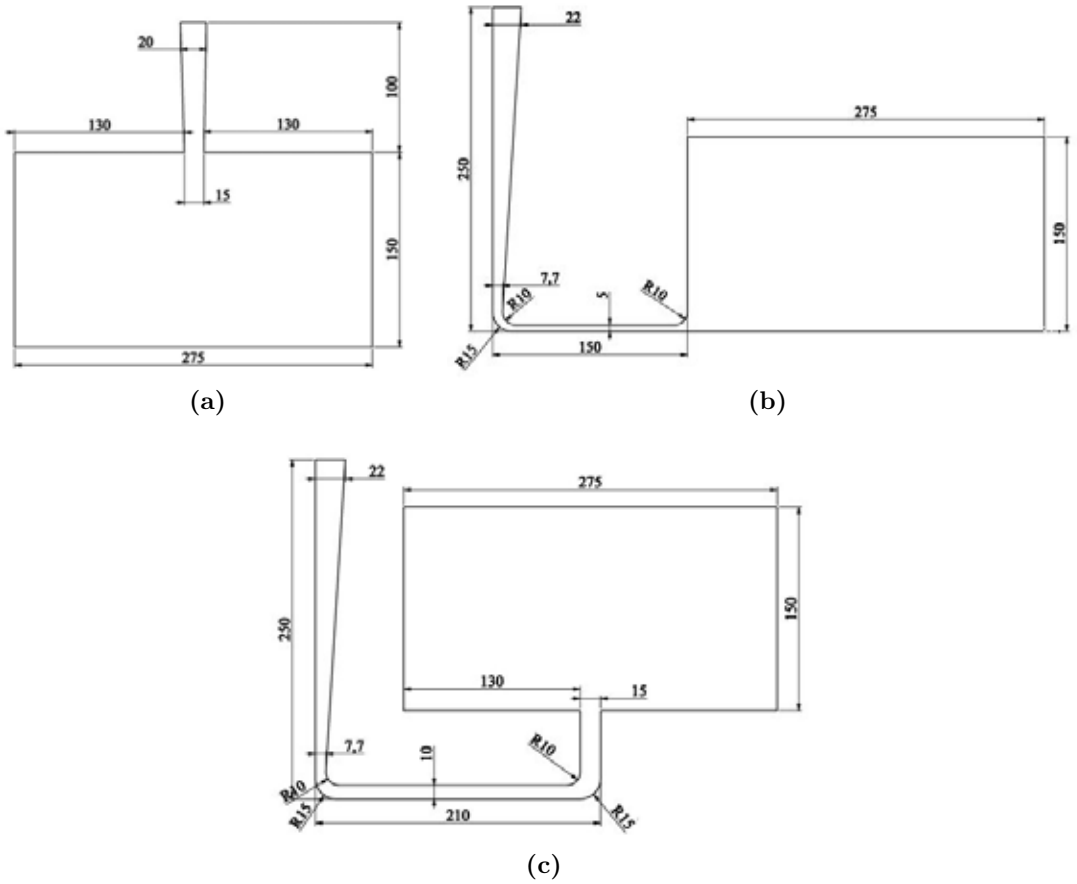

Figure 3.6: The geometries of the three moulds (Unit: mm). The thickness of moulds is 15 mm.(a). plunging jet mould; (b). return wave mould; (c). rising jet mould.

bottom end of the downsprue and the middle of the runner, as indicated in Figure 3.8c. The test bars were labelled as shown in Figure 3.9. All the samples were heat treated and the fatigue properties of randomly selected specimens from different locations were tested in pull-pull loading at maximum stresses of 150 and 240 MPa, *i.e.* high and low cycle tests respectively, with the stress ratio of R=+0.1.

Table 3.6 shows the average cycles to failure of specimens from different locations that calculated from Nyahumwa's result. It also shows the mean fatigue lives of specimens in each cast condition. The plot of the data is shown in later section in Figure 5.17. The standard errors (SE) at bottom of Table 3.6 are the standard deviation of the means of fatigue lives of samples from different locations, and the standard

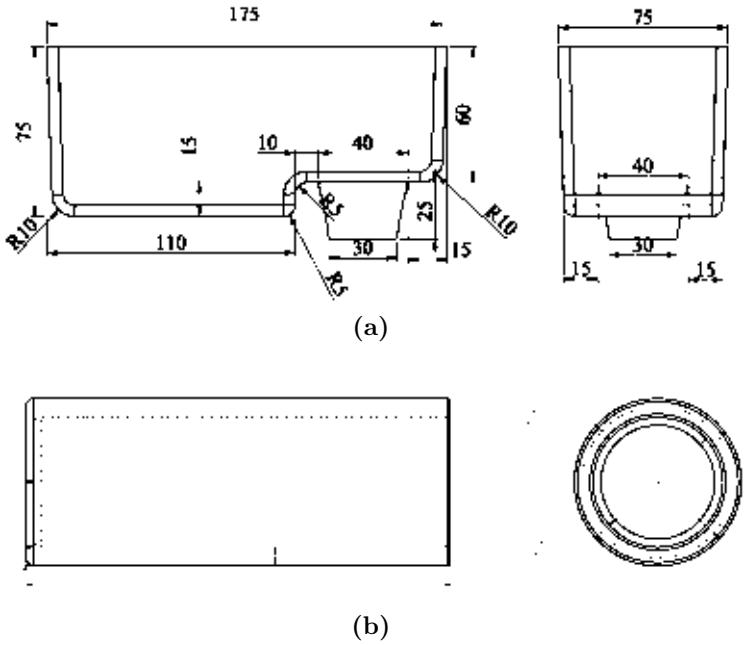

Figure 3.7: The geometries of the crucible and pouring basin used in Nyahumwa's experiments. (a). pouring basin; (b). crucible.

errors in each row in different conditions are the standard deviation of mean fatigue lives of samples in the specific location. Since the specimens were randomly selected from the castings, the number of specimens selected from each position was different, and the mean or standard error of fatigue lives of sample from that location in that test condition sometimes could not be obtained, which mark as "N/A" in the table. Standard error can be used to estimate the probability of distribution of sample means within a range of the population mean. Statistically, 95.6% of the sample means should fall between $\pm 2SE$. Therefore, if the sample mean is more than $2SE$ apart from the population mean, the sample would be considered as biased.

Clearly, the mean fatigue lives of the specimens to the left and right of downsprue at symmetric positions were distinct, although the specimens were located symmetrically besides the downsprue. For instance, in high cycle test, the average fatigue life of Specimen F from the unfiltered casting was three times as that of Specimen E. Table 3.6 shows that many of the mean fatigue lives of specimens in each position fall outside the

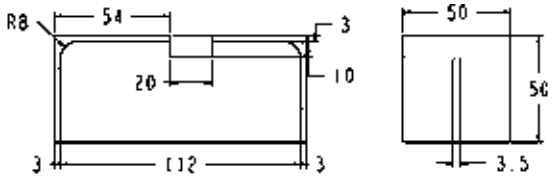

(a)

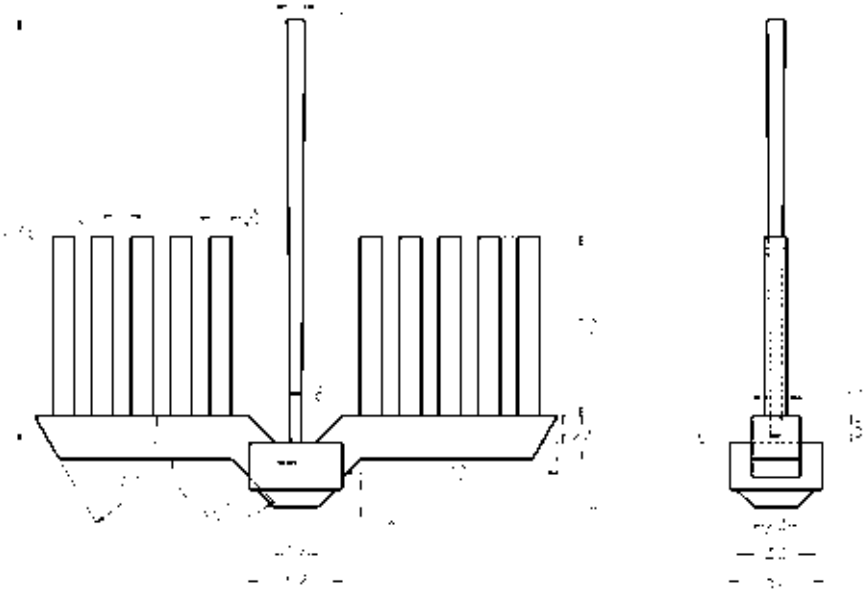

(b)

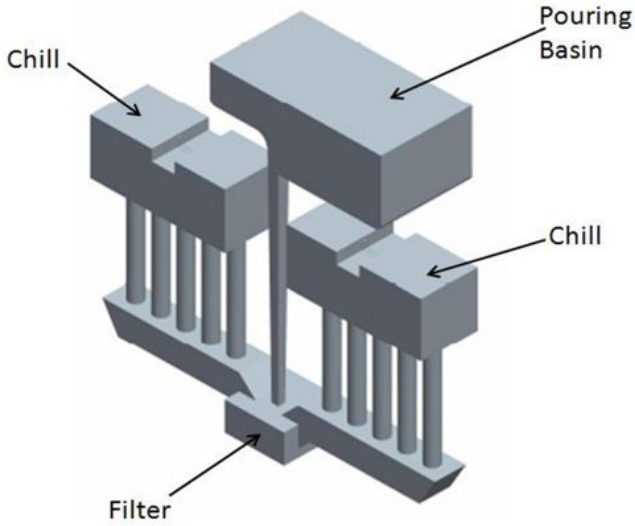

(c)

Figure 3.8: The geometries of the mould used in Nyahumwa's experiments. (a). chill; (b). runner system and test bars; (c). the assembly of the mould in 3D.

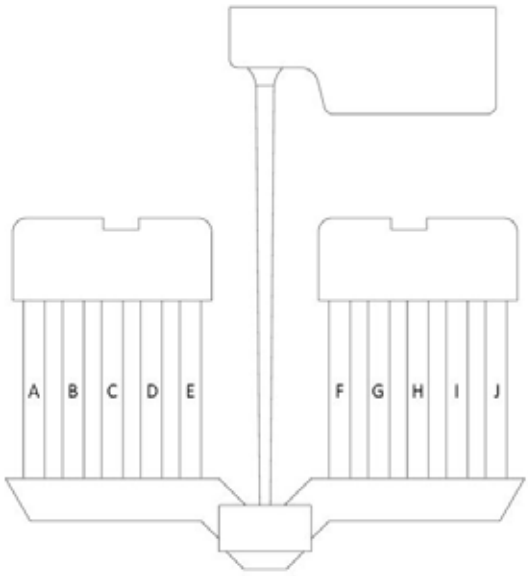

Figure 3.9: The labels of test bars in the mould for fatigue testing bars.

lower and upper limits of the intervals defined by the mean fatigue lives and standard errors of the means. The standard errors of fatigue lives of samples from each location also show a large range of variation. Therefore, the previous experimental data *per se* have flaws, which make the mean value of fatigue lives difficult to depict the general variation trends of fatigue lives of specimens in different positions. Therefore, attempts were made to compare the modelling and experimental results, but only a few results are report in later chapter.

Table 3.6: The mean fatigue lives and standard errors of specimens from different locations under four conditions.

Specimen	low cylce test				high cycle test			
	unfiltered		filtered		unfiltered		filtered	
	mean	SE	mean	SE	mean	SE	mean	SE
A	3.40E+04	2.08E+04	5.96E+04	1.50E+04	2.27E+05	7.45E+04	4.49E+06	1.72E+06
B	3.64E+04	8.06E+03	3.51E+04	1.49E+04	1.85E+06	1.67E+06	1.82E+06	9.84E+05
C	N/A	N/A	5.44E+04	8.49E+03	1.42E+05	2.83E+04	3.22E+05	
D	4.47E+04	1.20E+04	2.10E+04	5.86E+03	2.10E+06	1.92E+06	4.24E+06	2.48E+06
E	2.73E+04	7.85E+03	4.26E+04	N/A	4.77E+05	N/A	1.09E+06	4.32E+05
F	3.63E+04	1.30E+04	4.11E+04	3.13E+04	1.42E+06	1.01E+06	2.18E+06	1.73E+06
G	5.02E+04	2.91E+03	7.18E+04	2.53E+04	2.79E+05	3.81E+04	4.20E+05	6.66E+03
H	1.08E+04	8.57E+02	5.12E+04	N/A	2.21E+05	8.20E+03	N/A	
I	2.37E+04	1.26E+04	7.92E+04	1.58E+04	2.29E+05	N/A	3.90E+05	1.32E+05
J	2.63E+04	5.04E+03	3.81E+04	1.46E+04	2.76E+05	5.68E+04	3.94E+05	8.03E+04
Mean	3.26E+04		5.60E+04		8.80E+05		1.99E+06	
Standard error	3.72E+03		5.55E+03		2.40E+05		5.22E+05	
lower 2SE	2.52E+04		4.49E+04		4.00E+05		9.46E+05	
upper 2SE	4.00E+04		6.71E+04		1.36E+06		3.03E+06	

3.4.1.2 Set-up for the Validation Model

Three simulations of each mould (with and without filter) were completed, and the different factors used to investigate their impact on the final results are listed in Table 3.7. Mesh definitions of Simulations 1 to 3 are given in Figure 3.10 and the mesh size of each mesh block is detailed in Table 3.8. The physical properties of A356 alloy and silica sand listed in Tables 3.4 and 3.10 respectively were applied to the models. The global settings for these simulations are detailed in Table 3.9. In the simulations, the tilting of the crucible to pour the liquid into the basin was modelled. The simulations were allowed to run extra three seconds once the moulds were fully filled to consider the solidification process. It should be noted that the properties of the particle were assumed values owing to a lack of relative experimental data. A subroutine was written to count the number of particles come to rest in the test gauge length and whole volume of each test bar, and the data was used to study the distribution of particles in local area and for comparison between the predicted defect quantities and the fatigue

properties of specimens from different locations.

Table 3.7: Modelling conditions of the four simulations.

Simulation	Inlet condition	Particle placing interval (s)	Entrainment in basin
1	Pouring	0.02	Modelled
2	Pouring	0.005	Neglected
3	Pouring	0.02	Neglected

Table 3.8: Mesh size of each mesh block.

Block	1	2	3	4	5
Mesh size (mm)	4	1	2	2	2

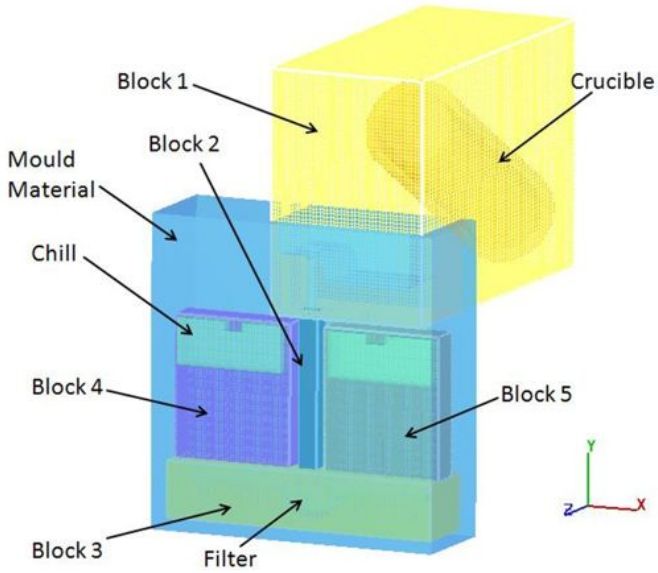

Figure 3.10: The mesh definitions of the fatigue life validation models.

3.4.2 Froude Number Validation Model

Reilly developed a Froude number criterion function in *FLOW-3D* to study the influence of flow condition in a horizontal running system on the mechanical properties of castings. The test bars which were cast in different moulds in Reilly's experiments were heat treated and tensile tested, and the results were compared with the modelling results using the customised Froude number criterion function, which has been reviewed

Table 3.9: The global setting for the modelling in *FLOW-3D*.

Module	Setting	Value and Unit
Gravity	Gravity component in the Y-direction	-9.81 $N \cdot kg^{-1}$ (minus sign indicates downwards)
Particles	Mass particles	Variable diameter
	Particle density	2200 $kg \cdot m^{-3}$
	Maximum number of particles allowed	1.00E+07
	Diffusion coefficient	0
	Inverse Schmidt number	0
	Coefficient of restitution	-1
	Drag coefficient	1
	Free surface interaction	Particles can move in fluid only
	Initialization	By customised code
Surface tension	Surface tension coefficient, σ	1
	Contact angle	160°
	Numerical approximation for surface tension pressure	Explicit
	Viscosity options	Newtonian viscosity
Viscosity and turbulence	Turbulence models	Renormalized group (RNG) model
	Turbulent mixing length	0.001 mm
	Wall shear boundary conditions	No-slip or partial slip
	Friction coefficient	-1
	Vertical viscosity multiplier	1
Porous media	Porosity	0.753
	Drag Coefficient 'a'	29.37
	Drag Coefficient 'b'	7.368

Table 3.10: The physical properties of silica sand used in the model [157].

Properties	**Value**	**Unit**
Heat transfer to fluid	1500	$W \cdot m^{-2}$
Component contact angle	160	°
Initial temperature	298	K
Thermal conductivity	0.65	$W \cdot m^{-1} \cdot K^{-1}$
Density * Specific heat capacity	1500240	$J \cdot m^{-3}\, kg^{-1}$

in Section 2.2.2.4 [8]. The tensile test results were used to validate the OFEM model. It should be noted that the tensile strength of test bars from the high moulds without filter (explained later) was not available due to very low mechanical properties caused by trapped gas bubbles in the gauge length.

3.4.2.1 Set-up for Validation Model

Figure 3.11 shows the dimensions of the moulds used in the Froude number criterion function model. The different heights of the ingates and downsprues of the "high" and the "low" moulds would generate different levels of surface turbulence in the running system and the difference would be reflected in the number of particles generated by the OFEM algorithm.

The mesh layouts used in the simulation of the two kinds of moulds are shown in Figure 3.12. The modelling considered the pouring process from the crucible to the pouring basin and the detail of the pouring conditions were obtained from Reilly [8]. The particle placing codes in OFEM method was not activated in Block 1 as shown in Figure 3.12, since the initial study of the effect of pouring basin on the distribution of particles in the mould cavity was minimal. The particle placing time interval was set to 0.02 s, in order to reduce the computational expense resulting from the significant number of particles generated in the mould. Other settings of the *FLOW-3D* modelling conditions were the same as listed in Table 3.9.

A code which was similar to the one used in the fatigue life validation model was used to count the number of particles in each test bar in the gauge length in this model. The reciprocals of these particle counts were then deduced and compared with the tensile strength variation tendency of test bars in different location shown in Figure 3.13.

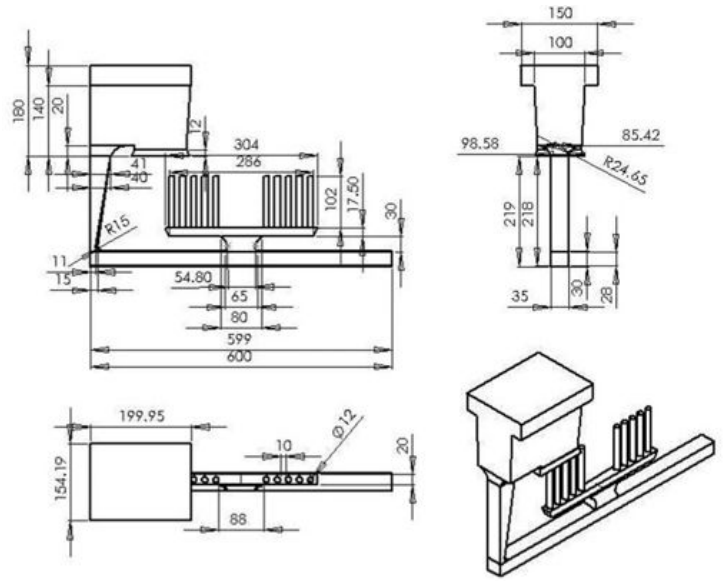

(a)

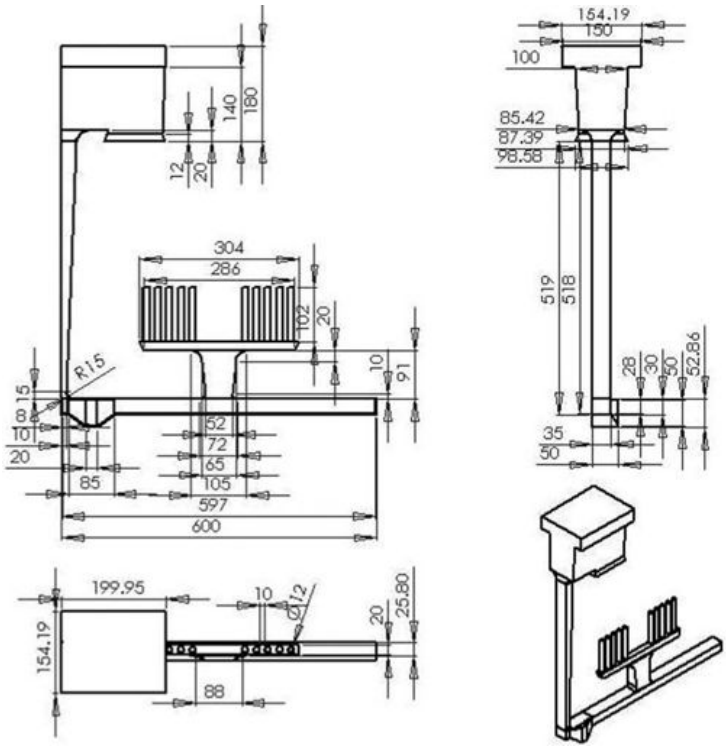

(b)

Figure 3.11: The examples of geometrical dimensions of the four moulds used in Froude number criterion function validation model. The dimensions of the low mould with filter and high mould without filter were similar to those shown here. (a). low mould without filter; (b). high mould with filter.

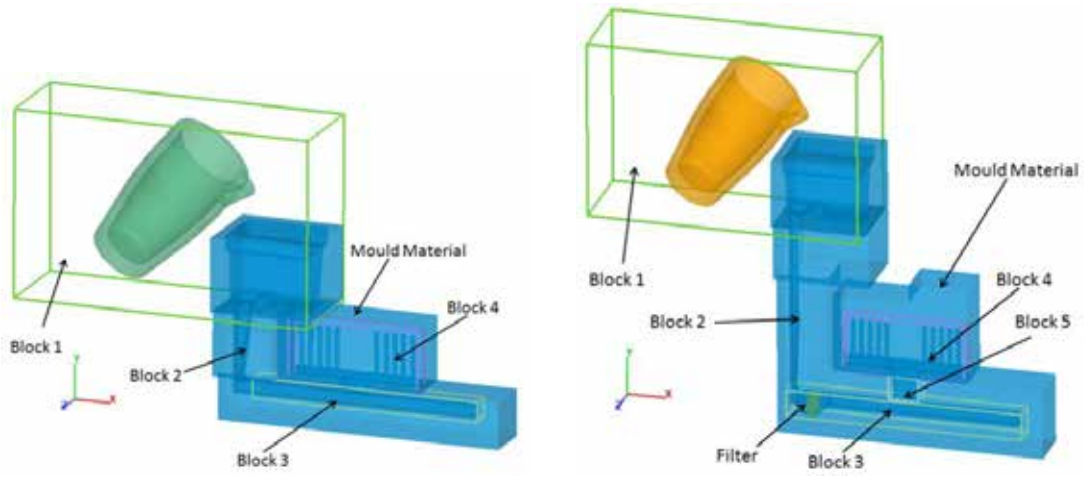

(a) (b)

Figure 3.12: The mesh definitions of Froude number validation models. (a). low mould; (b). high mould.

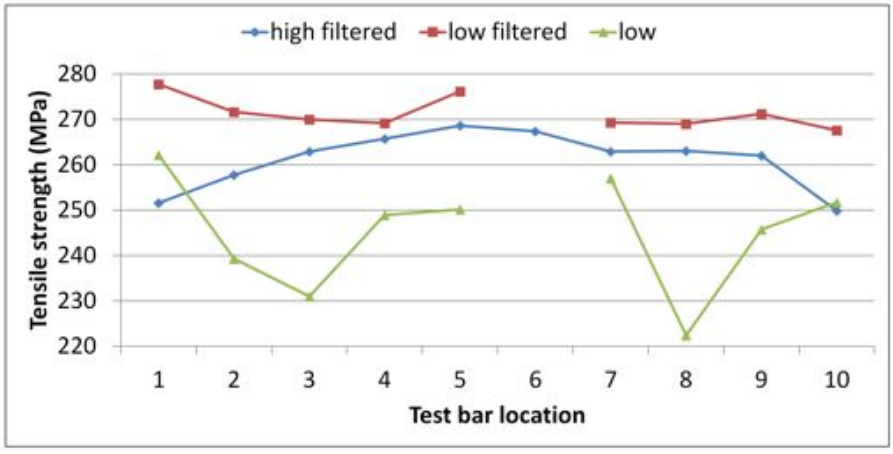

Figure 3.13: The mean UTS of the test bars from Froude number validation moulds. Test Bar 1 is closest to the downsprue and 10 furthest from it.

3.5 The Three Entrainment Mechanisms

Different flow structures formed in a running system will generate different levels of surface turbulent flow, and hence, alter the number of entrainment defects during filling. The common entrainment mechanisms have been discussed in Section 2.1.1. However, the amount of entrainment defects generated by these mechanisms has not been compared quantitatively in any previous study. In order to study the influences of the different entrainment mechanisms on the mechanical properties and reliability of castings and their relative significance, the three common entrainment mechanisms, namely, plunging jet (PJ), return wave (RW) and rising jet (RJ) were studied using the OFEM model and the results were validated against experimental results. A series of models was completed to study the influence of several factors, such as particle properties, wall boundary conditions, on the particle distribution in the mould cavity.

3.5.1 Mould Geometries and Mesh Setup

Three moulds with the same cavity dimensions, but different running systems, were designed and employed for both modelling and experiment. The running system was designed to minimize the entrainment in this region and allow the preferred flow structure to be generated in the mould cavity. Figures 3.6 shows the geometries of the moulds. The pouring basin and crucible used in both experiment and model were the same as reported in Figure 3.7.

Figure 3.14 illustrates an example of the assembled mould cavity within the mould components in *FLOW-3D*. A solid component was created as the mould material which had the properties of a sand mould, and the computer-aided design (CAD) drawing of the mould cavity was imported into the solid mould as a "hole" type component to remove the material within the component. A crucible component with a pre-defined rotation was imported in *FLOW-3D* to model the controlled pouring, and the vertical movement of the stopper at the desired time was also defined in the model. The time

when the stopper was pulled out of the downsprue was based on the liquid level in the pouring basin, which was the same in the model as in the corresponding experiments.

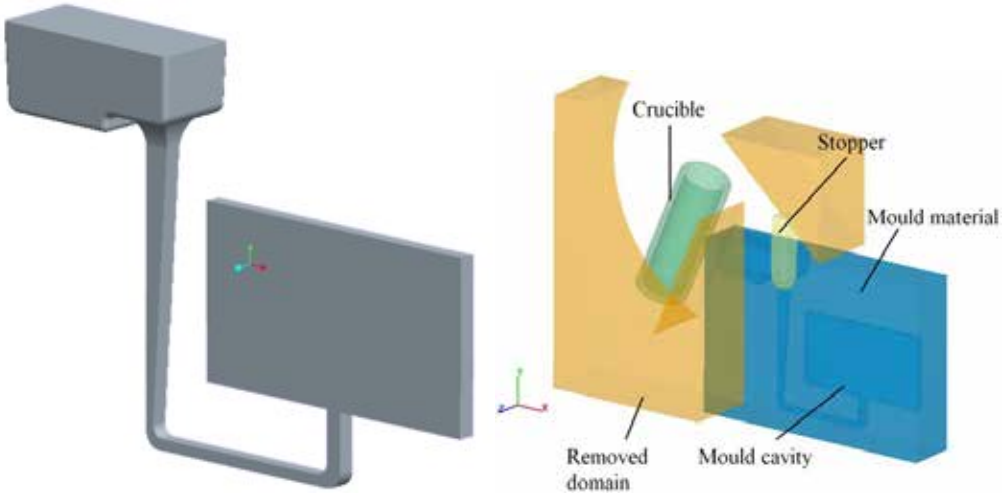

Figure 3.14: Example of the assembly of the mould in 3D and corresponding setting in *FLOW-3D* components. (a). Example of the assembly of the mould cavity (RJ); (b). The components setting in *FLOW-3D* (RJ).

Figure 3.16 shows the mesh zones in the three models, in which two or three mesh blocks were employed depending on the geometries of the mould cavity. The mesh size of each block is given in Table 3.11. In all models, Block 1 contained the crucible, the pouring basin, the downsprue and the stopper. It resolved the rotation of the crucible and the upwards removal of the stopper. The particle generation in this block was deactivated in order to accelerate the simulation speed. Block 2 contained the mould cavity. An in-house code was written for Block 2, which divided the plate into 30 sub-regions as shown in Figure 3.15, and counted the number of particles in each region. The definition of the sub-region was the same as the bend test specimen definition on the plate. Block 3 was only used in the Return Wave and Rising Jet models to solve the fluid movement in the horizontal runner. All the mesh block boundaries were set to be symmetry boundaries.

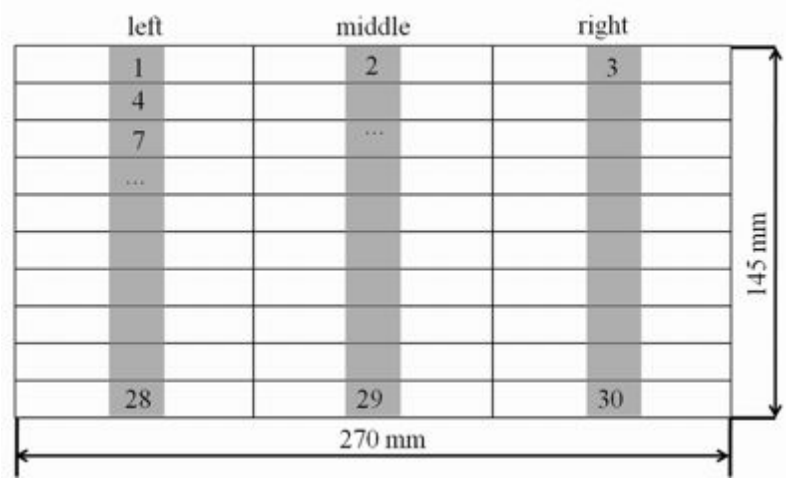

Figure 3.15: The specimen layout on the casting plate. The specimen sequence was marked from top left to the bottom right. 30 specimens were obtained from each plate in total. Gauge length is in shadow.

Table 3.11: The mesh cell size of each block in three entrainment mechanisms models.

Block number	Block 1	Block 2	Block 3
Cell size (mm)	5	2	2

3.5.2 General Model Setting

The alloy properties in Table 3.4 were used in the models. Figure 3.17 shows the initial location of the crucible and the mould. A component that defined the liquid alloy as shown in Figure 3.17b was added at the beginning of the simulation to model the melted alloy in the crucible. The pouring was then modelled by rotating the crucible. The rotation speed and the time to pull the stopper out in the three models are listed in Table 3.12. Preliminary models neglected the solidification of castings, only considered the filling process. Table 3.13 lists the input parameters of the preliminary models.

Table 3.12: The rotation speed of the crucible and pulling time of the stopper.

Model	**Rotation speed (rad/s)**	**Rotation duration (s)**	**Stopper pulling time(s)**	**Total filling time(s)**
Plunging jet	0.307	4.0	2.8	5.5
Return wave	0.291	4.4	4.35	9.8
Rising jet	0.252	4.3	4.51	7.9

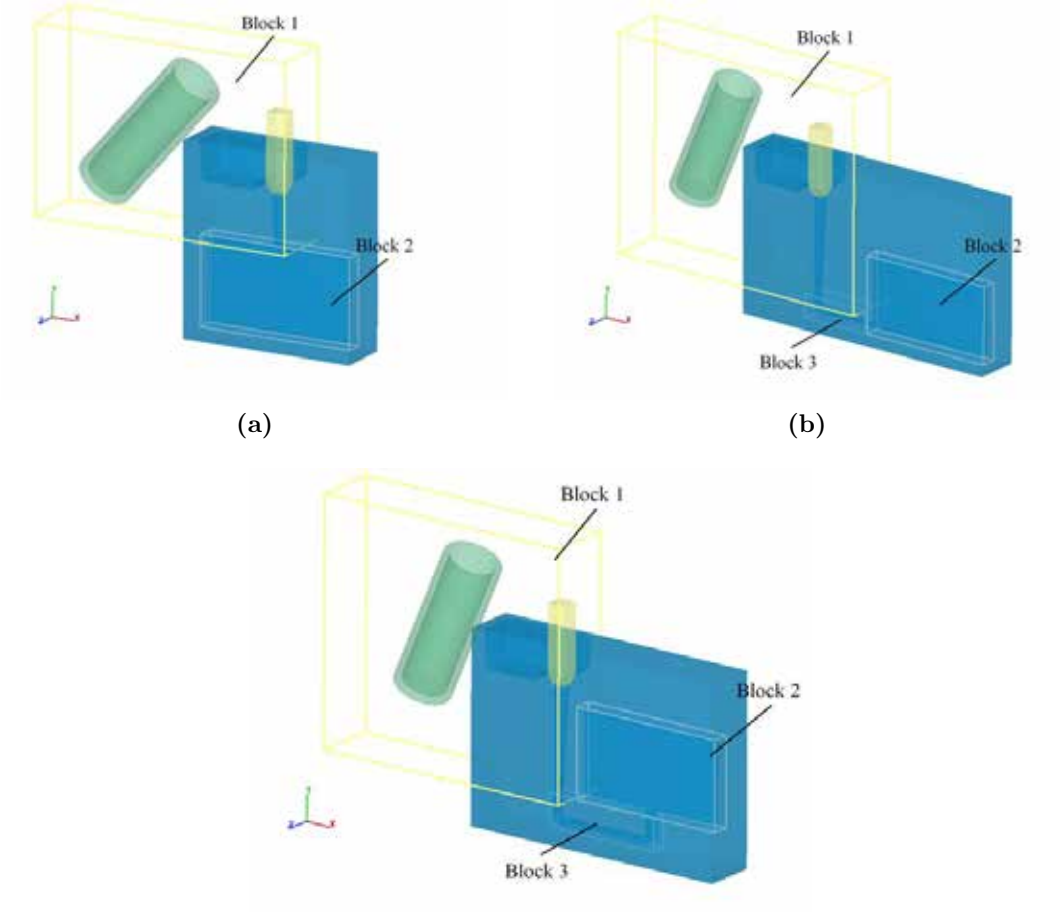

Figure 3.16: The mesh block setup for three entrainment mechanisms models.(a). Plunging Jet model; (b). Return Wave model; (c). Rising Jet model.

3.5.3 Comparative Model Setting

Since the modelling predictions did not correlate with the experimental data, a series of models considering different factors, including particle density, particle stickiness, and initial particle locations were compared with the preliminary modelling results to study the influences of these parameters. Table 3.14 gives the details of the parameters in the comparative models. The particle stickiness was controlled by changing the "coefficient of restitution" from "-1" (sticky) to "1" (non-sticky). The "old" oxide films were modelled by placing a layer of particles on the free surface of liquid alloy in the crucible shown in Figure 3.17 at the beginning of the simulation. The density

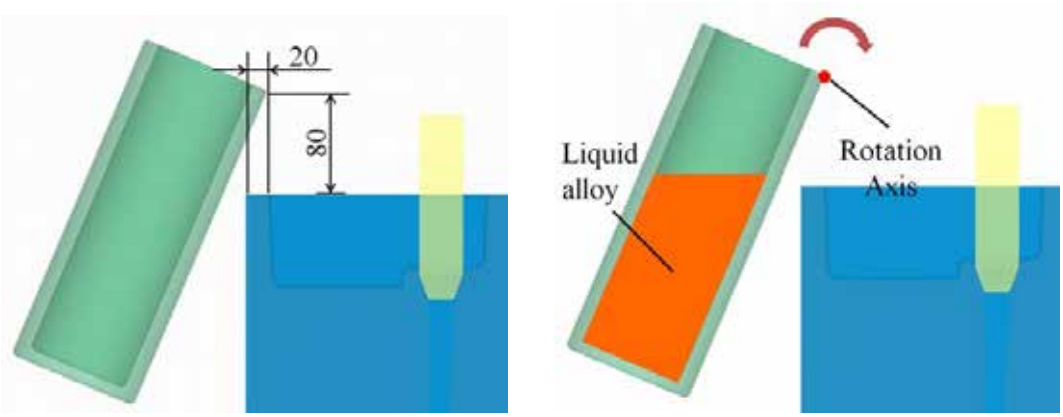

(a) **(b)**

Figure 3.17: The initial layout of the crucible and mould. (Unit: mm) (a). The relative location of the crucible and pouring basin. (b). The location of rotation axis and initial fluid region. The angle between the mould and the crucible for Return Wave and Rising Jet models was 23°; for Plunging Jet model, it was 43° because of the location of the pouring basin in the mould.

Table 3.13: Preliminary input parameters of models in three entrainment mechanisms modelling.

Module	Setting	Value and Unit
Gravity	Gravity component in the Y-direction	9.81 $N \cdot kg^{-1}$
Particles	Mass particles	Variable diameter
	Particle density	2200 $kg \cdot m^{-3}$
	Maximum number of particles allowed	1.00E+07
	Diffusion coefficient	0
	Inverse Schmidt number	0
	Coefficient of restitution	-1 (sticky)
	Drag coefficient	1
	Free surface interaction	Particles can move in fluid only
	Initialization	By customised code
Surface tension	Surface tension coefficient, σ	1
	Contact angle	160°
	Numerical approximation for surface tension pressure	Explicit
	Viscosity options	Newtonian viscosity
Viscosity and turbulence	Turbulence models	Renormalized group (RNG) model
	Turbulent mixing length	0.001 mm
	Wall shear boundary conditions	No-slip or partial slip
	Friction coefficient	-1
	Vertical viscosity multiplier	1

of the "old" oxide particles was set to 2400 kg· m^{-3}. The turbulence model in later simulations were switched from RNG model to $\kappa - \varepsilon$ model after ran several test cases, which showed the latter model was more robust and gave consistent results in simulations.

Table 3.14: Parameters used in comparative models in later simulations.

Particle density	Preliminary models	2200 kg· m^{-3}
	Comparative models	2000 kg· m^{-3}
		2300 kg· m^{-3}
		2400 kg· m^{-3}
		3000 kg· m^{-3}
Particle restitution (stickiness)	Preliminary models	Sticky particles
	Comparative models	Non-sticky particles
Initial particle location	Preliminary models	only in mould ("young" film)
	Comparative models	only in the crucible ("old"film)

Since entrainment defects (or particles in the model) within the liquid alloy can still move before the temperature of the fluid reaches the coherency point owing to the momentum of the fluid, models with heat transfer and solidification modules are necessary for studying the final distribution of the defects. Full models including both filling and solidification of the castings were also carried out. The input settings for these models is shown in Table 3.15.

3.6 X-ray Tomography Heating Profile

The synchrotron-based *in situ* X-ray tomographic observation conducted in the TOMCAT beamline required external heating of the cylindrical sample to melt it [158]. The temperature gradient of the sample between the heating spot and the surrounding liquid might result in convection in the sample, which might consequently affect the location and morphology of any entrainment defects it contained, and also blur the images captured during the scan. To understand the temperature field distribution

Table 3.15: The input parameters of final models of three entrainment mechanisms.

Module	Setting	Value and Unit
Gravity	Gravity component in the Y-direction	9.81 $N \cdot kg^{-1}$
Particles	Mass particles	Variable diameter
	Particle density	2400 $kg \cdot m^{-3}$
	Maximum number of particles allowed	2.00E+05
	Diffusion coefficient	0
	Inverse Schmidt number	0
	Coefficient of restitution	1
	Drag coefficient	1
	Free surface interaction	Particles can move in fluid only
	Initialization	By customised code
Surface tension	Surface tension coefficient, σ	1.01
	Contact angle	163°
	Numerical approximation for surface tension pressure	Explicit
	Viscosity options	Newtonian viscosity
Viscosity and turbulence	Turbulence models	Two-equation ($\kappa - \varepsilon$) model
	Turbulent mixing length	0.001 mm
	Wall shear boundary conditions	No-slip or partial slip
	Friction coefficient	-1
	Vertical viscosity multiplier	1
Heat transfer	Fluid internal energy advection	First order
	Fluid to solid heat transfer	Full energy equation
	Numerical Approximations	Implicit
Solidification	Solidification shrinkage	No shrinkage

and the convection behaviour of the liquid sample under continuous heating, a heating model was run in *FLOW-3D* to simulate the heating profile of samples.

The simulation was conducted in a structural mesh setup with a 0.2 mm uniform mesh in three dimensions. In the model, a cylindrical object was placed in the centre of the vessel as shown in Figure 3.18a. The inner surface of a ring object in contact with the vessel was used as a heat transfer boundary with defined heat flux to model the laser heating around the object. Figure 3.18b shows the dimensions of the cylinder, the glass vessel and the contact area of the ring object with the tube.

The model considered the thermal expansion and density variation of A356 alloy in both the solid and liquid state. Since *FLOW-3D* uses a drag model to simulate the

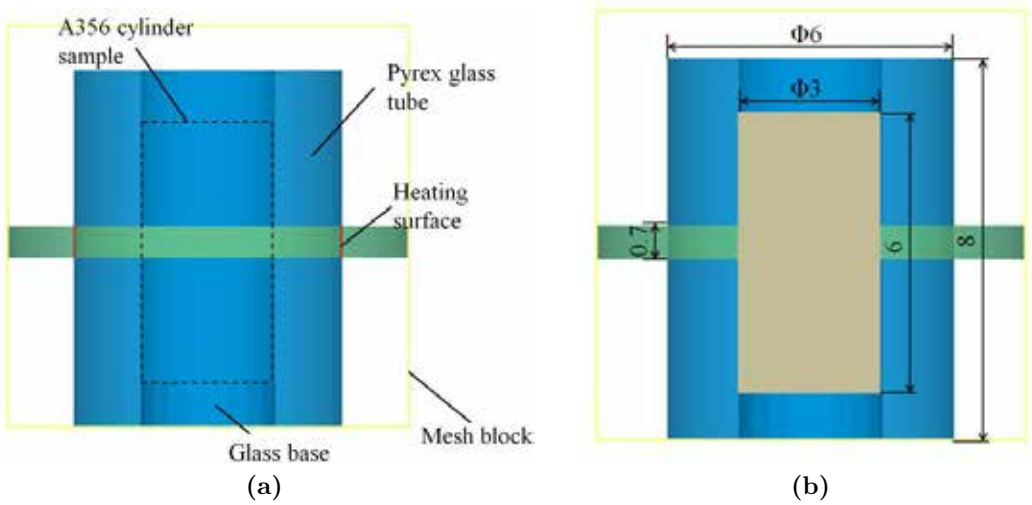

Figure 3.18: The layout and dimensions of the components in the heating profile model. (unit:mm)(a). components in the simulation; (b).dimensions of components.

liquid-to-solid phase change, the solidification drag coefficient, the critical and coherent solid fraction of the alloy are all assumed value, and hence, may not model the solidification accurately. In the simulations considered the influence of surface tension, the free surface of liquid were not stable and the simulations did not converge. Therefore, the influence of surface tension of the alloy was neglected, due to the difficulties of modelling the surface curvature formation during phase change of *FLOW-3D*. The physical properties of Al-7Si-0.3Mg alloy (A356) and the Pyrex glass container listed in Tables 3.16 and 3.17 were assigned to the cylinder and vessel respectively, to model the heat transfer and melting behaviour of the A356 cylindrical sample in a Pyrex glass vessel. The initial boundary conditions shown in Table 3.18 were applied in the simulations. The initial temperature of all objects was set to room temperature (298.15 K). A constant heat flux was then applied to the heating surface. Three different heating rates, which were approximately 10 $K \cdot s^{-1}$ (the same as the experimental condition in TOMCAT), 4 $K \cdot s^{-1}$ and 40 $K \cdot s^{-1}$, were modelled to demonstrate the velocity magnitude of any convection in the fluid during heating. One additional model considered the surface roughness of the vessel was ran in order to study the effect of the addi-

tional drag force on the boundary layer between the liquid and the vessel. This was modelled by defining a surface drag coefficient in *FLOW-3D*. lThe results are reported in Section 5.4.2.1.

Table 3.16: Physical properties of A356 alloy.(*FLOW-3D* database)

Properties	**Value**	**Unit**
Density (liquid)	2420	$kg \cdot m^{-3}$
Thermal expansion (liquid)	43.6E-6 [1]	K^{-1}
Dynamic viscosity	0.00119	$Pa \cdot s$
Specific heat (liquid)	1194	$J \cdot kg^{-1} \cdot K^{-1}$
Thermal conductivity (liquid)	86.9	$W \cdot m^{-1} \cdot K^{-1}$
Density (solid)	2570	$kg \cdot m^{-3}$
Thermal conductivity (solid)	185	$W \cdot m^{-1} \cdot K^{-1}$
Specific heat (solid)	1265	$J \cdot kg^{-1} \cdot K^{-1}$
Thermal expansion (solid)	2.35E-05	K^{-1}
Coefficient of solidification drag	500	(dimensionless)
Critical solid fraction	0.68	(dimensionless)
Coherent solid fraction	0.23	(dimensionless)
Liquidus temperature	884	K
Solidus temperature	828	K
Latent heat of fusion	4.29 E+05	$J \cdot kg^{-1}$

Table 3.17: Physical properties of Pyrex glass (Solid) [159].

Properties	**Value**	**Unit**
Density	2230	$kg \cdot m^{-3}$
Thermal expansion	4.0 E-06	K^{-1}
Specific heat	750	$J \cdot kg^{-1} \cdot K^{-1}$
Thermal conductivity	1.14	$W \cdot m^{-1} \cdot K^{-1}$
Static friction coefficient	0.6	(dimensionless)
Surface roughness	0.01	mm

Table 3.18: Boundary condition in simulation.

Condition	Value	Unit
Global initial temperature	298.15	K
Void initial pressure	101325	Pa
Laser spot width	6	mm
Laser spot height	0.7	mm

3.7 The Tensile Bar Model

Previous studies have shown that a higher population of entrainment defects in a casting result in lower and more scattered mechanical properties. The initial intention of studying three different entrainment mechanisms was to validate the OFEM algorithm by an inverse relationship between the particle count from the model and mechanical properties of the casting, and to study the relative importance of the entrainment-generating flow conditions in entrainment defects formation. However, later experiments showed that the bending strength of some samples from cast plates was affected by shrinkage porosity in the centre of the plates. Additionally, bend testing only tested the strength of a sample in the gauge length, *i.e.* only 22% of the material could be tested. This could not represent the bulk properties of the sample, which were the model predicted. Therefore, another set of experiments was conducted to avoid the adverse influence of shrinkage porosity and to test larger volumes of materials in the test region.

3.7.1 Mould Geometries and Mesh Setup

Figure 3.19 shows the geometry of a mould for making tensile test bars. The pouring basin used in the models was the same as shown in Figure 3.7a. Figure 3.20 shows the mesh block layout of the model and the mesh cell sizes in each block are shown in Table 3.19.

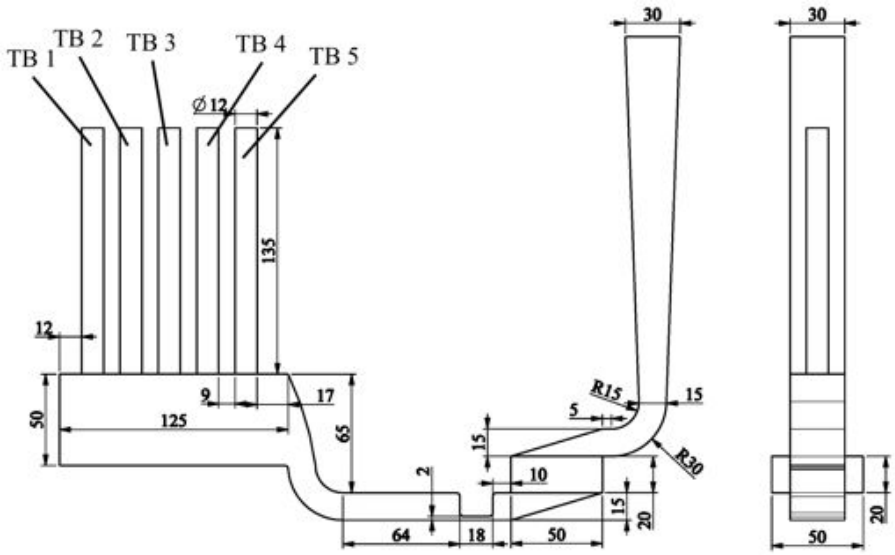

Figure 3.19: The geometries of the mould used for making test bars. (Unit: mm)

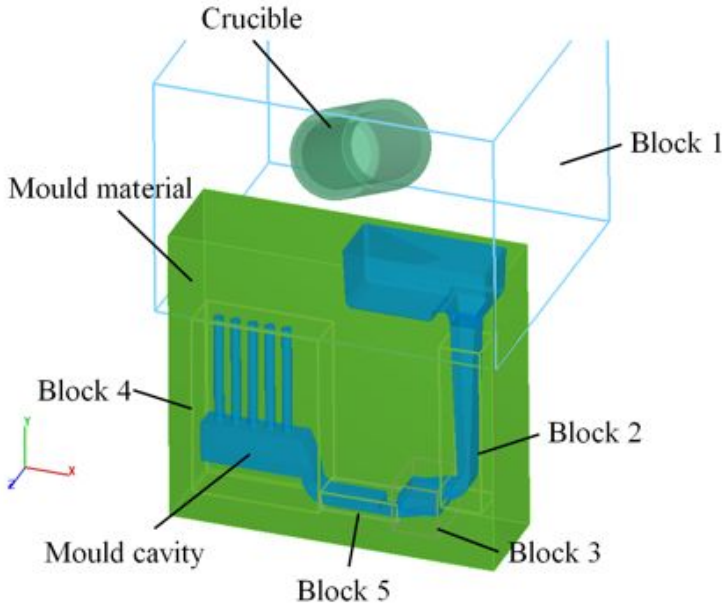

Figure 3.20: The mesh layout for tensile bar mould in the model.

Table 3.19: The cell size of each block in tensile bar model.

Block number	Block 1	Block 2	Block 3	Block 4	Block 5
Cell size (mm)	4	2	2	1	2

3.7.2 General Model Setting

Figure 3.21 shows the initial position of the crucible and the mould, which was the same as in the experiment. A liquid object with the properties listed in Table 3.20 was loaded into the crucible to represent a melt of 2.5 kg A356 alloy, and the physical properties of sand listed in Table 3.10 were applied to the component around the mould cavity to represent the sand mould. The crucible started rotation at a speed of 0.25 rad·s^{-1} around the x-axis at the beginning of the simulation and a time period of 4.5 s was used to pour the liquid into the mould. The gravitational direction was set along y direction to model the rotation of the sand mould upside down and subsequent feeding for the test bar region. The interaction between the particles and the mould wall, *i.e.* particle stickiness, was studied with two restitution factors. The influence of pouring basin was also considered. The total particle counts and particle number density within the whole and gauge length of the test bars were later exported to be compared with the experimental results.

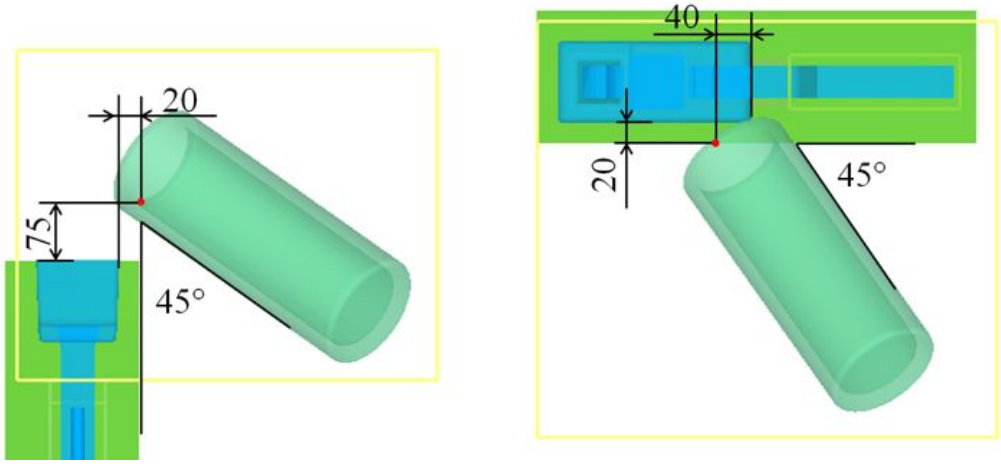

(a) X-axis projection **(b)** Y-axis projection

Figure 3.21: The initial relative position of the crucible and the mould. (Unit: mm).

To study the pouring position sensitivity of the model and model the pouring adjustment in experiment, five additional simulations were conducted with adjusted

Table 3.20: The modelling parameters of tensile bar model.

Module	Setting	Value and Unit
Gravity	Gravity component in the y-direction	9.81 $N \cdot kg^{-1}$
Particles	Mass particles	Variable diameter
	Particle density	2400 $kg \cdot m^{-3}$
	Maximum number of particles allowed	2.50E+05
	Diffusion coefficient	0
	Inverse Schmidt number	0
	Coefficient of restitution	-1 or 1
	Drag coefficient	1
	Free surface interaction	Particles can move in fluid only
	Initialization	By customised code
Surface tension	Surface tension coefficient, σ	1.01
	Contact angle	163 $\circ$
	Numerical approximation for surface tension pressure	Explicit
	Viscosity options	Newtonian viscosity
Viscosity and turbulence	Turbulence models	$\kappa - \varepsilon$ model
	Turbulent mixing length	0.001 mm
	Wall shear boundary conditions	No-slip or partial slip
	Friction coefficient	-1
	Vertical viscosity multiplier	1
Heat transfer	Fluid internal energy advection	First order
	Fluid to solid heat transfer	Full energy equation
	Numerical Approximations	Implicit
Solidification	Solidification shrinkage	No shrinkage

initial pouring positions. The initial rotating points were set at $x = \pm 10mm$, $y = \pm 10mm$ and $z = +10mm$ in each model according to the reference point (red dot) in Figure 3.21. These models considered the particle generation in pouring basin and used a non-sticky particle model. The results were later exported and analysed following the same methods applied to the initial study.

Chapter 4

Experimental Methods

4.1 Casting and Filling Observation

4.1.1 Pattern and Mould-making

The geometries of the patterns used in each experiment are described in Sections 3.5 through to 3.7 in Chapter 3. Handmade resin-bonded sand moulds were used in all of the casting experiments. Dry silica sand (AFS 60) was blended with "Pepset" urethane resin binder 5112 and 5230 (Ashland Foundry Products), in a 1000:6 sand to resin ratio (by mass). The completed moulds were placed in open air for at least two days before casting for volatilisation of the solvent.

4.1.2 Casting Alloy Preparation

An Al-Si-Mg alloy (A356.0), British standard 2L99, was employed in all casting experiments. Table 4.1 gives the chemical composition of the alloy as supplied. For each casting experiment, a certain weight of ingot was measured and heated to 650 °C in a clay bonded graphite crucible in an induction furnace, then held for 30 minutes to allow the hydrogen concentration in the melt to reach an equilibrium with the atmosphere. After this passive degassing, the molten alloy was rapidly heated to 750 °C and either manually poured or poured by an automated mechanism into the mould at 720 ± 5 °C.

Table 4.1: The chemical composition of cast aluminium alloy used (A356.0)

Element	Si	Mg	Fe	Ti	Cu	Mn	Cr	Ni	Zn	Pb	Sn	Al
%Weight	7.13	0.41	0.09	0.14	0.01	0.01	0.01	0.01	0.01	0.01	0.01	Bal

4.1.3 Heat Treatment

The castings obtained from the three entrainment mechanism experiments and the tensile bar moulds underwent a T6 heat treatment before being machined. The heat treatment began with a solution treatment at 560 °C for six hours, followed by quenching in hot water (60 – 80°C) and artificial aging at 180 °C for four hours, then cooling in air. This heat treatment gave the maximum tensile strength of the casting [2].

4.1.4 Real Time X-ray Radiographic Observation

Real-time X-ray radiography was used to study the fluid flow in the mould cavity or in the running system during mould filling in an YXLON (YXLON International GmbH) X-ray booth. In the X-ray booth, the X-ray source was tuned to 160 kV to allow enough contrast between the mould and the liquid alloy, and the filling pattern was recorded using a high-speed X-ray camera at a frame rate of 100 s^{-1} at a resolution of 800 × 600 pixels, giving a field of view of 250 × 190 mm of the mould.

The assembled and clamped mould was placed on a bench in the X-ray booth, with the X-ray projected perpendicularly to the mould. Figure 4.1 shows the layout of the mould and X-ray machine in the booth. The pouring in the X-ray booth was controlled by a robot mechanism, and the rotation speed of the crucible was recorded by a data logger and input as pouring condition in *FLOW-3D* models. A graphite stopper operated by compressed air was applied to some experiments completed within the X-ray booth. In these experiments, the stopper was placed in the inlet to block the downsprue and was then removed vertically, when the liquid metal reached the desired level in the pouring basin.

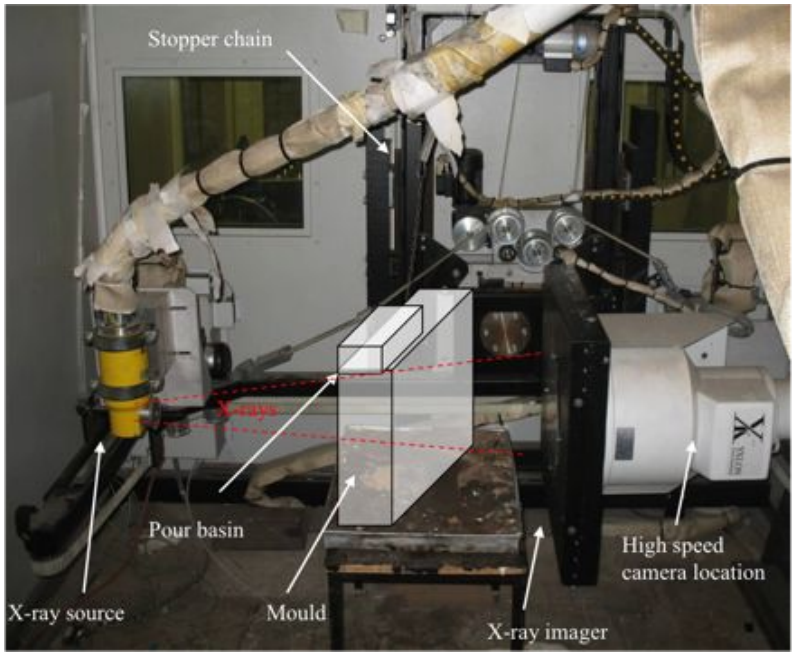

Figure 4.1: The layout of the mould and X-ray equipment in the X-ray booth. The schematic of mould is slightly repositioned to show its shape, which should parallel to the X-ray image.

4.2 Three Entrainment Mechanisms Experiments

Sand moulds were made according to the geometries shown in Figure 3.6, to validate the modelling work described in Section 3.5. Castings were made from three sets of moulds in A356.0 alloy and the castings were then heat treated to T6 condition and the bend strength of the specimens was determined.

4.2.1 Casting Sample Preparation

Figure 4.2 shows the relative position of the crucible and the pouring basin in the experiment. A 2.5 kg A356.0 alloy charge was melted and cast following the procedures detailed in Section 4.1.2. The X-ray imaging was activated once the pouring was initiated and the stopper was removed when the liquid nearly filled the pouring basin. Three castings were made for each entrainment mechanism. Table 4.2 summarise the casting conditions for the three sets of experiments. The castings then underwent heat treatment as described in Section 4.1.3. About 1 mm material was machined off from

Table 4.2: The casting conditions of three entrainment mechanisms experiments.

Parameter	Value
Alloy	A356
Charge Weight (kg)	2.5 ± 0.002
Pouring height (mm)	80 ± 3
Pouring overlap (mm)	20 ± 3
Crucible tilting angle to the vertical (°)	23 ± 0.3 (43 ± 0.3 for plunging jet moulds)
Pouring temperature (°C)	720 ± 5

the surface of the heat-treated cast plates to obtain clean, flat surfaces, which left the plates with dimensions of 270 mm×145 mm×14 mm. Electric discharge machining (EDM) was used to section the casting plate into 30 specimens labelled as shown in Figure 3.15, the same as used in the computational models.

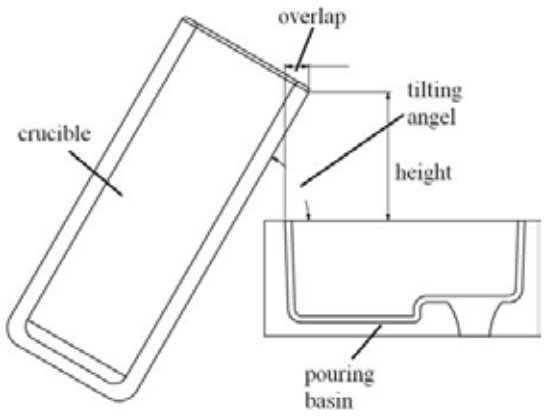

Figure 4.2: The pouring layout of the crucible and pouring basin. Values are listed in Table 4.2.

4.2.2 Bend Testing and Defects Characterisation

Figure 4.3 shows the dimensions of the specimens for the four-point bend testing, carried out in a Zwick/Roell servo-hydraulic universal testing machine. The specimens were placed in the centre of a test rig, which consisted of a platform with two supports and two 6 mm diameter loading rollers on top, as shown in Figure 4.4a. Figure 4.4b shows the spans and forces applied in the tests. The inner span between the loading

pins was 20 mm, one third of the outer span between the supports. This followed the free-bend method for four-point bend testing suggested in ASTM Standard E 290 for bend testing of material for ductility [160].

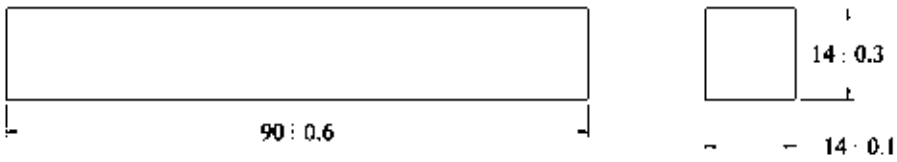

Figure 4.3: The geometries of the machined specimens used in bend tests. (Unit: mm).

The crosshead speed of the testing machine was 0.5 mm/min downwards with a maximum load of 60 kN. The bend strength of the specimens was calculated using Equation 4.1 [161], where F is the recorded load when the specimen failed (N), σ is the maximum bending stress (MPa), L is the outer span between the supports (mm), L_i is the inner span between the loading rollers (mm), b and d are the specimen width and thickness of the sample respectively (mm). The bend strength of the specimens was later analysed using a two-parameter Weibull distribution, as discussed in Section 2.1.3, to study the reliability of the castings and the reproducibility of their properties.

$$\sigma = \frac{3F(L - L_i)}{2bd^2} \tag{4.1}$$

In four-point bend testing, the bottom surface of the specimen between the two loading rollers endures the maximum tensile stress. Figure 4.5 shows the normal stress and bending moment distribution in the specimen during a four-point bend test. The tensile stress decreases inwards to the neutral axis of the specimen, then becomes compressive and increases towards the top surface. The bending moment of the specimen is constant across the length of the inner span. Since defects damage the integrity of the castings, failures of the specimens would be supposed to be initiated from sites with defects. Fractography was conducted to characterise the defects on the fracture surface of the specimens. Six specimens were chosen from each type of mould, two with high

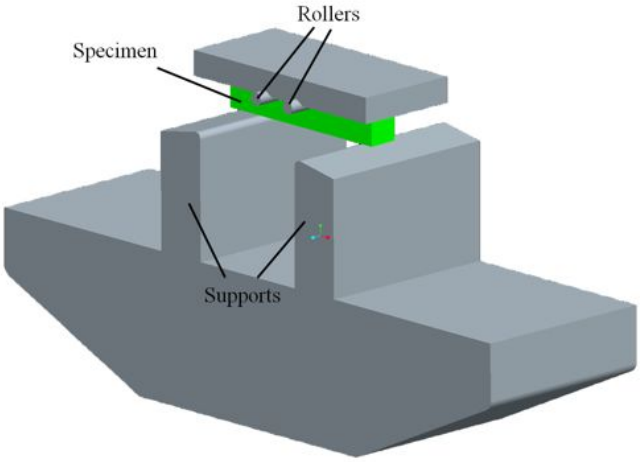

(a) 3D schematic of the bending test layout on the machine

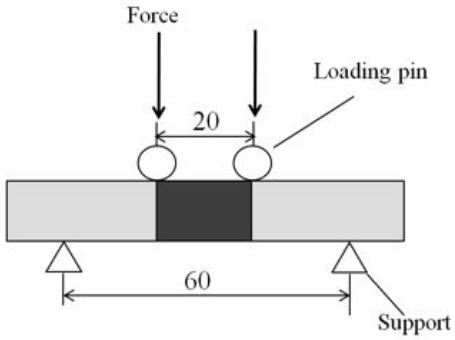

(b) The position of the rollers and supports on the specimen, the gauge length is in shadow

Figure 4.4: The schematic layout of the four-point bending test (Unit: mm).

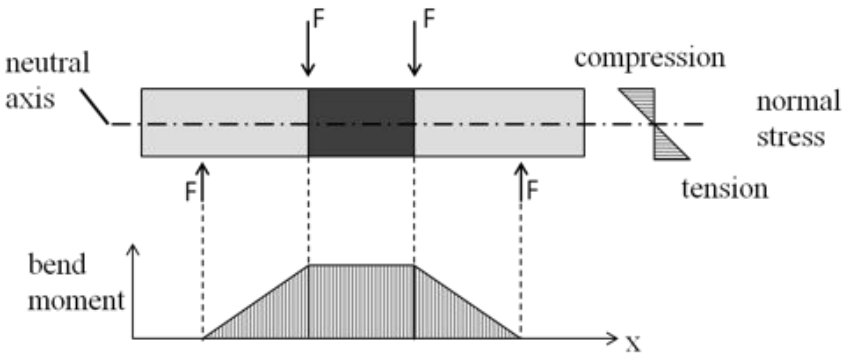

Figure 4.5: The normal stress and bend moment distribution on the specimen during four-point bend test. Gauge length is in shadow in the specimen.

bend strength, two with middle and two with low strength. The fracture surfaces of the specimens were viewed in a JEOL JSM-6060 scanning electron microscope (SEM), while a cross section view of the specimens was obtained from polished samples cut from the region 3 mm behind the fracture surface.

4.3 *In situ* Characterisation of Entrainment Defects

Although the idea of entrainment defects has developed during the past two decades, there is still a lack of fundamental understanding of the properties of the defects, especially the evolution of defects in the liquid metal and their behaviour during solidification, *e.g.* the furling and unfurling mechanisms of the double oxide films in the liquid alloys have not yet been observed or reported in details. To understand the entrainment defects at a fundamental level, samples were prepared that contained entrainment defects and were scanned in the liquid state and during solidification at the Swiss Light Source [1]. The tomographic images were reconstructed and analysed to study the properties of entrainment defects.

4.3.1 Mould Geometries

The pattern work and moulding for the casting was the same as described previously in Section 4.1.1. Figure 4.6 shows a drawing of the mould. The mould was deliberately designed to generate highly turbulent flow and to create entrainment defects during filling. It was expected that the entrainment defects generated during filling would be passed the two millimetre thin section in the horizontal runner and entered the bars above the runner bar. The pouring basin used was the same one as shown in Figure 3.7, with the inlet area modified to match the size of the downsprue of the mould in this experiment.

[1] SLS, Villigen, Switzerland

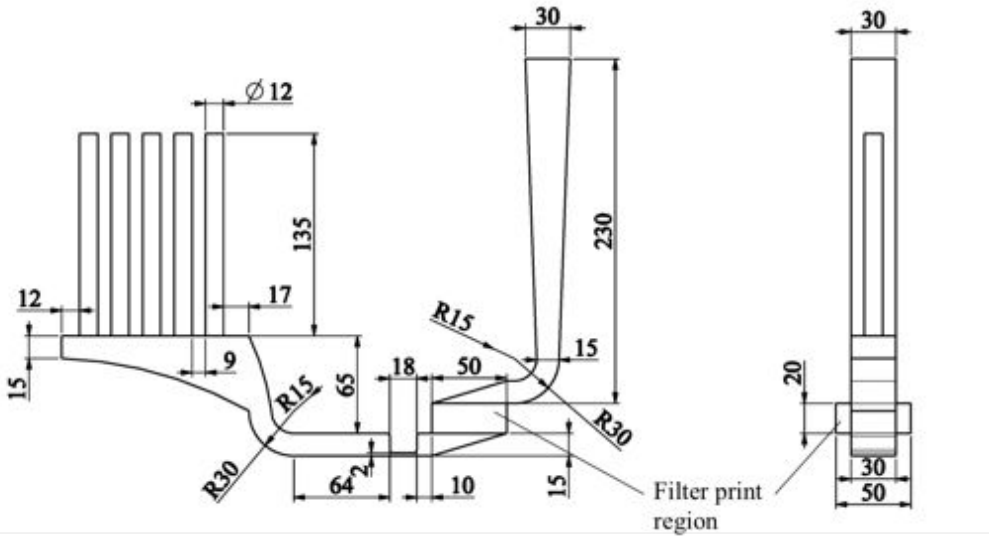

Figure 4.6: The dimensions of the mould with a 2 mm thin section in the runner.

4.3.2 Casting Procedure

Ten resin-bonded sand moulds were made to obtain 50 test bars in total. A 20 pore per inch (ppi) ceramic foam filter was embedded in each mould in the filter print region, as shown in Figure 4.6, in order to remove inclusions and oxide films formed during melt preparation. The mould was then cast in the X-ray booth using 2.2 kg A356 alloy charge following the procedure detailed in Section 4.1.2. The flow of liquid alloy in the running system was recorded by real time X-ray radiography. After the castings were cool, the cast test bars were marked and cut off from the running system.

4.3.3 Sample Preparation

The samples were scanned by X-ray to get two projections at 0° and 90° of the bars at an external non-destructive testing service firm, Exova [1]. The position of defects in the bar was then identified according to the relationship shown in Figure 4.7. 31 bars with defects revealed by this film X-ray radiography exercise were selected and the location of each defect identified. The distances of the defects to the edge and end of the bars, *i.e.* the x and y distances shown in Figure 4.8, were measured and marked on the

[1] Exova Group, Dudley, UK

bars. The bars were then fixed on the working platform of an EDM machine and the track of the wire followed the trace shown in Figure 4.8. The material removed from the bars were therefore cylinder-shaped pins with cambered top and bottom surfaces, containing defects.

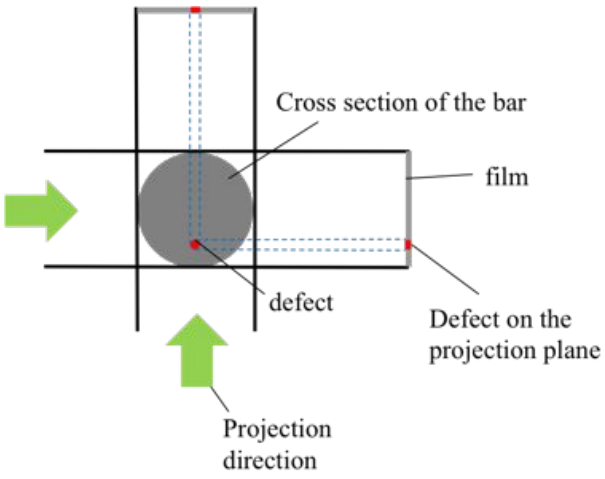

Figure 4.7: The position relationship between the defect in the bar and on the two projection planes. (Top view)

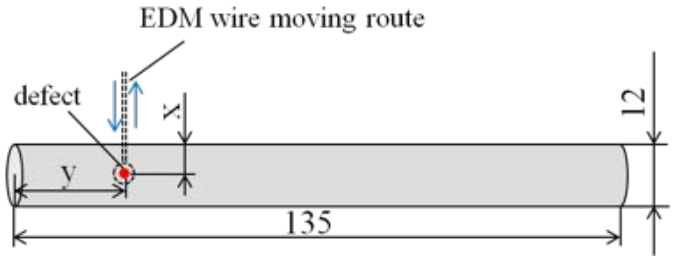

Figure 4.8: Schematic of the EDM cutting route. Defect location can be identified according to the x and y values.

The 31 samples with defects were scanned at the μ-VIS CT Imaging Centre at the University of Southampton to get two projection views. The location of the defects in the pin was identified according to the same method as shown in Figure 4.7. The pins were then manually ground to 3 mm in diameter and 6 mm in length. The vessels used to contain the pins were borosilicate glass tubes (6 mm outer diameter, 3 mm inner diameter, 10 mm length). Before scanning with synchrotron X-ray radiography,

the samples were categorised into three groups, one containing large defects, one small defects and one with defects on the surface of the pins.

4.3.4 Synchrotron X-Ray Radiography

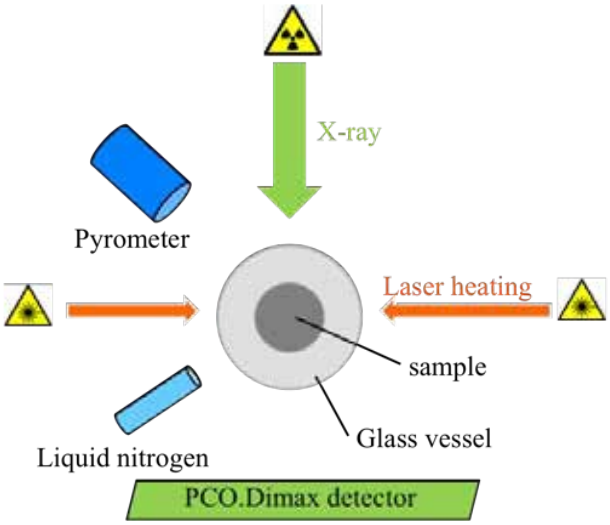

(a) Schematic of the position relationship of the facility on the platform

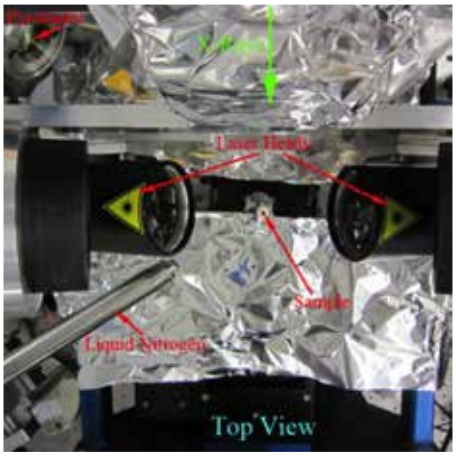

(b) Real setup on the platform.

Figure 4.9: The experimental setup on the TOMCAT beamline platform.

Synchrotron-based X-ray tomographic microscopy observations of the entrainment defects were conducted at the beamline for TOmographic Microscopy and Coherent rAdiology experimenTs (TOMCAT) at the X02DA port of the Swiss Light Source at the Paul Scherrer Institut [1]. The TOMCAT beamline used a PCO.Dimax camera that acquires and reads-out data orders of magnitude faster than traditional charge coupled device (CCD) technology. Coupled with an ultra-fast data requisition end station, full three-dimensional data consisting of several hundreds of projections (X-ray radiographs) can be captured within a second [162], which allows the *in situ* characterisation of entrainment defect evolution in real time. In addition, a general-purpose moderate-to-high-temperature furnace, powered by two diode lasers, provided controlled heating of the sample on the scan platform. A detailed introduction of the experimental setup

[1] SLS, Paul Scherrer Institut, Villigen, Switzerland

of the TOMCAT beamline can be found in the paper written by Stampanoni *et al.* [163], Marone *et al.* [164] and Fife *et al.* [158].

The sample was placed in the centre of a vessel and then fixed on the rotation stage as shown in Figure 4.9. The sample was scanned using polychromatic radiation with an energy of 8 to 45 keV distributed across the length of the sample following a Gauss distribution. The radiograph projected the profile of the sample, excluding the glass vessel, on a 2048×2048 pixel detector, giving a resolution of 3.15 μm on the reconstructed image and 6 mm field of view (FOV). On the TOMCAT platform, the two heating laser heads sat opposite to each other, and were perpendicular to the X-ray beam, with liquid nitrogen used as a cooling agent and a pyrometer besides to control the heating and cooling rate. The spot sizes of the two lasers were 6×0.7 mm. The laser was targeted at the centre of the sample and the temperature gradient across the sample was approximately 2 $\mathrm{K \cdot mm^{-1}}$. Each sample was scanned initially at room temperature and then heated up to 1000 K at a heating rate of 10 $\mathrm{K \cdot s^{-1}}$, scanned in the fully liquid state, and subsequently scanned 6-8 additional times at approximately 200 s intervals. Finally, the sample was scanned during solidification and at room temperature after the sample had solidified.

4.3.5 Image Reconstruction and Analysis

The sample was rotated 180 ° during each scan, and then rotated back to the start position. Each scan generated 4.8 GB data with 1111 projections, which were reconstructed to form an image stack consisting of 2016 slice views along the length of sample. Since the PC was not capable of analysing large image data sets, different parts of the image stacks were sectioned from the original data using open source software Fiji [165]. The contrast adjustment and noise reduction were completed in Fiji before exporting the image data for segmentation. Due to the short scanning time, the acquisition images generally had low quality, which were difficult to analyse directly. Therefore, the

semi-automatic segmentation of the images was conducted in open source segmentation software ITK-SNAP using a SNAKES (active contour model) technique [166] to identify the defects and measure the relative volumetric and area information. The volume of the defect was measured based on the quantity of voxels it occupied in the segmented images. The segmented defects were then exported as STereoLithography (STL) files to visualise the 3D structure. The surface area and volume information of the defects was also analysed to understand the behaviour of the defects in the liquid state.

4.4 Tensile Bar Mould Experiments

4.4.1 Casting Procedure and Sample Preparation

The same mould as shown in Section 3.7.1, Figure 3.19 was used in the experiments. It was similar to the one described in Section 4.3.1, and also had a thin section to generate surface turbulent flow, but with a larger ingate beneath the bars. The volume of the ingate was 2.54 times that of the bars, as $V_{ingate} = 50 \times 140 \times 30 = 210000$ mm^3 and the volume of the bars was $V_{bars} = 135 \times 6.252 \times \pi \times 5 \approx 82834$ mm^3. According to Chvorinov's Rule (Equation 4.2 [167]), where t is the solidification time, V is the volume of the casting, A is the surface area of the casting that contacts the mould, n is a constant, and B is a mould constant, the ratio of solidification time of the ingate t_{ingate} to the solidification time of test bars t_{bars} was 2. Effective feeding requires the feeder to be 1.2 times larger than the test bars and the solidification time of the feeder must be longer than that of the bars [167]. The above calculation shows that the ingate beneath the bars could effectively feed the test bars.

$$t = B\left(\frac{V}{A}\right)^n \tag{4.2}$$

In the first group of castings, six sand moulds were made using the procedure stated in Section 4.1.1. After three days standing to allow for volatilisation of the redundant

solvent, the moulds were then assembled and ready to cast. A 2.5 kg A356.0 alloy charge was melted in each casting experiment following the preparation method described in Section 4.1.2. Once the mould was filled, the mould was then rolled upside down. Since the liquid alloy could not escape from the running system owing to the thin section in the bottom of the runner, enough liquid alloy remained in the feeder to give effective feeding to the test bars.

The test bars and feeders were cut off from the running system and heat treated following the procedure stated in Section 4.1.3. The test bars were then machined to the dimensions shown in Figure 4.10, following the ASTM standard B557M-07: Standard test methods for tension testing: wrought and cast aluminium-and-magnesium-alloy products [168]. The feeders were then machined and the hydrogen contents of the castings were measured at Sci-Lab Analytical ltd [1].

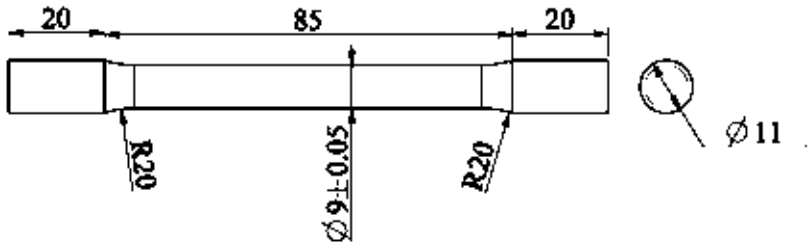

Figure 4.10: The dimensions of the tensile bar.(Unit:mm)

To weaken the potential influence of the hydrogen content on the porosity formation in the castings and to get a clearer idea about the effects of oxide film defects on the tensile strengths of castings, the second group of seven castings were made in sand moulds. Six moulds had been kept in a vacuum chamber (5000 Pa below standard atmospheric pressure) for two weeks before casting to allow the redundant solvent to volatilise. Another casting made from a fresh-made sand mould was used as a control group. The casting procedure of these seven castings was the same as described above.

[1] Sci-Lab Analytical ltd, Chester, UK

The subsequent heat treatment and machining followed the same procedure as the first group of castings.

4.4.2 Tensile Testing and Defect Characterisation

The tensile strength of the specimens was determined using two different Zwick/Roell tensile testing machines, due to the availability of the machines. The 1st group of test bars were tested at Aeromet ltd. The 2nd group of test bars were tested at the Mechanical Testing Lab at School of Metallurgy and Materials. The specimens were fixed in the machine with a 100 N preload before testing. The crosshead speed of the testing machine was set to 1 mm/minute with a maximum load of 60 kN. The maximum load, ultimate tensile strength, proof stress ($R_{e0.2}$) and elongation were recorded.

The fracture surfaces of specimens were directly observed using a JEOL JSM-6060 SEM and the composition of the defects on the fracture surface were analysed using EDX. Several samples were also viewed using optical microscopy to analyse the defects observed on the fracture surface, which were supposed to be oxide films.

Chapter 5

Results

5.1 OFEM Algorithm Investigation

This investigation studied the particles generated by the pre-defined entrainment forms in different entrainment structures in a running system, and compared the influence of gravitational effects along different axes and the potential for mesh sensitivity of the algorithm.

5.1.1 Preliminary Modelling of Different Entrainment Events

The modelling results of the three types of moulds detailed in Section 3.3.1 are reported here. The number of particles placed by each pre-defined entrainment form in the simulations was exported and analysed. Since the Colliding Fronts mechanisms and Shear Flow mechanisms, *i.e.* Forms 1 to 36 (see Appendix), are relatively unusual, for simplicity, the numbers of particles entrained by these two kind of mechanisms were summed and a total reported. The entrainment forms vs. number of particles entrained by these three types of moulds are shown in Tables 5.1 to 5.3.

These tables show that more than 99% of particles were entrained by the Impingement forms, and the results were independent of the type of moulds used in the simulations, *i.e.* Impingement forms dominated the entrainment mechanisms in the simulation irrespective of the flow patterns generated in the mould cavity. The results also showed that the twelve Impingement forms have different relative importances.

Table 5.1: Entrainment forms and corresponding particle counts in plunging jet moulds.

Entrainment forms	**Plunging_jet_4**	**Plunging_jet_5**	**Plunging_jet_11**	**Sum**	**Percentage**
	Block 1	Block1	Block1		
Colliding Fronts	1	0	1	2	0.006
Shear Flows	30	1	42	73	0.223
Form37	2	9	76	87	0.266
Form38	2775	5929	3155	11859	36.299
Form39	3334	7509	3868	14711	45.019
Form40	28	2	34	64	0.196
Form41	41	123	978	1142	3.495
Form42	33	245	233	511	1.564
Form43	69	1	20	90	0.274
Form44	688	1353	469	2510	7.681
Form45	86	368	121	575	1.759
Form46	78	16	121	215	0.658
Form47	41	43	183	267	0.817
Form48	15	431	125	571	1.747
Impingement	7190	16029	9383	32602	99.770
Total	7221	16030	9426	32677	100

Table 5.2: Entrainment forms and corresponding particle counts in return wave moulds.

Entrainment forms	**return_wave_1**	**return_wave_5**	**return_wave_6**	**Sum**	**Percentage**
	Block 2	Block 2	Block 2		
Colliding Fronts	0	0	0	0	0
Shear Flows	4	0	2	6	0.037
Form37	53	24	17	94	0.575
Form38	1430	1950	1609	4989	30.516
Form39	804	448	1409	2661	16.276
Form40	32	6	0	38	0.232
Form41	435	126	104	665	4.068
Form42	71	32	11	114	0.697
Form43	499	12	1	512	3.132
Form44	3480	1263	1303	6046	36.981
Form45	168	148	85	401	2.453
Form46	166	4	72	242	1.48
Form47	81	25	8	114	0.697
Form48	307	36	124	467	2.856
Impingement	7526	4074	4743	16343	99.963
Total	7530	4074	4745	16349	100

Table 5.3: Entrainment forms and corresponding particle counts in rising jet moulds.

Entrainment forms	**rising_jet_1**	**rising_jet_3**	**rising_jet_7**	**rising_jet_10**	**Sum**	**Percentage**
	Block 3	Block 3	Block 3	Block 3		
Colliding Fronts	0	0	0	0	0	0
Shear Flows	0	35	28	0	63	0.087
Form37	63	119	216	0	398	0.552
Form38	4439	4942	6917	6121	22420	31.082
Form39	3260	6980	15363	1724	27327	37.885
Form40	0	35	0	0	35	0.048
Form41	84	2038	866	63	3050	4.229
Form42	35	0	670	0	705	0.977
Form43	63	475	426	0	963	1.335
Form44	195	4858	7357	161	12571	17.428
Form45	279	342	558	7	1187	1.645
Form46	175	1026	216	0	1417	1.964
Form47	0	126	447	42	614	0.852
Form48	21	426	712	223	1382	1.916
Impingement	8613	21366	33748	8341	72069	99.913
Total	8613	21401	33776	8341	72131	100

For instance, Forms 38, 39, 44 placed more than 88% of the particles in the simulation of the rising jet model (Table 5.3). On the contrary, the number of particles placed by Form 40 accounted for less than 0.1% of the total. The dominance of the same Impingement forms was consistently observed in different moulds, although the percentage of each Impingement form varied in different moulds. For example, Forms 38, 39, 44 in Table 5.1 accounted for more entrainment than others. Figure 5.1 shows the sum of the percentage of entrained particles by each Impingement form in different moulds. Clearly, there are four Impingement forms that were more significant than the others. They are Forms 38, 39. 41 and 44. The relative importance of different forms are discussed in Section 6.1.2.

5.1.2 The Rule of Gravity in Placing Particles

The results of simulations with the gravitational force along the x-direction, explained in Section 3.3.2, are reported in Table 5.4. The output from the models with gravity along the x-axis were similar to previous models, as the particle counts in Tables 5.3

and 5.4 are almost the same. Once again, the Impingement forms entrained most of the particles in the models. The histogram in Figure 5.2a gives the percentage of particles entrained by each Impingement form. Instead of the four predominant Impingement forms mentioned before, Figure 5.2a shows that Forms 40, 42, 45 and 47 placed most of the particles when the gravitational force was along the x-axis. Figure 5.2b shows the corresponding percentage when gravity was along y-axis, which also shows there were four important forms. Since OFEM works in three-dimensions, the four significant Impingement forms in Figure 5.2a correspond to the four forms shown in Figure 5.2b if the gravity direction is rotated accordingly. This shows that the direction of the gravitational force (or potentially, another body force, such as centrifugal force) affects the internal particle placing mechanisms in OFEM, but does not significantly change the output (here, the number of particles). Therefore, for convenience of model setting, the gravitational force can be set along x, y or z direction in *FLOW-3D* with OFEM with some confidence. It should be mentioned that the intention of this study was to understand the role of gravity in a general mesh set-up, therefore, the deflection of mesh setting resulted in the distinction of percentage of each form in Figure 5.2.

5.1.3 Modelling of Colliding Fronts and Shear Flows

To test the Colliding Fronts and Shear Flow forms, specially designed moulds with laminar flow were used. The results in Table 5.5 show that in ideal conditions particles could be entrained by Colliding Fronts and Shear Flow forms, but the proportion of particles entrained was still smaller than those entrained by Impingement forms, as shown in Figure 5.3.

Modelling of Colliding Fronts (with or without consideration of gravity) showed that some particles generated by the Colliding Front forms were placed before the real liquid fronts contacted each other, when the fluid fronts moved towards each other along the x-direction. These particles were placed in the flow by Form 3, of which the entrainment was defined by two fluid fronts colliding in the z-direction. Figure 5.4 shows snapshots

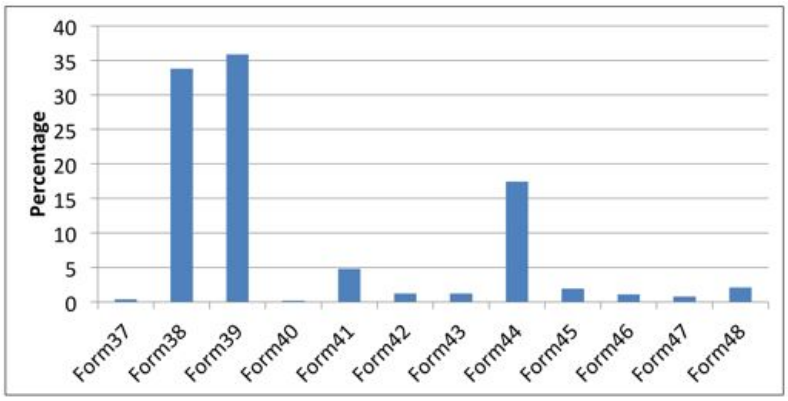

Figure 5.1: Impingement forms and the percentage of particles placed by each form.

Table 5.4: Entrainment forms and corresponding particle counts with the gravity along X-axis in rising jet moulds.

Entrainment form	Rising_jet_1_X	Rising_jet_10_X	Sum	Percentage
Colliding Fronts	0	0	0	0
Shear Flows	0	5	5	0.033
Form37	199	63	262	1.728
Form38	263	437	700	4.618
Form39	30	42	72	0.475
Form40	2904	2035	4939	32.581
Form41	197	133	330	2.177
Form42	3703	1275	4978	32.839
Form43	25	30	55	0.363
Form44	62	99	161	1.062
Form45	1097	1180	2277	15.021
Form46	0	72	72	0.475
Form47	116	1126	1242	8.193
Form48	43	23	66	0.435
Impingement	8639	6515	15154	99.967
Total	8639	6520	15159	100

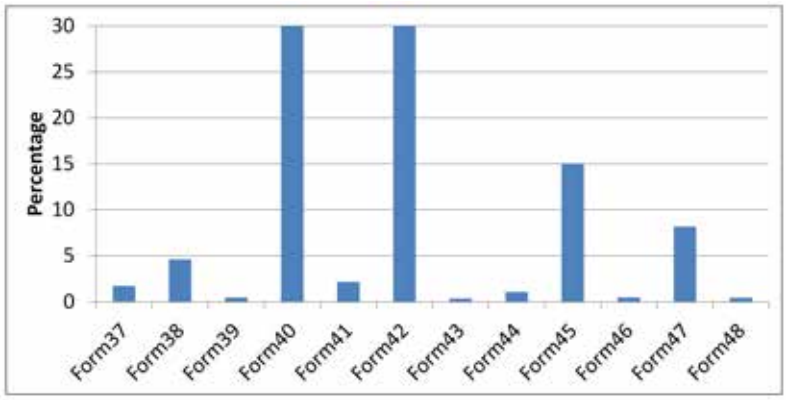

(a)

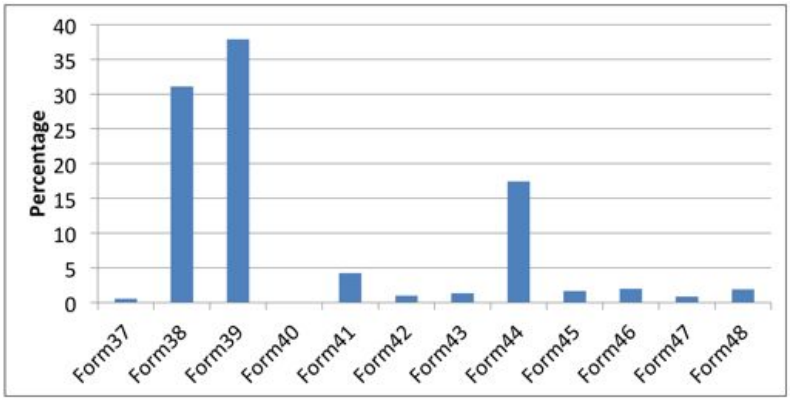

(b)

Figure 5.2: The percentage of particles placed by each Impingement form in the mould with gravity applied along different directions. (a). gravity along x-axis; (b). gravity along y-axis.

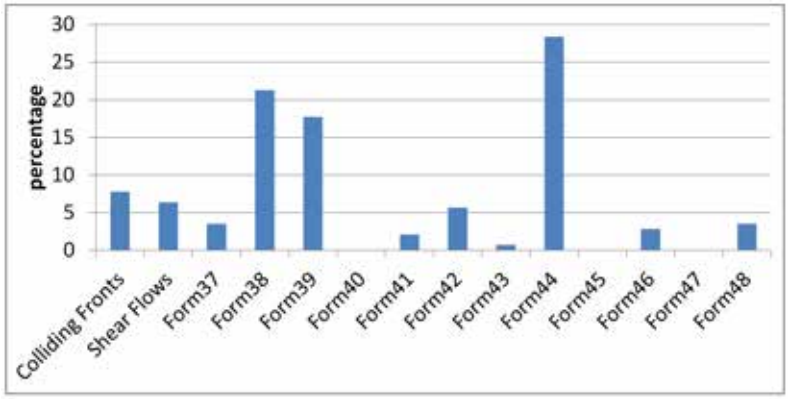

Figure 5.3: Entrainment forms and the percentage of particles placed by each entrainment forms in Colliding Fronts and Shear Flow moulds.

Table 5.5: The number of entrainment events by each form in Shear Flow and Colliding Fronts moulds.

Entrainment Forms	Colliding Fronts	Colliding Fronts (no Gravity)	Shear Flow (no Gravity)
Colliding Fronts	4	6	1
Shear Flows	1	0	8
Impingement	69	17	35

on the x-y plane of the simulation results of colliding fronts in successive time steps. The white dots above the grey cells are the particles placed by Form 3. In addition, when the fluid fronts collided, particles were placed, but by the Impingement forms rather than the Colliding Fronts forms. It was observed at the end of the simulation, when the fronts collided with each other and rolled back, that more particles placed by the Impingement forms.

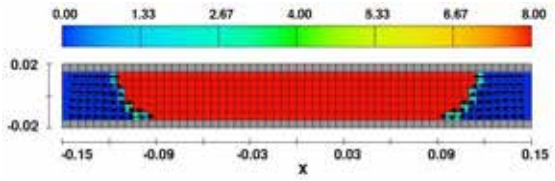

(a) t=0.05478 s

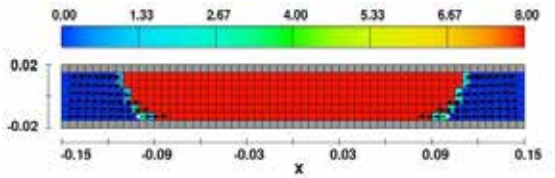

(b) t=0.05983 s

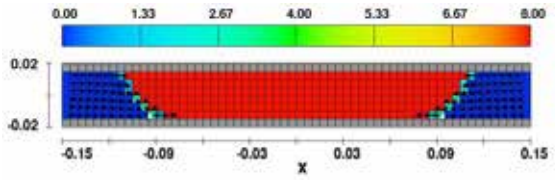

(c) t=0.06485 s

Figure 5.4: Snapshot of two fluid fronts moving towards each other on X-Y plane. The colour shade indicates the Nf value of mesh cell. The grey cells are the solid mould wall. The white dots are the particles.

The ideal Shear Flow structure defined in OFEM was achieved in the simulation shown in Figure 5.5. The Shear Flow form placed a particle in the centre (highlighted

by the circle in Figure 5.5b) and the Impingement forms placed two other particles in the snapshot. Since Shear Flow forms require two surface planes with an initial position that was parallel, then move towards each other, and in the end of a time cycle the boundary or vertex contact, it was not easy to achieve both conditions simultaneously in the simulation. Therefore, they are unusual in the normal modelling conditions.

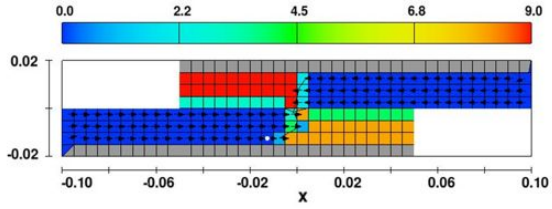

(a) t=0.1209 s

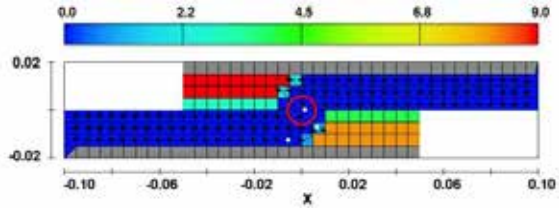

(b) t=0.1297 s

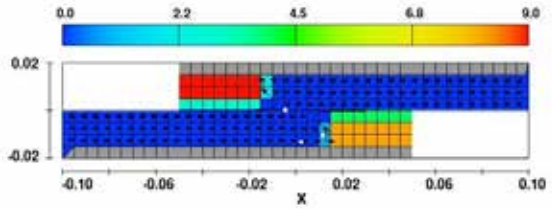

(c) t=0.1395 s

Figure 5.5: Particle placement by Shear Flow forms. The colour shade indicates the Nf value of mesh cell. The white dots are the particles.

5.1.4 Mesh Sensitivity of the Algorithm

Observation of modelled flow structure showed that the overall flow characteristics could be captured by the model using different sizes of meshes, as evidenced in Figure 5.6, which shows a comparison of modelled flow structures using 5 mm and 2 mm meshes in the Plunging Jet mould. It can be seen that the free surface shapes obtained at the same moment showed similar patterns, and the turbulence in the bulk liquid

showed similar motion according to the colour scale. In Figure 5.6a, the liquid jet rose slightly higher in the model using the 5 mm mesh, which was possibly related to the boundary layer condition in the model, since a model with finer mesh can solve the drag force along the wall boundary more accurately. Therefore, a higher velocity at the bottom of the mould was achieved in the model with coarse mesh, 2.1 $m \cdot s^{-1}$ to 1.9 $m \cdot s^{-1}$ in the model using 2 mm mesh, and hence a higher flow level obtained.

Table 5.6: The particle counts in the three models in mould cavity under five mesh sizes

	Mesh size of Block 2				
Mould	5 mm	4 mm	3 mm	2.5 mm	2 mm
Plunging jet	17164	64193	165632	173162	289755
Return wave	14935	22421	43605	68631	118454
Rising jet	13458	28255	59093	119527	111689

The study considered the difference in the total population of particles being placed and the particle distributions in the mould cavities under different modelling conditions. Table 5.6 shows the number of particles distributed in mesh Block 2 (containing the mould cavity) modelled using five different mesh sizes in the three moulds. The results showed that in general, a finer mesh resulted in higher particle population in all three models, but increased in a non-linear trend, as shown in Figure 5.7. Also, the rates of increment were different in the three models. The Plunging Jet mould showed the highest rate of change, approximately two times higher than that in the other two moulds, when the mesh was refined from 5 to 2 mm.

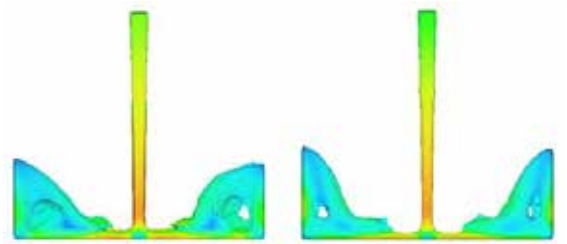

(a) t = 0.58 s

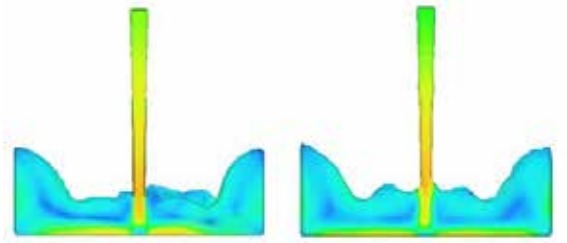

(b) t = 0.82 s

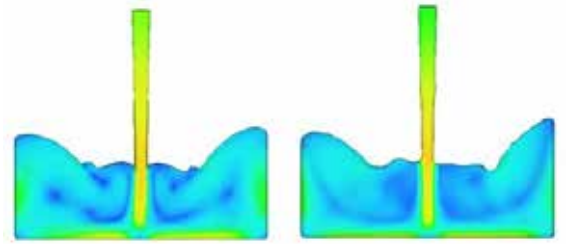

(c) t = 1.13 s

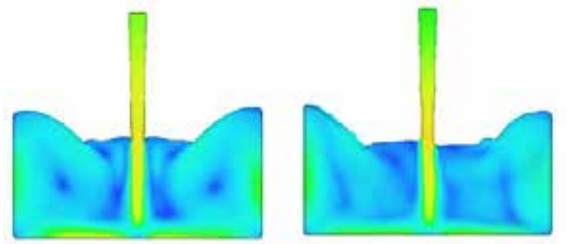

(d) t = 1.42 s

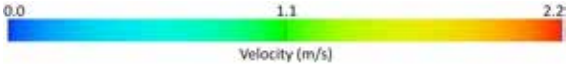

(e)

Figure 5.6: Comparison of flow patterns between models using 2 mm and 5 mm meshes in the Plunging Jet mould. The colour scale represents the velocity magnitude as shown in the scale bar in (e). (left: model using 2 mm mesh; right: model using 5 mm mesh.)

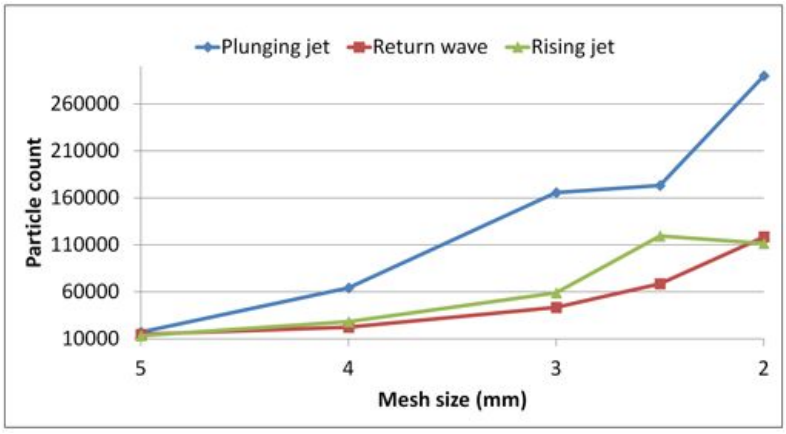

Figure 5.7: The relationship between particle counts increment and the mesh size refinement in the three models.

Figures 5.8, 5.9 and 5.10 show the particle distribution contours within the cast plate when the models using different mesh sizes in Plunging Jet, Return Wave and Rising Jet moulds respectively. The colour scales on the side indicate the predicted concentration of the particles in the plate, where warmer colours represent higher concentrations of particles. It should be noted that since the particle counts were different when using different mesh size, the colour scales on the contours are all normalised to 10 colour levels to be used for direct comparison of the particle distribution patterns.

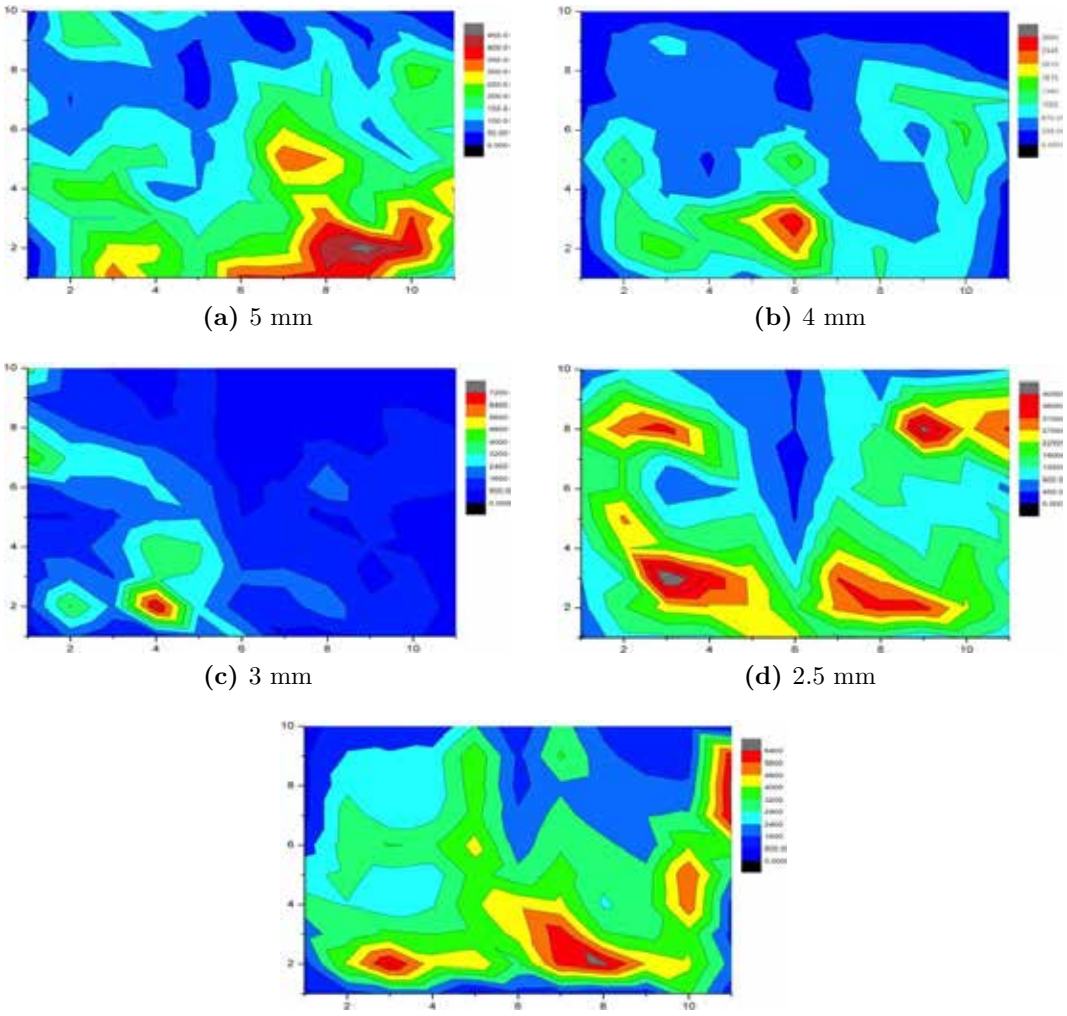

(a) 5 mm **(b)** 4 mm

(c) 3 mm **(d)** 2.5 mm

(e) 2mm

Figure 5.8: Particle distribution in the casting plate from the Plunging Jet mould using various mesh sizes in mesh Block 2.

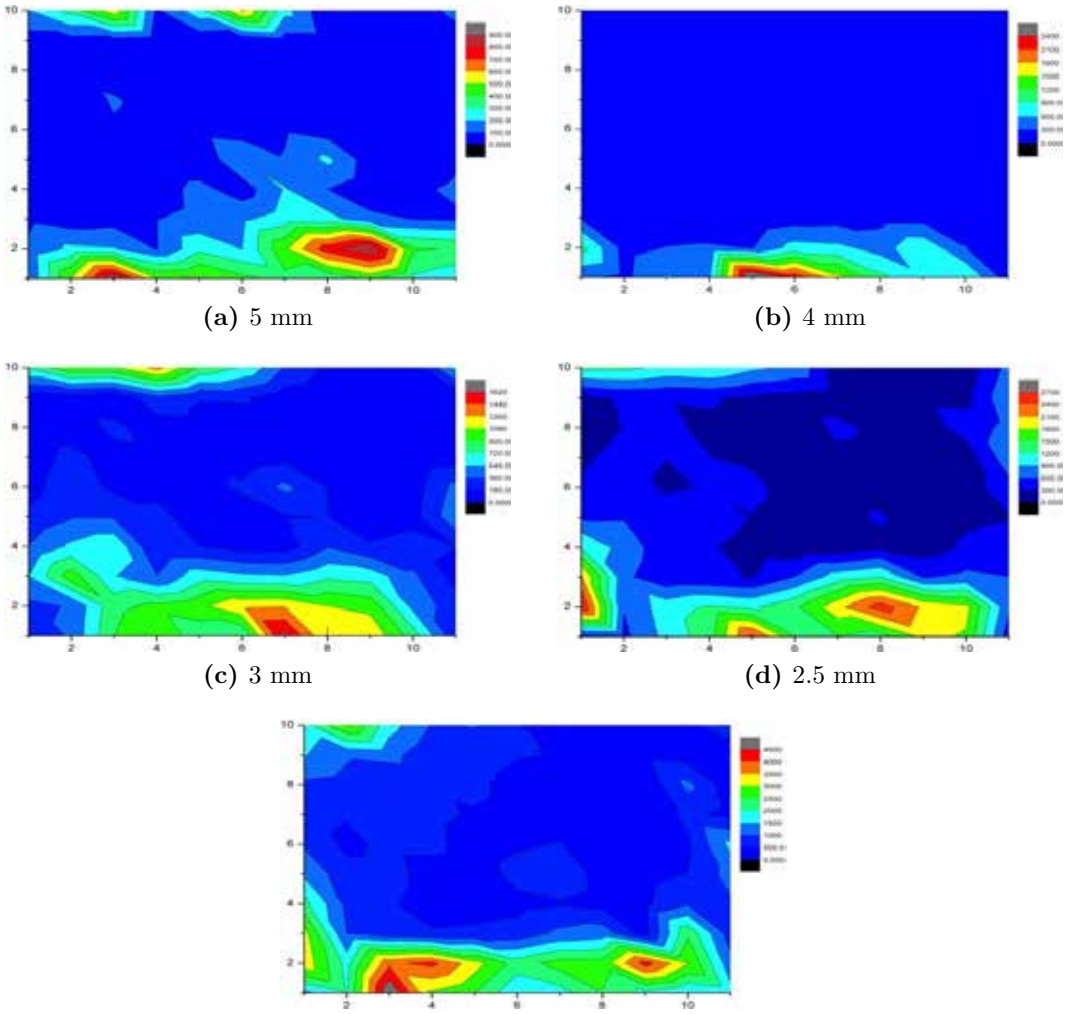

(a) 5 mm

(b) 4 mm

(c) 3 mm

(d) 2.5 mm

(e) 2mm

Figure 5.9: Particle distribution in the casting plate from the Return Wave mould using various mesh sizes in mesh Block 2.

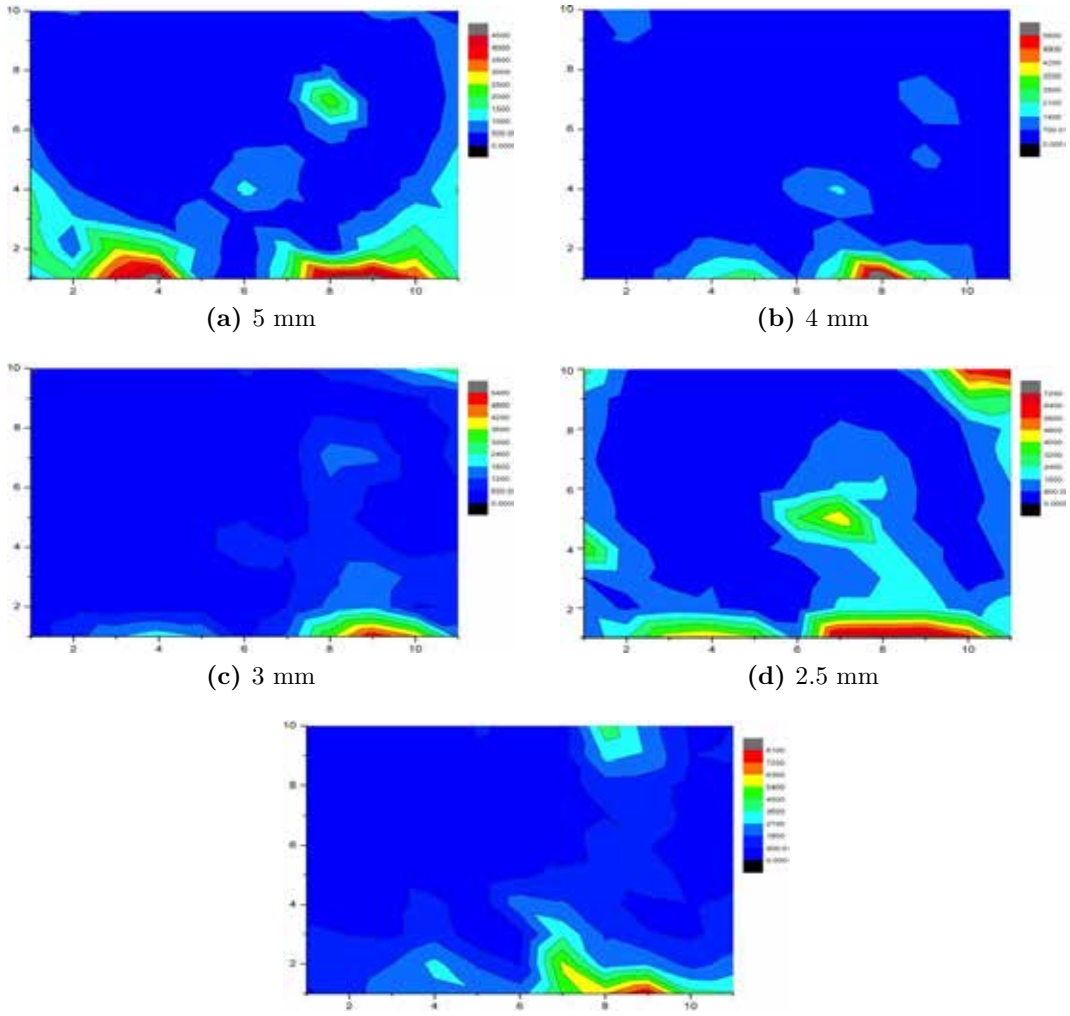

(a) 5 mm **(b)** 4 mm

(c) 3 mm **(d)** 2.5 mm

(e) 2mm

Figure 5.10: Particle distribution in the casting plate from the Rising Jet mould using various mesh sizes in mesh Block 2.

The distribution of predicted particles in the Plunging Jet mould in Figure 5.8 showed relatively chaotic patterns. There was no distinct distribution pattern of the particles found in the series of simulation. But, generally particles were distributed to the two sides of the stream from the downsprue, became aggregated in the lower part of the plate, and did not symmetrically spread throughout the plate. On the other hand, the contours in Figures 5.9 and 5.10 show a consistency of particle distribution patterns in the Return Wave and Rising Jet moulds. In the Return Wave mould

particles became concentrated in the bottom and the top left corner of the plate, while in the Rising Jet mould particles were distributed to both sides of the ingate in the bottom and top right corner of the plate.

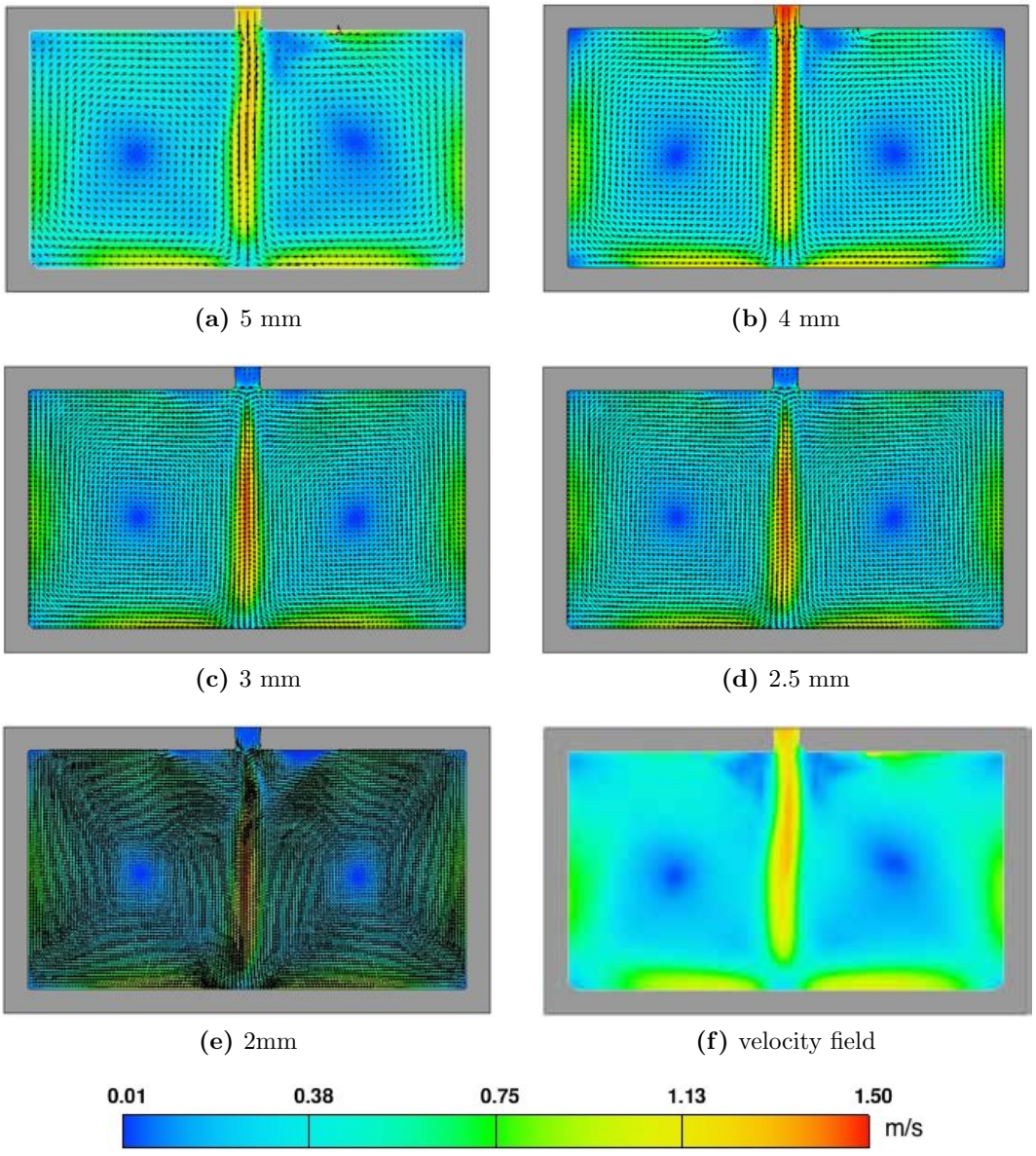

(a) 5 mm **(b)** 4 mm

(c) 3 mm **(d)** 2.5 mm

(e) 2mm **(f)** velocity field

(g) colour scale of the velocity magnitude

Figure 5.11: Flow field in Plunging Jet mould when the mould is filled. The models used various mesh sizes. The colour scale represents velocity magnitude of the flow and black arrows are the velocity vectors.

Figure 5.11 plots the flow field in the Plunging Jet mould when the mould cavity

was fully filled. Clearly, the models that using different mesh settings showed quite similar velocity distribution in the mould cavity, and the differences between maximum velocities calculated by different models were less than 2%. The similar flow fields also obtained from the Return Wave and Rising Jet moulds, when various mesh sizes were used. These results imply that *FLOW-3D* can simulate various flow conditions and achieve reasonable agreement between results that obtained using different mesh sizes in simulations. However, the number of particle placed by the algorithm is sensitive to the mesh cell size applied in the simulation, and the distribution patterns can be severely affected by the highly turbulent flow structures, which generate much greater number of particles in the simulation using fine mesh, such as in the Plunging Jet models. But it can also be found that when the mesh size reduce from 3 mm to 2 mm in the Plunging Jet mould, weak similarity of particle distribution was observed. Since using finer mesh in simulation would take longer computing time to run and generate much more particles as shown in Figure 5.7, which would make the post-processing difficult, further simulations applied 2 mm mesh cell in mould cavity to balance the accuracy and computing time of models.

It must be admitted that the relationship between the number of particles placed by the OFEM and the mesh size refinement is not clear at the current stage. Therefore, when different mesh setups are applied in simulations, the predicted particle count cannot be used to compare the possible entrainment severity of a mould, but when the same mesh setup is used, the predicted number of particles may provide a measure of the relative predicted entrainment level in the mould (see the results in Section 5.5.5). In addition, the particle distribution pattern can still be used to predict the defects distribution in castings with some confidence in later research.

5.2 Modelling vs. Previous Experiments

5.2.1 Fatigue Life Validation Model

5.2.1.1 Modelled Flow Structure

The typical filling scenarios of the fatigue life validation model without a filter is shown in Figure 5.12. Filling of filtered mould is similar. The black dots are the particles placed by OFEM and the colour scale represents the velocity magnitude, with warmer colour indicating higher velocity.

Figure 5.12 clearly shows that the plunging jet developed at the bottom of the downsprue entrained large numbers of particles into the fluid. When the liquid impinged upon the bottom of the sprue, particles were continuously generated at that region, but the severity of the entrainment was reduced as the well was filled. Since the earlier generated particles were apt to be pushed to the far ends of the mould along the horizontal runner by the the flow, the particles entered easily into the bars at the end of the mould and were then frozen in, leading to more particles in the bars at the two ends, rather than in the middle part of the mould (see Figure 5.12i).

Figures 5.13 and 5.14 compare X-ray radiographs of the experimental filling scenarios with modelling results in filtered and unfiltered conditions respectively. The mould filling footage was captured by real-time X-ray radiography from the same mould (obtained from unpublished work of Green and Campbell). The modelling results were the profile from the cross section (2D view). The starting time of both figures were normalised to the point when the liquid entered the filter print region. In the filtered condition the downward stream initially contacted the top of the filter, then passed through the porous medium and impacted onto the bottom of the sprue. The filter decreased the velocity of the fluid flow. On the contrary, in the unfiltered condition the downward stream of liquid metal from the sprue directly impacted onto the bottom of the downsprue, splashing and entraining more defects. Generally, at least 25% more particles were generated in the unfiltered condition (see Table 5.7).

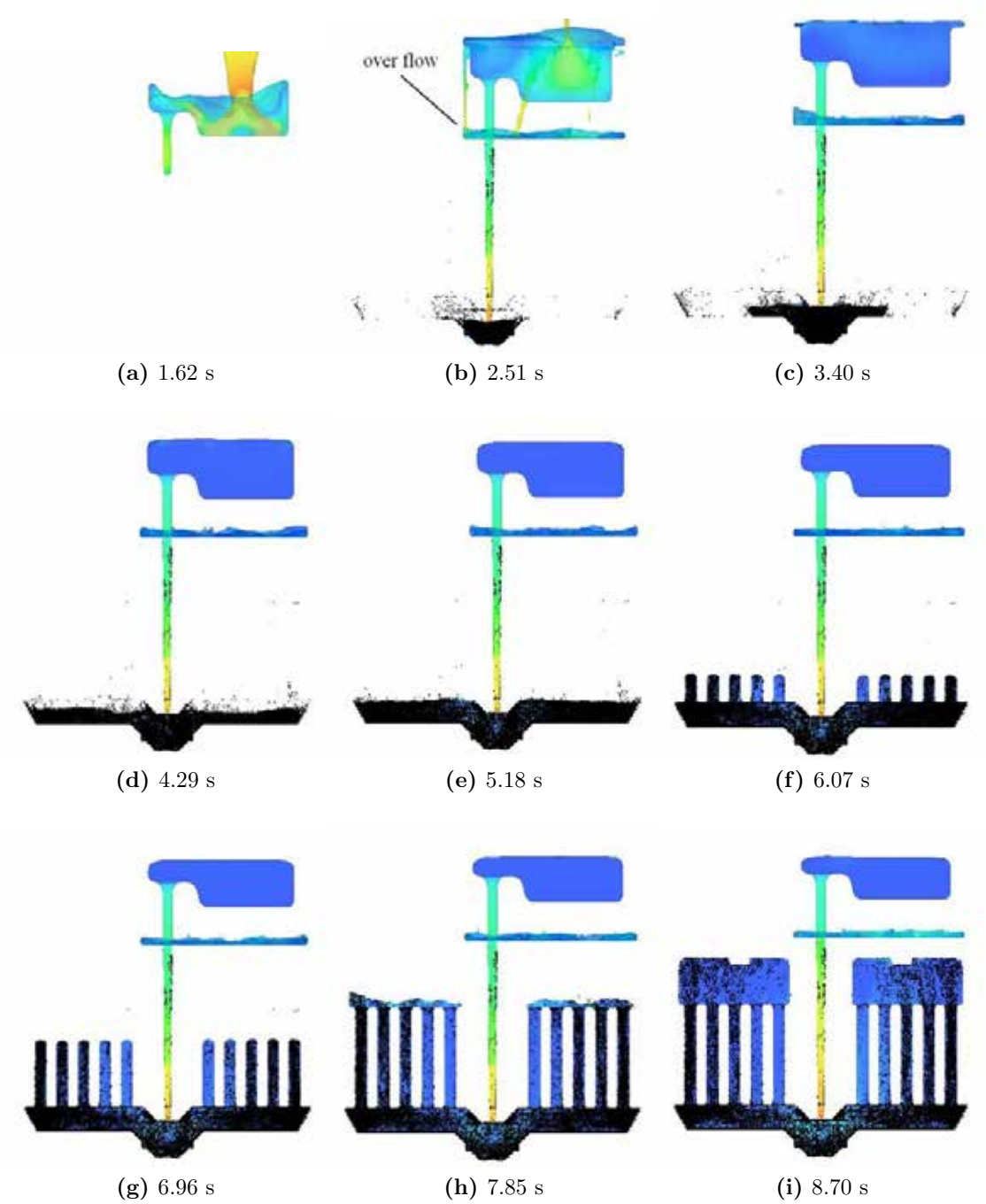

(a) 1.62 s **(b)** 2.51 s **(c)** 3.40 s

(d) 4.29 s **(e)** 5.18 s **(f)** 6.07 s

(g) 6.96 s **(h)** 7.85 s **(i)** 8.70 s

Figure 5.12: Filling scenario of fatigue life validation model. (without a filter)

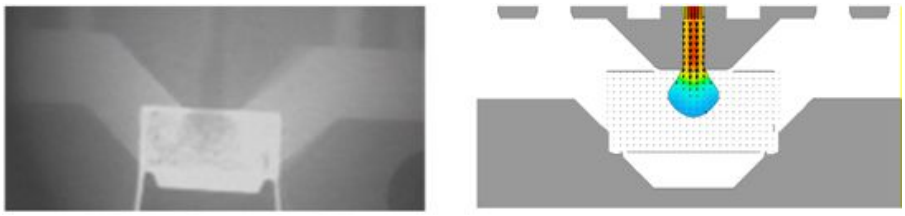

(a) t = 0.00 s

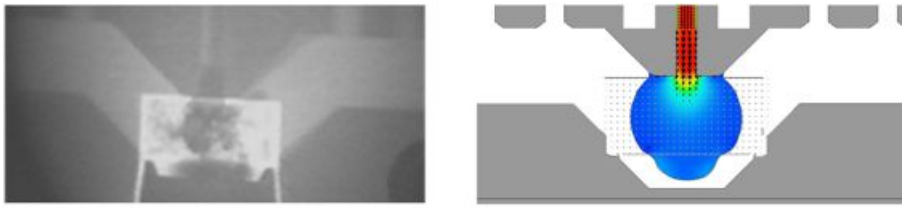

(b) t = 0.32 s

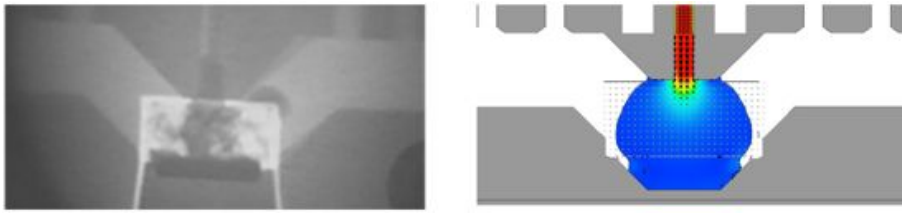

(c) t = 0.64 s

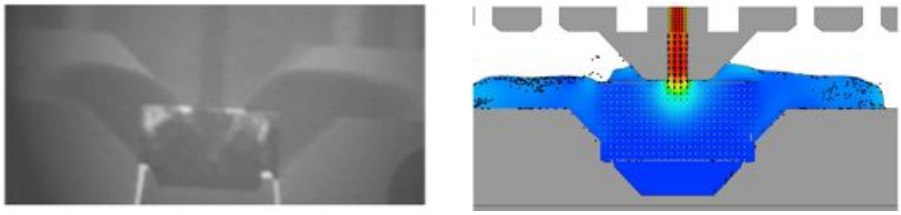

(d) t = 1.60 s

Figure 5.13: Comparison between the real-time X-ray footage and the modelled flow condition in the bottom of downsprue in the filtered condition. The black dots represent particles. The starting time was adjusted for easier comparison. left: real-time X-ray footage (unpublished data from Green and Campbell); right: the cross section view of modelled results.

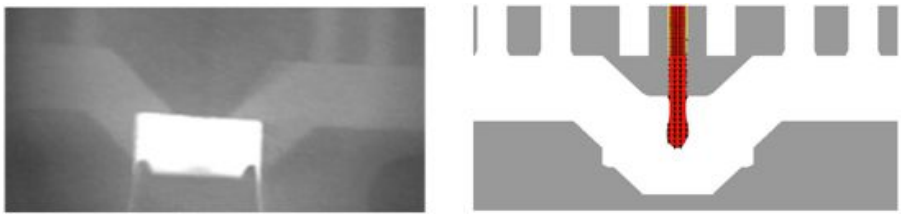

(a) t = 0.00 s

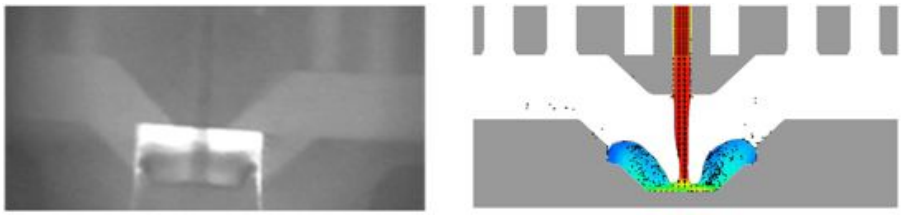

(b) t = 0.32 s

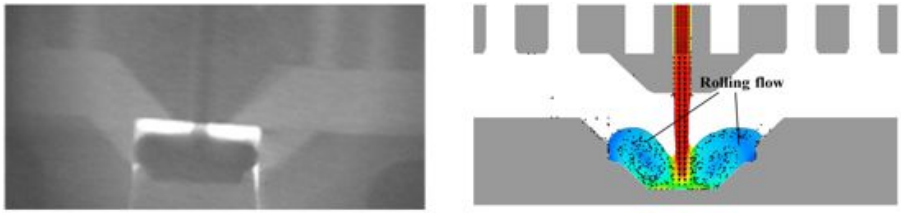

(c) t = 0.64 s

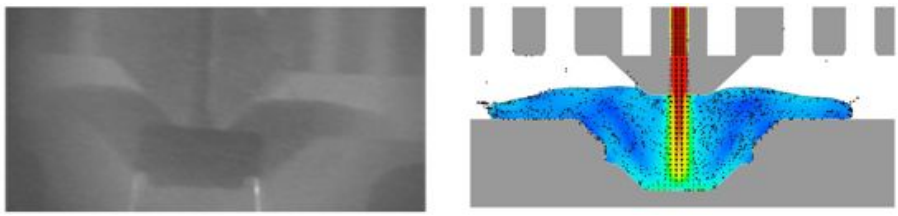

(d) t = 1.60 s

Figure 5.14: Comparison between the real-time X-ray footage and the modelled flow condition in the bottom of downsprue in the unfiltered condition. The black dots represent particles. The starting time was adjusted for easier comparison. left: real-time X-ray footage (unpublished data from Green and Campbell); right: the cross section view of modelled results.

Comparing these two results, it is clear that the simulation of the unfiltered condition gave a better description of the filling patterns, and reproduced the detail of the filling, such as the rolling flow near the stream (highlighted in Figure 5.14c). The filling patterns from the model with a filter did not correlate well with the X-ray observations, in terms of the shape of the liquid fronts formed inside the filter. The models applied the *FLOW-3D* porous media model to simulate the effect of the ceramic foam filter. In this model, an extra drag force was applied to the fluid in the filter print region, but without considering the internal structure of the ceramic filter. Therefore, the flow path in the filter could not be reproduced in the simulation. This may affect the model prediction of particle generation and distribution in the simulations.

5.2.1.2 Comparison between Particle Count and Fatigue Life of Castings

Table 5.7 lists the predicted particles counts in the different modelling conditions. The total of the particles distributed in the bars and placed in the mould cavity are listed at the bottom of the table. On average, 15% out of the total particles were distributed into the test bar region, the rest were trapped in the running system or became stuck on the mould wall. The results showed that the models that considered the entrainment in the pouring basin created two times more particles than those that neglected the entrainment in the pouring basin, but the numbers of particles trapped in the test bars in these two conditions were similar. Besides, when the higher particle placing frequency was used in the model, more particles were generated in the simulation. But the multiple of this increase was not associated with the multiple of the time interval linearly.

The simulations only considered the filtration conditions and did not differentiate between fatigue test methods, which means that the number of particles predicted in the models for high cycle and low cycle fatigue tests were the same. Since Section 3.4.1.1 has mentioned that the experimental results had flaws, here only several examples are shown to illustrate the comparison. Figures 5.15 and 5.16 show the plots of the numbers

Table 5.7: Model predicted particle counts in different model conditions.

	particle placing interval=0.02 s				particle placing interval=0.005 s	
	no basin		with basin		no basin	
No.	filtered	unfiltered	filtered	unfiltered	filtered	unfiltered
A	2674	3630	2545	4456	4803	4020
B	1875	1703	1818	1272	3794	2875
C	335	1333	598	980	1315	2079
D	160	264	155	257	292	543
E	45	95	34	117	61	304
F	50	123	50	138	149	150
G	239	366	100	315	422	567
H	497	1374	249	1270	985	2397
I	1520	1830	1345	1967	1442	3276
J	2105	4250	3606	3518	3919	5107
Total in all bars	9500	14968	10500	14290	17182	21319
Total count in the mould	47477	70916	177552	174007	73057	136031

of particles in the test bars against the fatigue life of these bars in low cycle experiment in unfiltered and filtered conditions respectively. The vertical axes of the figures are a logarithmic scale to show the cycles to failure of the samples.

Clearly, the fatigue lives of the samples are scattered widely on the figures. However, a very weak right downward trend can be obtained between the predicted particle counts and the fatigue properties of the samples. Other plots from high and low cycle tests in unfiltered and filtered conditions are alike. But the slopes of the trend lines obtained from the filtered conditions were flatter as shown in Figure 5.16. Since the particles represent the predicted defects, a right downward sloping trend line on the figure, which represents that more particles in the model indicated lower fatigue life of the casting, is the desired relationship, and the models without the application of a ceramic filter obtained slightly better predictions.

As shown in Table 5.7, the different modelling conditions affected the predicted numbers of particles. However, comparing the plots of each experimental result against the modelling results from the three modelling conditions, similar trend are achieved, which suggests that the time interval of particle placing and the entrainment condition

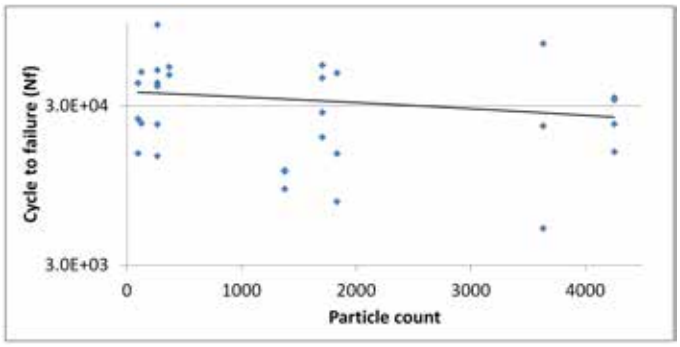

(a)

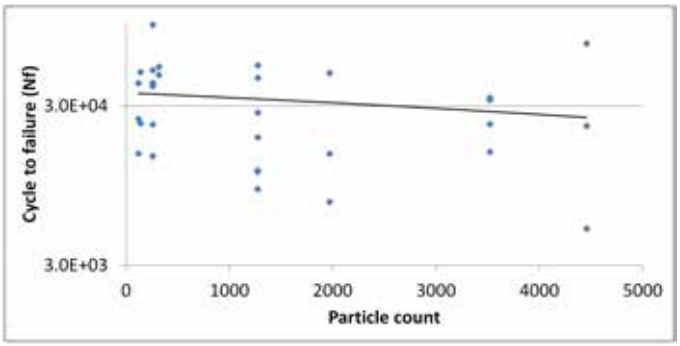

(b)

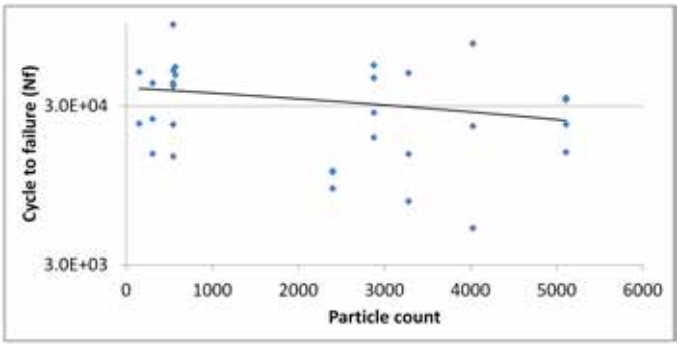

(c)

Figure 5.15: The relationship between predicted particle count in the samples and fatigue life of the samples under low cycle experiment without filtration. Test condition: σ_{max}= 240 MPa, R=+0.1. The vertical axis is in logarithmic scale. (a). entrainment in pouring basin neglected; (b). entrainment in pouring basin considered; (c). high particle placing frequency (0.005 s^{-1}).

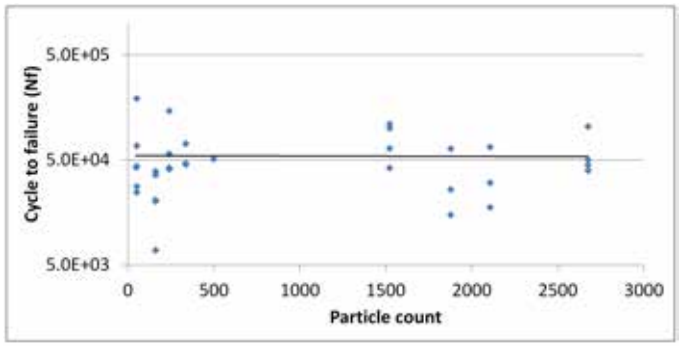

(a)

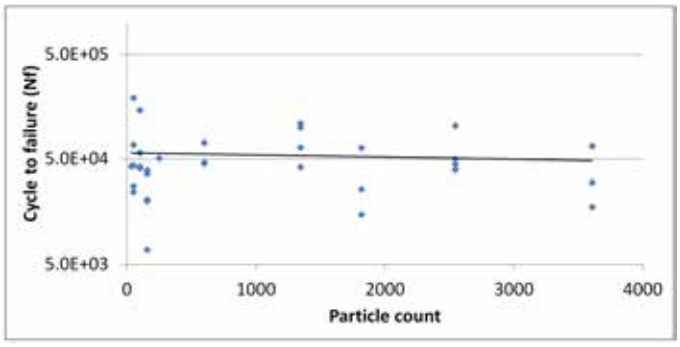

(b)

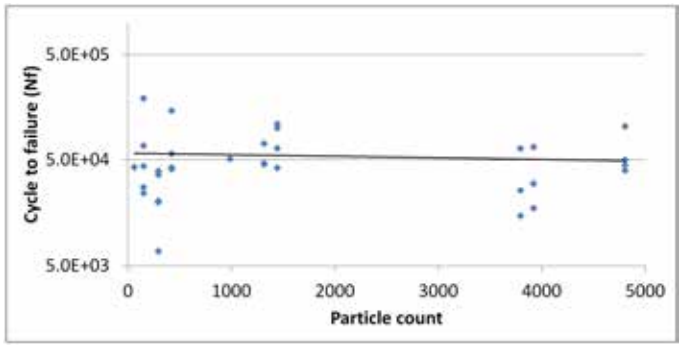

(c)

Figure 5.16: The relationship between predicted particle count in the samples and fatigue life of the samples under low cycle experiment with filtration. Test condition: $\sigma_{\max}$= 240 MPa, R=+0.1. The vertical axis is in logarithmic scale. (a). entrainment in pouring basin neglected; (b). entrainment in pouring basin considered; (c). high particle placing frequency (0.005 s^{-1}).

in the pouring basin in these models had limited influences on the relationship between the the predicted defects quantity and the fatigue lives of samples.

5.2.1.3 Comparison between Fatigue Life Variation of Test Bars and Predicted Particle Distribution

Figure 5.17 shows the mean fatigue lives of the cast bars obtained from each position of the castings. The position is defined in Figure 3.9 and the fatigue lives of bars are shown in Table 3.6. The breaking points, *i.e.* Position H in the filtered casting in Figure 5.17a and Position C in the unfiltered casting in Figure 5.17b, are because no data was reported by Nyahumwa [156].

Clearly, the fatigue life variations of the cast bars were asymmetrical to the downsprue. Figure 5.17 shows that the fatigue lives of the bars varied randomly across the different positions of the mould, and the variation trends were affected by filtration. The specimens responded differently to the test conditions, as the variation trends of the fatigue lives of specimens tested in high-cycle or low-cycle conditions were completely different. Besides, although filtration in the mould increased the fatigue lives of the cast bars, as the mean fatigue lives of bars from the filtered mould at different positions were generally higher than in the unfiltered condition. However, the influence of filtration on the variation trend was not clear, as the fatigue life variation trends in high and low cycle tests responded differently to the filtration. Therefore, it is difficult to validate the model predicted fatigue variation trends from the fatigue life data reported previously.

The modelling results report here are used to study the influences of the filtration, the particle-placing interval and the entrainment condition in pouring basin on the predictions. Figure 5.18 shows different models predicted a consistent particle distribution pattern, that is, more particles were trapped at the far ends of the mould, and the number of particles trapped increased as the distance of the test bar from the downsprue increased. This pattern was confirmed by the particle distribution in Figure 5.12i,

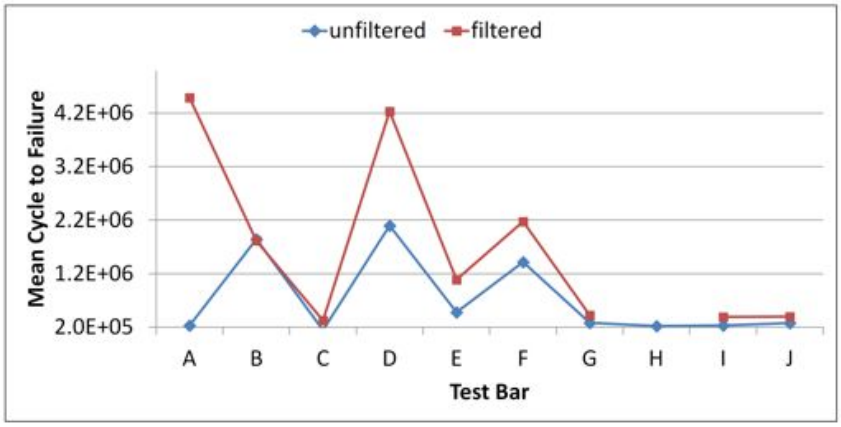

(a)

(b)

Figure 5.17: The mean cycles to failure of test bars from different locations at different test conditions. (a). high-cycle test; (b). low-cycle test.

but the pattern did not correlate to any experimental results shown in Figure 5.17. Modelling results showed that the higher particle placing frequency or consideration of the entrainment condition in the pouring basin did not change the predicted trends of particle distribution in the casting. This may imply that the particle distribution in the mould was mainly determined by the mould design. The filtration could alter the model predictions, but the experimental results could not prove the these predictions, the effects of application of filter in the model are still not clear.

The main influence of consideration of entrainment in the pouring basin is the excessive particles being placed. Figure 5.19 plots the quantity of entrained particles

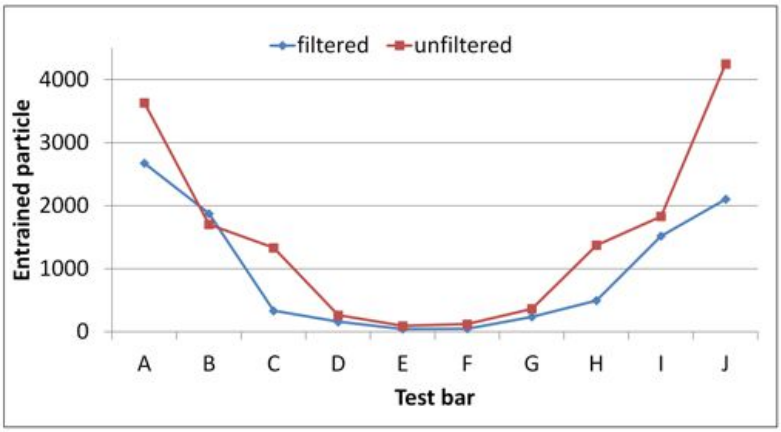

(a)

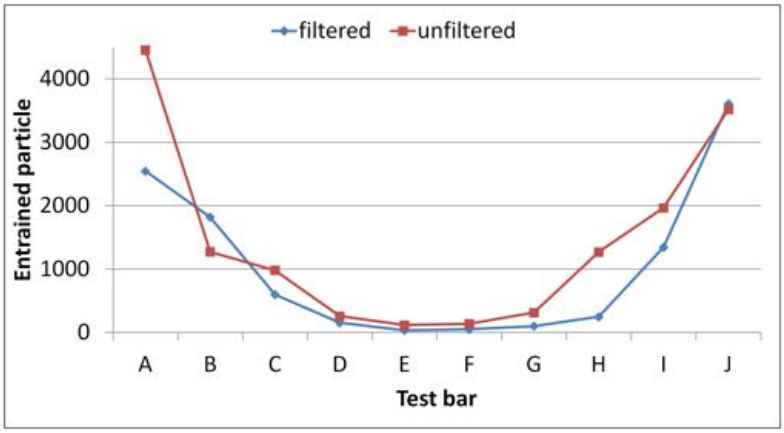

(b)

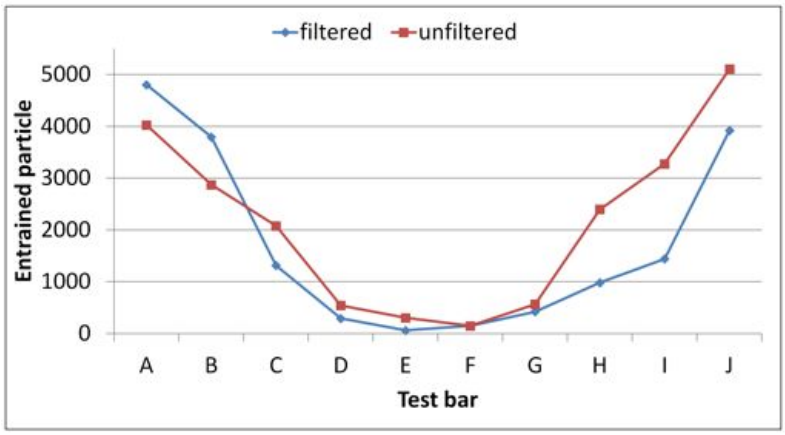

(c)

Figure 5.18: Modelling results of particle distribution in each bar under different modelling conditions. The bar locations are labelled from A to J (left to right). (a). entrainment in pouring basin neglected; (b). entrainment in pouring basin considered; (c). high particle placing frequency (particle placing time interval=0.005 s).

increasing with time in the models, with and without the consideration of entrainment in pouring basin in unfiltered conditions. It can be seen that pouring the liquid into the basin continuously entrained particles. The elapsed time of the simulation with the pouring basin and without was 53.5 and 37.3 hours respectively, and a large amount of particles in the flow enormously increased the post-processing time of the results. Table 5.8 details the number of particles trapped in each mesh block in different modelling conditions. It is clear that: *a*). more than half of the total particles were trapped in the pouring basin and surrounding area when considering entrainment in the basin; *b*). the numbers of particles trapped in the test bars in different models were not significantly affected when considering the entrainment in pouring basin. These results suggest that neglect of the entrainment in the pouring basin during simulation can reduce the computational effort, give reasonable simulation and post-processing times and still provide credible modelling results.

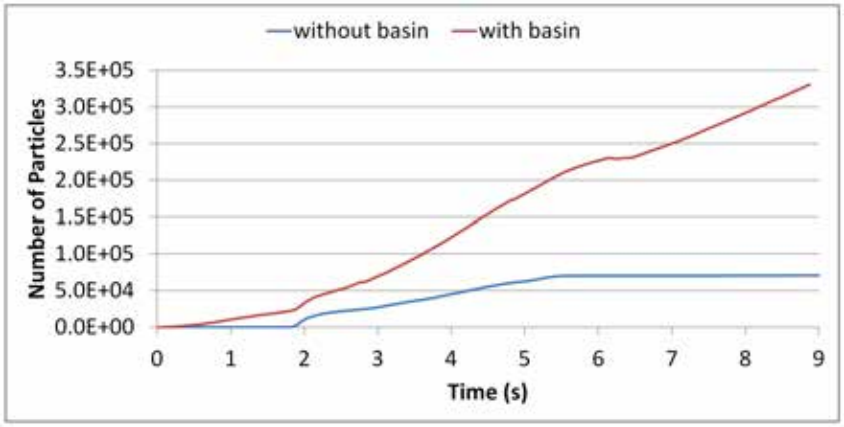

Figure 5.19: The number of entrained particles vs. filling time with and without consideration of entrainment in the pouring basin. (no filtration).

5.2.2 Froude Number Validation Model

5.2.2.1 Modelled Flow Structure

To reduce the computing effort, the Froude Number Validation models disregarded particle placement in the pouring basin. Figures 5.20 and 5.21 show the filling sequences

Table 5.8: The number of particles in each mesh block in four models.

Mesh Block	filtered (no basin)	unfiltered (no basin)	filtered (with basin)	unfiltered (with basin)
Block 1	0	0	121846	250836
Block 2	186	227	568	271
Block 3	35640	50893	48583	60298
Block 4	6326	9534	7031	9104
Block 5	5325	10262	7287	9872
Sum	47477	70916	185315	330386

of unfiltered high and unfiltered low models respectively. The colour scales represent the velocity magnitude of the flow during filling. Typical surface turbulent structures are highlighted in cycles.

The modelled filling structures were generally correlated with Reilly's observation of the real filling pattern examined using real-time X-ray [8]. Figure 5.22 illustrates the locations and specifies the sequence of the occurrences of entrainment in the two moulds. In the unfiltered high mould, once the fluid dropped down the tapered downsprue and entered the horizontal runner, the change of flow direction resulted in splashes and entrainment at the runner-downsprue junction (Location 1 in Figure 5.22a). The difference in size between the outlet of the downsprue and the runner meant that only the bottom part of the runner was filled during filling initially, and this consequently caused a returning wave at the end of the runner (Location 2), once the far end of the runner was filled. The return back wave then collided with the incoming flow, resulting in highly surface turbulent flow at the vertical ingate (Location 3). The upper left part of the runner (near the sprue, Location 4) was filled after the flow entered the vertical ingate. The particles were continuously generated at the contacting points where the returning wave and the incoming flow met. The main difference in the filling between the high and low mould was the severity of entrainment in the mould, as the different height of the downsprue and the ingate of the moulds led to different velocities of the flow developed during pouring. The taller mould had a highly turbulent filling pattern

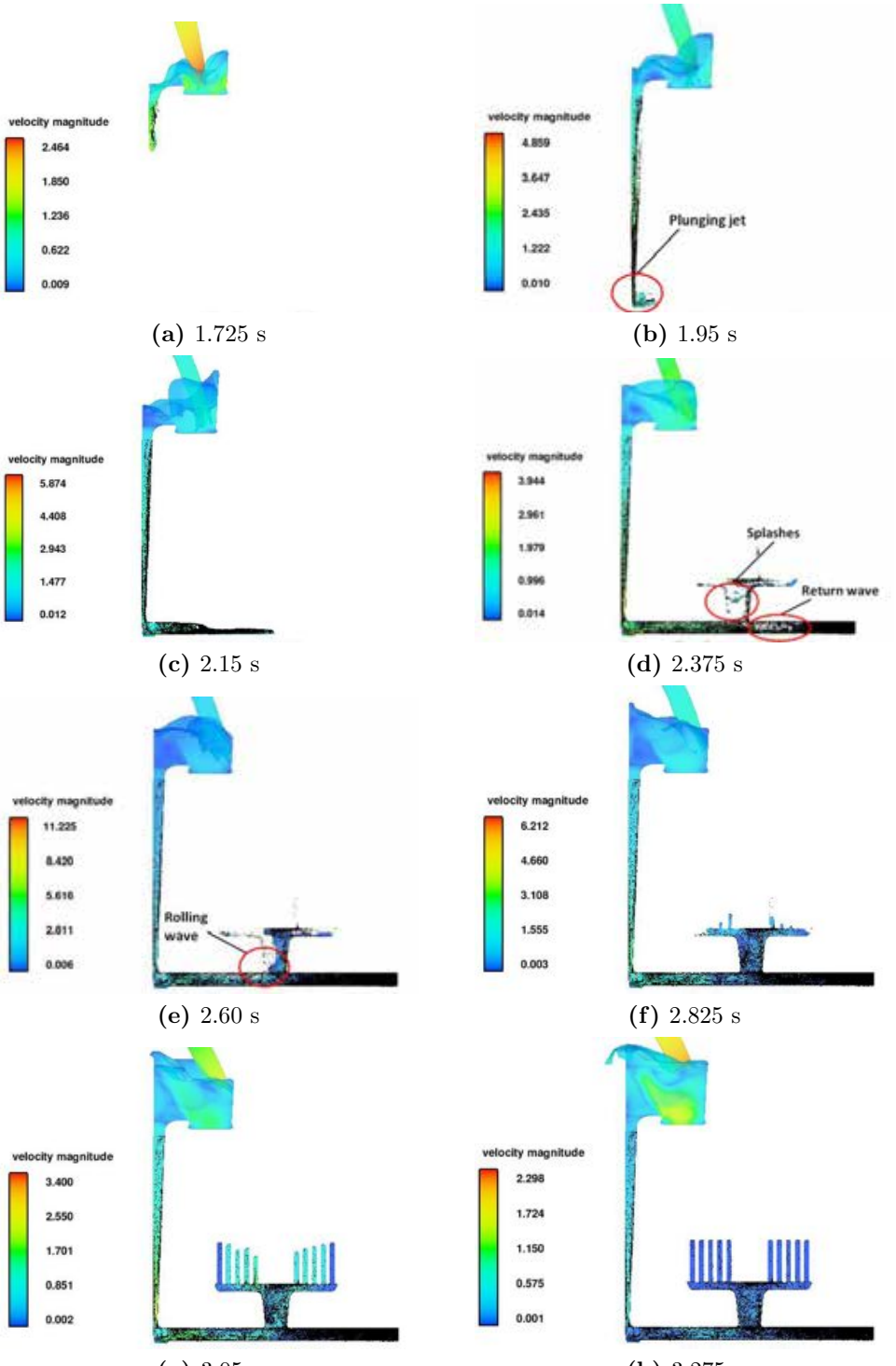

(a) 1.725 s **(b)** 1.95 s

(c) 2.15 s **(d)** 2.375 s

(e) 2.60 s **(f)** 2.825 s

(g) 3.05 s **(h)** 3.275 s

Figure 5.20: Filling scenario of high Froude Number validation mould. The liquid in the pouring basin is not displayed. (unfiltered condition, entrainment location highlighted)

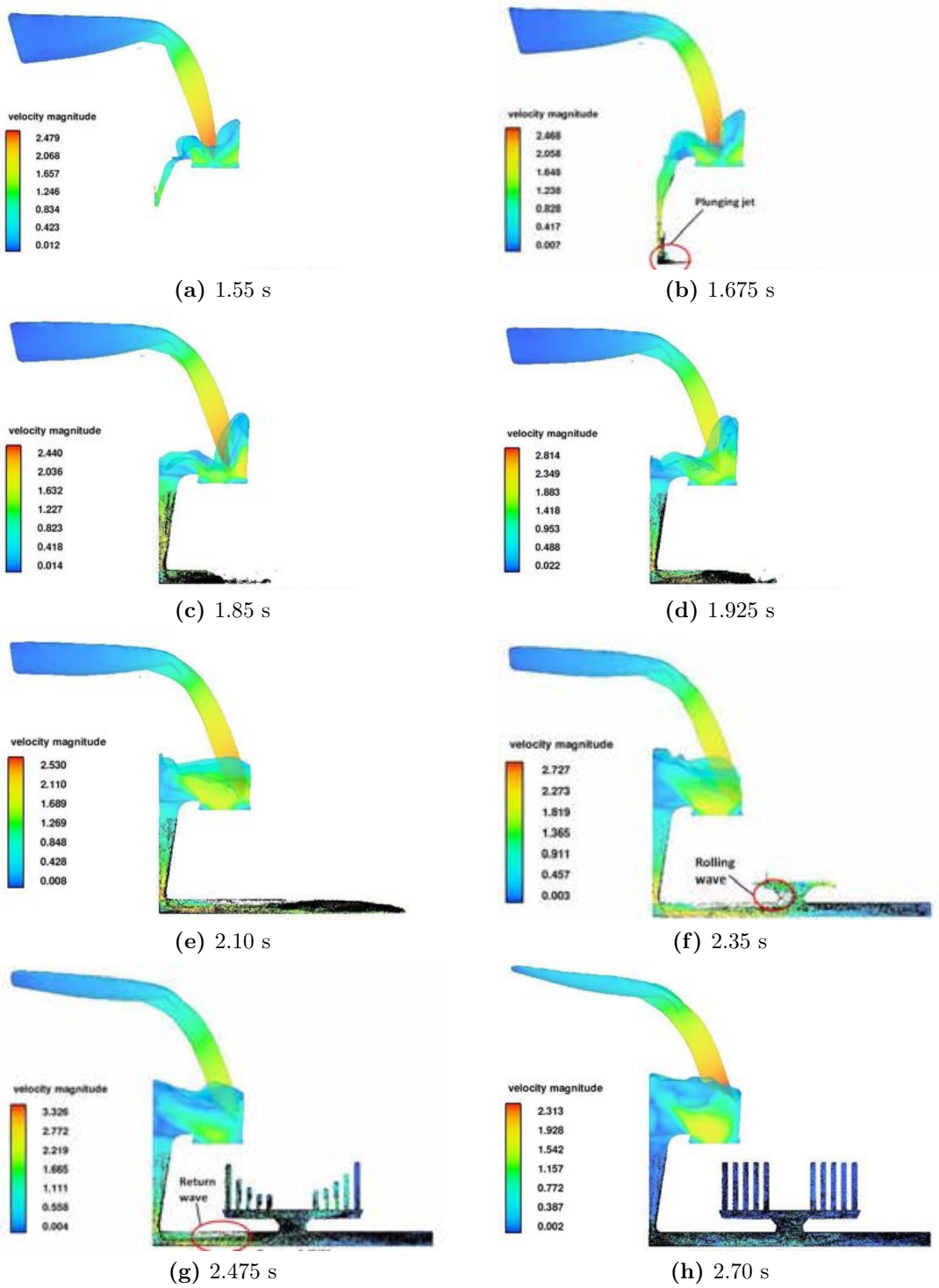

(a) 1.55 s **(b)** 1.675 s

(c) 1.85 s **(d)** 1.925 s

(e) 2.10 s **(f)** 2.35 s

(g) 2.475 s **(h)** 2.70 s

Figure 5.21: Filling scenario of low Froude Number validation model. (unfiltered condition, entrainment location highlighted)

in the simulation, and in the practical experiment, the test bars were full of entrained air bubbles [8].

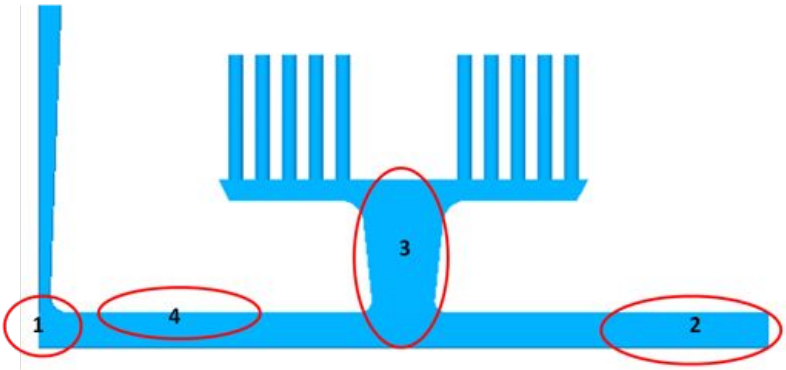

(a)

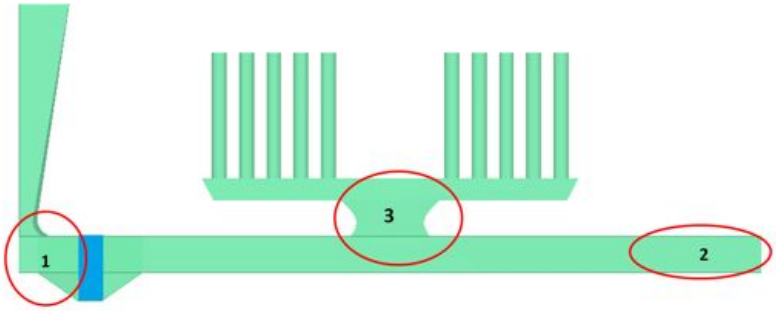

(b)

Figure 5.22: The main entrainment positions in the mould. The number identifies the sequence of the entrainment occurred during filling. (a). high mould; (b). low mould with filter.

Figure 5.22b shows the entraining points when a filter was used. The application of the filter partially blocked the entrance of the runner, which caused the flow to accumulate in front of the filter. The difference between the unfiltered and filtered conditions was that the flow in the filtered condition initially filled the whole height of the horizontal runner after it passed the porous filter, and then the front moved downwards due to gravity and formed a return wave when the front impacted the end of the bar. The return wave also collided with the incoming liquid (Location 2 in Figure 5.22b) and developed surface turbulence (Location 3 in Figure 5.22b) in the ingate.

5.2.2.2 Comparison between Particle Count in the Model and UTS of the Test Bar

Tables 5.9 to 5.11 list the number of particles trapped in each test bar as predicted by the models in the low, low filtered and high filtered moulds respectively. To understand the influence of the particle stickiness to the wall on the modelling result, the particles in these simulations were allowed to stick to the mould wall, which meant that the particles stayed at the positions where they first came into contact with the walls and could not move afterwards in these models. The number of particles that distributed into the whole length or the gauge length of the test bars were reported to understand the scatter of particles in the test bars, with consideration of the effect of the particle stickiness.

Table 5.9: The model predicted particle count in low Fr number validation mould.

Test Bar	Total	Total (Not on the wall)	In gauge length	In gauge length (Not on the wall)
1	1670	453	1004	331
2	1172	289	633	218
3	1090	306	578	265
4	1135	300	534	246
5	2610	395	667	306
6	800	122	201	99
7	507	131	250	101
8	446	157	197	103
9	370	79	120	46
10	526	125	223	86
Sum	10326	2357	4407	1801

The gauge length (the middle part) of the test bars accounted for 40% volume of the whole test bars. Results in Tables 5.9 to 5.11 showed that approximately 40% to 50% of the total particles were trapped in the gauge length of the test bars, suggesting that the particles were distributed evenly in the test bars. Comparing the total particle counts and the number of particles that were not on the mould walls, it can be seen that more than half of the particles in the test bar regions were stuck to the mould wall,

Table 5.10: The model predicted particle count in low filtered Fr number validation mould

Test Bar	Total	Total (Not on the wall)	In gauge length	In gauge length (not on the wall)
1	2061	948	1261	775
2	3089	1231	1999	1061
3	2009	765	1211	616
4	628	190	269	136
5	1581	50	121	31
6	1099	67	190	55
7	504	103	233	87
8	335	99	153	75
9	418	113	230	109
10	986	357	570	299
Sum	12710	3923	6237	3244

Table 5.11: The predicted particle counts in high filtered Fr number validation mould.

Test Bar	Total	Total (Not on the wall)	In gauge length	In gauge length (not on the wall)
1	282	81	173	62
2	600	231	426	212
3	426	138	182	122
4	715	233	233	192
5	785	158	224	108
6	475	106	244	93
7	364	81	99	69
8	135	39	59	33
9	208	91	130	58
10	609	165	491	146
Sum	4599	1323	2261	1095

and more than 75% of the particles, which were not on the mould wall, were distributed into the gauge length of the test bars. This implies that most of the particles were stuck to the bottom and top ends of the bars, where they initially contacted with and finally pushed to. The particle stickiness could alter the predicted results. Table 5.11 showed that in the high filtered mould, in which much severer surface turbulence was supposed to be generated, fewer particles were trapped in the test bars when compared with the number of particles in the low and low filtered mould, as shown in Tables 5.9 and 5.10. This was because the majority of the particles generated in the high mould were stuck to the mould walls of the running system, although more particles were created in the high and high filtered moulds, as shown in Table 5.12.

Table 5.12: Particle count in each mesh block in Fr number validation moulds.

	Block 2 (downsprue)	Block 3 (runner)	Block 4 (test bars)	Block 5 (ingate)	Total
High	31794	52845	52885	12462	149988
High filter	65288	49461	8814	1372	124961
Low	14512	44508	26758	N/A	85778
Low filter	17077	25994	25271	N/A	68342

Figure 5.23 plots the results in Table 5.9, showing the particle counts in the whole length and only in the gauge length of the test bars, with or without consideration of particles stuck to the mould wall. When considering the total particle counts in the whole length of the bars, it can be seen a large number of particles trapped in the first bar on the left (Test Bar 5). A possible explanation is that the rolling back wave moving from right to left collided with the incoming flow and rose into the ingate, while some of the rising liquid impacted the wall of ingate and bounced back directly into the mould cavity in the low moulds because of the low height of the ingate. Modelled filling pattern in Figure 5.21f has showed the splash enter the Test Bar 5 before the vertical ingate filled. This resulted in a peak on the curve of total particle count within the whole length at the position of Test Bar 5. But generally, the variation trends of

particle counts were similar in consideration of four different conditions. The results of other models were quite similar, with the particles distributed evenly in each test bar.

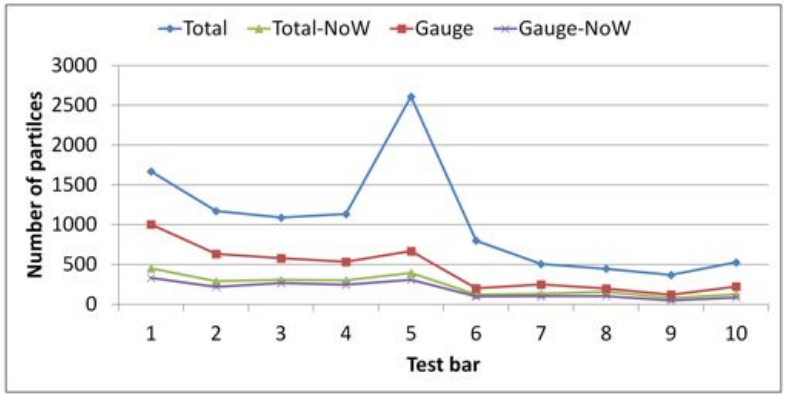

Figure 5.23: The particle distribution in test bars in the low unfiltered mould using different counting methods. ("NoW" is short for "not on the mould wall".)

The plots of predicted number of defects against tensile strengths of samples for the Froude number validation models did not show the correct trends. Figure 5.24 shows the results of the low unfiltered mould, with other results being similar. The linear trend lines in the figures showed slight right upwards slopes. This suggests a relationship where higher tensile strengths of the samples were associated with higher defect populations, which contradicted the previous experimental observations [56]. However, it can be seen that the data points were scattered widely in the figures whichever way the particle counting method was chosen. Thus, a conclusive relationship between the experimental and modelling results cannot be given.

In terms of the variation of the tensile strengths of test bars, Figure 5.25 does not show a consistent variation in UTS across the different positions in the castings. The discontinuity in the trends of the low and the low filtered moulds, was because the UTS of the test bars were so low that the bars could not be machined, due to the presence of trapped air bubbles in that position (Test Bar 6). The UTS of test bars shown in Figure 5.25 showed that the bars filled with filtration had higher strength and

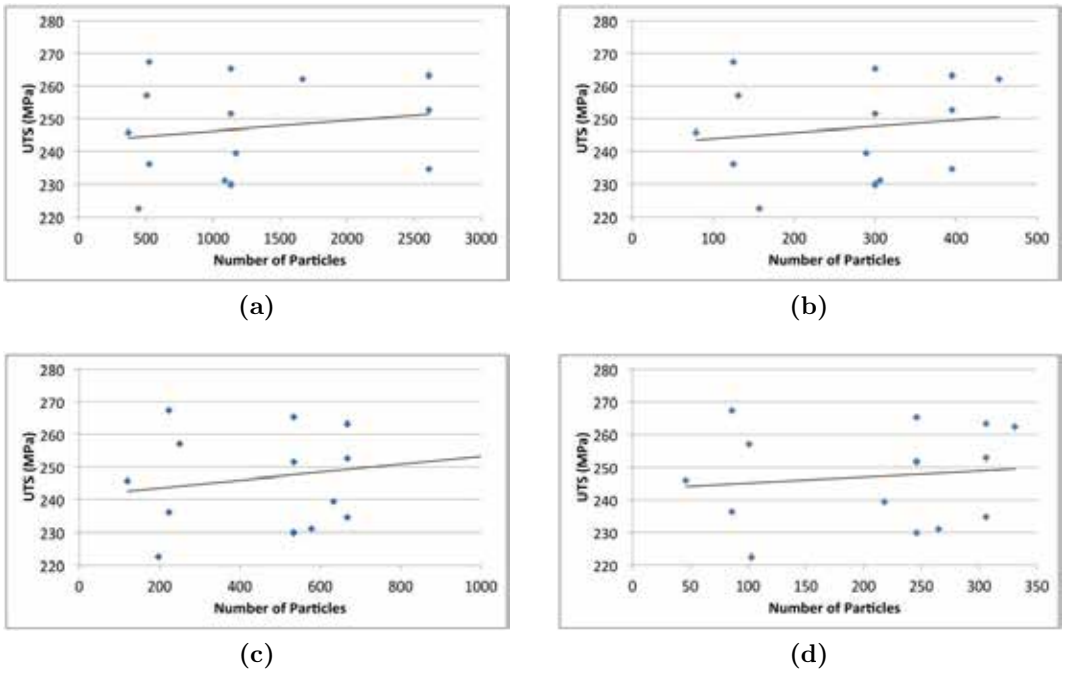

Figure 5.24: The relationship between the predicted particle counts and UTS of the samples from the low unfiltered mould. (a). Total particle count in the test bar vs. UTS; (b). The non-sticky particle count in the test bar vs. UTS; (c). Total particle count in gauge length in the bar vs. UTS; (d). The non-sticky particle count in gauge length in the bar vs. UTS.

a narrower scatter of properties in general. The bars from the the low filtered moulds had higher strength than those from the high filtered mould.

Figure 5.26 shows the plot of the total number of particles within the whole length of test bars in each model against each position of the test bar. The plots of the particle counts within the gauge length were similar. The model estimated that generally there were more particles trapped in the bars on the left side (Test Bar 1 to 5), predicted the lower tensile strengths of the test bars on the left part of the mould. This did not correlate with the experiment results. The modelling results did not show a clear effect of the application of the filter in the model on reducing the particles generated in the model, either.

As mentioned earlier, the UTS of test bars showed large scatter and hence, the trend in variation of strength had a low confidence level. Besides, the discontinuity in

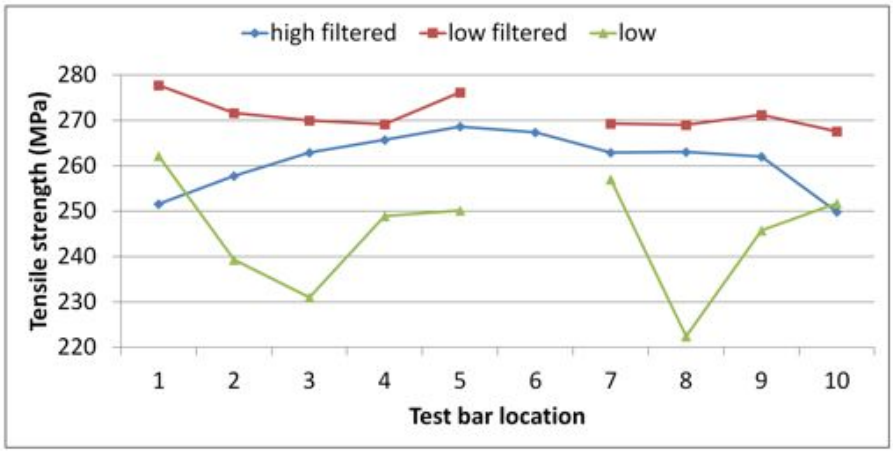

Figure 5.25: The mean UTS of the test bars from Froude number validation moulds. (Figure 3.13 is reprinted here.)

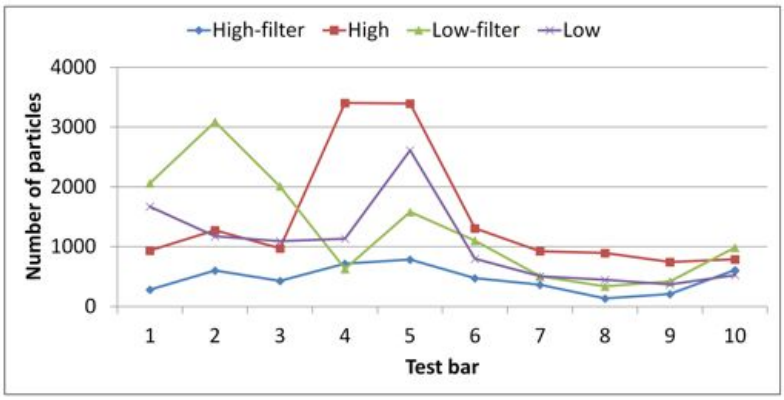

Figure 5.26: The total number of particles in each test bar in four models.

the curves in Figure 5.25 were mainly caused by air bubbles, as reported by Reilly [83]. These bubbles represented large individual defects rather than large quantities of small defects, which was predicted directly by the model. On the other hand, models of the low moulds with and without filter showed that the quantity of entrained particles in the bars was close to or even higher than that in the high moulds, although a greater number of particles was placed in the high moulds. That was because the majority of the particles remained in the ingate/runner beneath the test bars, or became attached to the wall of the mould cavity before entering the test bars, and hence less particles were entrapped in the test bar regions. This result was associated with the effect of the particle stickiness setup in the models. Besides, similar amount of particles were trapped in the low moulds models wether the filter used or not, showing the modelling of the effects of the filter in the models were not accurate. Since there was no correlation between the quantities of particles in the test bars and their tensile properties found in this study, partly owing to the low quality of the validation data, further experiments and validation of OFEM were required.

5.3 Modelling of the Three Entrainment Mechanisms

The three common entrainment mechanisms, namely the Plunging Jet, Return Wave and Rising Jet are abbreviated to PJ, RW and RJ in this text. The modelled filling behaviours were compared with real-time X-ray footage and the experimental data were used to try to validate the model of predicted particle distributions in the castings. However, the shrinkage porosity formed in the casting plates severely affected the validation of the OFEM model.

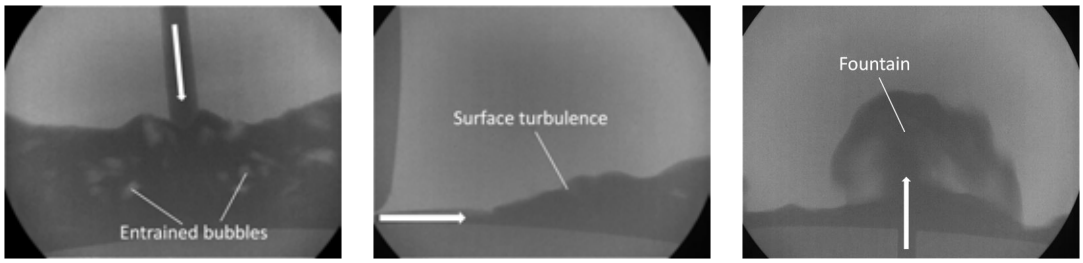

(a) (b) (c)

Figure 5.27: Typical flow structures of three entrainment mechanisms obtained by real-time X-ray radiography. The arrows indicate the flow direction. (a). Plunging Jet; (b). Return Wave; (c). Rising Jet.

5.3.1 Experimental Results

5.3.1.1 Filling Structures in the Three Moulds

Figure 5.27 shows typical flow structures generated in the types of moulds. The different entry directions of the liquid led to three types of flow structures: *a*). the incoming downward stream in the PJ mould directly impacted onto the free surface of the liquid pool in the mould cavity; *b*). the stream injected into the bottom of the mould cavity in the RW mould, sheared surface films and air into the bulk fluid at the contact point between the incoming stream and returning back flow; *c*). the upcoming stream in the RJ mould formed a fountain in the mould cavity and dropped splashes onto the main liquid body. The flow structures displayed in Figure 5.27 visually suggest that the plunging jets led to the highest entrainment level, followed by the rising jet and return wave structures.

5.3.1.2 Bend Test Properties and Weibull Analysis

Tables 5.13 to 5.15 show the actual dimensions and bend strengths of samples from the three types of moulds. The samples contained a great number of defects, which resulted in a large variation of bending strength. The highest and lowest bending strength achieved from these samples were 581.8 MPa (from a RW mould) and 104.1 MPa (from a PJ mould) respectively.

Table 5.13: The bend strength and actual dimensions of plunging jet specimens.

ID	Fmax (N)	d (mm)	b (mm)	Bending strength (MPa)	ID	Fmax (N)	d (mm)	b (mm)	Bending strength (MPa)
pj1-1	22594.37	14.56	13.45	475.5	pj1-16	19068.77	14.16	14.48	394.1
pj2-1	23948.52	14.57	13.59	498.1	pj2-16	20528.89	14.2	14.49	421.6
pj3-1	22120.88	14.55	13.79	454.6	pj3-16	16741.84	14.35	14.46	337.4
pj1-2	15023.39	14.52	14.01	305.2	pj1-17	7534.027	14.13	14.48	156.4
pj2-2	9678.142	14.54	13.93	197.2	pj2-17	6422.046	14.12	14.49	133.4
pj3-2	14821.76	14.55	13.77	305.1	pj3-17	10210.39	14.13	14.5	211.6
pj1-3	25160.87	14.54	14.24	501.5	pj1-18	29089.76	14.44	16.14	518.6
pj2-3	25072.29	14.55	14.21	500.1	pj2-18	27078.03	14.42	15.82	493.9
pj3-3	27112.92	14.58	14.43	530.3	pj3-18	23083.99	14.5	15.97	412.5
pj1-4	24380.17	14.56	14.06	490.8	pj1-19	22182.47	13.93	14.51	472.7
pj2-4	25115.07	14.53	14.05	508	pj2-19	24058.56	13.93	14.47	514.1
pj3-4	25357.32	14.53	14.06	512.6	pj3-19	18926.95	13.93	14.49	403.9
pj1-5	19824.69	14.5	13.69	413.3	pj1-20	12245.41	13.95	14.49	260.6
pj2-5	8884.469	14.5	13.96	181.6	pj2-20	9429.76	13.93	14.49	201.2
pj3-5	19082.99	14.52	13.96	389	pj3-20	10180.09	13.93	14.5	217.1
pj1-6	23803.16	14.55	14.02	481.2	pj1-21	20196.07	13.93	14.44	432.5
pj2-6	24413.63	14.51	13.98	497.7	pj2-21	20845.35	13.93	14.48	445.1
pj3-6	24552.67	14.53	13.98	499.1	pj3-21	21710.41	13.93	14.51	462.6
pj1-7	21870	14.52	13.8	451	pj1-22	24138.25	13.91	14.51	515.9
pj2-7	23921.48	14.51	13.8	494	pj2-22	24760.29	13.92	14.48	529.5
pj3-7	21134	14.49	13.8	437.6	pj3-22	22692.77	13.92	14.48	485.3
pj1-8	18485.85	14.45	13.67	388.6	pj1-23	20398	13.92	14.5	435.6
pj2-8	4897.661	14.46	13.97	100.6	pj2-23	22819.59	13.91	14.5	488
pj3-8	14997.2	14.51	13.96	306.2	pj3-23	18563.57	13.91	14.54	395.9
pj1-9	18764.29	14.5	13.98	383	pj1-24	23858.71	13.97	14.45	507.6
pj2-9	22035.76	14.49	13.97	450.8	pj2-24	25181.65	13.96	14.45	536.5
pj3-9	22667.43	14.51	13.96	462.7	pj3-24	22448.85	13.97	14.47	477
pj1-10	32901.26	16.27	14.49	514.7	pj1-25	25688.82	13.92	14.54	547.1
pj2-10	33552.18	16.65	14.48	501.5	pj2-25	25775.98	13.92	14.5	550.5
pj3-10	26267.45	16.81	14.47	385.4	pj3-25	23172.52	13.93	14.5	494.1
pj1-11	14847.06	14.28	14.7	297.2	pj1-26	24113.15	13.93	14.52	513.5
pj2-11	10421.75	14.35	14.49	209.6	pj2-26	24764.69	13.92	14.49	529.2
pj3-11	9809.298	14.38	14.51	196.2	pj3-26	22477.13	13.93	14.52	478.7
pj1-12	17420.5	14.46	13.93	358.9	pj1-27	23098.86	14	14.46	489
pj2-12	23175.28	14.45	13.93	478.1	pj2-27	26043.56	14	14.44	552.1
pj3-12	21972.36	14.5	13.92	450.5	pj3-27	21652.39	13.99	14.49	458.1
pj1-13	18938.78	14.25	14.47	386.7	pj1-28	16989.77	14.56	13.92	345.4
pj2-13	25881.98	14.23	14.47	530	pj2-28	21556.96	14.52	13.61	450.8
pj3-13	20801.63	14.22	14.47	426.6	pj3-28	21379.78	14.52	13.11	464.1
pj1-14	8092.853	14.48	16.08	144	pj1-29	24155.83	14.05	14.55	504.6
pj2-14	9674.928	14.48	16.15	171.4	pj2-29	20586.61	13.8	14.53	446.4
pj3-14	12216.53	14.51	16.16	215.4	pj3-29	20424.32	13.42	14.56	467.3
pj1-15	21286.41	14.41	13.84	444.4	pj1-30	29987.85	14.11	14.49	623.7
pj2-15	23322.11	14.4	14.18	475.9	pj2-30	26073.46	13.96	14.48	554.4
pj3-15	21014.69	14.44	14.04	430.7	pj3-30	18567.53	13.66	14.5	411.8

Table 5.14: The bend strength and accurate dimensions of return wave specimens.

ID	Fmax (N)	d (mm)	b (mm)	Bending strength (MPa)	ID	Fmax (N)	d (mm)	b (mm)	Bending strength (MPa)
rw1-1	32846.04	14.57	18.78	494.3	rw1-16	20832.25	13.96	14.52	441.7
rw2-1	32581.53	14.64	18.87	483.4	rw2-16	20055.42	13.97	14.52	424.6
rw3-1	34419.54	14.53	19.11	511.9	rw3-16	18128.36	13.97	14.43	386.2
rw1-2	26546.81	14.64	17.58	422.7	rw1-17	14533.24	13.94	14.51	309.3
rw2-2	31085.78	14.71	17.84	483.2	rw2-17	12729.94	13.96	14.46	271
rw3-2	28094.78	14.54	17.86	446.4	rw3-17	18107.84	13.97	14.48	384.5
rw1-3	20663.9	14.6	15.16	383.7	rw1-18	18361.1	13.95	14.44	392
rw2-3	25964.3	14.67	16.2	446.8	rw2-18	20586.93	13.95	14.46	439
rw3-3	20988.83	14.54	15.06	395.5	rw3-18	11351.42	13.95	14.43	242.5
rw1-4	24272.46	14.58	14.59	469.6	rw1-19	21123.78	13.34	14.5	491.2
rw2-4	23679.37	14.21	14.65	480.3	rw2-19	19642.41	13.32	14.52	457.5
rw3-4	26966.98	14.23	14.5	551.1	rw3-19	21609.59	13.34	14.47	503.5
rw1-5	20020.85	14.2	14.59	408.3	rw1-20	15168.97	13.56	14.51	341.1
rw2-5	18489.14	14.18	14.64	376.9	rw2-20	15156.51	13.54	14.52	341.6
rw3-5	23760.98	14.18	14.51	488.6	rw3-20	13573.21	13.55	14.52	305.5
rw1-6	20252.78	13.93	14.54	430.7	rw1-21	19034.11	13.95	14.44	406.4
rw2-6	21033.76	13.89	14.55	449.6	rw2-21	17566.47	13.99	14.48	371.9
rw3-6	20979.02	13.91	14.54	447.4	rw3-21	17518.37	13.88	14.49	376.5
rw1-7	19378.99	14.24	14.53	394.6	rw1-22	15610.04	11.94	14.54	451.8
rw2-7	22548.43	14.31	14.57	453.4	rw2-22	14803.06	11.87	14.54	433.5
rw3-7	21464.79	14.14	14.46	445.5	rw3-22	15916.88	11.9	14.55	463.5
rw1-8	17758.95	14.17	14.56	364.5	rw1-23	16314.37	12.38	14.56	438.7
rw2-8	19294.75	14.34	14.6	385.6	rw2-23	13286.76	11.95	14.56	383.4
rw3-8	21834.84	14.3	14.48	442.4	rw3-23	16521.61	12.14	14.5	463.9
rw1-9	20931.56	14.38	14.49	419.1	rw1-24	18783.22	12.9	14.47	468
rw2-9	19000.66	13.95	14.53	403.2	rw2-24	14080.59	12.79	14.51	355.9
rw3-9	21598.28	14.41	14.5	430.4	rw3-24	18889.82	13.11	14.44	456.7
rw1-10	20079.22	13.97	14.49	426	rw1-25	21595.7	13.45	14.68	487.9
rw2-10	19276.2	13.99	14.51	407.3	rw2-25	21514.03	13.33	14.66	495.5
rw3-10	18422.29	13.96	14.46	392.2	rw3-25	20472.77	13.42	14.52	469.7
rw1-11	13026.98	13.93	14.51	277.6	rw1-26	17551.29	13.92	14.56	373.3
rw2-11	13856.25	13.94	14.53	294.4	rw2-26	20785.63	13.9	14.57	443
rw3-11	18445.77	13.93	14.47	394.2	rw3-26	16351.97	13.9	14.5	350.2
rw1-12	16456.2	13.94	14.44	351.9	rw1-27	17249.18	14.01	14.47	364.4
rw2-12	19391.02	13.93	14.48	414.1	rw2-27	19981.26	13.95	14.51	424.6
rw3-12	19790.04	13.93	14.46	423.2	rw3-27	15112.23	13.95	14.49	321.6
rw1-13	16473.68	13.36	14.5	381.9	rw1-28	29544.33	14.64	14.47	571.6
rw2-13	16748.03	13.33	14.5	390	rw2-28	29887.83	14.54	14.58	581.8
rw3-13	19385.73	13.33	14.45	453	rw3-28	22804.59	14.56	14.79	436.4
rw1-14	13656.03	13.58	14.57	304.9	rw1-29	26129.3	14.55	14.69	504.1
rw2-14	12908.89	13.55	14.54	290.1	rw2-29	28049.68	14.57	14.61	542.6
rw3-14	16625.99	13.56	14.46	375.2	rw3-29	23758.82	14.67	14.54	455.6
rw1-15	17661.66	13.85	14.44	382.6	rw1-30	25385.86	14.54	14.54	495.5
rw2-15	17587.72	13.89	14.55	375.9	rw2-30	28150.19	14.58	14.71	540.1
rw3-15	16973.54	13.91	14.54	362	rw3-30	27505.33	14.61	14.51	532.8

Table 5.15: The bend strength and accurate dimensions of rising jet specimens.

ID	Fmax (N)	d (mm)	b (mm)	Bending strength (MPa)	ID	Fmax (N)	d (mm)	b (mm)	Bending strength (MPa)
rj1-1	27648.77	15.72	14.54	461.7	rj1-16	27755.17	15.16	14.47	500.8
rj2-1	30612.54	15.67	14.59	512.7	rj2-16	28331.07	15.06	14.53	515.8
rj3-1	28559.52	15.9	14.52	466.8	rj3-16	25513.63	15.25	14.43	456.2
rj1-2	21159.35	14.55	14.3	419.4	rj1-17	11811.36	14.66	14.45	228.2
rj2-2	24143.75	14.6	14.85	457.6	rj2-17	11799.15	14.76	14.54	223.5
rj3-2	21196.38	14.52	15.06	400.5	rj3-17	21482.66	14.99	14.46	396.7
rj1-3	21663.67	13.72	14.52	475.6	rj1-18	23078.19	14.23	14.4	474.9
rj2-3	23736.44	13.96	14.58	501.2	rj2-18	25366.56	14.57	14.47	495.5
rj3-3	22478.71	14.03	14.5	472.5	rj3-18	23780.79	14.78	14.41	453.3
rj1-4	21207.38	13.93	14.51	451.9	rj1-19	21919.17	13.54	14.51	494.4
rj2-4	21438.85	13.95	14.56	454	rj2-19	21434.06	13.55	14.53	482.1
rj3-4	23196.65	13.94	14.5	494	rj3-19	18965.97	13.48	14.47	432.8
rj1-5	22006.02	13.93	14.49	469.6	rj1-20	12816.24	13.22	14.47	304.1
rj2-5	23712.97	13.94	14.56	502.9	rj2-20	18887	14.17	14.57	387.4
rj3-5	18384.85	13.94	14.5	391.5	rj3-20	22146.84	14.1	14.48	461.6
rj1-6	25372.48	13.99	14.47	537.5	rj1-21	25901.86	14.25	14.32	534.5
rj2-6	25670.19	14	14.56	539.7	rj2-21	25536.89	14.25	14.46	521.8
rj3-6	19619.18	14	14.47	415.1	rj3-21	21390.29	14.04	14.42	451.5
rj1-7	22880.26	13.89	14.48	491.4	rj1-22	25475.06	14.09	14.51	530.6
rj2-7	22716.51	13.89	14.53	486.2	rj2-22	25925.14	14.08	14.64	536
rj3-7	18032.02	13.9	14.46	387.3	rj3-22	24790.23	14.11	14.48	516
rj1-8	13843.02	13.89	14.48	297.3	rj1-23	19045.44	13.82	14.49	412.9
rj2-8	17081.98	13.9	14.56	364.3	rj2-23	18898.59	13.82	14.56	407.8
rj3-8	15694.75	13.92	14.48	335.6	rj3-23	17505.1	13.82	14.47	380
rj1-9	22619.88	13.96	14.45	482	rj1-24	24496.35	14.23	14.42	503.4
rj2-9	20592.37	13.98	14.52	435.4	rj2-24	21479.01	14.24	14.49	438.6
rj3-9	17786.9	14	14.46	376.6	rj3-24	21302.58	14.23	14.45	436.8
rj1-10	18419.75	13.92	14.46	394.4	rj1-25	22399.8	13.88	14.74	473.3
rj2-10	18726.45	13.92	14.52	399.4	rj2-25	24207.78	13.9	14.75	509.7
rj3-10	17713.04	13.93	14.45	379	rj3-25	23234.93	13.92	14.59	493.1
rj1-11	10538.73	13.91	14.46	226	rj1-26	27460.54	14.13	14.42	572.3
rj2-11	13010.28	13.94	14.55	276.1	rj2-26	26659.35	14.21	14.6	542.6
rj3-11	15775.7	13.96	14.47	335.7	rj3-26	24624.28	14.22	14.5	503.9
rj1-12	24076.63	13.95	14.43	514.4	rj1-27	27178.9	14.13	14.42	566.4
rj2-12	24822.81	13.99	14.5	524.8	rj2-27	25932.97	14.15	14.5	535.9
rj3-12	21068.33	13.92	14.46	451.2	rj3-27	24386.01	14.17	14.46	503.9
rj1-13	23140.74	13.92	14.46	495.5	rj1-28	25604.37	14.78	14.08	499.5
rj2-13	23409.11	13.92	14.51	499.6	rj2-28	27278.49	14.25	14.8	544.6
rj3-13	20883.01	13.94	14.43	446.8	rj3-28	22569.89	14.72	13.85	451.2
rj1-14	11640.94	13.91	14.46	249.6	rj1-29	29947.82	14.56	15.72	539.2
rj2-14	10998.27	13.97	14.56	232.2	rj2-29	28430.56	14.62	15.44	516.9
rj3-14	17366.65	13.96	14.45	370	rj3-29	27061.35	14.56	15.12	506.6
rj1-15	21992.96	13.93	14.4	472.2	rj1-30	28823.53	14.45	15.95	519.3
rj2-15	22603.27	13.99	14.47	478.9	rj2-30	28592.08	14.25	14.54	581
rj3-15	19944.31	13.98	14.42	424.6	rj3-30	26822.97	14.54	14.48	525.7

Figure 5.28 shows frequency histograms of bending strength distributions for the three types of moulds. Several samples from PJ and RJ moulds had very low strength, below 250 MPa, as highlighted in the boxes on the figures. Specifically, samples from PJ moulds had a wider strength distribution and more samples had low strength compared with other moulds. This might be attributed to the large entrained bubbles, of 1 to 2 mm diameter, found beneath the top surface of the cast plate, since similar large entrained bubbles were not found in the RW and RJ plates. Regarding the higher strength samples, the bending strength of samples from both PJ and RJ moulds was concentrated in the range of 450 to 550 MPa, whilst the strength of test bars from the RW moulds were mainly distributed in the range of 350 to 500 MPa, lower than the other two cases.

Figure 5.29 shows Weibull plots of the bend strength of samples from the three types of moulds, which were all similar, and very low. Elimination of the data obtained from the centre of the cast plates, which were severely affected by shrinkage porosity, increased the moduli approximately two times, revealing the adverse influences of shrinkage porosity on the bend strength of the castings. Considering all samples, the highest Weibull modulus achieved was 7.4 from the RW moulds, followed by 5.7 and 3.1 from the RJ and PJ moulds respectively. The Weibull modulus of each mould generally correlated with the surface turbulence levels during filling, as shown in Figure 5.27. However, the Weibull plot of the samples without data from the centre of the plates still showed that the RJ samples had a higher Weibull modulus (12.3) than the PJ samples did (10.9), but with the RW having the lowest (8.6). This result implied that the RJ castings had less entrainment defects than PJ castings. In fact, the large scatter of mechanical properties of these samples was a combined effect from several different defects. Removing those data gained from the samples in the centre of the casting plates could decrease the influence of shrinkage porosity and disclose the importance of entrainment defects, but the efforts were limited to PJ and RJ cast-

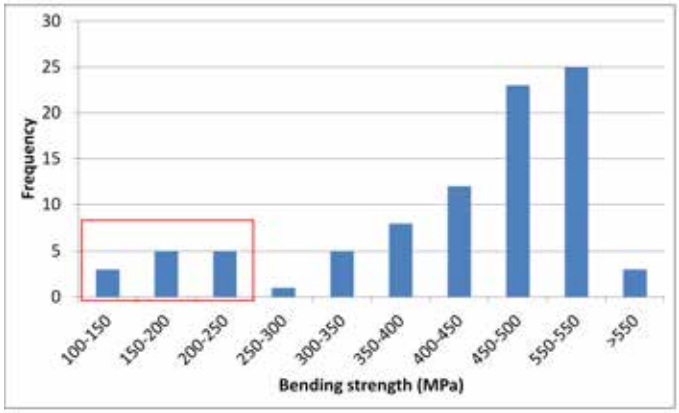

(a)

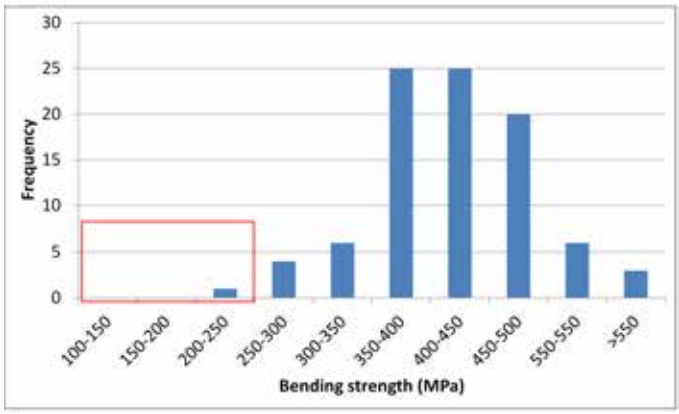

(b)

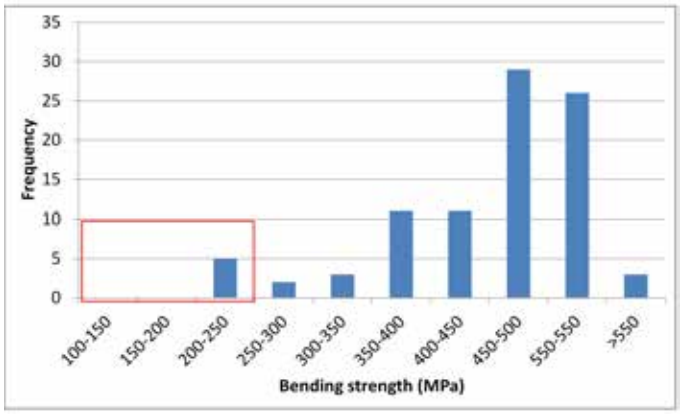

(c)

Figure 5.28: The frequency distribution of bending strength of samples obtained from three entrainment mechanisms mould. (a). Plunging Jet; (b). Return Wave; (c). Rising Jet.

ings as the shrinkage pores were mainly in the centre of these plates, while they were distributed widely in the RW plates. Therefore, the lowest Weibull modulus attained in the RW samples from the filtered data did not necessarily mean that RW castings contained more entrainment defects than the other two.

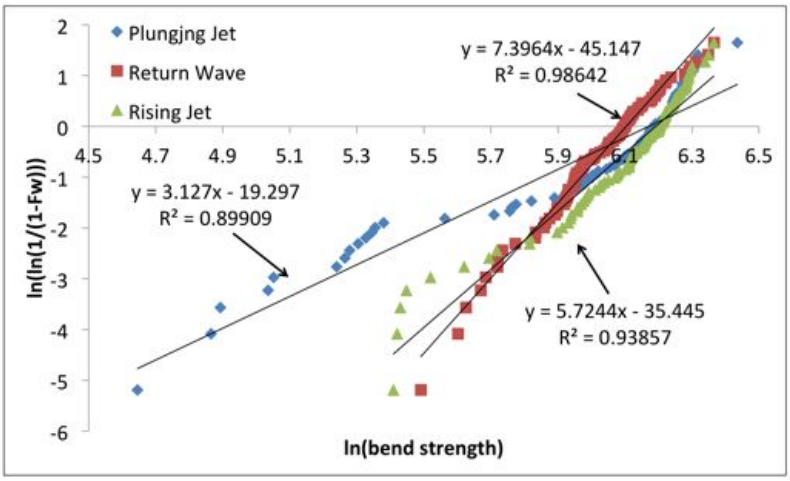

(a)

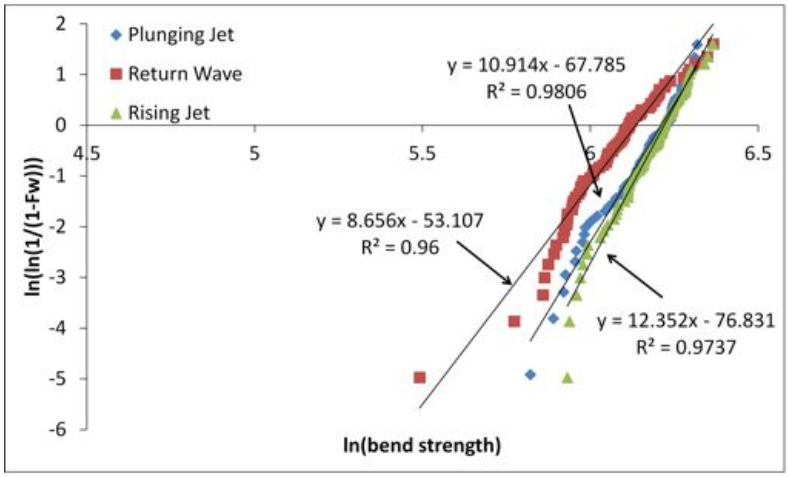

(b)

Figure 5.29: Two-parameter Weibull plot of the bending strength of samples from three entrainment mechanisms moulds. (a). all samples; (b). shrinkage porosity affected samples eliminated.

Although the reproducibility of properties of these castings was low, some strength variation was achieved from these tests and used to validate the predicted defect distribution from the models.

5.3.1.3 Defect Characterisation

Figures 5.30 to 5.32 show the results of X-ray observation of cast plates from the three moulds with visible defects marked. The entrained small bubbles near the outlet of the downsprue in the PJ castings were later located in the gauge length of the samples, resulting in very low strengths of the PJ samples, while the bubbles trapped in the top two corners of the RJ castings had less impact as they were located outside the gauge length of the samples. The size of defects in the RW plates were below the resolution of the X-ray image, and therefore no visible defects were observed in the film X-ray images shown in Figure 5.31.

Figure 5.33 shows typical defects found on the metallographic and fracture surfaces of samples. Shrinkage and gas porosity, cracks and oxide film defects were all found in the castings. This meant that the failure of the samples could be attributed to several kinds of defects. But in general observation, samples containing less porosity had higher strength.

Figures 5.34 and 5.35 show EDX analysis results of selected defects in the samples, which shows that the crack was a folded double oxide film. The morphology of the fracture surface shown in Figure 5.35 suggested an old oxide film and the oxygen peak in the spectrum supported this.

5.3.2 Computational Modelling Results

5.3.2.1 Modelled Filling Structures in Three Moulds

The moulds geometries of Plunging Jet (PJ), Return Wave (RW) and Rising Jet (RJ) are shown in Figure 3.6. Figures 5.36 through to 5.38 illustrate the filling scenario obtained from real-time X-ray radiography footage and modelled filling of the three entrainment mechanisms. Owing to the limitation of the field of view of the X-ray camera, only part of the mould cavity was viewed, and this field of view has been highlighted as a red square in the model results. The colour scheme in the flow profiles

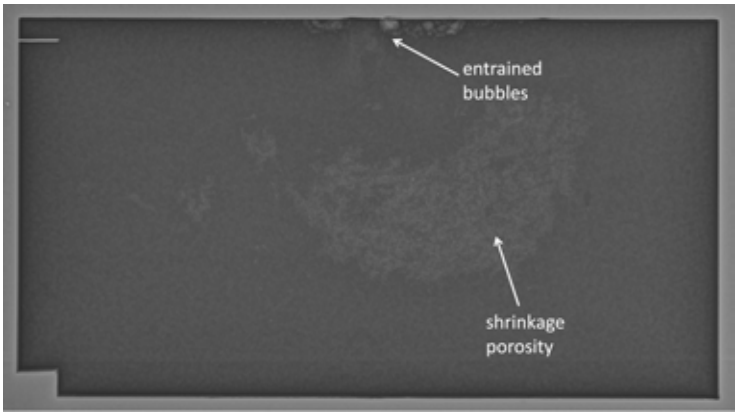

(a)

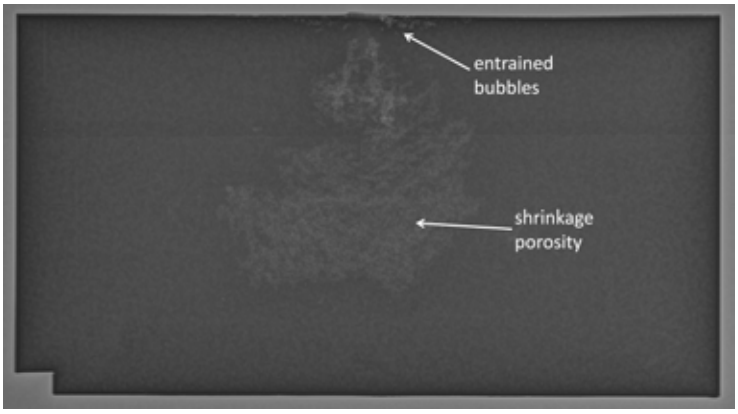

(b)

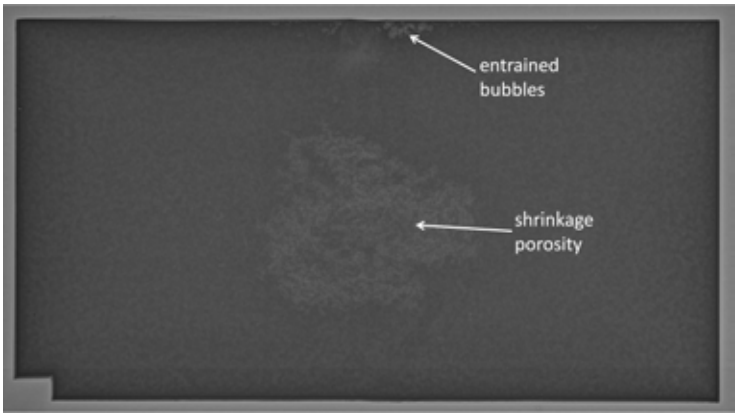

(c)

Figure 5.30: Film X-ray observation of the defects distribution in the PJ plates. (a). PJ1; (b). PJ2; (c). PJ3.

(a)

(b)

(c)

Figure 5.31: Film X-ray observation of the defects distribution in the PJ plates. (a). RW1; (b). RW2; (c). RW3.

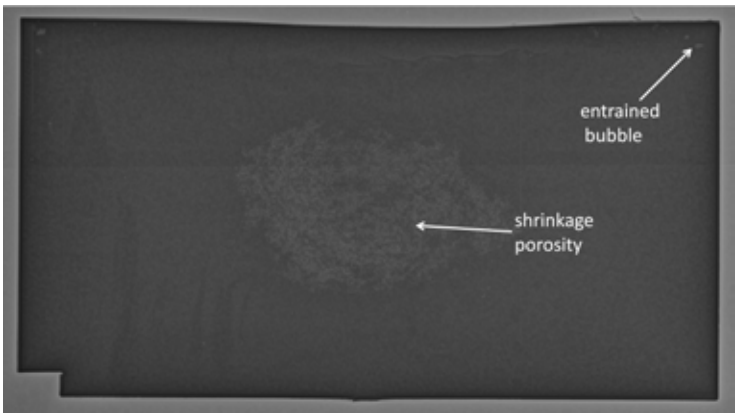

(a)

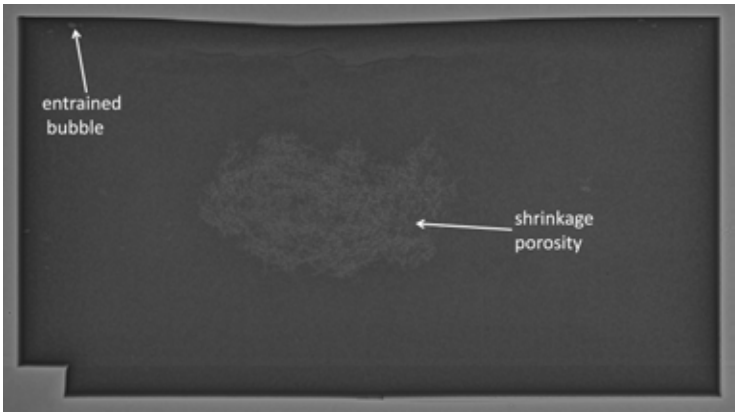

(b)

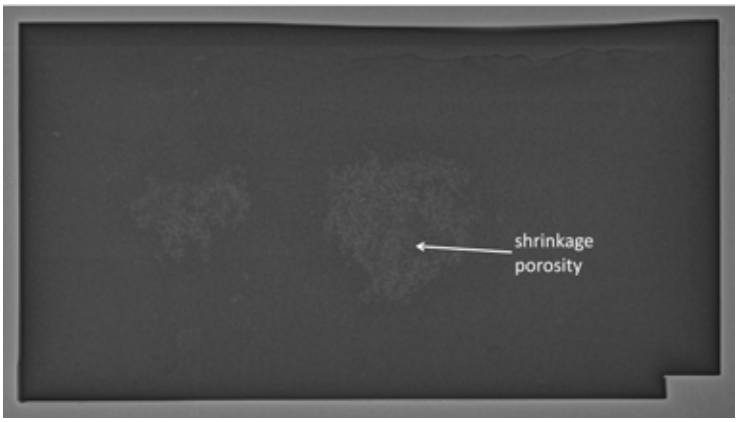

(c)

Figure 5.32: Film X-ray observation of the defects distribution in the PJ plates. (a). RJ1; (b). RJ2; (c). RJ3.

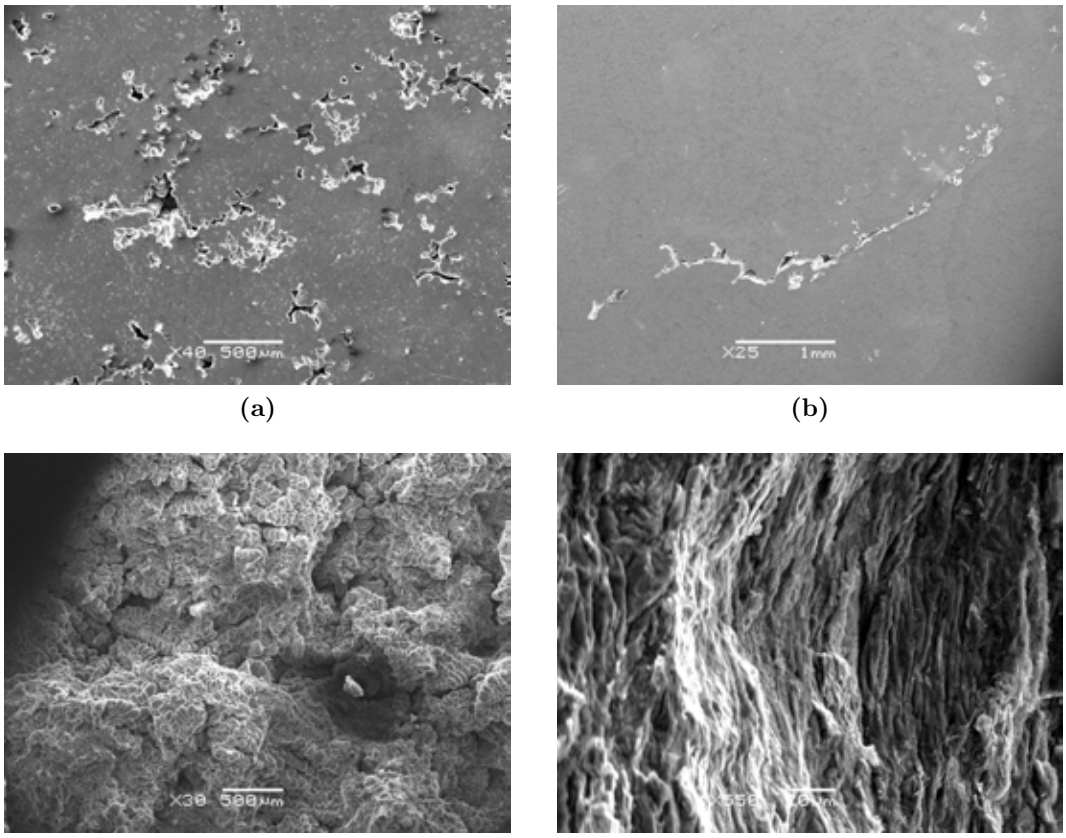

(a) (b)

(c) (d)

Figure 5.33: Selected SEM images of defects observed on the metallographic and fracture surfaces. (a). shrinkage porosity; (b). crack (folded double oxide films); (c). dendrites on the fracture surface; (d). oxide film on the fracture surface.

represent the velocity magnitude, with a warmer colour indicating higher velocity magnitude. Although each frame of filling of the models did not exactly correlate to the X-ray image at the same moment, the modelled free surface movement during filling captured the features of the three different entrainment mechanisms and showed good agreement with the real-time X-ray footages.

Figure 5.39 shows the main entraining locations of the three entrainment mechanisms in the mould cavity during filling. The formation of entrainment defects in the three moulds was caused by a combination of both entrained oxide films and entrained air. The oxide films on the slower-moving alloy were rolled into the melt, while air bubbles were directly entrained, both occurring at the impingement points in the flow.

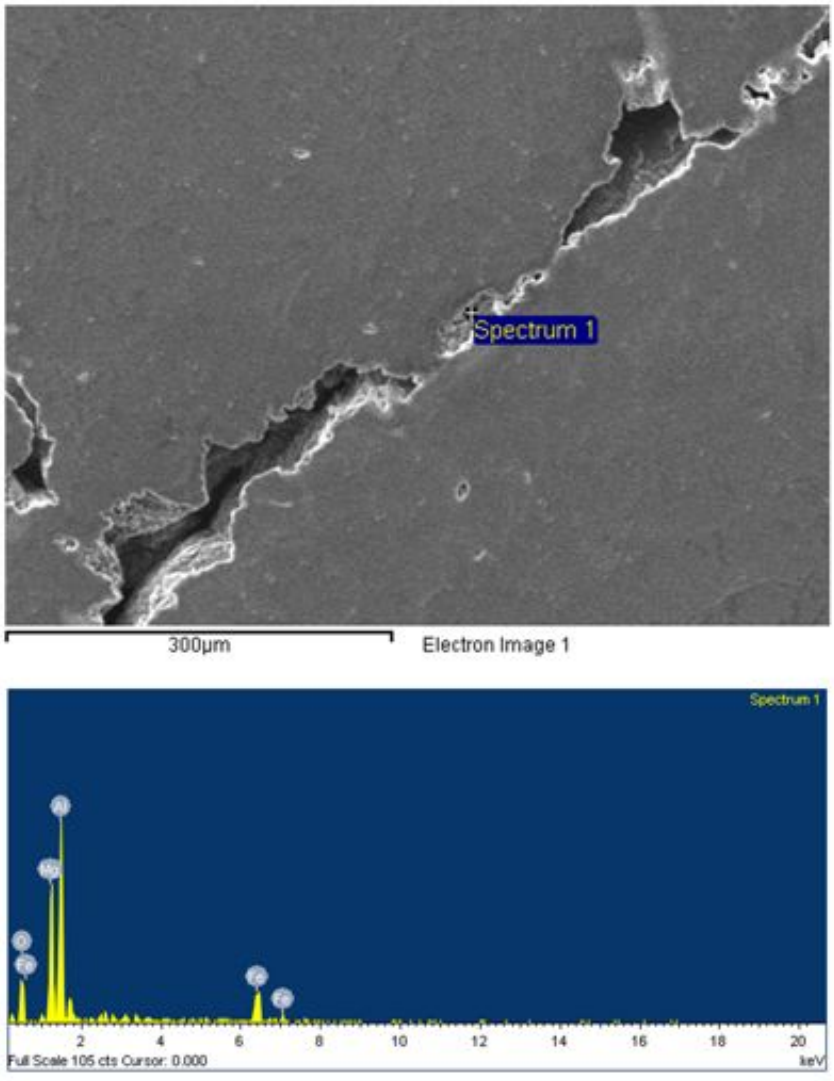

Figure 5.34: An example of EDX analysis of a crack on the fracture surface of the samples from the three types of moulds.

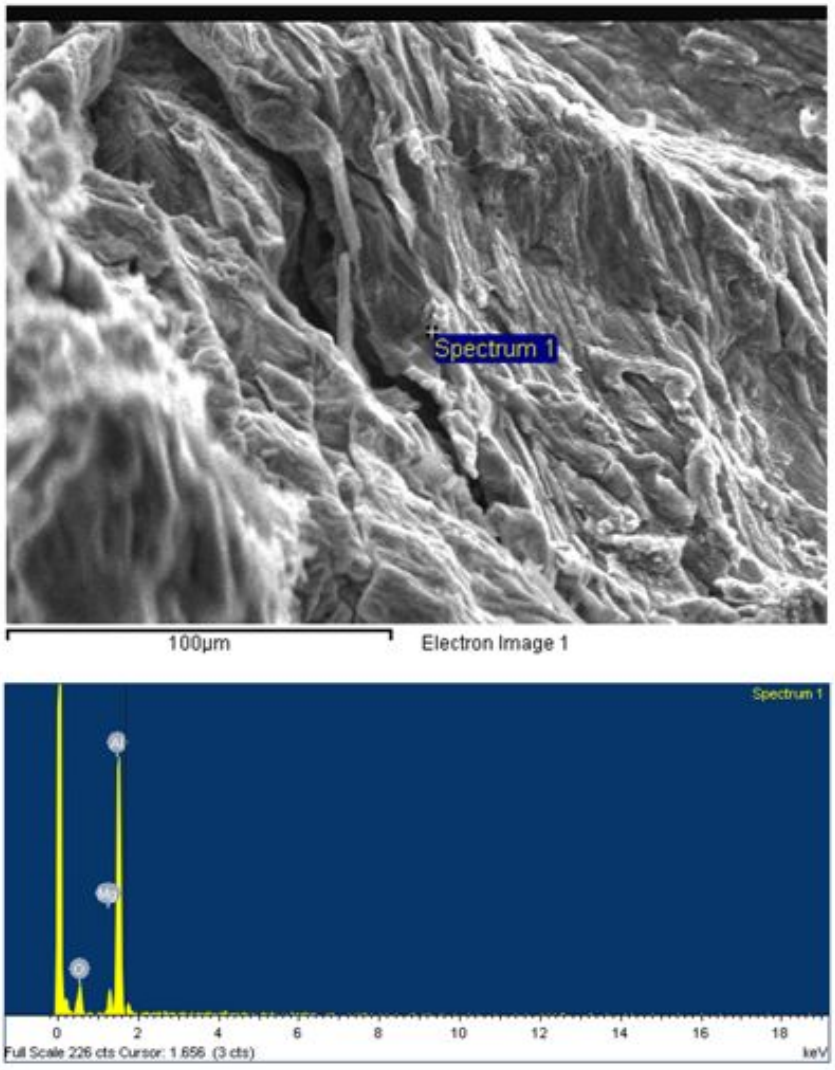

Figure 5.35: An example of EDX analysis of an oxide film on the fracture surface of the samples from the three types of moulds.

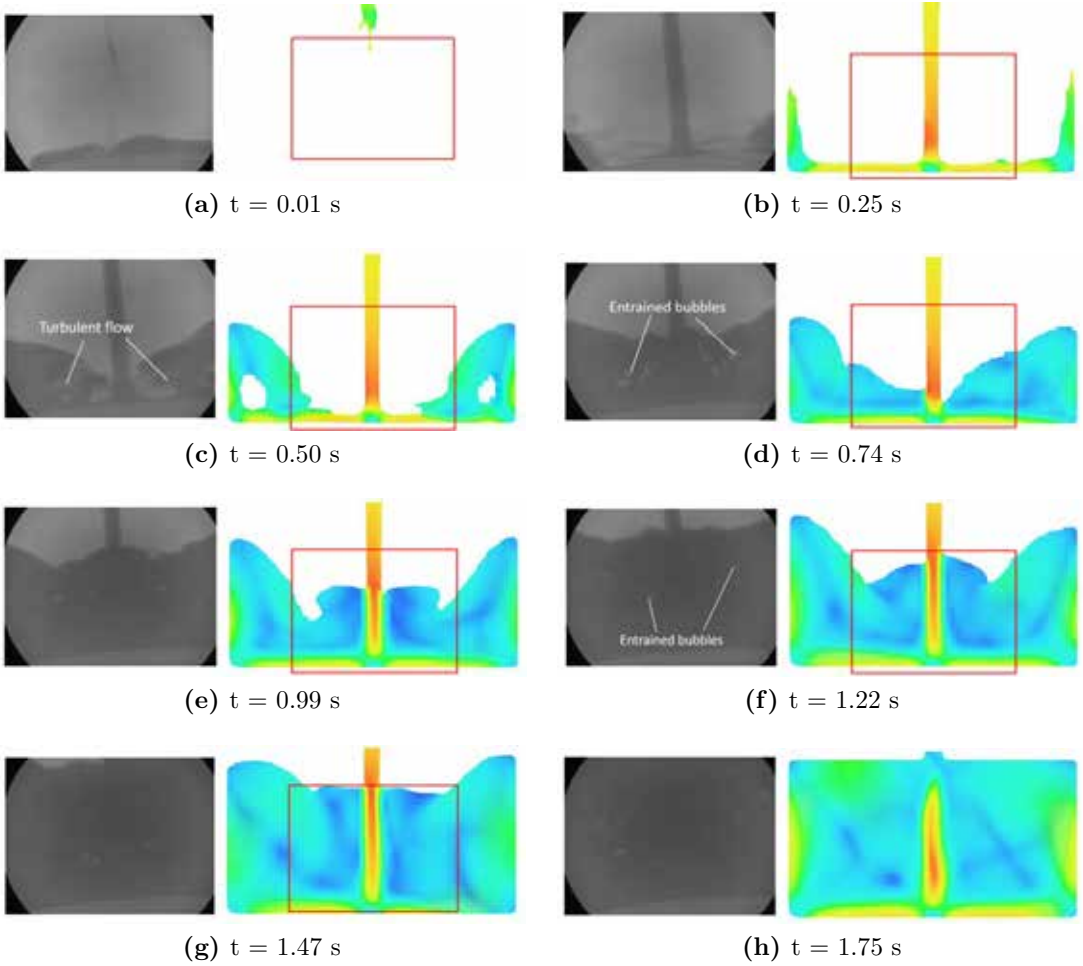

(a) t = 0.01 s **(b)** t = 0.25 s

(c) t = 0.50 s **(d)** t = 0.74 s

(e) t = 0.99 s **(f)** t = 1.22 s

(g) t = 1.47 s **(h)** t = 1.75 s

Figure 5.36: Comparison between the real time X-ray footage and *FLOW-3D* modelled filling scenario of Plunging Jet mould. Time is normalised from the fluid entering the mould cavity in simulation. (left: real-time X-ray footage; right: *FLOW-3D* modelled scenario).

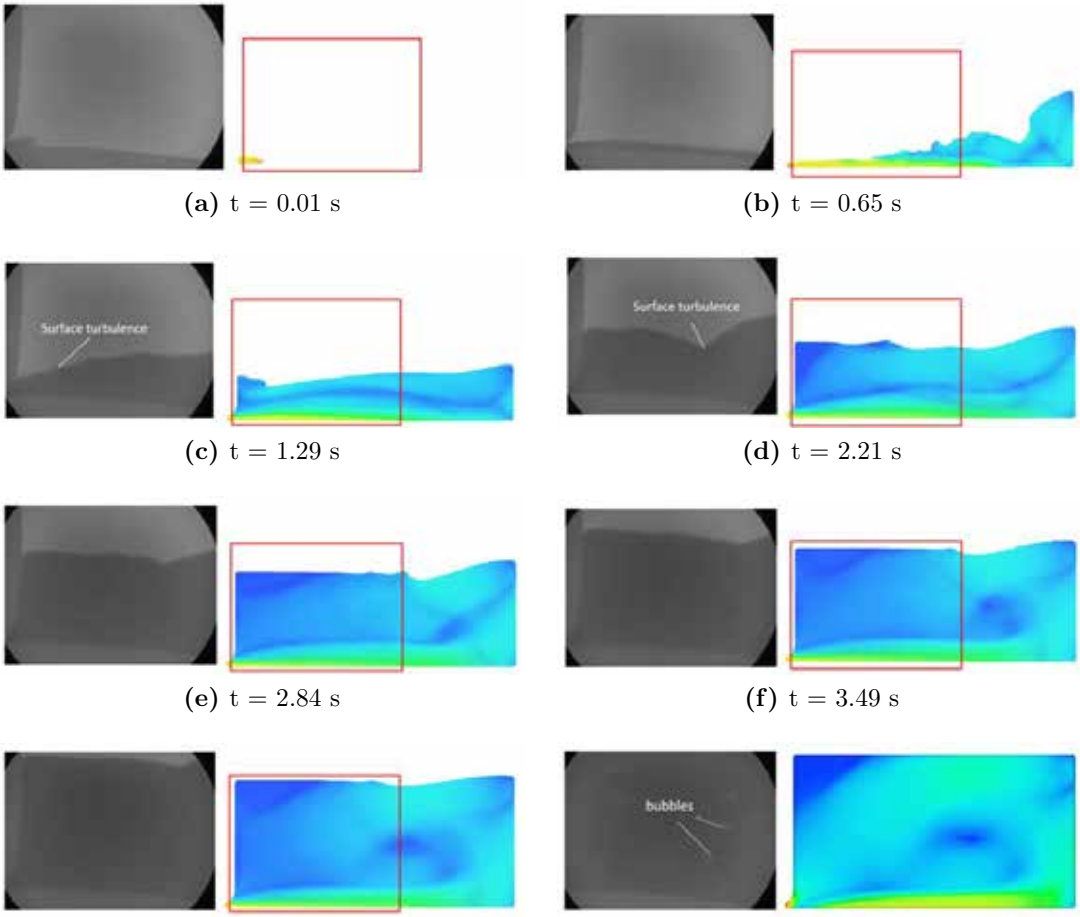

(a) t = 0.01 s **(b)** t = 0.65 s

(c) t = 1.29 s **(d)** t = 2.21 s

(e) t = 2.84 s **(f)** t = 3.49 s

(g) t = 4.13 s **(h)** t = 5.09 s

Figure 5.37: Comparison between the real time X-ray footage and *FLOW-3D* modelled filling scenario of Return Wave mould. Time is normalised from the fluid entering the mould cavity in simulation. (left: real-time X-ray footage; right: *FLOW-3D* modelled scenario).

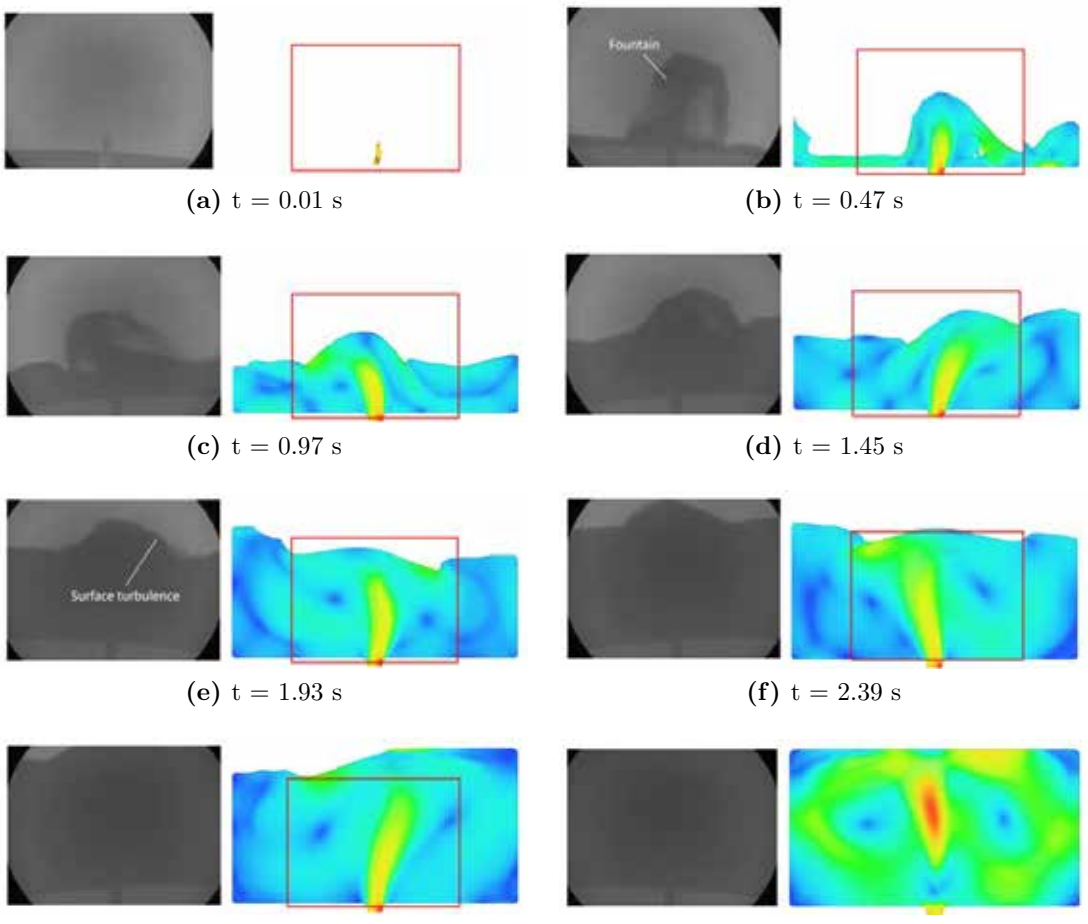

(a) t = 0.01 s **(b)** t = 0.47 s

(c) t = 0.97 s **(d)** t = 1.45 s

(e) t = 1.93 s **(f)** t = 2.39 s

(g) t = 2.87 s **(h)** t = 3.37 s

Figure 5.38: Comparison between the real time X-ray footage and *FLOW-3D* modelled filling scenario of Rising Jet mould. Time is normalised from the fluid entering the mould cavity in simulation. (left: real-time X-ray footage; right: *FLOW-3D* modelled scenario).

Some large bubbles could even be viewed clearly in the real-time X-ray frames. In the PJ mould, large amounts of gas bubbles were entrained at the impingement point as shown in Figure 5.36d, but the entrained gas bubble could not be directly simulated in the model because of the single phase nature of the *FLOW-3D* software. Instead, the model placed a great number of particles along the plunging jet, as shown in Figure 5.39a. In the RW mould, the initial fluid stream collided with the mould wall and returned back, with the incoming stream horizontally impacting on the returning back wave at the rolling point. In the RJ mould, since the velocity of the liquid in the mould exceeded the critical gate velocity [82], a fountain formed in the mould cavity and splashed on the bulk liquid, creating large areas of entrained oxide films.

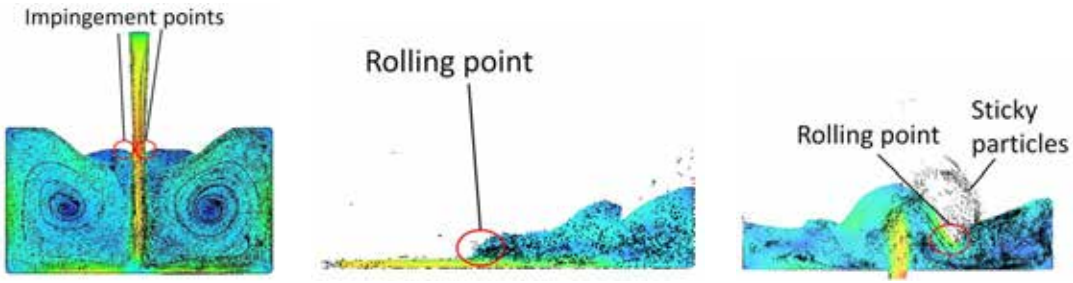

Figure 5.39: Main entraining location in the mould cavity during filling in three entrainment mechanisms. (a). Plunging Jet; (b). Return Wave; (c). Rising Jet.

In the physical experiments, the flow entered the PJ, RW and RJ moulds from different directions, but the flow bore some similarities, as the flow either horizontally or vertically impacted on the bulk liquid in these moulds. However, the varying levels or directions of impingement formed different entrainment behaviours. In the PJ mould the higher velocity of the liquid led to more gas entrained, and the gas pockets moved downwards, and took a longer time to float up. In the RW mould the jet moved horizontally and gas entrained was carried only a little way into the melt and could easily float to the surface. The velocity differences also lead to volume differences of the entrained gas, *i.e.* large gas pockets in the PJ mould, but micro-bubbles in the

RW mould. In RJ mould the collapsed jet fronts splashed onto the surface of the flow, resulting in extensive surface films being enfolded, but with less gas trapped due to the small relative velocity between the dropping splashes and the bulk liquid. The floating of bubbles left bubble trails in the castings, which might cause more damage in the PJ and RW cases, than in the RJ moulds during solidification.

In addition, the evolution of flow structures had an impact on the entrainment level. As demonstrated in Figures 5.37 and 5.38, the chaotic surface turbulence in the RJ and RW moulds was reduced dramatically when the moulds were filled gradually, but the gas was constantly entrained in PJ mould by the vertically moving impinging jet. These would also result in different amounts of entrainment defects entrained in three moulds.

5.3.2.2 Weibull Analysis of the Predicted Defects Population

Table 5.16 lists the initial model predicted defect populations in the whole length, and in the gauge length of the test bars. The number of particles in the gauge length of each bar was generally in proportion to that in the whole sample.

Table 5.16: Defects population in each sample predicted by model.

	Plunging Jet		Return Wave		Rising Jet	
ID	**Whole length**	**Gauge length**	**Whole length**	**Gauge length**	**Whole length**	**Gauge length**
1	144	36	598	250	152	53
2	196	54	280	83	162	75
3	189	34	77	18	120	61
4	129	57	78	6	19	11
5	131	51	1	0	25	9
6	133	63	10	1	36	12
7	168	71	29	3	19	5
8	162	50	9	1	38	13
9	155	73	1	0	161	18
10	225	90	8	3	33	6
11	150	58	6	0	170	10
12	233	79	2	0	185	39
13	284	66	21	11	16	4
14	223	65	28	13	86	11
15	539	140	10	0	148	13
16	280	83	38	13	51	25
17	233	76	19	7	187	55
18	249	85	16	3	144	56
19	248	111	81	40	36	17
20	242	66	31	13	252	103
21	216	74	49	4	160	80
22	418	157	128	37	79	39
23	357	119	84	34	201	55
24	221	67	130	32	293	124
25	317	107	79	26	59	26
26	412	157	179	62	314	65
27	416	103	206	99	377	132
28	160	51	171	69	264	113
29	344	120	206	68	408	59
30	305	113	166	75	806	348
Total	7479	2476	2741	971	5001	1637

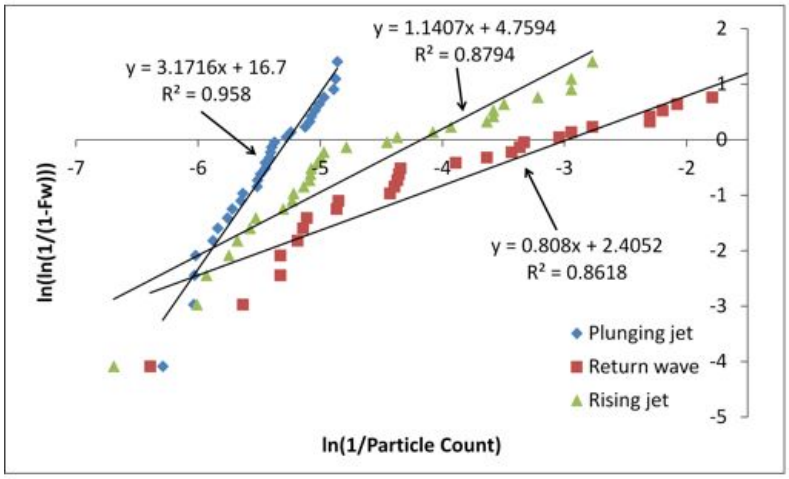

(a)

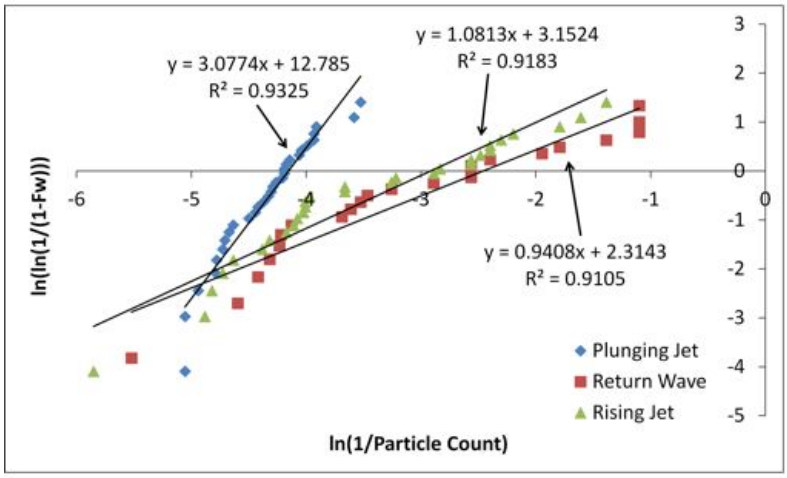

(b)

Figure 5.40: The Weibull plots of the modelling results of the three types of moulds. Model used sticky particles with a density of 2200 kg$\cdot$ m^{-3}. (a). particle count in whole length of the sample; (b). particle count in gauge length of the sample.

Based on the assumption that the strength of samples is in inverse proportion to the predicted particle counts in the sample, a Weibull analysis was conducted on the reciprocal of the particle counts in each sample from the three types of moulds. Figure 5.40 shows the Weibull plots of the reciprocal of particle counts in the three types of moulds. The general tendency of the Weibull plot, from consideration of the whole length and the gauge length of samples were similar, with the PJ samples having the highest Weibull modulus (3.1), followed by the RJ (1.1) and RW (0.8) samples,

which were opposite to that found with the bending test results. The x-intercepts of the trend lines on the figures show that the RW samples had the greatest position parameter (-3 when considering the particle counts in the whole length of the test bar), while the PJ samples had the smallest (-5.3). In Weibull analysis, a high Weibull modulus represents a low variation of data, while a low position parameter reflects low mean value. Therefore, the modelling results predicted that the PJ samples would have the most defects among the three types of moulds and suggested consistent low properties of PJ samples, compared with samples from the RW and RJ moulds, which did not directly correlate with the mechanical testing results, in which the PJ test bars had the highest variation in the strength, but not necessarily the lowest average bending strength.

5.3.2.3 Model Predicted Defects Distribution

Since the samples in the centre of the plates were affected by shrinkage porosity, the study of the strength variation of test bars from different locations only considered bars on the left and right sides of the cast plates. The definition of "left" and "right" samples is shown in Figure 5.41.

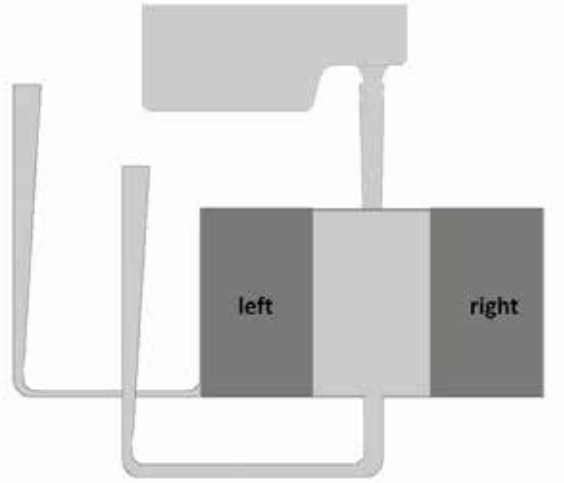

Figure 5.41: Schematic of the locations of "left" and "right"samples in the plate.

Figures 5.42 to 5.44 show comparison between the mean bending strength of sam-

ples and the normalised reciprocals of particle counts in the corresponding samples in different regions. The error bars indicate the standard deviation of bending strength of samples at that location. The missing data points in Figure 5.43 are because there was no particle trapped within the gauge length and hence, no reciprocal obtained.

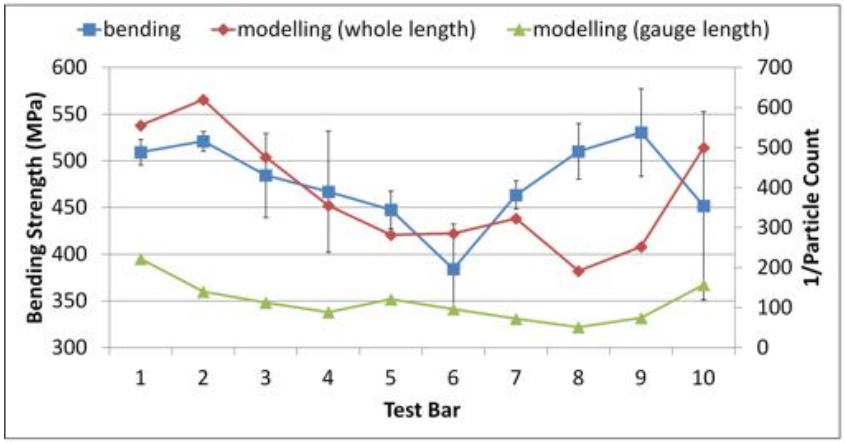

(a)

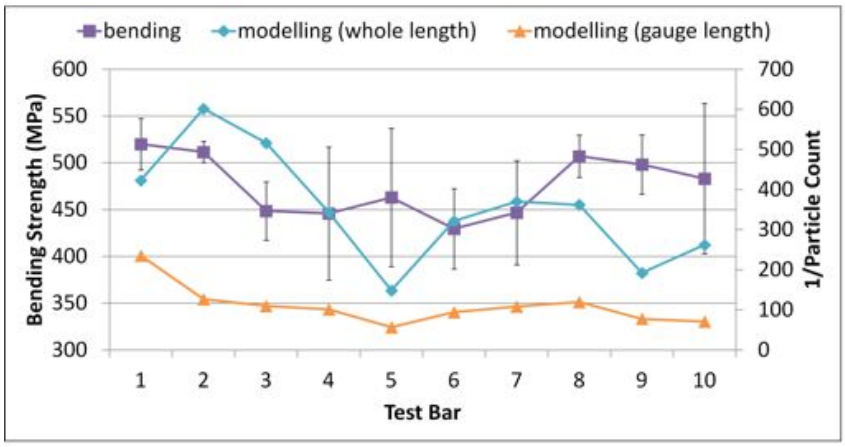

(b)

Figure 5.42: The bend strength variation of PJ sample on the two sides from top to bottom (1 to 10). Error bars indicate the standard deviation of the bend strength from three castings in each type of mould. (a). left; (b). right.

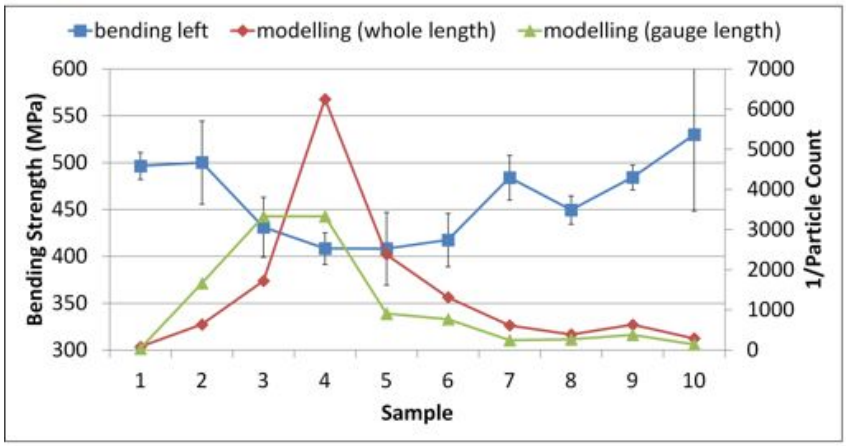

(a)

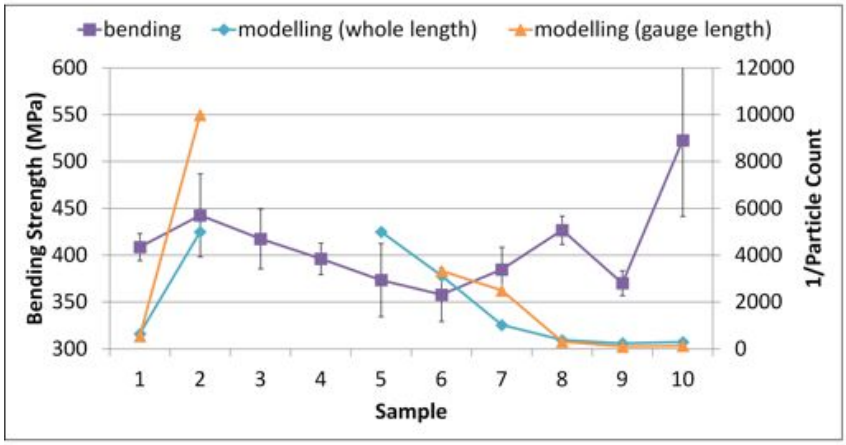

(b)

Figure 5.43: The bend strength variation of RW sample on the two sides from top to bottom (1 to 10). Error bars indicate the standard deviation of the bend strength from three castings in each type of mould. (a). left; (b). right.

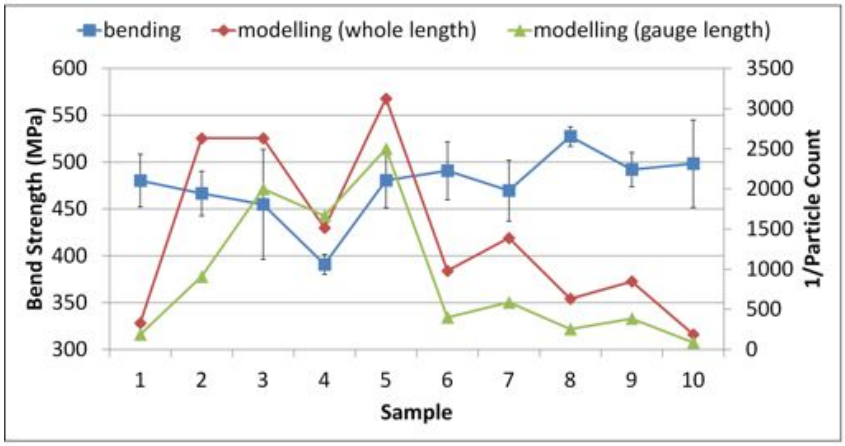

(a)

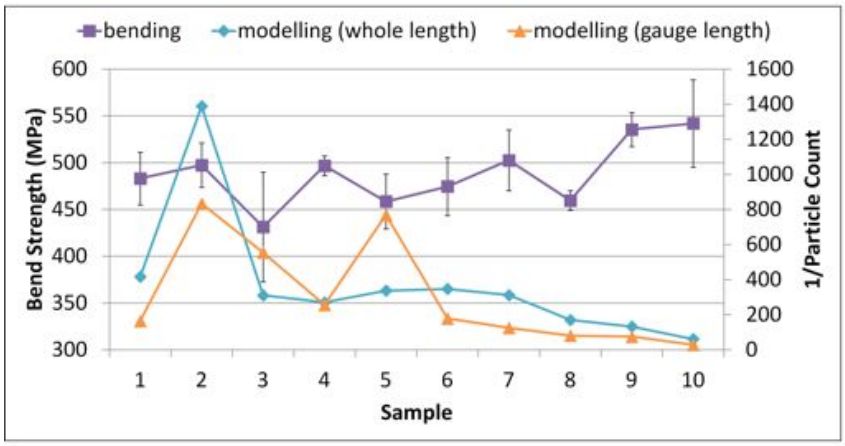

(b)

Figure 5.44: The bend strength variation of RJ sample on the two sides from top to bottom (1 to 10). Error bars indicate the standard deviation of the bend strength from three castings in each type of mould. (a). left; (b). right.

The high standard deviations of bending strength of samples indicate low reproducibility of the castings. The variation curves of the normalised reciprocals of the particles generally predicted disparate trends, irrespective of whether particle counts of the whole length or of the gauge length of samples were considered. Therefore, further experiments were conducted to improve the accuracy of the model.

5.3.2.4 Validation with Different Particle Properties

The bending strength of samples from the RJ and RW castings showed slightly better reproducibility, which was proved by the smaller standard deviation of the results compared with the test bars from the PJ mould. The RJ samples from left and right parts of the plates contained less shrinkage porosity than the RW samples, thus further validation of the particle distribution initially used the RJ data as the benchmark.

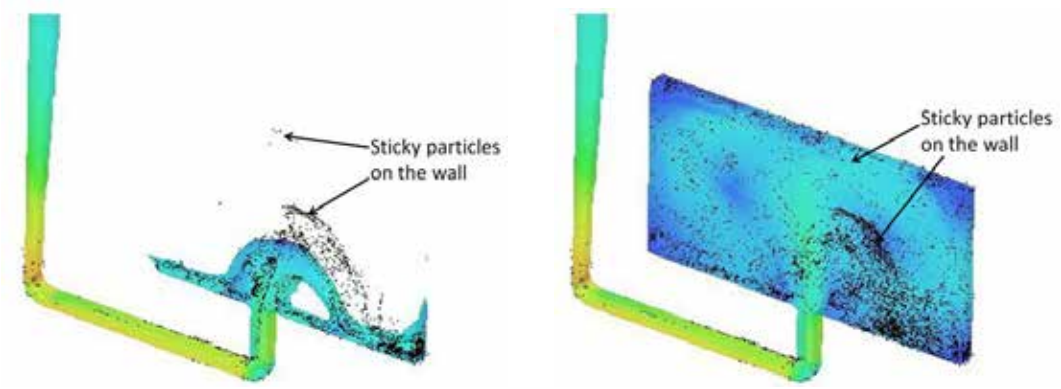

(a) t = 5.32 s **(b)** t = 8.16 s

Figure 5.45: Example of sticky particles distribution on the RJ plate during filling. The particles were displayed as black dots.

The preliminary models used sticky particles, which by default would lose all their kinetic energy when they first contacted the mould wall and stayed at the collision location. Figure 5.45 shows two profiles during filling of the RJ mould with some particles adhering on the mould wall highlighted. It can be seen that when the jet entered the mould cavity, the particles on the front that were generated in the running system adhered to the mould wall without further movement during the subsequent filling. The highly turbulent flow even splashed some liquid drops containing particles on the mould wall, resulting in the particles being stuck in the mould which had not yet been reached by the main liquid body, as shown in Figure 5.45a. The particles stuck in the bottom half of the casting, shown in Figure 5.45, led to a low strength of Samples 6 to 10 predicted by the model, as shown highlighted in the box in Figure 5.46a, which

was different from the experiments.

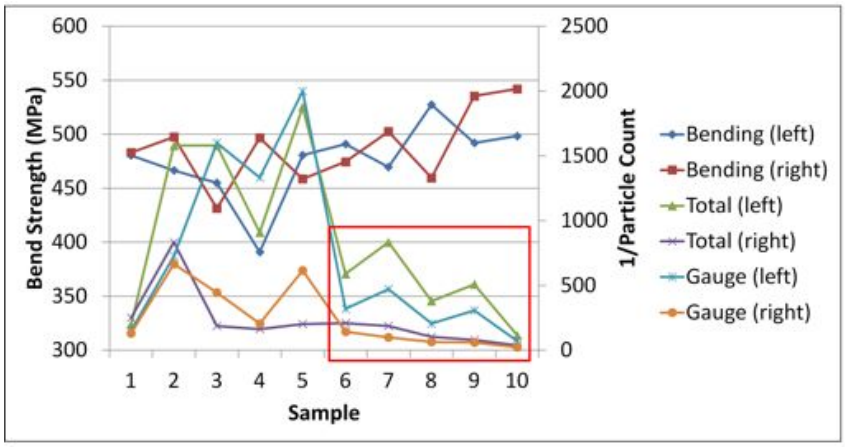

(a)

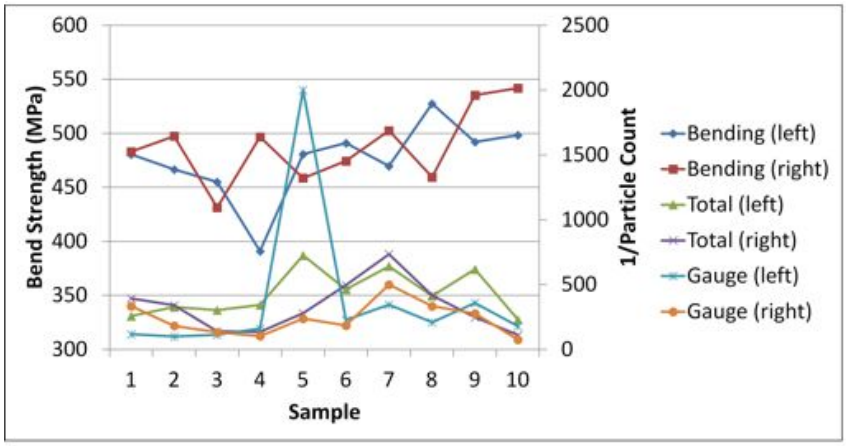

(b)

Figure 5.46: Bending strength variation vs. predicted particle count variation of RJ mould. (a). sticky particles (The box highlights the low strength of samples predicted by the model); (b). non-sticky particles.

Simulations using the same boundary conditions but with a non-sticky particle model were run to study the influence of particle stickiness on the modelling results. Figure 5.46 compares the model predicted strength variation trends of RJ samples using sticky and non-sticky particle models. It shows generally that the model using non-sticky particles had less spikes on the trend lines, was closer to the experimental trends, but still not correlated with them. Similar results obtained from the simulations of the PJ and RW models did not correlate the experimental results, either.

Since *FLOW-3D* only considers mass related properties of particles, *e.g.* density and momentum, rather than volume or shape [155,169], to increase the accuracy of the model, another trial carried out was the manipulation of the mass density of particles. The initial OFEM considered the gas phase trapped between the two layers of films and

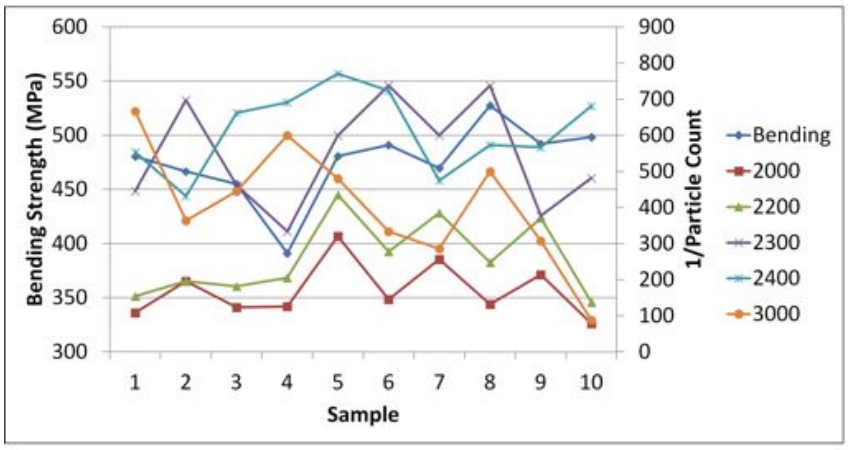

(a)

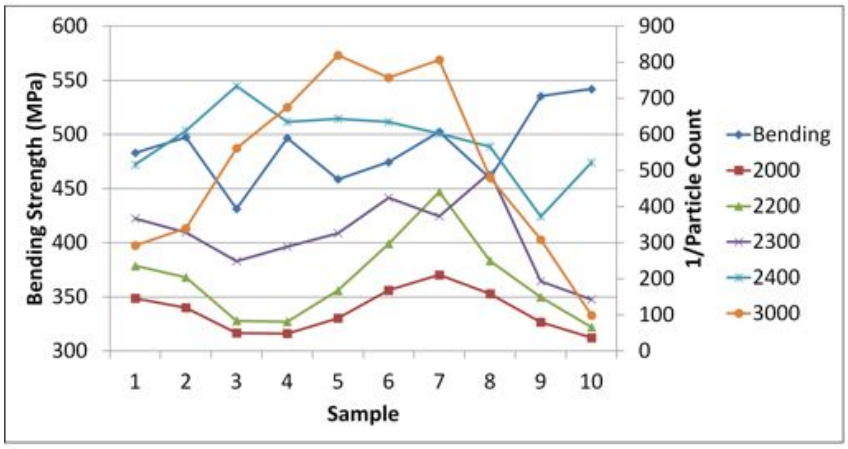

(b)

Figure 5.47: Model predicted strength variation of RJ samples with different densities of non-sticky particles. (a). left part; (b). right.

assumed the density of an entrainment defect was 2200 kg$\cdot$ m^{-3}, close to that of liquid aluminium alloy, but lighter than an oxide, where densities would be in a range of 2660 to 3970 kg$\cdot$ m^{-3} [170]. This simplified assumption ignored the size of the defects and the amount of gas trapped, owing to the limitation of the *FLOW-3D* particle model and lack of experimental evidence. The validation inherited the assumption that the

defects were lighter than the liquid alloy. Four different densities of particles were used to test the effect of particle density on the modelling results.

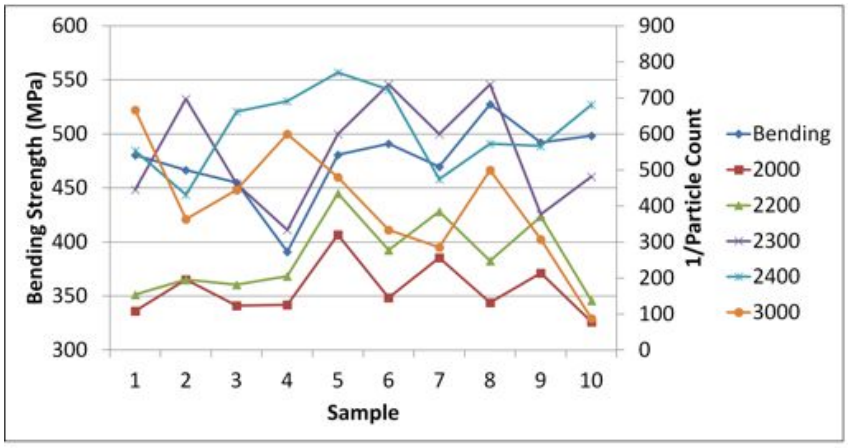

(a)

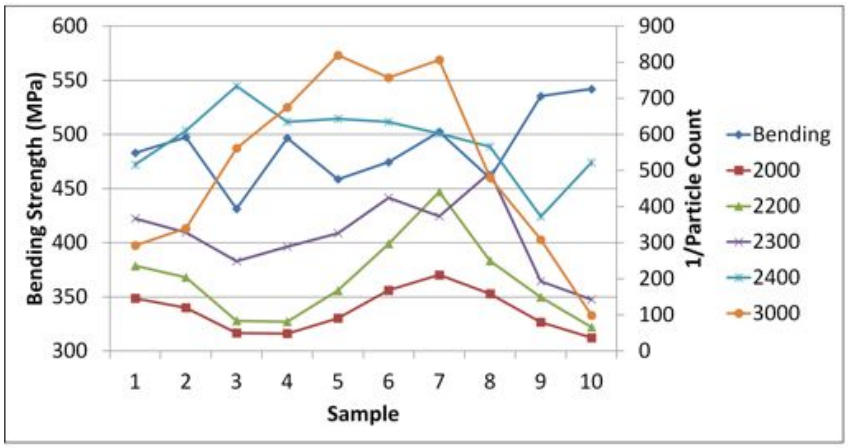

(b)

Figure 5.48: Model predicted strength variation of RJ samples with different densities of non-sticky particles. (a). left part; (b). right.

Figure 5.48 shows a comparison between the bending strength variation trends and different non-sticky particle distribution trends predicted by the model. The reciprocal of particle counts were normalised for easier viewing of the general trends. Clearly, density variations affected the distribution of particles in the casting, and the distributions of lighter particles (compared to the liquid alloy) bore some similarity as they had the spikes in the graph at similar positions. However, as the density increased, the spikes on the reciprocal curves moved toward the left side on the figure, which

meant the defects tended to concentrate at the lower part of the casting plate under the gravity. Significant changes were found when the densities of particles were tuned to 2400 kg$\cdot$ m^{-3}, as the spikes on this trend were in distinct locations compared with the other three lower densities. The amplitude of variation of the curves showing the 2400 kg$\cdot$ m^{-3} density results, was in the same scale as that of the bending strength curves. The 3000 kg$\cdot$ m^{-3} curve indicated much lower strengths of samples at the bottom half of the cast plate, which was different to the experiments, and hence, it is believed that a particle model with higher density than the liquid density would have lower accuracy.

Since the curves of the three low densities models (2000, 2200, 2300 kg$\cdot$ m^{-3}) had similar variation tendency, Figure 5.49 compares the Weibull plots of the particles with 2200 kg$\cdot$ m^{-3} and 2400 kg$\cdot$ m^{-3} densities, to study the validity of the model. The Weibull plots of the particle counts only within in the gauge length were alike. Results showed that the Weibull moduli of the samples from the three moulds were quite close. The ranking of moduli of particles with a density of 2200 kg$\cdot$ m^{-3} was PJ (6.7)>RJ (5.6)>RW (5.1), opposite to the experiment results. On the other hand, the ranking of moduli of particles with a density of 2400 kg$\cdot$ m^{-3} was RW (9.0)>RJ (7.4)>PJ (4.0), the same as that in the experimental results. The low moduli also agreed with the experimental results, which were less than 10 as shown in Figure 5.29. The results suggest particles with the density of 2400 kg$\cdot$ m^{-3} gave better description of defects distribution in the casting plates. The effects of particle density is discussed in Section 6.3.4.

5.3.2.5 Validation with Old Oxide Films

The predicted old oxide film distribution in the whole samples and within the gauge length of samples showed similar trends. Figure 5.50 compared the bending strength variation of samples with normalised old oxide film defect counts and the sum of both young and old oxide film defects in the whole length of the RJ samples. Generally, the

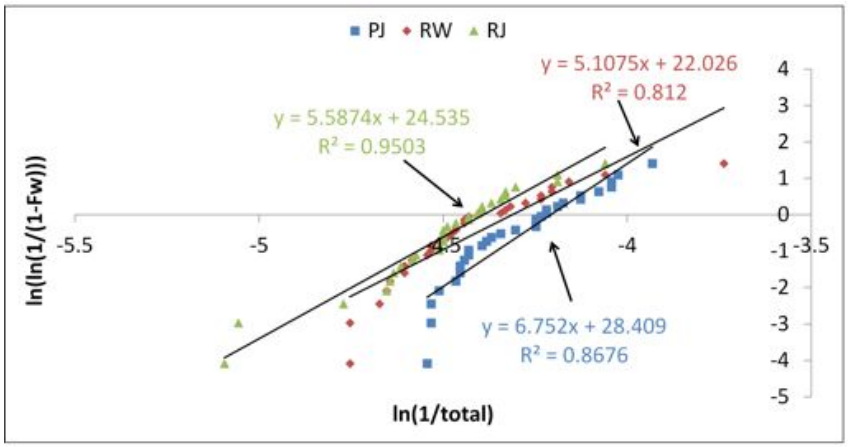

(a)

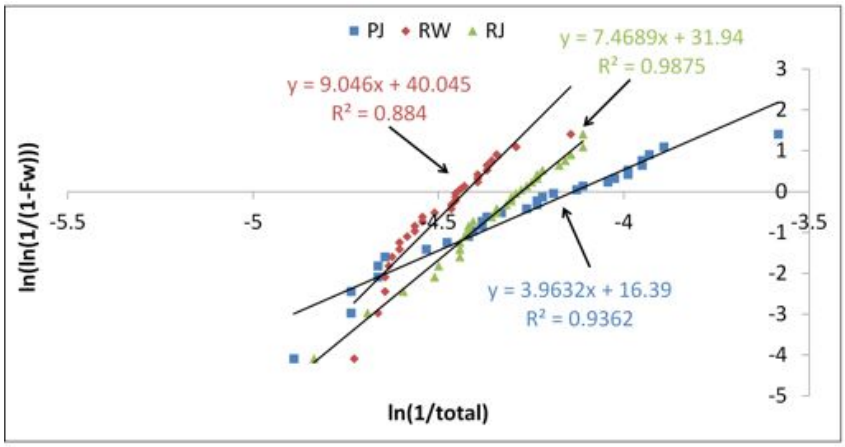

(b)

Figure 5.49: The Weibull plot of particle counts in the whole length of samples from the three types of moulds. Model used non-sticky particles. (a). particle density=2200 kg$\cdot$ m^{-3}; (b). particle density = 2400 kg$\cdot$ m^{-3}.

old film defects were distributed evenly in the plate, compared with previous modelling results. This was, possibly, because the old oxide films entered the mould at early stage of filling and therefore, were scattered uniformly by the fluid flow in the cast plate. Only slight variations in the particle counts in samples observed at different locations at both left and right parts of plate. The magnitude of variation of the particle counts was similar to that of the bending strength, but the trends still did not agree with the experimental results. This result was found in the PJ and RW models, also.

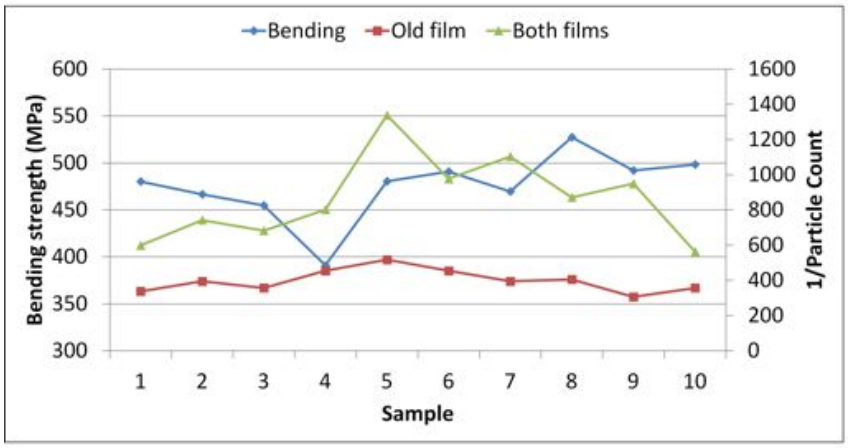

(a)

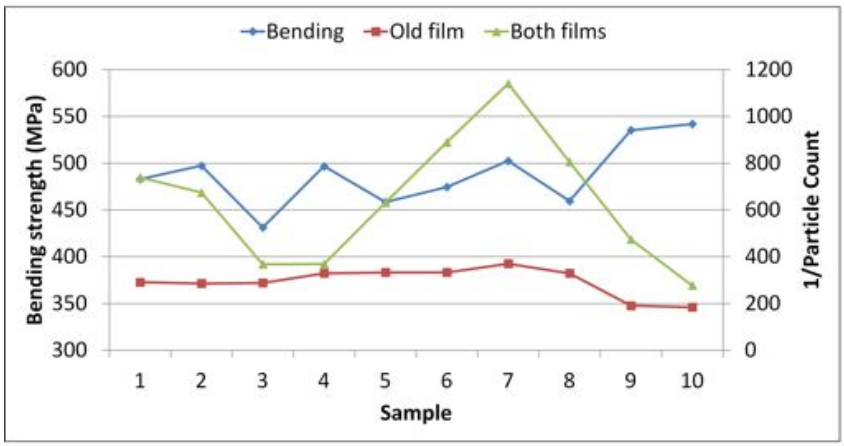

(b)

Figure 5.50: Comparison of variation trends between bending strength and model predicted old and young oxide film distribution in the whole length of RJ samples. (a). left part; (b). right part.

Modelling results also showed that the distribution of the combination of the old and young oxide films in these models was mainly determined by the young films, as the variation trends of the combination of both films shown in Figure 5.50 were similar to that of young oxide films shown in Figure 5.48. A possible reason was that the total quantity of old films was only about one third of the number of the young films, and the old oxide film defects were distributed relatively evenly in the plate, and hence, the total number of defects was increased, but the overall distribution trends of defects did not change. The modelling of old oxide film provided a solution to consider the

effects of the defects formed in the crucible during alloy preparation. With a carefully defined initial quantity of defects, the model may give more information about the defect distribution in solidified castings.

5.3.2.6 Final Validation of Three Entrainment Mechanisms

Figure 5.51 shows the Weibull plot of the final validation results. The ranking of the Weibull moduli of the samples from the three types of moulds was RJ (7.3)>RW (4.9)>PJ (2.8), which was different from the experimental results. However, the model predicted that the reliability of the PJ samples was lower than the other two, which agreed with the experiments. Figure 5.52 compares the bending strength variations of samples and the normalised particle counts variation of the three entrainment mechanisms, but still no correlation was found from these results.

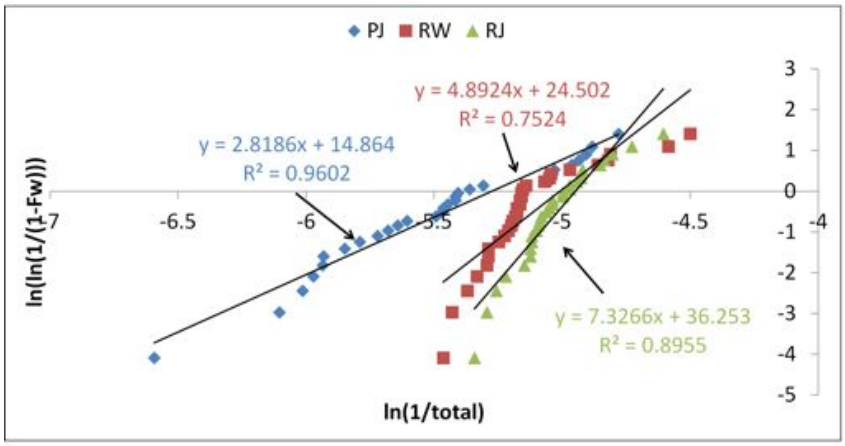

Figure 5.51: Weibull plot of final validation data of three entrainment mechanisms.

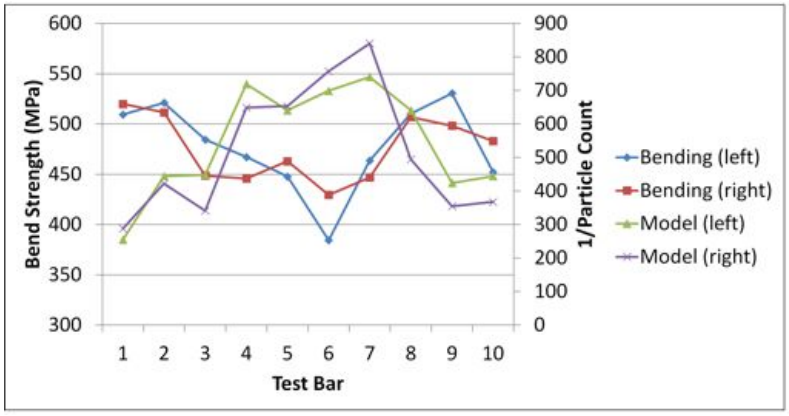

(a)

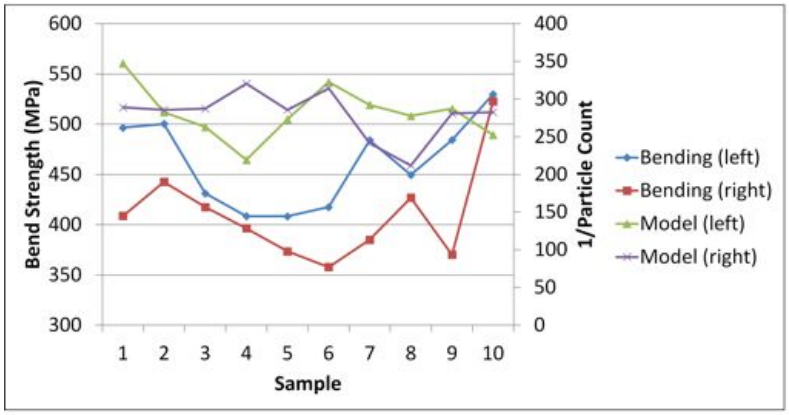

(b)

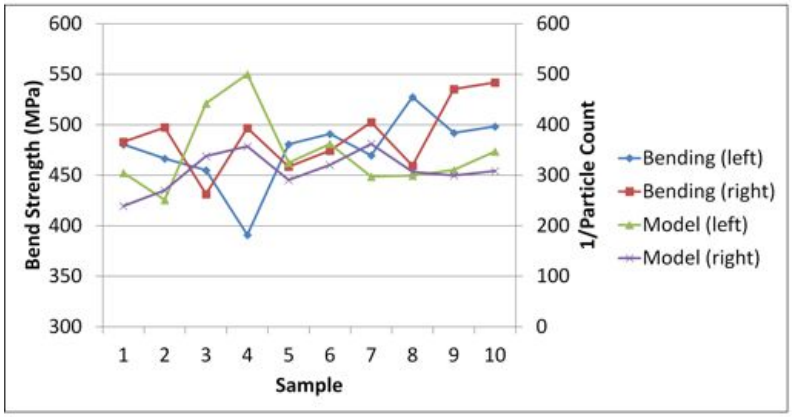

(c)

Figure 5.52: Comparison of variation trends between bending strength and model predicted particle distribution in the whole length of samples from three models. Both young and old oxide films were considered. (a). PJ; (b). RW; (c). RJ.

5.4 Synchrotron X-ray Characterisation of Entrainment Defects

Samples containing entrainment defects were prepared and scanned by synchrotron X-ray tomography in solid and fully liquid states. The three dimensional morphology of entrainment defects were reconstructed and the time dependent morphological changes of the defects were investigated.

5.4.1 Entrainment Defect Classification

Generally the entrainment defects observed in the solidified samples can be classified into three types according to their morphology. They were: *a*). entrained pores, *b*). closed cracks and *c*). tangled double oxide films. Figure 5.53 shows some typical 2D views of these defects. The entrained pores found in the experiment were usually larger than the other two types in both size and volume. They had nearly round shapes, trapping a pocket of gas inside the void. The closed cracks were much more angular voids, appearing as long and narrow shapes in some sections. The tangled double oxide films had very complex geometries, and sometimes would be seen as discontinuous pores or cracks in polished sections in the castings.

Figure 5.54 compares the 2D views of the defects on the cross sections with their 3D morphology, and shows that even an angular crack might have relatively complex shape in 3D. Its relatively flat morphology in the casting was actually folded two disconnected layers, which could easily result in stress concentration and provide sites for crack propagation. The tangled oxide films had very complex geometry with branches shown on the 2D views. Their 3D views were difficult to observe directly. They are shown as an object with irregular shape in an axonometric view, since different branches of the defects sheltered each other. All three types of entrainment defects existed as voids and might contain different amounts of gases depending on their morphology.

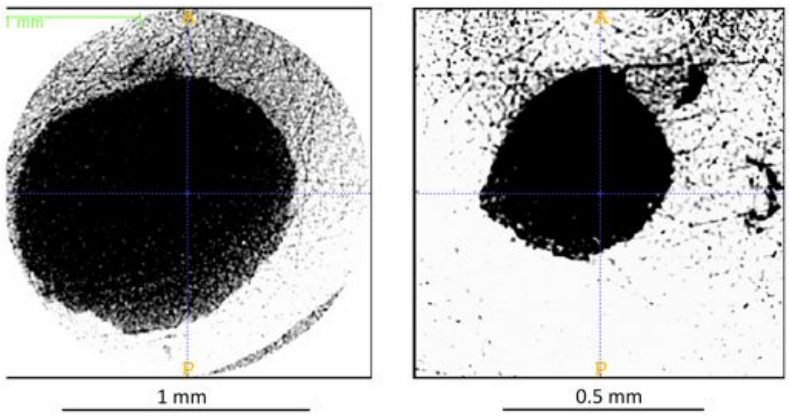

(a)

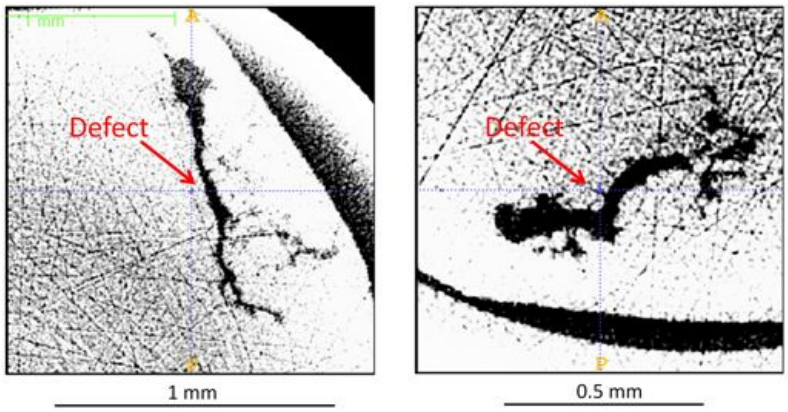

(b)

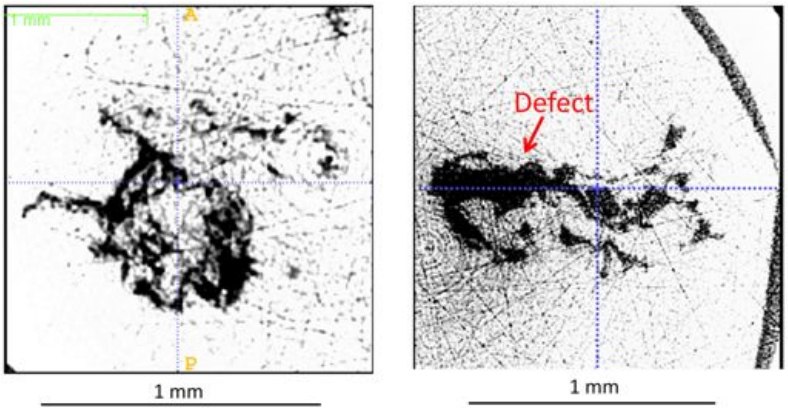

(c)

Figure 5.53: Examples of three types of entrainment defects in solidified castings. (2D view in cross section) (a). entrained pores; (b). closed cracks; (c). tangled double films.

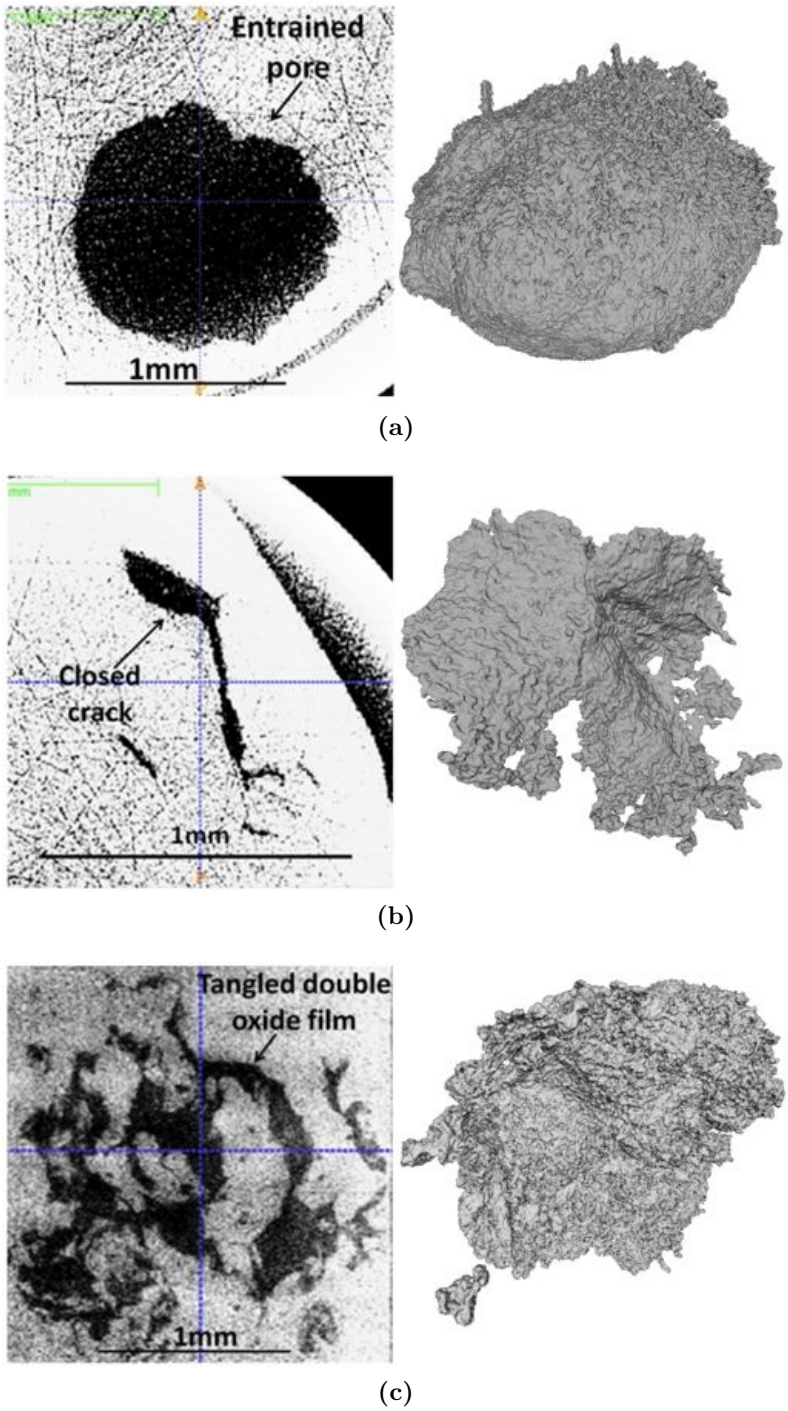

Figure 5.54: Examples of three types of entrainment defects and their 3D morphology. (a). entrained pore; (b). closed crack; (c). tangled double film.

It should be noted that the shrinkage porosity observed in the solid samples sometimes had similar morphology to entrainment defects, and was also shown as irregular voids on the 2D images. Figure 5.55 shows an example of shrinkage porosity in the casting (with a dendrite pointed out). But most of the dendrites of the alloy formed during solidification could not be viewed clearly, since the growth directions of the dendrites might not be parallel to the projection of the scanning profile, resulting in different patterns from the typical dendrites on the 2D views. However, shrinkage porosity could be differentiated from entrainment defects, as the voids caused by shrinkage porosity would disappear when the casting remelted, but the voids caused by entrainment defects could maintain their general geometry during holding in the liquid state.

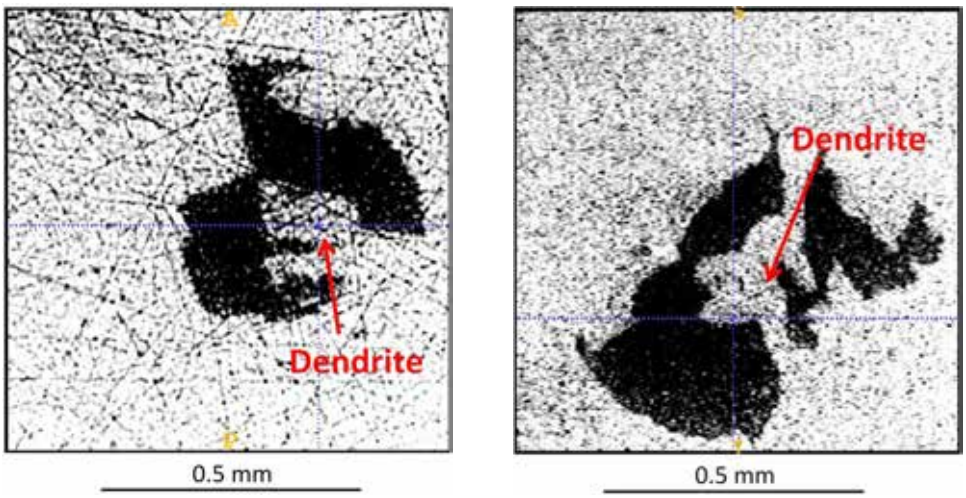

Figure 5.55: An example of shrinkage porosity in solidified casting. The primary dendrite is pointed out. (a). 2D view on cross section; (b). 2D view on projection.

5.4.2 Evolution of Entrainment Defects

5.4.2.1 Modelling of the Heating Profile

Modelling of the heating profiles considered three different heating rates, 10 $K \cdot s^{-1}$ (the experimental condition in PSI), 4 $K \cdot s^{-1}$ and 40 $K \cdot s^{-1}$, to demonstrate and understand

the convection in the sample during heating and its potential effect on the evolution of entrainment defects. Figures 5.56 through to 5.58 show modelled temperature fields and convection velocities of fluid in a two-dimensional cross section with heating rates of 10 $K \cdot s^{-1}$, 4 $K \cdot s^{-1}$ and 40 $K \cdot s^{-1}$ respectively. The colour scales show the temperature gradient in the sample. The results showed that the heating rate of the laser affected both the temperature gradient within the sample and the convection of the melt.

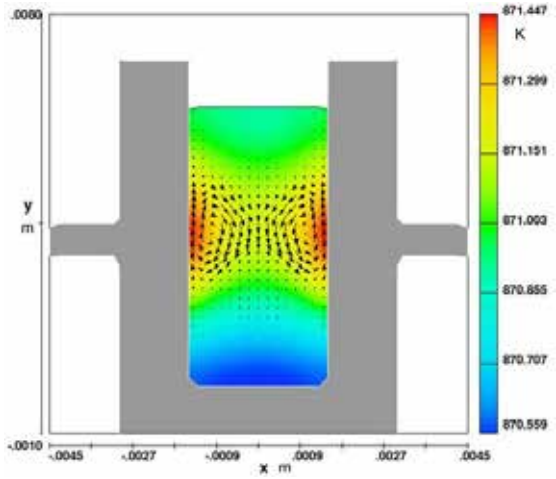

(a)

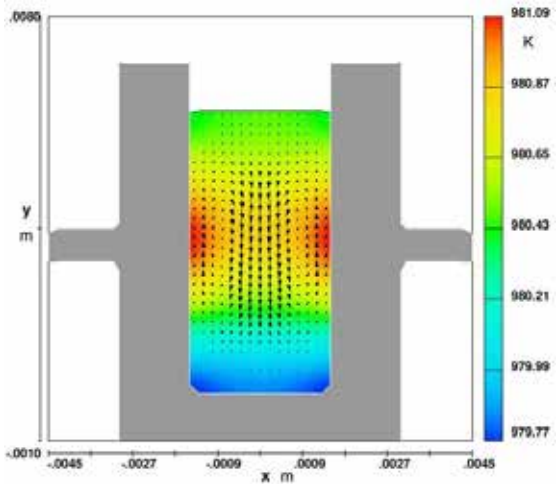

(b)

Figure 5.56: The temperature field and velocity magnitude in the sample during heating in a 10 $K \cdot s^{-1}$ heating rate. (a). During melting. Convection started from the centre part of the sample that fully melted. Maximum velocity magnitude is 22.7 μm/s; (b). In full liquid state. Arrows show the velocity direction and magnitude. Maximum velocity magnitude is 13.2 μm/s.

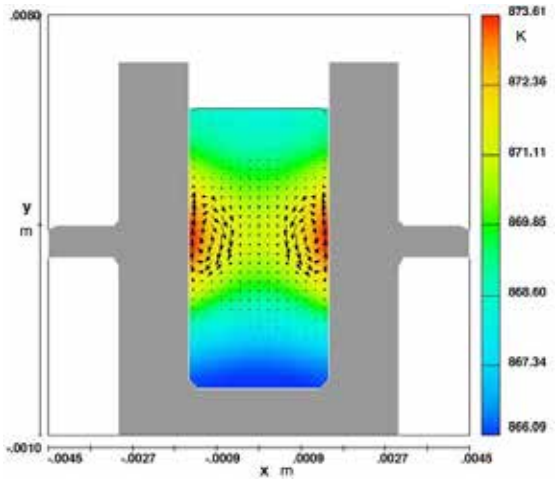

(a)

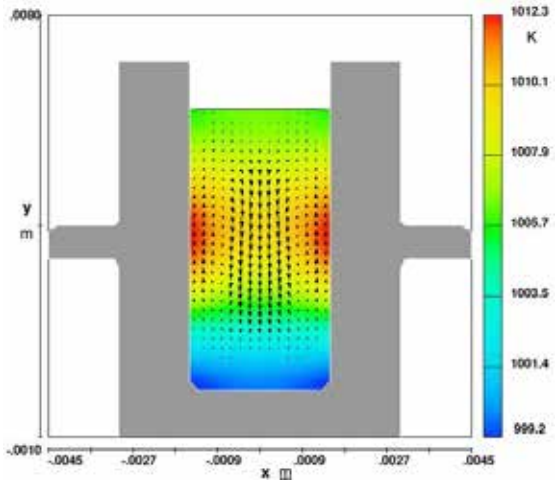

(b)

Figure 5.57: The temperature field and velocity magnitude in the sample during heating in a 4 $K \cdot s^{-1}$ heating rate. (a). During melting. Convection started from the centre part of the sample that fully melted. Maximum velocity magnitude is 22.7 μm/s; (b). In full liquid state. Arrows show the velocity direction and magnitude. Maximum velocity magnitude is 10.4 μm/s.

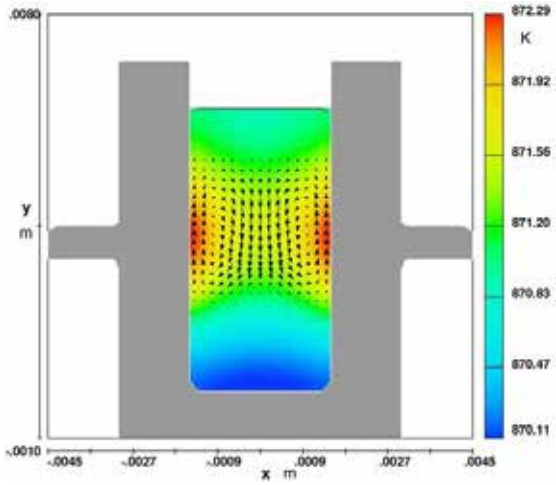

(a)

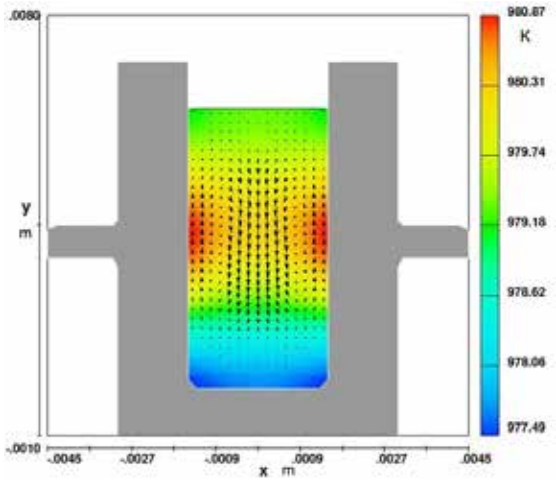

(b)

Figure 5.58: The temperature field and velocity magnitude in the sample during heating in a 40 $\mathrm{K}\cdot\mathrm{s}^{-1}$ heating rate. (a). During melting. Convection started from the centre part of the sample that fully melted. Maximum velocity magnitude is 167 μm/s; (b). In full liquid state. Arrows show the velocity direction and magnitude. Maximum velocity magnitude is 53.9 μm/s.

The temperature field distribution within samples with different heating rates had similar patterns. The temperature of the sample in the area that contacted directly with the heating source was the highest, and decreased around that area. The free surface of the liquid had the lowest temperature as it was in contact with the surrounding atmosphere. A high heating rate caused a greater temperature gradient in the sample. For example, the temperature variation in the sample heated at 4 $K \cdot s^{-1}$ was approximately 1 K, while the temperature variation in a sample heated at 40 $K \cdot s^{-1}$ was 7 K or even higher.

All the figures showed similar convection behaviour during heating. When the sample was heated above the solidus temperature, the convection of fluid started from the regions that melted first, *i.e.* the centre part near the heat source. When the sample was fully melted, two convection cells (in 2D section) formed inside the sample. Figure 5.59 uses white markers in the liquid to demonstrate the movement of the fluid during convection. As Figure 5.59b shows, the high temperature liquid near the contact surface flowed upward, and the liquid in the middle sank due to their density differences. The slower flotation speed of the liquid near the vessel wall was because of the drag force applied on the boundary layer of the fluid by the vessel wall.

The velocity magnitude of the convection was of the order of tens to hundreds of $\mu m \cdot s^{-1}$ and was associated with the heating rate. A higher heating rate resulted in a higher convection velocity. For instance, the convection velocity of the liquid in the fully liquid state with 40 $K \cdot s^{-1}$ heating rate could reach 53.9 $\mu m \cdot s^{-1}$. The highest convection velocity of each model was achieved when the centre part of the liquid was at approximately 872 K, *i.e.* the temperature at which the sample reached the critical solid fraction of the alloy defined by the model and started to melt, then the velocity decreased slightly and maintained a constant speed when a steady temperature field formed in the sample.

Figure 5.60 shows the results from the heating rate of 10 $K \cdot s^{-1}$ with consideration

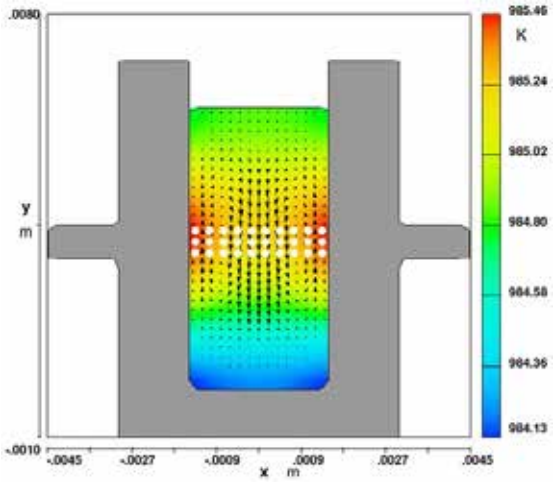

(a)

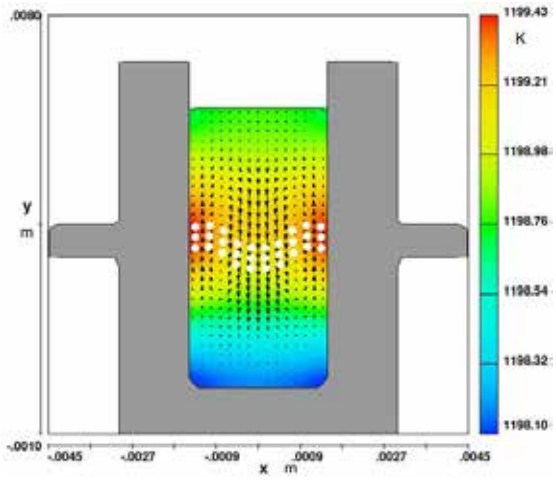

(b)

Figure 5.59: The movement of small parcels of liquid in samples, demonstrated by white markers. (a). Initial location of white markers. Maximum velocity magnitude is 8.20 μm/s; (b). Location of white markers after 50 s. Maximum velocity magnitude is 8.21 μm/s.

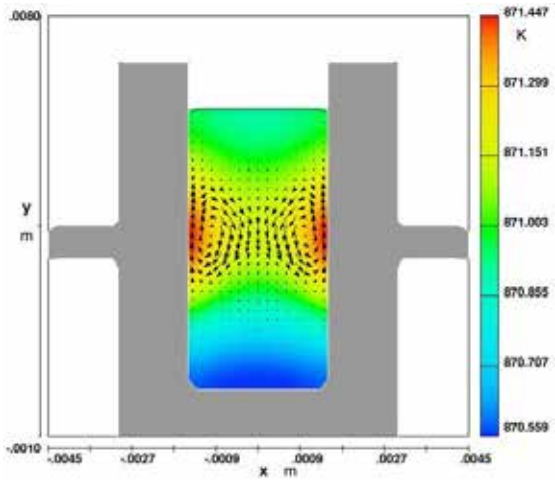

(a)

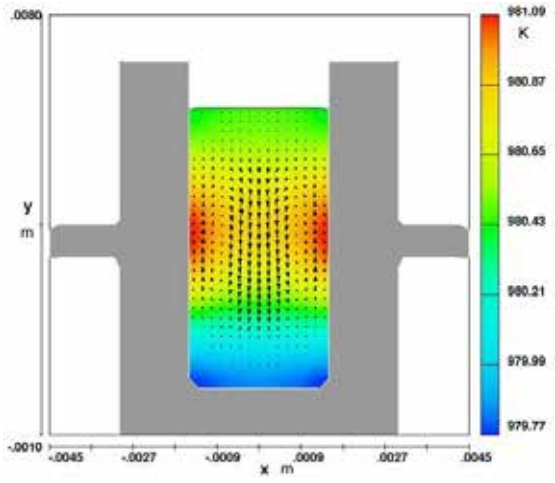

(b)

Figure 5.60: The temperature field and velocity magnitude in the sample during heating in a 10 $K \cdot s^{-1}$ heating rate. The surface roughness of the vessel was considered. (a). During melting. Convection started from the centre part of the sample that fully melted. Maximum velocity magnitude is 27 $\mu m \cdot s^{-1}$; (b). In full liquid state. Arrows show the velocity direction and magnitude. Maximum velocity magnitude is 8.9 $\mu m \cdot s^{-1}$.

of surface roughness of the vessel and demonstrated a significant decrease in the speed of liquid movement, since a rough surface would add extra drag force on the boundary layer of the liquid and reduce the speed of the movement. Comparing with the results in Figure 5.56b, the maximum velocity magnitude shown in Figure 5.60b decreased 30%, from 13.2 μm$\cdot$ s^{-1} to 8.9 μm$\cdot$ s^{-1}.

The temperature gradient in the sample during heating was related to the thermal conductivity and diffusivity of the materials. Since the model did not consider the temperature dependant variation of these two properties of materials, and only a constant heat flux was applied at the boundary, the absolute value of the temperature in the model might not be accurate, but the model illustrated the general temperature field in the sample. The model showed at the 10 K$\cdot$ s^{-1} heating rate, the temperature gradient in the sample was about 2 K across the sample, which correlated the experimental observation at PSI [158]. The small temperature gradient should have little effect on the thermal properties of our samples and should not change the geometries of the defects in the experimental at PSI.

In fluid dynamics, the Rayleigh number is used to determine the major heat transfer modes in the liquid, *i.e.* by conduction or by convection [171]. The Rayleigh number of the liquid sample in the experimental condition was 8.12, much smaller than the critical value for convection, which is 60. In this condition, heat transfer was primarily in the form of conduction and convection was weak in the sample, which was also demonstrated by the calculated velocity magnitude of the flow in the models. In reality, due to surface tension and surface roughness of the vessel, the convection velocity would be even smaller. Since in the experiment performed in TOMCAT, each scan was completed within 1 s, and during the scanning time the convection inside the sample should have negligible impact on the sharpness of the image. Besides, due to the viscosity of the liquid and the strength of the defects themselves, the weak convection had little impact on the morphology of the entrainment defects during holding in the

liquid state. This implied that the main driving force for the morphological evolution of entrainment defects was not the thermal related flow conditions in the sample.

5.4.2.2 Morphological Evolution of Entrainment Defects

The morphological evolution of entrainment defects observed in the experiment presented several different modes. In general, when the samples were melted, the defects contracted, changing in both shape and volume. Observation then showed that evolution of their morphology followed two separate routes: one with little change during holding in the liquid state, or one with contraction or expansion with time in the melt. During subsequent solidification the defects expanded slightly, probably due to solidification contraction. The volume and shape of the defects did not return to their initial state when the samples solidified.

Figures 5.61 and 5.62 show the morphological evolution of two entrained bubbles. Both bubbles underwent similar shape changes as they started as large pores, then collapsed and changed to irregular porosity in the images. Figure 5.62b was obtained at 560°C, slightly above the solidus temperature of A356 alloy. This demonstrated the morphological change that started when the sample started to melt. The initial pores might contain a mixed atmosphere of entrained gas (air) and hydrogen which diffused into the pore during solidification from the surrounding alloy. Therefore, when the sample was melted, the hydrogen would diffuse back into the melt while the entrained gas phase, which might be oxygen and/or nitrogen, would react with the melt and be consumed, resulting in a reduction of the volume of the defects. The remaining nitrogen may have started to react with liquid aluminium at a later stage and needed longer time than the scanning time to be consumed completely, as suggested by Griffiths and Raiszadeh [38], and hence a small portion of gas remained in the porosity in the figures.

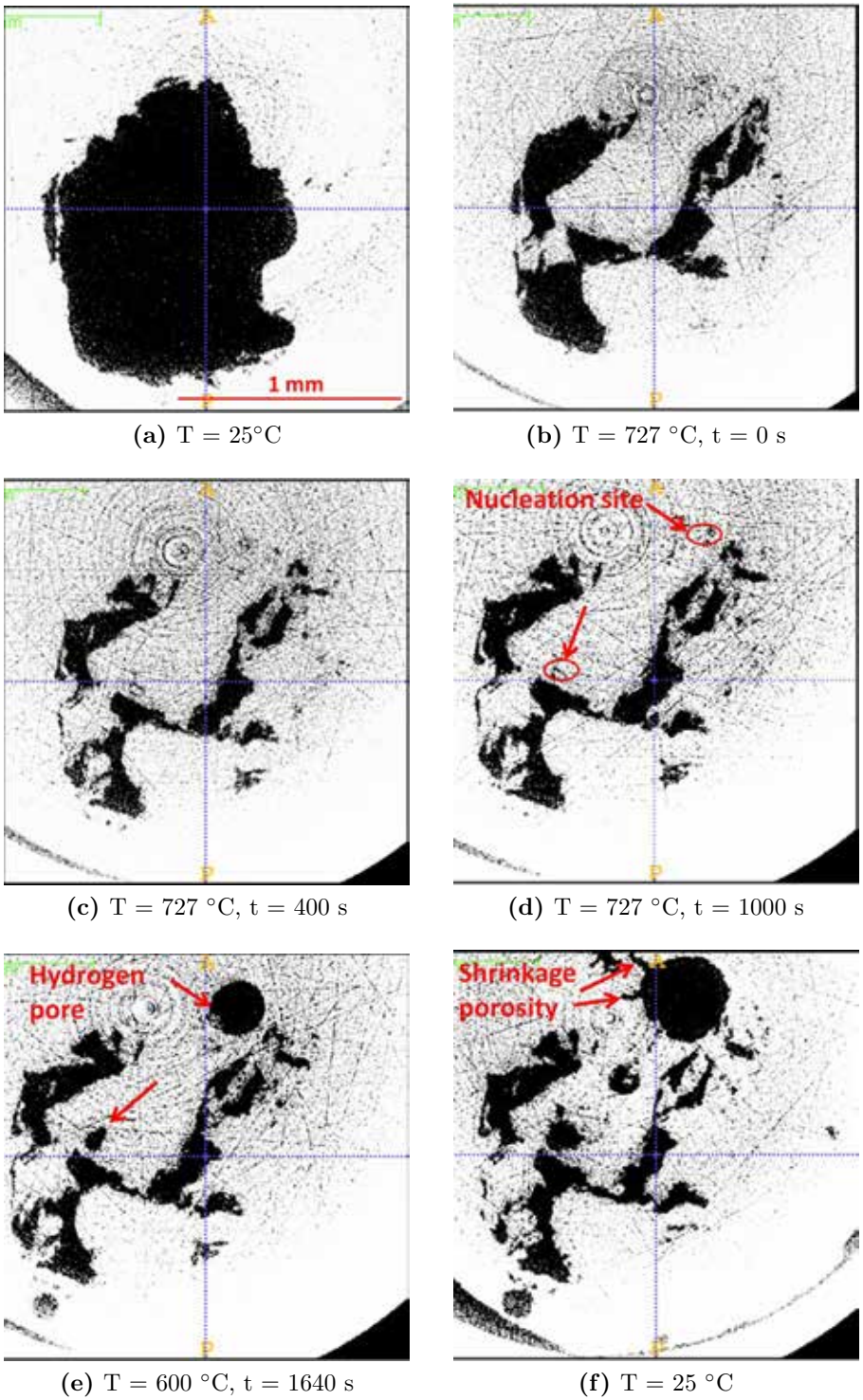

(a) T = 25°C

(b) T = 727 °C, t = 0 s

(c) T = 727 °C, t = 400 s

(d) T = 727 °C, t = 1000 s

(e) T = 600 °C, t = 1640 s

(f) T = 25 °C

Figure 5.61: Morphological evolution of an entrained pore (ID:4C1). The time, t, was measured from the time the sample temperature reached 727 °C.

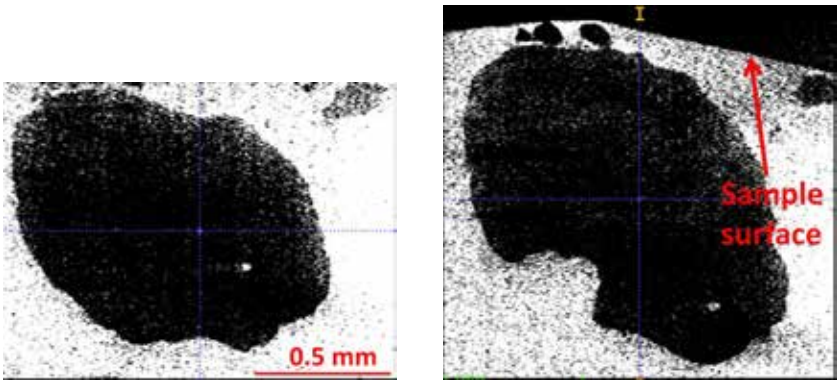

(a) T = 25 °C **(b)** T = 560 °C

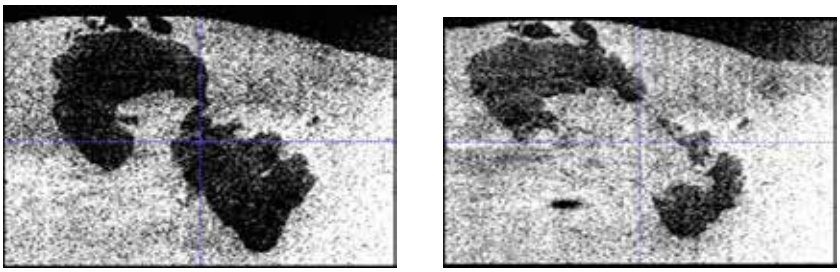

(c) T = 727 °C, t = 200 s **(d)** T = 727 °C, t = 800 s

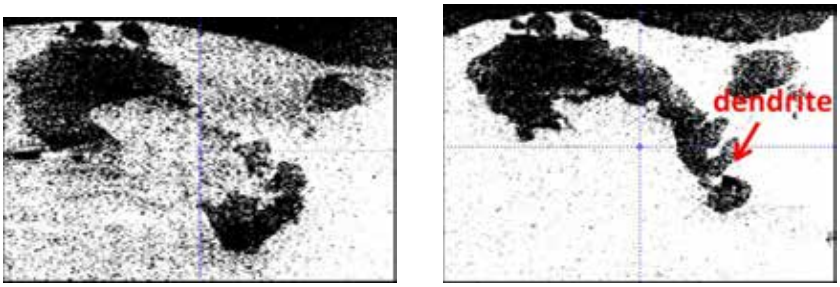

(e) T = 727 °C, t = 1400 s **(f)** T = 25 °C

Figure 5.62: Morphological evolution of an entrained pore(ID:6C1). The time, t, was measured from the time the sample temperature reached 727 °C.

Figure 5.63 shows the morphological change of a closed crack. Compared with the bubbles the crack was smaller in volume and consequently contained less gas, therefore, both the reaction between the remaining gas and the melt and the hydrogen exchange between the void and the liquid alloy were weak, and led to limited shape and size changes of this defect.

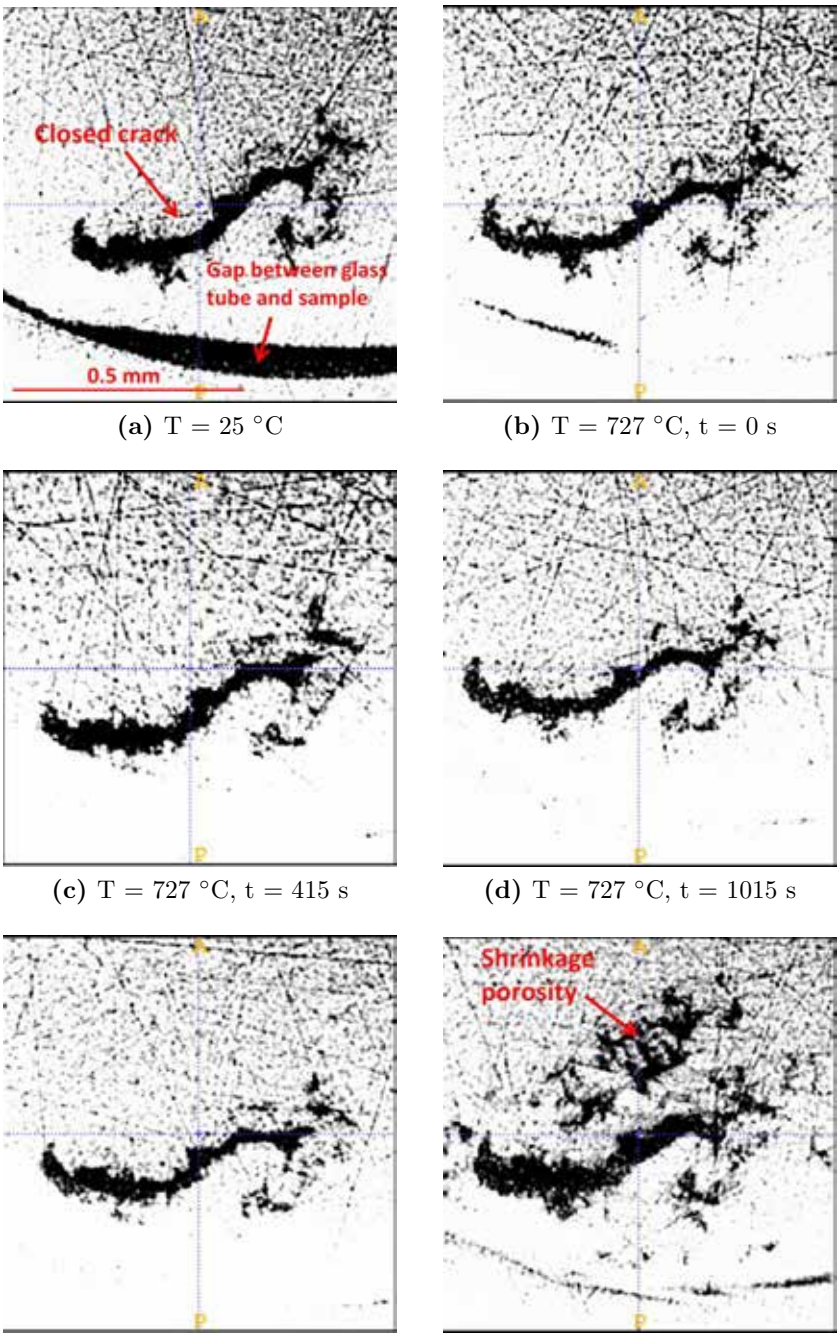

(a) T = 25 °C

(b) T = 727 °C, t = 0 s

(c) T = 727 °C, t = 415 s

(d) T = 727 °C, t = 1015 s

(e) T = 500 °C, t = 1415 s

(f) T = 25 °C

Figure 5.63: Morphological evolution of an entrained pore(ID:10D1). The time, t, was measured from the time the sample temperature reached 727 °C.

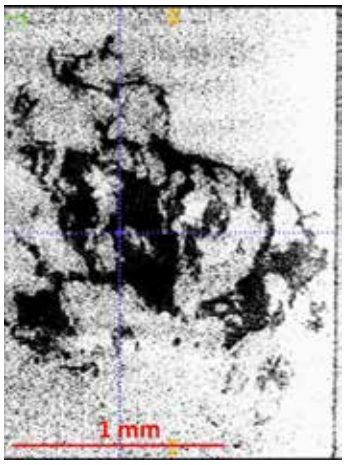

(a) T = 25 °C

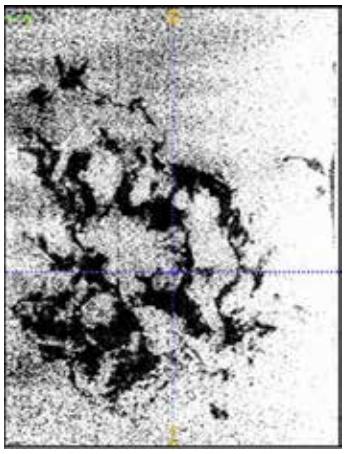

(b) T = 727 °C, t = 200 s

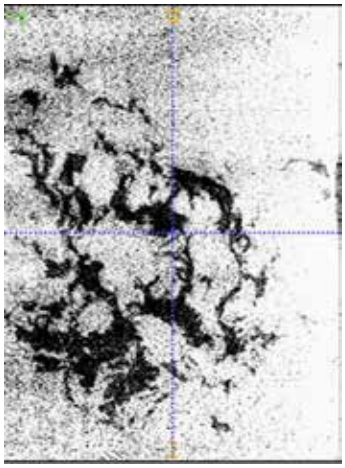

(c) T = 727 °C, t = 270 s

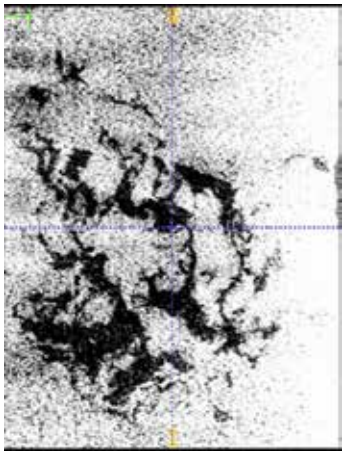

(d) T = 727 °C, t = 550 s

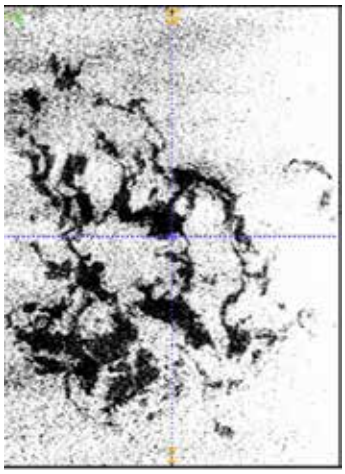

(e) T = 727 °C, t = 730 s

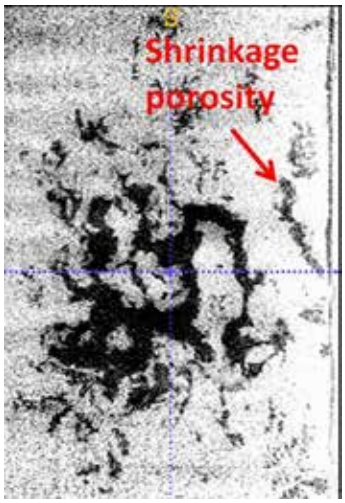

(f) T = 25 °C

Figure 5.64: Morphological evolution of an entrained pore(ID:10C1). The time, t, was measured from the time the sample temperature reached 727 °C.

Figure 5.64 is a further example of the evolution of an entrainment defect that contained a small amount of gas within the void. It shows little change of the morphology of the defect, considering its complex shape. The excessive complexity of the defect and its strength might mean that it endured a greater drag force and prevented the shape change of the defect.

5.4.3 Behaviour of Entrainment Defects in the Liquid State and during Solidification

The experiments showed that large entrained bubbles could float up to a location beneath the free surface of samples, as the surface oxide skin might prevent further movement of a bubble (see Figure 5.62). Smaller entrainment defects, regardless of their geometry and the volume of entrained gas within them, could generally maintain their position in a tranquil liquid metal. This may imply that entrainment defects have a similar density to that of the liquid metal around them. Morphological changes of the defects from simple pores to tangled networks might result in greater drag forces on the defects with complex geometries, reducing their mobility further. This suggests that the movement of entrainment defects in the liquid metal relies on external momentum. Therefore, the distribution of entrainment defects is determined by the turbulent flow of the liquid metal, rather than their buoyancy. Since the oxide film entrainment defects are expected to be brittle, turbulent flow during processing may break up the defects and affect their behaviour further.

5.5 Tensile Test Bar Model

5.5.1 Modelled Flow Structure

Figure 5.65 shows the modelled filling of the tensile test bar mould. The mould geometries and the notation of each test bar are shown in Figure 3.19 in Section 3.7. A comparative model that used a similar mould, but without the thin runner section, was simulated to study the influence of the mould design on the number of particles

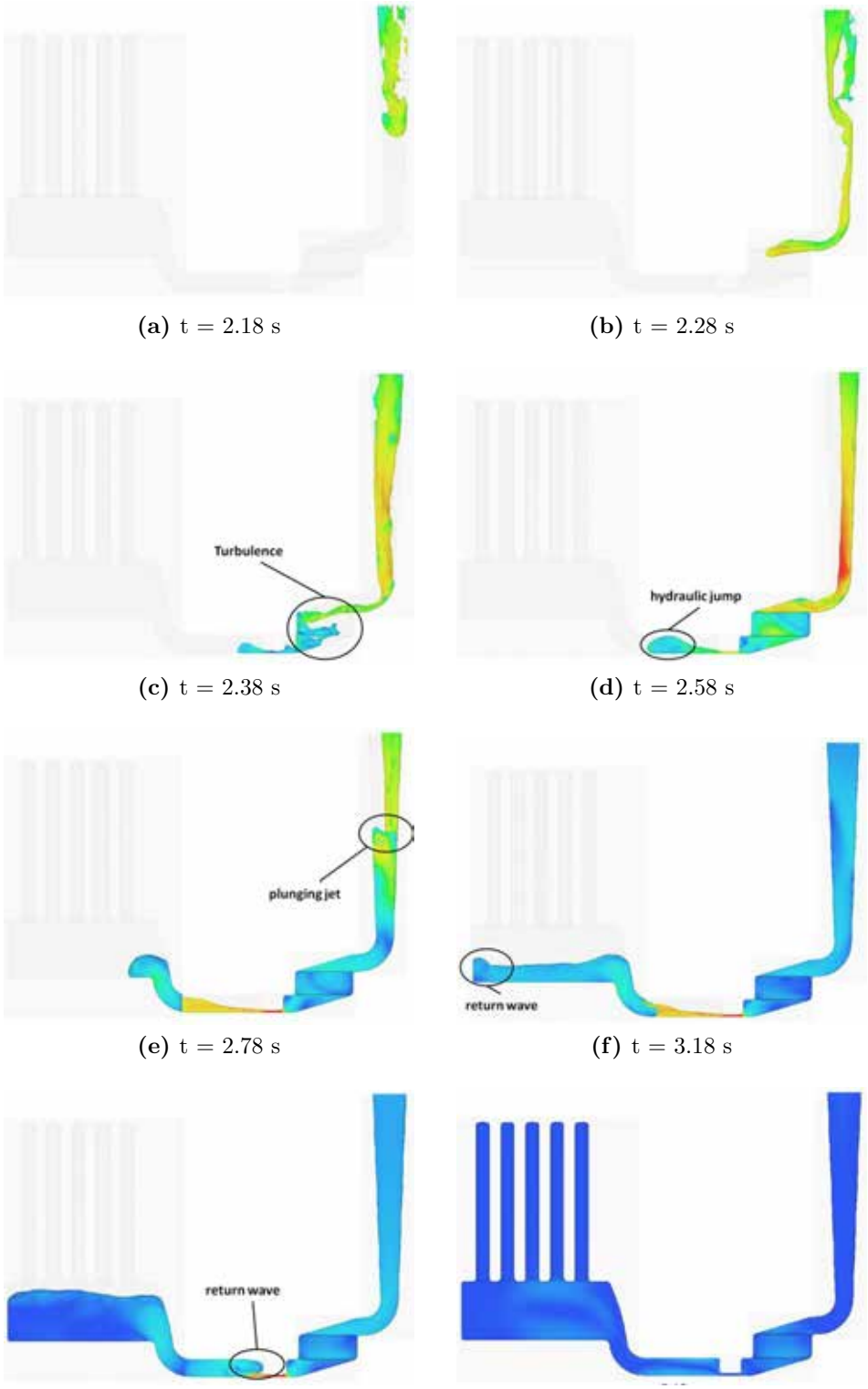

(a) t = 2.18 s **(b)** t = 2.28 s

(c) t = 2.38 s **(d)** t = 2.58 s

(e) t = 2.78 s **(f)** t = 3.18 s

(g) t = 3.98 s **(h)** t = 5.18 s

Figure 5.65: The modelled filling pattern of the tensile bar mould in a 2D section. The colour scheme represents velocity magnitude. High velocity is in warm colour. The entrainment locations are highlighted.

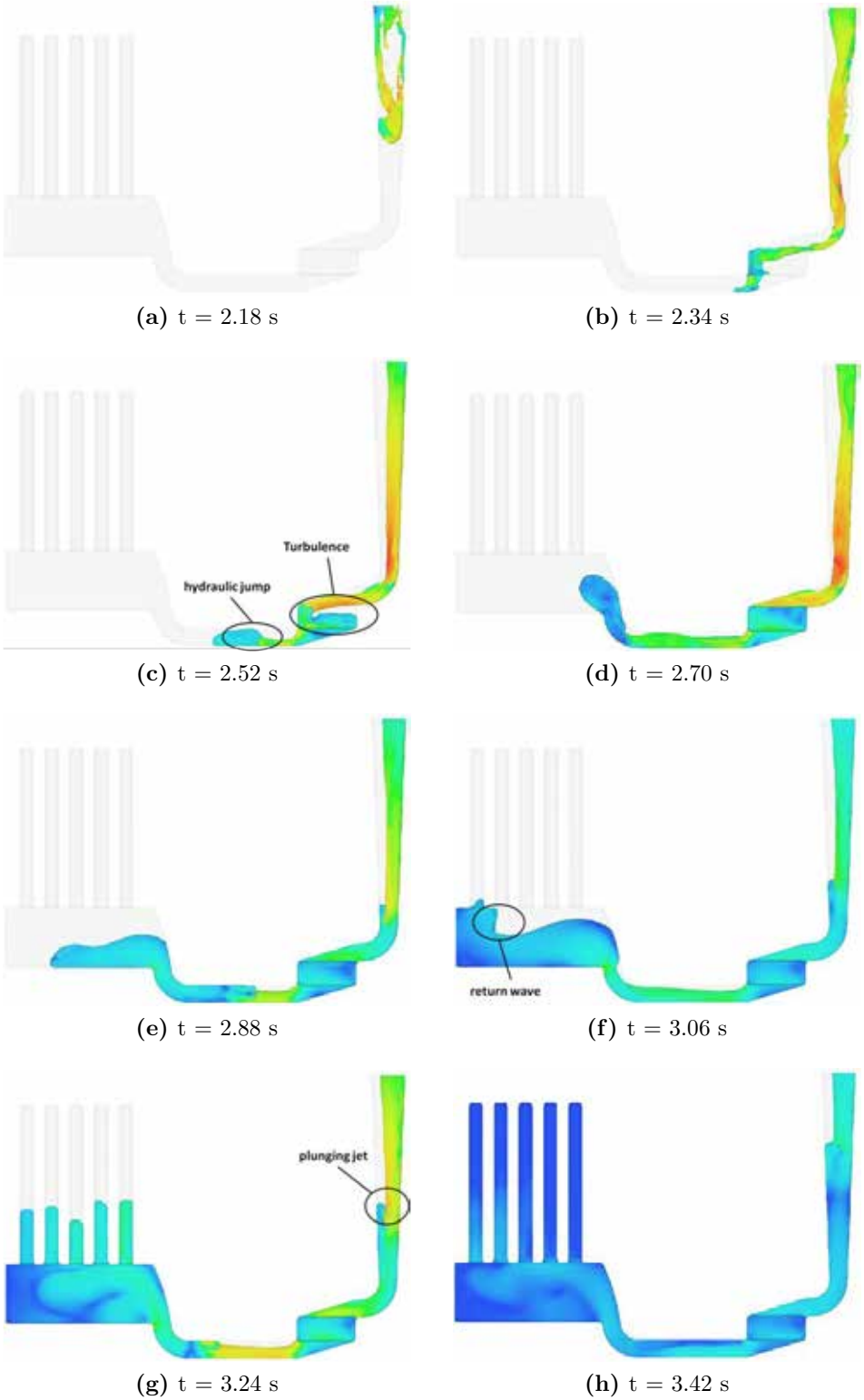

(a) t = 2.18 s **(b)** t = 2.34 s

(c) t = 2.52 s **(d)** t = 2.70 s

(e) t = 2.88 s **(f)** t = 3.06 s

(g) t = 3.24 s **(h)** t = 3.42 s

Figure 5.66: The modelled filling pattern of the comparative tensile bar mould with thick runner in a 2D section. The colour scheme represents velocity magnitude. High velocity is in warm colour. The entrainment locations are highlighted.

entrained during filling. The filling of this mould is shown in Figure 5.66. The entrainment locations and forms in both moulds are highlighted. It should be noted that for simplicity of display only filling of the mould cavity and running system is shown here, but the filling of the pouring basin (above the downsprue in the figures) was also considered in the model.

Both simulations showed similar filling patterns in the moulds, where initially the liquid alloy dropped down the downsprue and formed splashes and surface turbulence at the bottom of the sprue. When the fluid entered the horizontal runner, a return wave formed and collided with the incoming metal stream, rolling surface films and entrained gas into the bulk liquid during the filling of the runner. After the runner was fully filled, the fluid front became relatively stable and rose up the test bars smoothly with limited numbers of defects being further generated. The main difference in the filling between the two kinds of mould was that in the mould with a thin runner, the surface turbulence levels of the hydraulic jump and return wave behind the thin section were much higher than those in the thick runner mould. Consequently, more entrainment defects should have been generated in the thin runner mould, which could manifest itself as more particles placed in the simulation.

5.5.2 Defect Characterisation

Figures 5.67 to 5.71 show typical defects found on the fracture surfaces of the tensile test bars. SEM analysis found that a large area of fracture surface on Test Bar 3B and 5A was covered by inclusions with an oxide film around them, as shown in Figure 5.69, which might explain the exceptionally low tensile strength of these two samples. According to the calculation of effective feeding from Chvorinov's rule, there should be little or no shrinkage porosity in the cast bars. Therefore, the unfractured dendrites shown in Figure 5.67 might be caused by entrained micro bubbles wrapped by oxide films during filling. The spherical or nearly round pores shown in Figure 5.68 could be induced either by gas bubbles trapped during filling, forming a bubble trail

as indicated by the small hole on the bottom of the bubble in Figure 5.68a, or hydrogen porosity formed during solidification. The shining inclusions in Figure 5.69 were examined by EDX (see Figure 5.76) and were some sand particles wrapped by oxide films. The cracks on the fracture surfaces were associated with entrained double oxide films in the castings, both old and young films, as shown in Figure 5.71. As introduced in Section 2.1 in Literature Review, the "young" and "old" oxide films are only descriptive definitions. Here, the young and old oxide films in the SEM images can be generally differentiated by their thickness and morphology, and also the height of oxygen peak on the EDX spectrum. The fractographic analysis revealed that the fracture mechanisms of the bars were complicated, with combined effects from several different kinds of defects, such as micro-porosity, entrained bubbles, and oxide films.

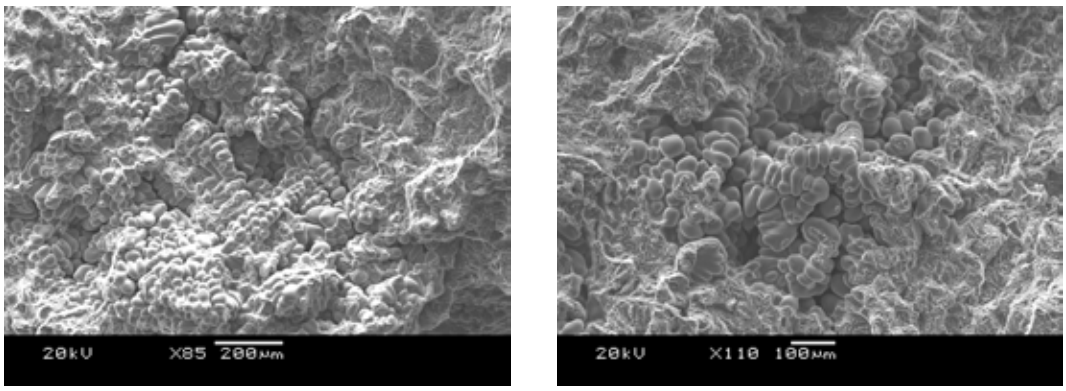

(a) **(b)**

Figure 5.67: SEM images of two examples of shrinkage porosity on the fracture surfaces of test bars. (a). Test Bar 1E; (b). Test Bar 5E.

Figures 5.72 to 5.76 showed some representative secondary electron images and corresponding EDX spectra of the oxide film defects found on the fracture surfaces. From the morphology, size and the oxygen peaks of the spectrum of the oxide film defects, they could be generally differentiated as old and young oxide films, such as shown in Figures 5.73 and 5.74 respectively. Observation showed that the fragments of old oxide films were distributed randomly on the fracture surfaces, perhaps because

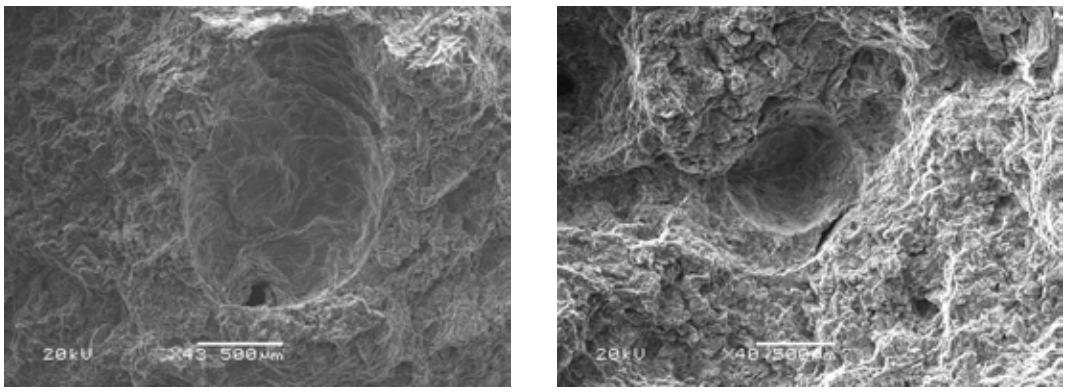

(a) **(b)**

Figure 5.68: SEM images of examples of entrained bubble/hydrogen porosity on the fracture surfaces of test bars. (a). Test Bar 2E; (b). Test Bar 3D.

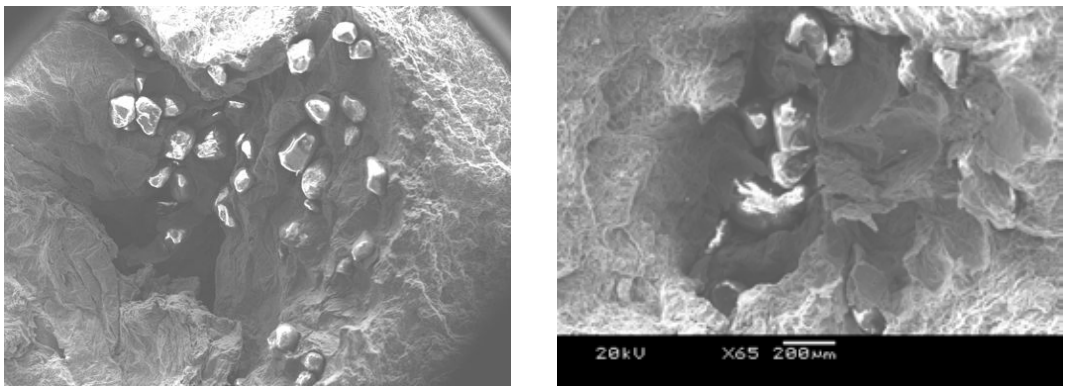

(a) **(b)**

Figure 5.69: SEM images of exogenous inclusions on the fracture surfaces of test bars. (a). Test Bar 3B; (b). Test Bar 5E.

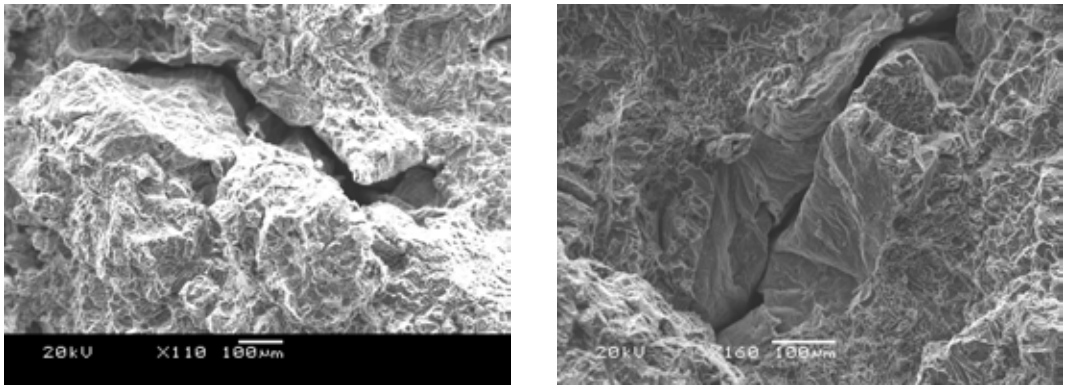

(a) (b)

Figure 5.70: SEM images of pre-formed cracks on the fracture surfaces of test bars. (a). Test Bar 4A; (b). Test Bar 2E.

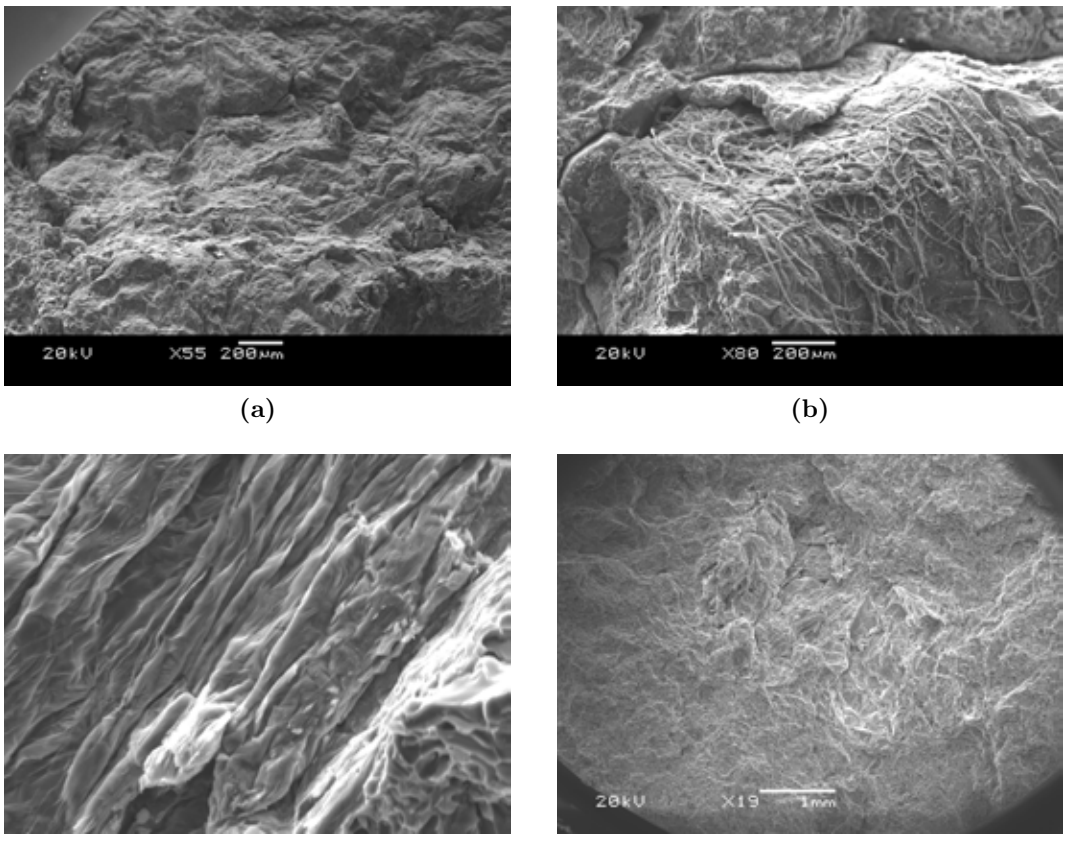

(a) (b)

(c) (d)

Figure 5.71: SEM images of old and young oxide films on the fracture surfaces of test bars. (a). old film (Test Bar 1E); (b). old film (Test Bar 5C); (c). young film (Test Bar 3B); (d). young film (Test Bar 4D).

the brittle films were broken up by the turbulent flow during filling, while the young films showed more film-like properties which covered a larger area of the matrix alloy and wrinkled on the fracture surface, showing a furled morphology as suggested by Campbell [45].

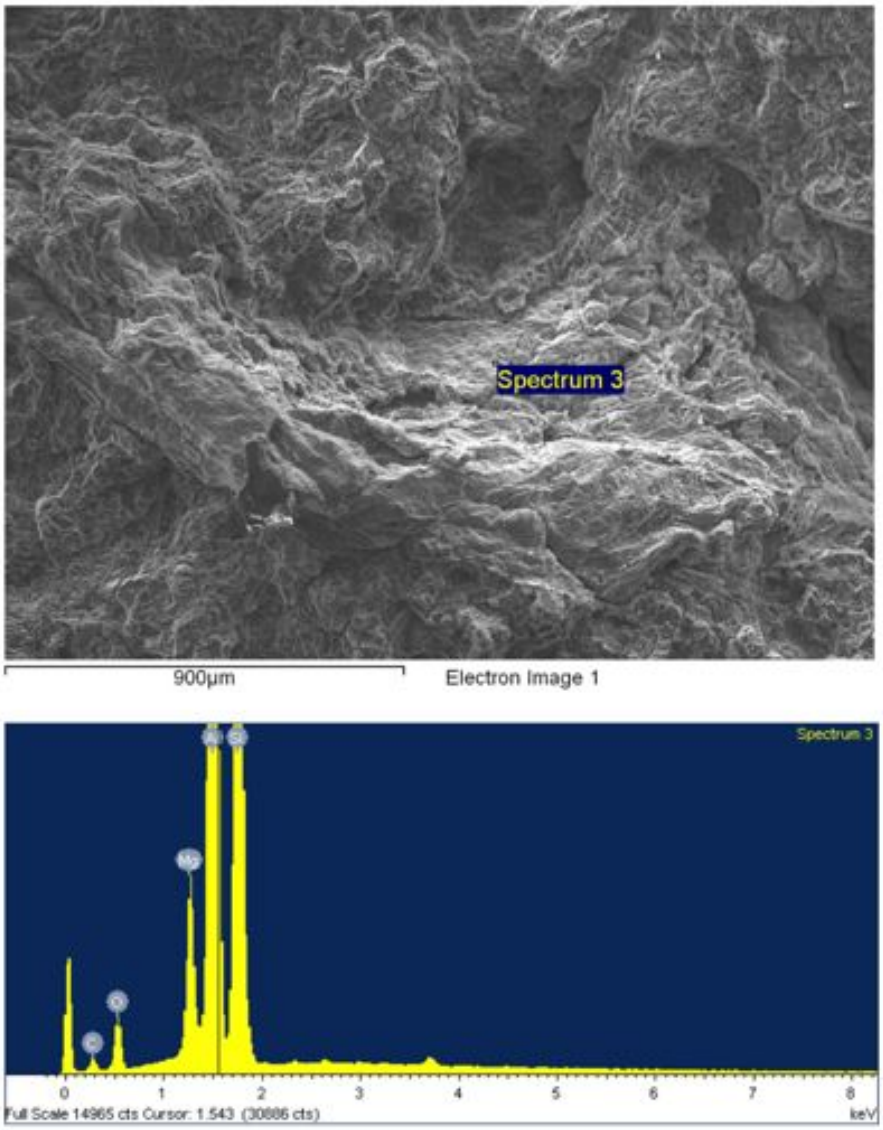

Figure 5.72: SEM image and EDX spectrum showing oxide film on the fracture surface of a test bar (Test Bar 3A).

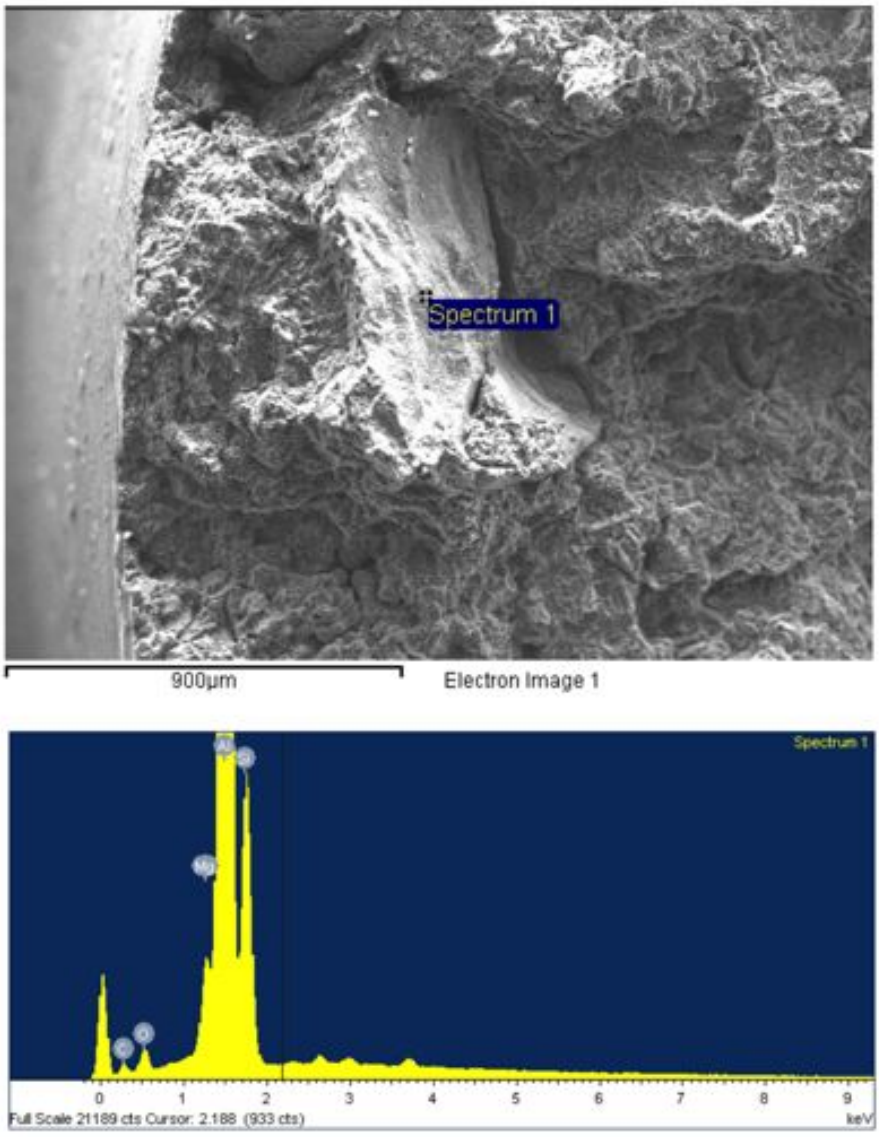

Figure 5.73: SEM image and EDX spectrum showing an old oxide film on the fracture surface of a test bar (Test Bar 3D).

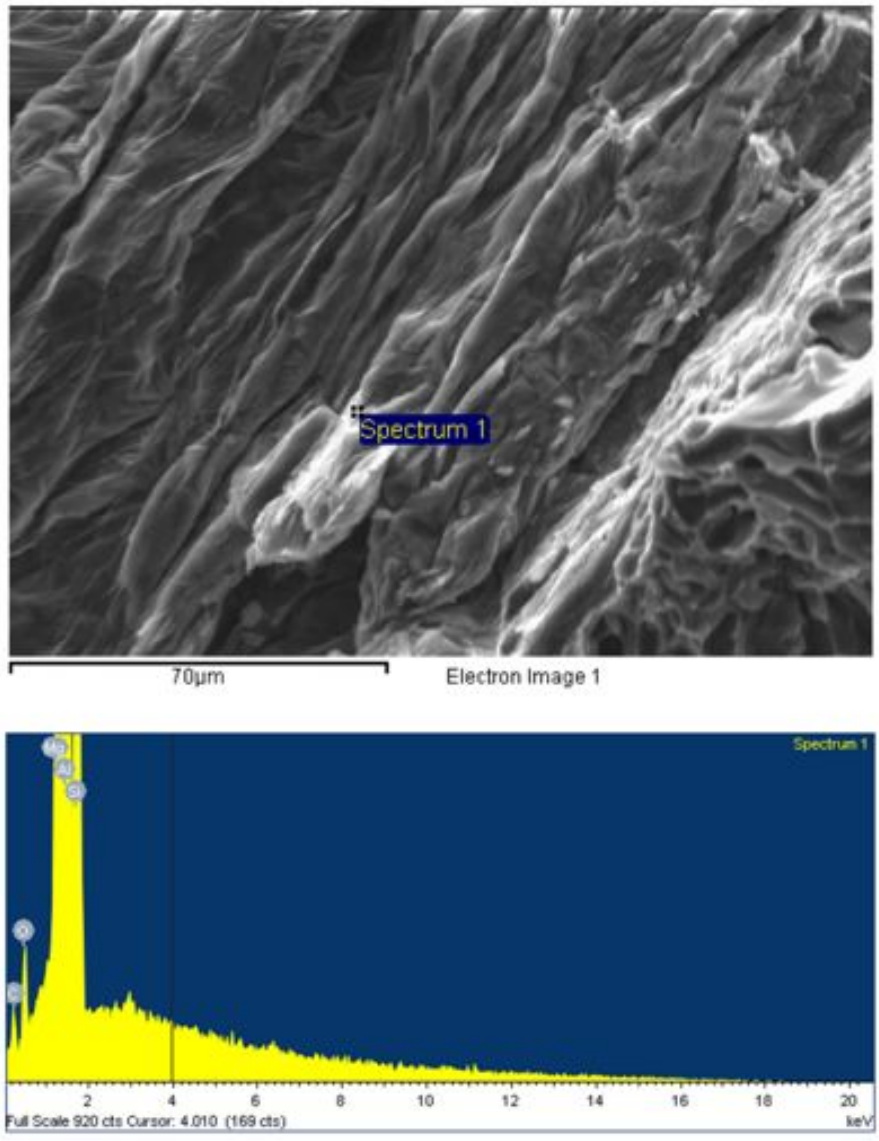

Figure 5.74: SEM images and EDX spectrums showing a young oxide film on the fracture surface of a test bar (Test Bar 3B).

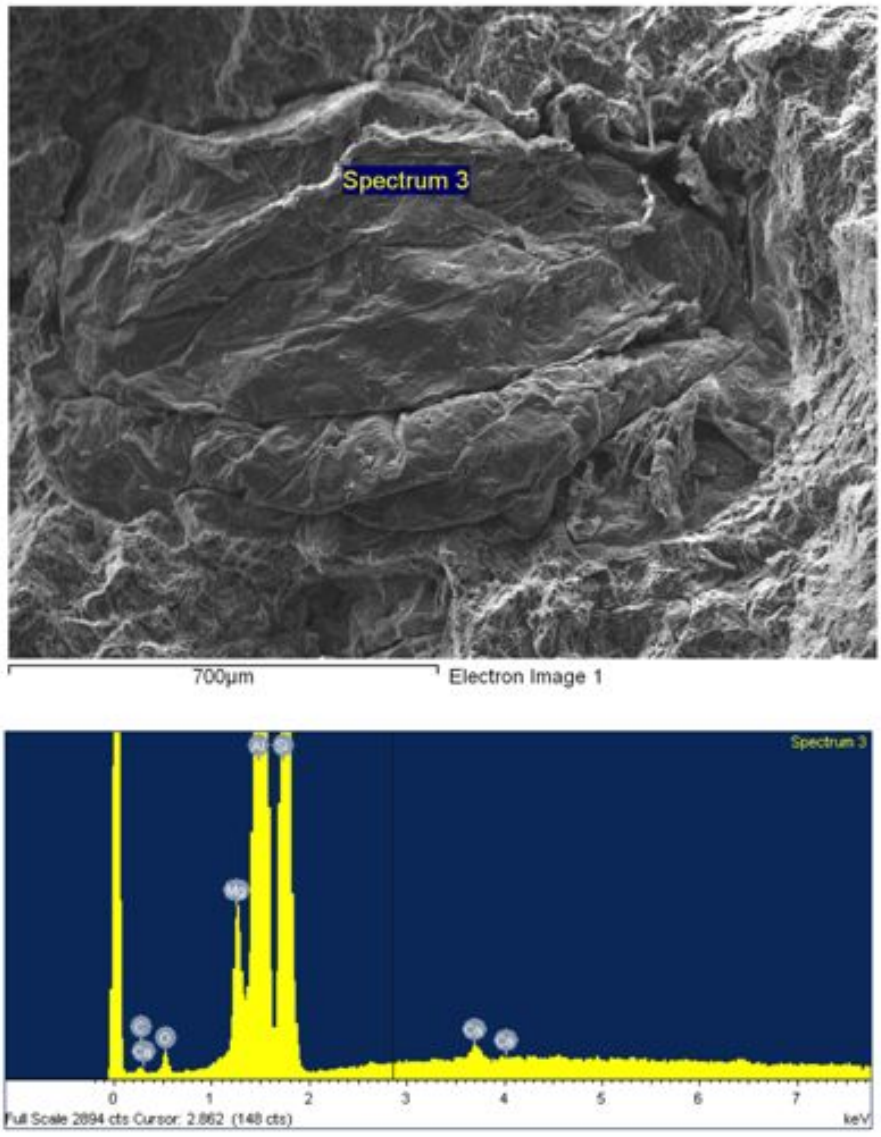

Figure 5.75: SEM image and EDX spectrum showing a tangled oxide film on the fracture surface of a test bar (Test Bar 5C).

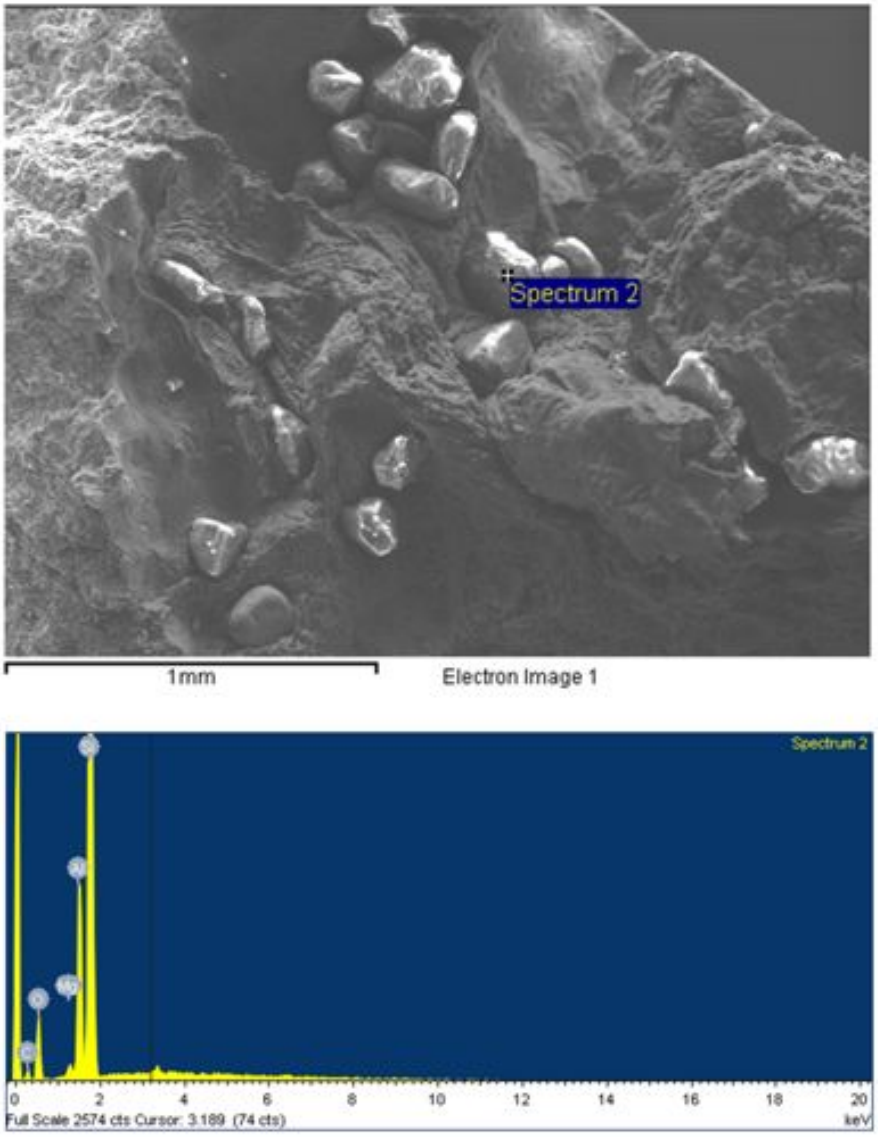

Figure 5.76: SEM images and EDX Spectrum showing inclusions on the fracture surface of a test bar (Test Bar 6C).

Characterisation of the fracture surfaces of the 2nd groups of castings showed that large areas of the fracture surfaces were covered by oxide films, as was seen in the 1st group, *i.e.* the majority of fractures was caused by entrainment defects. An example of an oxide film found on the fracture surface of a test bar is shown in Figure 5.77.

(a) (b)

Figure 5.77: Examples of oxide film found on the fracture surface of castings (the 2nd group).

5.5.3 Tensile Strength of the Test Bars and Strength Variation Trends (the 1st group)

Table 5.17 shows the tensile strength and elongation of 30 cast test bars in the 1st group of experiments. Compared to the typical ultimate tensile strength (UTS) and elongation of A356.0 T6 sand casting, which are 230 MPa minimum and above 3.5% minimum respectively [35], the UTS of two samples (Test Bars 3B and 5A) was below the typical value, and the elongation of all the samples was below the typical value. This was believed to be caused by defects in the samples. Generally, the tensile strength and elongation of the 30 samples showed a large variation as the frequency histogram shown in Figure 5.78. The Weibull modulus of the test bars shown in Figure 5.79 is 18, which is much lower than the modulus of 37 obtained from a surface turbulence free bottom-filled casting reported in the literature [22], which also confirmed the low reproducibility of mechanical properties of these cast bars.

Figure 5.80 shows the mean and median tensile strengths of the five test bars from six castings in the 1st group of testing. The elongation of the test bars from each

Table 5.17: The tensile test results of cast test bars from the tensile bar mould (the 1st group).

No.	ID	UTS (MPa)	Elongation (%)	No.	ID	UTS (MPa)	Elongation (%)
1	1A	256	0.9	16	4A	271	1.2
2	1B	259	0.9	17	4B	270	1.3
3	1C	261	0.9	18	4C	251	0.7
4	1D	263	0.9	19	4D	271	1
5	1E	257	0.8	20	4E	267	1.1
6	2A	261	1.3	21	5A	207	0.4
7	2B	241	0.6	22	5B	271	1.1
8	2C	240	0.6	23	5C	262	1
9	2D	256	0.9	24	5D	265	1
10	2E	247	0.7	25	5E	275	1.2
11	3A	247	0.7	26	6A	258	1
12	3B	212	0.7	27	6B	255	0.9
13	3C	251	0.9	28	6C	257	0.8
14	3D	242	0.6	29	6D	273	1.4
15	3E	258	0.9	30	6E	278	1.6

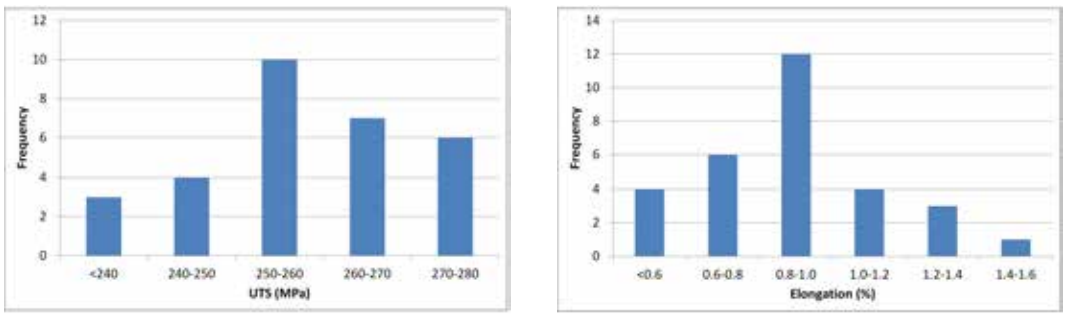

(a) **(b)**

Figure 5.78: Frequency distribution of the ultimate tensile strength and elongation of 30 test bars (the 1st group). (a). UTS (MPa); (b). Elongation (%).

casting was closely related to its tensile strength, the mean and median elongation in Figure 5.81 showed similar results to those in Figure 5.80. Statistically, the two test bars with exceptionally low strength in Casting 3 (Test Bar 3B) and Casting 5 (Test Bar 5A) severely reduced the mean values of tensile strength and elongation of the two castings, but had less influence on the median values. Since the median can be used as a measure of skewed data, such as the tensile strengths of the castings which followed the Weibull distribution rather than the Normal distribution, the median values give better description of the general trends of tensile strength and elongation of the castings, and were used in the rest of study.

The relatively low UTS and elongation of Castings 2 and 3, as shown in Figures 5.80 and 5.81, could be partly associated with the high hydrogen content in the castings (above 0.195 ppm). Table 5.18 shows the hydrogen contents in the six castings. The hydrogen content in Castings 1, 4, 5 and 6 were similar (0.165 ˜0.185 ppm), which also corresponded with similar tensile strengths and elongation of these castings, suggested that hydrogen content was one of the factors that affected the mechanical properties of the castings.

Table 5.18: The hydrogen content in the tensile bar castings (the 1st group). (Unit: ppm)

Batch	Surface	Bulk	Total
1	0.018	0.148	0.166
2	0.027	0.239	0.266
3	0.023	0.172	0.195
4	0.017	0.15	0.167
5	0.019	0.166	0.185
6	0.016	0.157	0.173

Figure 5.82 plots the UTS and elongation of five test bars from each casting and the median value of each bar. Due to the wide scatter of the test results, it is difficult to find a consistent trend of either UTS or elongation across the five test bars from the six castings. In terms of UTS, Castings 2, 4 and 6 showed similar trends to some extent,

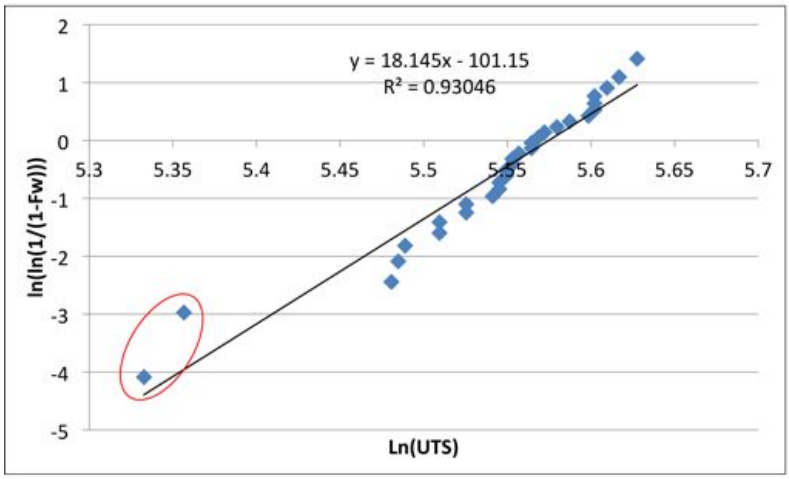

Figure 5.79: Weibull plot of the UTS of test bars from tensile bar mould, with the two data points that had exceptional low strength circled. (the 1st group)

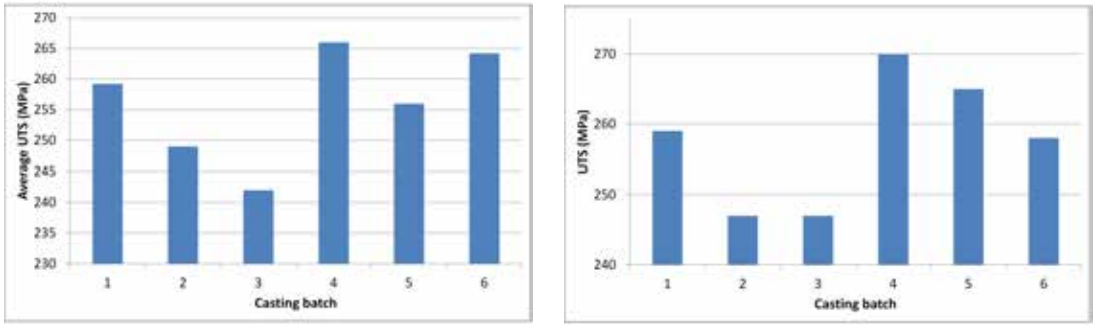

(a) **(b)**

Figure 5.80: The mean/median tensile strengths of the test bars in six castings from the tensile bar mould. (a). mean UTS; (b). median UTS.

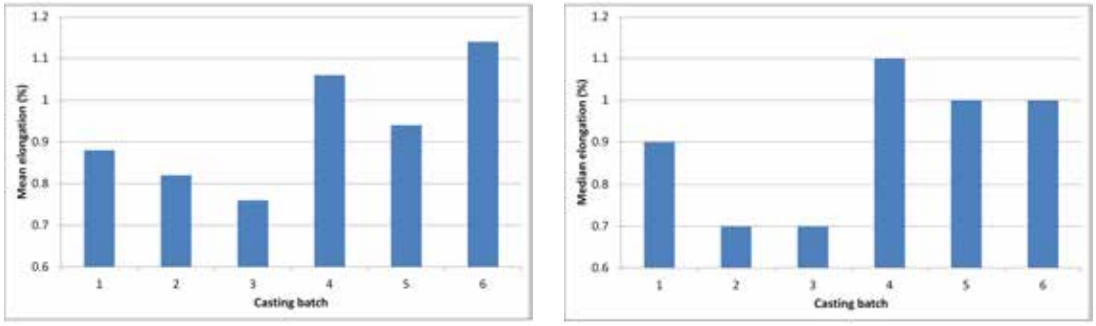

(a) **(b)**

Figure 5.81: The mean/median elongation of test bars in six castings from tensile bar mould. (a). mean elongation; (b). median elongation.

in that Test Bar 3 had the lowest strength and Test Bar 4 had the highest strength, with the strength of Test Bar 5 between them. However, the trend in Casting 3 was opposite to these three castings and the elongation trends of those three castings did not agree with the trend in UTS. A correlation between the trends in median UTS and median elongation was not found across the five test bars, possibly because the median UTS and elongation of the test bars in the five different locations were quite similar, any subtle differences in the value would vary the general trend. This inconsistency of the variation trends in UTS and elongation of the test bars from different locations affected the validation of the modelling results.

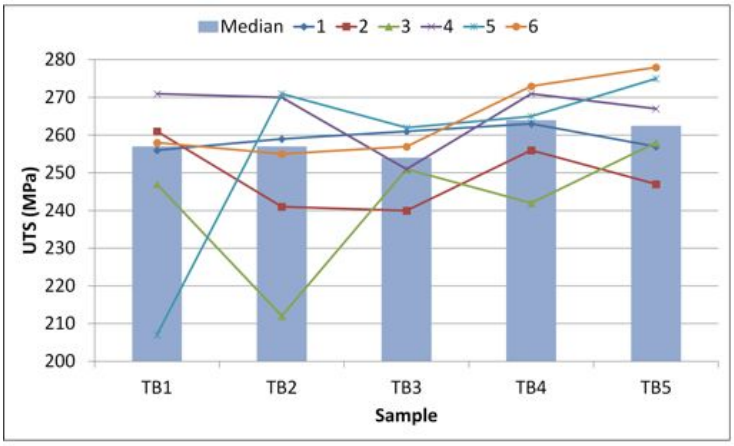

(a)

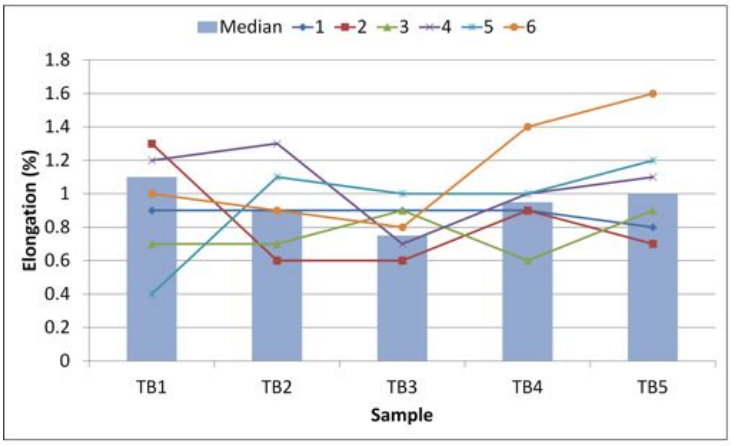

(b)

Figure 5.82: The tensile strength and elongation of samples obtained from five locations in six castings. (a). UTS; (b). elongation.

5.5.4 Tensile Strength of the Test Bars and Strength Variation Trends (the 2nd group)

Table 5.19 shows the tensile strength and elongation of the 2nd group of castings. Test Bars 1A to 1E were from the control mould, which was freshly made and cast. Test Bars 2A to 7E are the test bars from the Moulds 2 to 7, held in vacuum for two weeks before being cast. The casting from Mould 1 is referred to as the control group, while castings from Moulds 2 to 7 are referred to as the 2nd group in the text. The mean UTS of the control group was 229 MPa, similar to the mean UTS from the 2nd group of castings, which was 228 MPa. This is close to the reported value for A356 T6 alloy in the literature, but about 11% lower than the average UTS of the 1st group of castings. A possible reason is that the test conditions of the two groups of castings were different. The mean elongation of test bars from control group was the same as that of the second group. Both were 0.6%, much lower than the typical value of A356 T6 alloy reported (above 3.5%), and also lower than that of the 1st group castings, which was 0.9%.

Figure 5.83 shows the median UTS and elongation of the five test bars in each casting. The castings showed a similar response in UTS and elongation, with Castings 4 and 6 having slightly lower properties in general. Since the differences in elongation between each casting was quite small as shown in Figure 5.83b, the analysis of results from the 2nd group of castings focused on the tensile strength, with only differences of elongation emphasised.

The Weibull modulus of the UTS of the 2nd group was 18.4 (Figure 5.84), almost the same as that of the 1st group (18.1). This is correlated with the frequency histograms shown in Figure 5.85, which show that the distribution frequencies of the UTS and elongation of the 2nd group of castings that were similar to those of the 1st group of castings. This result implies similar reliability of castings was achieved in both groups of castings, *i.e.* consistent experimental results were obtained, in spite of the highly

Table 5.19: The tensile test results of cast bars from the test bar mould (the 2nd group).

No.	ID	UTS (MPa)	Elongation (%)	No.	ID	UTS (MPa)	Elongation (%)
1	1A	218.7	0.6	19	4D	239.8	0.7
2	1B	223.7	0.6	20	4E	214.8	0.5
3	1C	242.7	0.8	21	5A	222.6	0.5
4	1D	227.8	0.5	22	5B	236.1	0.6
5	1E	232.4	0.6	23	5C	246	0.8
6	2A	208.5	0.4	24	5D	248.1	0.7
7	2B	234.7	0.5	25	5E	235.6	0.6
8	2C	234.1	0.5	26	6A	196.5	0.4
9	2D	226.8	0.4	27	6B	213.3	0.5
10	2E	238	0.6	28	6C	234.8	0.7
11	3A	227	0.5	29	6D	225.8	0.6
12	3B	239.2	0.7	30	6E	228.2	0.6
13	3C	199.5	0.4	31	7A	248.7	0.9
14	3D	256.7	1	32	7B	201.1	0.4
15	3E	245.9	0.8	33	7C	224.1	0.5
16	4A	219.3	0.6	34	7D	232.8	0.6
17	4B	217.3	0.5	35	7E	230.9	0.6
18	4C	218.2	0.5				

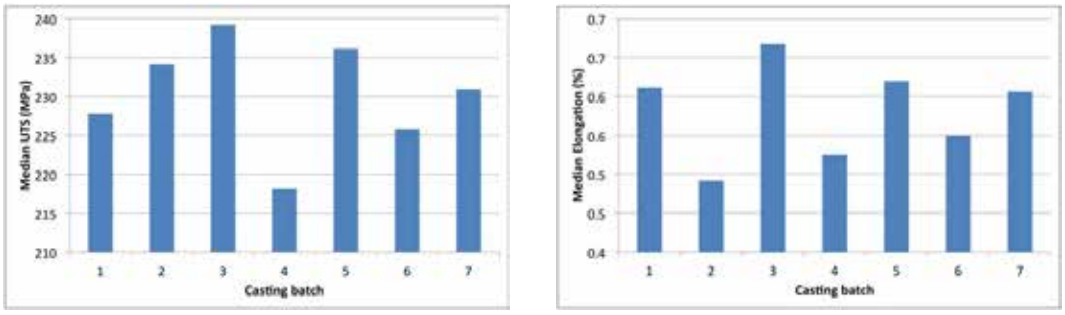

(a) **(b)**

Figure 5.83: The median UTS and elongation of the test bars from seven castings (the 2nd group). (a). median UTS; (b). median elongation.

surface turbulent filling during casting.

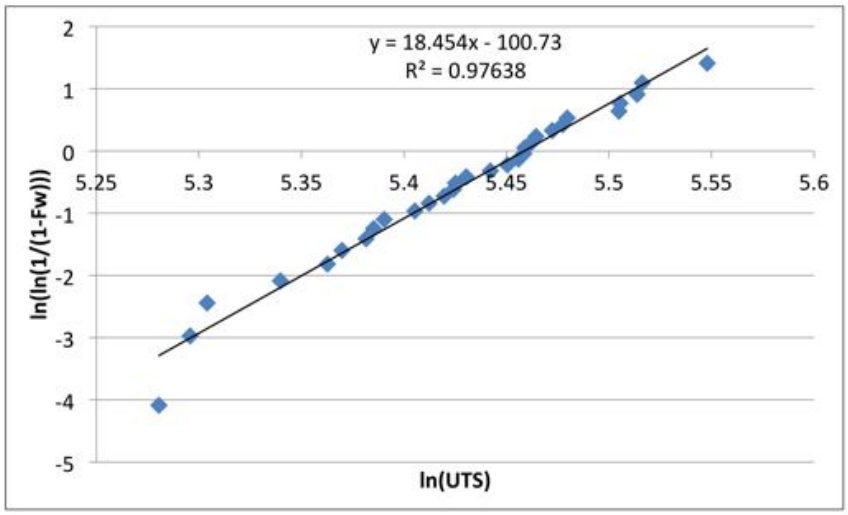

Figure 5.84: The Weibull plot of the UTS of test bars from 2nd group.

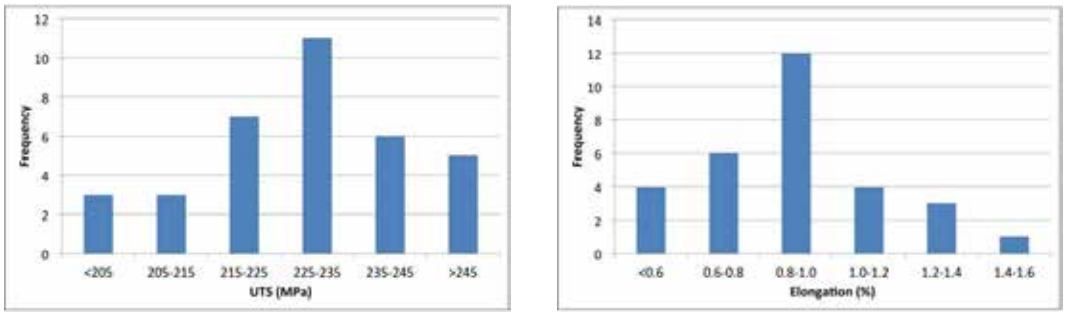

(a) **(b)**

Figure 5.85: Frequency distribution of the ultimate tensile strength and elongation of 30 test bars (the 2nd group). (a). UTS (MPa); (b). Elongation (%).

Figure 5.86 plots the UTS variation in the test bars from different locations. Similar to the 1st group of castings, it is still difficult to find a consistent pattern of UTS across the five test bars from the seven castings, owing to the wide scatter of the test results. However, an interesting general trend in UTS was observed in the comparison between the 1st and the 2nd group of castings, as shown in Figure 5.87, which shows a slight trend, in that the UTS of the test bars was increased from the far end of the runner (Test Bar 1) to the end near the downsprue (Test Bar 5). This was initially observed in the 1st group of castings, but then confirmed by the 2nd group of castings.

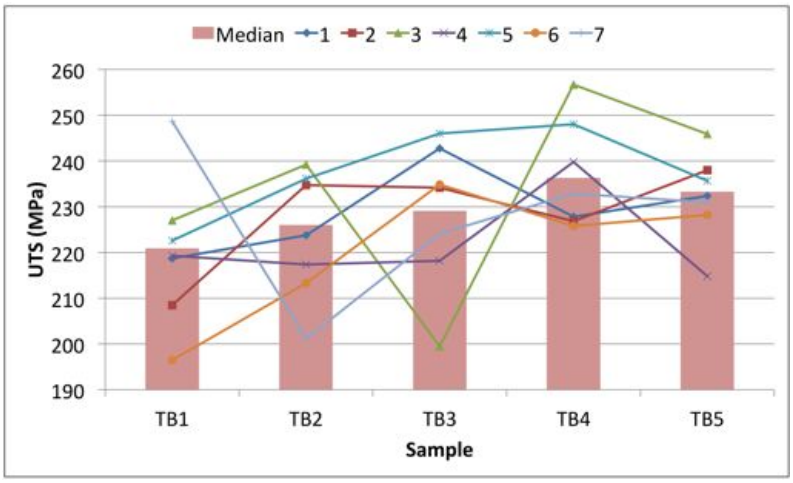

Figure 5.86: Variation trend of the test bars in UTS from different locations (the 2nd group).

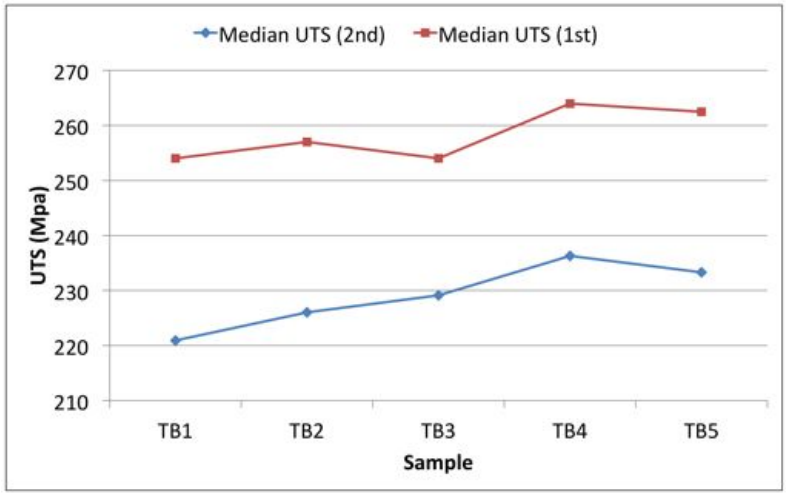

Figure 5.87: Comparison of median UTS of the test bars from different location between the 1st and 2nd groups of castings.

Investigation on the hydrogen content in the castings revealed that the UTS and elongation of test bars from the 2nd group of castings could not be simply linked with the hydrogen content in the castings. The average hydrogen content in the 2nd group of castings was 0.14 ppm, lower than that in the 1st group of castings, which was 0.19 ppm. Table 5.20 shows that the control group had a slightly higher hydrogen content than in the 2nd group. This proved that placing the sand mould in vacuum before making casting could reduce the hydrogen content in the solidified casting, as demonstrated by Elsayed [172]. However, the effects of the hydrogen content reduction in the castings were not reflected in the UTS and elongation of the test bars, since the test bars from the control group had similar properties to those from the 2nd group. Besides, the average UTS and elongation of the control group and 2nd group were lower than the 1st group. Both results suggested that the mechanical properties of castings in this later experiment were not determined by the hydrogen porosity.

Table 5.20: The hydrogen content in the 2nd group of castings. (Unit: ppm)

Casting	Bulk hydrogen content
1 (control group)	0.161
2	0.143
6	0.134

5.5.5 Model Predicted Defects Distribution

Table 5.21 shows the model predicted particle counts in each mesh block with different modelling conditions. It can be seen that in the simulation without considering entrainment in the pouring basin, a small number of particles could enter the mesh block that containing the pouring basin (Mesh Block 1) because of the surface turbulence during filling. Comparing the number of non-sticky and sticky particles trapped in the mould, it is clear that many more sticky particles stayed in the mould rather than entered the test bar region during filling, which resulted in fewer sticky particles trapped in the test bars than non-sticky particles, as shown in Tables 5.22 to 5.25.

Table 5.21: Particles trapped in each mesh block in tensile bar mould in different modelling conditions.

Mesh Block	Non-sticky Particles	Sticky Particles	Non-sticky Particles with Basin	Sticky Particles with Basin	Non-sticky Particles in Thick Runner	Sticky Particles in Thick Runner
1 (pouring basin)	1	217	22584	32430	0	1028
2 (downsprue)	107	16559	3762	14558	3385	26007
3 (filter print)	1763	14766	3595	14506	3532	26689
4 (feeder and cavity)	165843	89355	185020	102189	109426	59240
5 (runner)	23449	25204	21561	40538	5512	22357
Total	191163	146101	236522	204221	121855	135321

Comparison of the total particle counts in the thin and thick runner moulds showed more particles placed in the thin-runner mould, especially in Mesh Block 4 (containing the feeder and test bars) and Mesh Block 5 (containing the horizontal runner), which included most of the particles that were generated behind the thin section. This result suggested that the number of particles that were generated by the OFEM algorithm was sensitive to the mould design and the number of particles can be an indicator for differentiating less entraining mould designs.

Figure 5.88 shows profiles of the tensile test bar mould cavity with modelled particles shown in each test bar. As the particles from different modelling conditions were all of the same size, higher particle number density in the model is seen as a darker region in the profiles. It can be seen clearly that more particles were delivered into the ingate and test bars when using the non-sticky particle model, but the similar eddy patterns of particles formed in the large ingate in the different models. Since the simulations consider the interaction between particles and the fluid, this implied that particles had limited effects on the fluid movement, whether sticky or non-sticky particles were used.

Tables 5.22 and 5.23 show both the total number of particles entrained and the maximum particle concentration in the mesh cell within the whole test bar and within the gauge length of the test bars. The results were obtained from simulations using

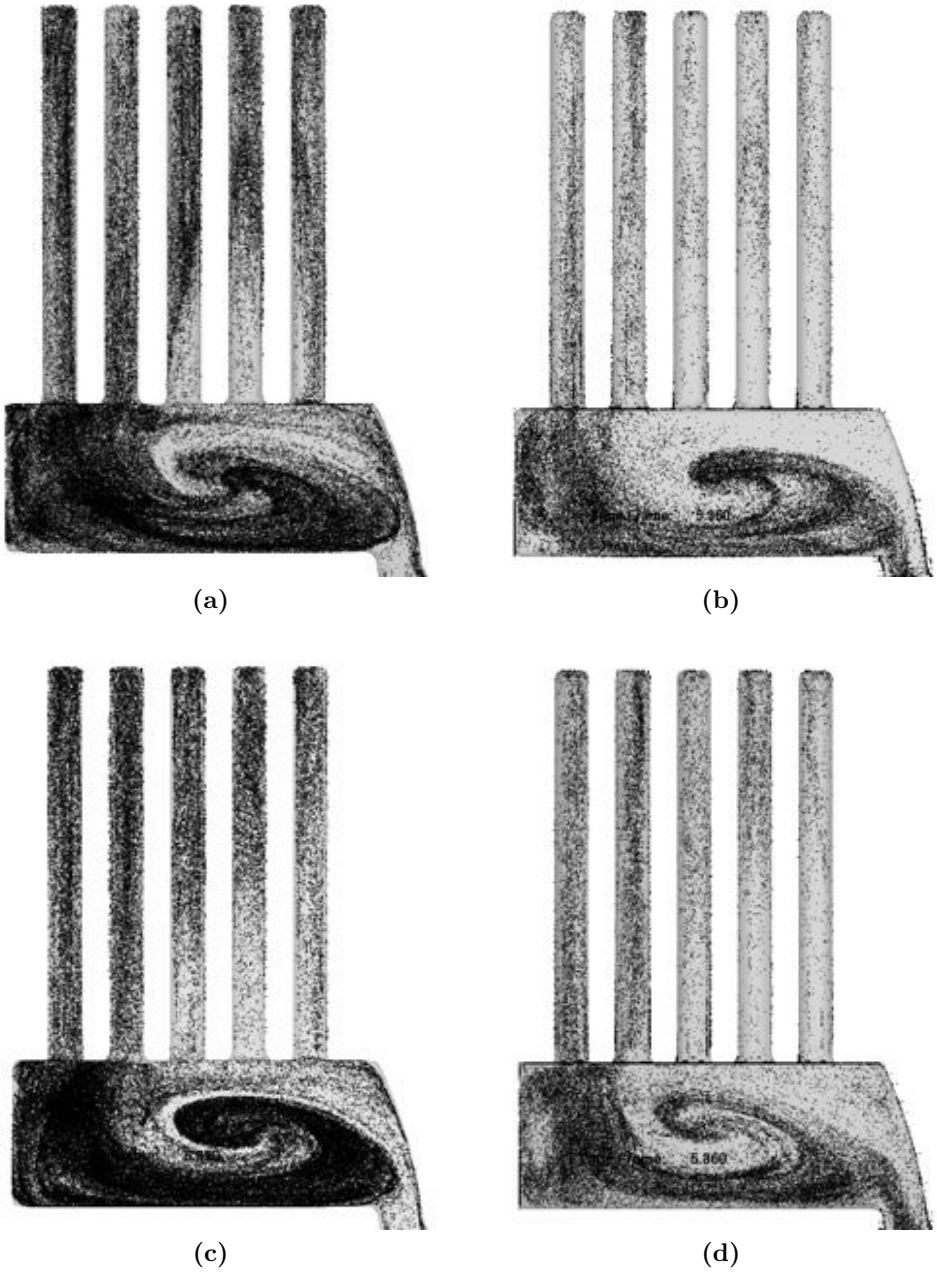

(a) **(b)**

(c) **(d)**

Figure 5.88: Profiles of tensile bar mould showing modelled particles distribution. (a). non-sticky particle model; (b). sticky particle model; (c). non-sticky particle model with entrainment in pouring basin; (d). sticky particle model with entrainment in pouring basin.

Table 5.22: Predicted non-sticky particle counts in the tensile bar mould.

ID	Total of Non-sticky Particles	Total of Non-sticky Particles in Gauge Length	Particle Concentration of Non-sticky Particles	Particle Concentration of Non-sticky Particles in Gauge Length
TB1	14829	7399	152	69
TB2	11858	6111	127	127
TB3	12751	8477	203	203
TB4	8925	5720	76	51
TB5	9420	5294	135	135

Table 5.23: Predicted sticky particle counts in the tensile bar mould.

ID	Total of Sticky Particles	Total of Sticky Particles in Gauge Length	Particle Concentration of Sticky Particles	Particle Concentration of Sticky Particles in Gauge Length
TB1	5067	2242	84	59
TB2	4144	1838	74	74
TB3	1414	723	37	20
TB4	1824	1083	36	21
TB5	1572	693	61	61

sticky and non-sticky particles respectively. Tables 5.24 and 5.25 show the results of similar simulations, in which entrainment in the pouring basin during filling was also considered. Obviously, entrainment in the pouring basin led to more particles entrained in the test bars. As the plunging jet developed during filling, the pouring basin created a large amount of particles, which could further be transferred into the mould cavity.

Table 5.24: Predicted non-sticky particle counts in the tensile bar mould with entrainment in the pouring basin.

ID	Total of Non-sticky Particles	Total of Non-sticky Particles in Gauge Length	Particle Concentration of Non-sticky Particles	Particle Concentration of Non-sticky Particles in Gauge Length
TB1	16228	8806	432	433
TB2	14359	7870	90	72
TB3	9913	5484	377	57
TB4	8018	4580	64	64
TB5	6828	3054	95	96

The maximum particle concentration in each test bar was also influenced by consid-

Table 5.25: Predicted sticky particle counts in the tensile bar mould with entrainment in the pouring basin.

ID	Total of Sticky Particles	Total of Sticky Particles in Gauge Length	Particle Concentration of Sticky Particles	Particle Concentration of Sticky Particles in Gauge Length
TB1	6697	2894	61	59
TB2	8021	3929	69	47
TB3	3229	1662	48	38
TB4	3394	1525	54	44
TB5	1880	672	42	42

eration of the entrainment in the pouring basin and particle stickiness. When considered the entrainment in pouring basin, the extra generated particles were transferred into the test bars, either increasing the maximum particle concentration in mesh cells in the test bars, as shown in Tables 5.22 and 5.24, when non-sticky particles used, or stayed similar as seen in Tables 5.23 and 5.25, when sticky particles used. The different responses of the maximum particle concentration to different particle stickiness might be because, during the filling of the test bars, non-sticky particles could rise up with the liquid and cluster together. Therefore, a greater total number of non-sticky particles in the bars could result in higher particle concentration in each bar. Alternatively, the sticky particles might adhere to the mould wall during filling and lead to a more even distribution of particles in the test bars, and hence had limited effects on the maximum particle concentration.

Figure 5.89 shows the variation trends of the predicted particles counts in each test bar in the mould that obtained from the different modelling conditions. Figure 5.90 shows the trends of the maximum particle concentration in the corresponding conditions. The trends of total particle counts in the test bars were different from the trends of particle concentrations. For example, the total particle counts in Test Bars 1 and 2 were generally greater than those in Test Bars 4 and 5, which can be seen visually in Figure 5.88. However, the maximum particle concentration in these test bars was similar.

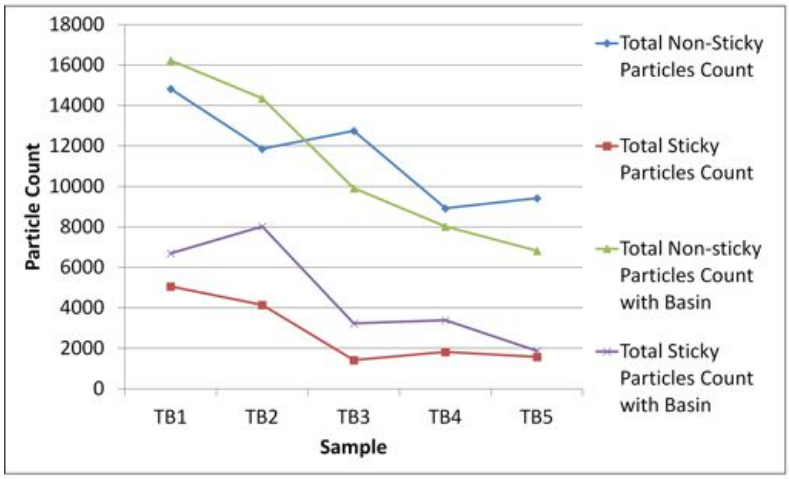

(a)

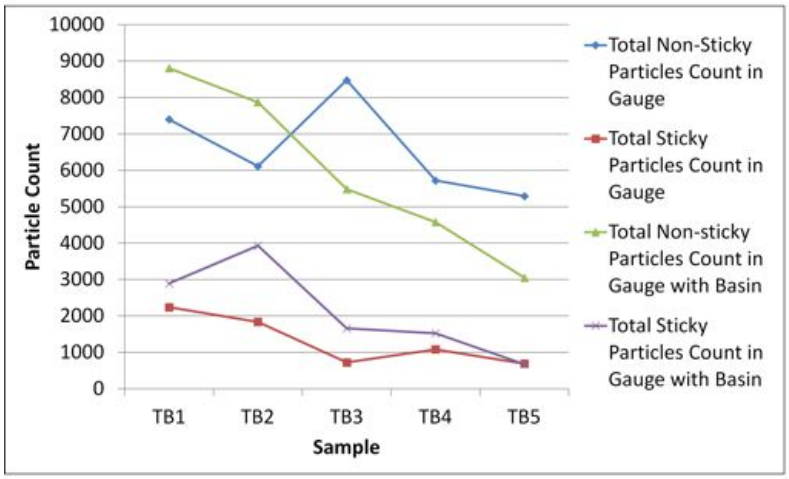

(b)

Figure 5.89: Model predicted particle counts in each test bar in four modelling conditions. (a). total particle counts within whole length of the bars; (b). total particle counts within gauge length of the bars.

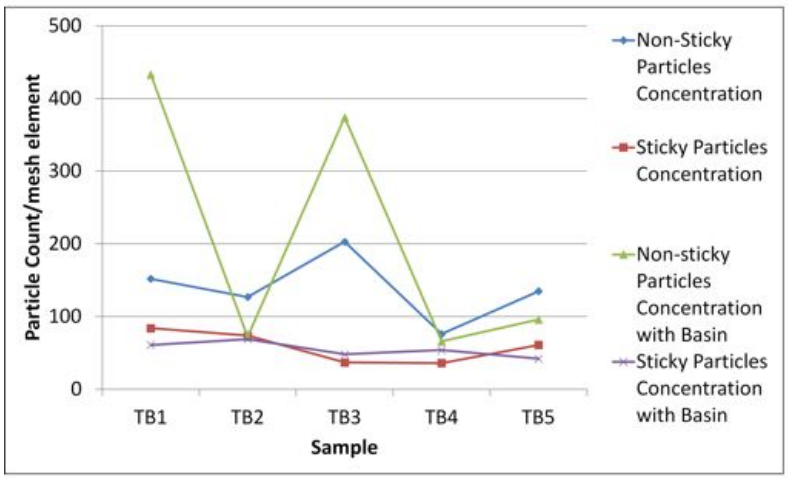

(a)

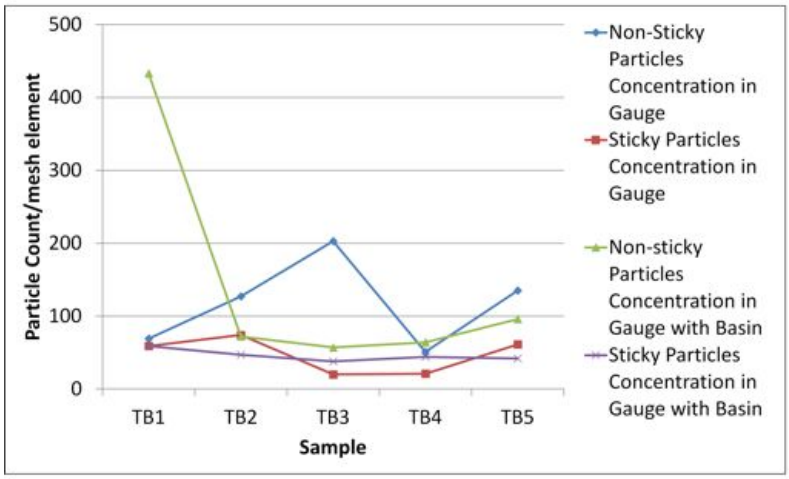

(b)

Figure 5.90: Model predicted maximum particle concentration in each test bar in four modelling conditions. (a). the maximum particle concentration in the bars; (b). the maximum particle concentration within gauge length of the bars.

With regard to the total particle counts in the whole test bars or in the gauge length of the bars, the trends were similar whether non-sticky or sticky particles were used. Although the profiles in Figure 5.88 show that the particles were not evenly distributed inside the test bars, the similar trends obtained from the two volumes (the whole length or the gauge length) suggested that the particles did not aggregate to some specific region in the bars. The trends of maximum particle concentration in the whole test bars or in the gauge length of the bars from left to right showed greater variability, as these trends were more sensitive to extreme values. For instance, the results of the non-sticky particle model that considered entrainment in the pouring basin, shown in Figures 5.90a and 5.90b, revealed an agglomerate of particles distributed outside the gauge length of Test Bar 3 and affected the trend significantly.

Generally, the trends of total particle count and maximum particle concentration obtained from the non-sticky particle model were different from those obtained from the sticky particle model. However, a conclusion about the accuracy of these two models cannot be given as further experimental validation is required.

5.5.6 Comparison between Experimental and Modelling Results

5.5.6.1 Correlation between Modelling and Experimental Results (the 1st group)

Figures 5.91 to 5.94 show the correlation between the median tensile strength of the test bars and the predicted particle counts and maximum particle concentration in test bars from different modelling conditions. The results differentiated between the particles in the whole length of the test bars and only in the gauge length of the test bars. The same scale of the vertical axis is applied in these figures, but different scales for the horizontal axes are used, as the particle counts in the different models varied. In spite of the large variation in the tensile strength of the test bars, the trend lines showed a slight right downward relationship between median UTS and predicted particle counts or particle

concentration, *i.e.* the median UTS of the test bars decreased when the total number of particles or maximum particle concentration in the bars increased. This correlation was found in the models using either non-sticky or sticky particles, and whether the entrainment in the pouring basin was considered or not. The correlation was also found when only considering the particles trapped within the test bar gauge length.

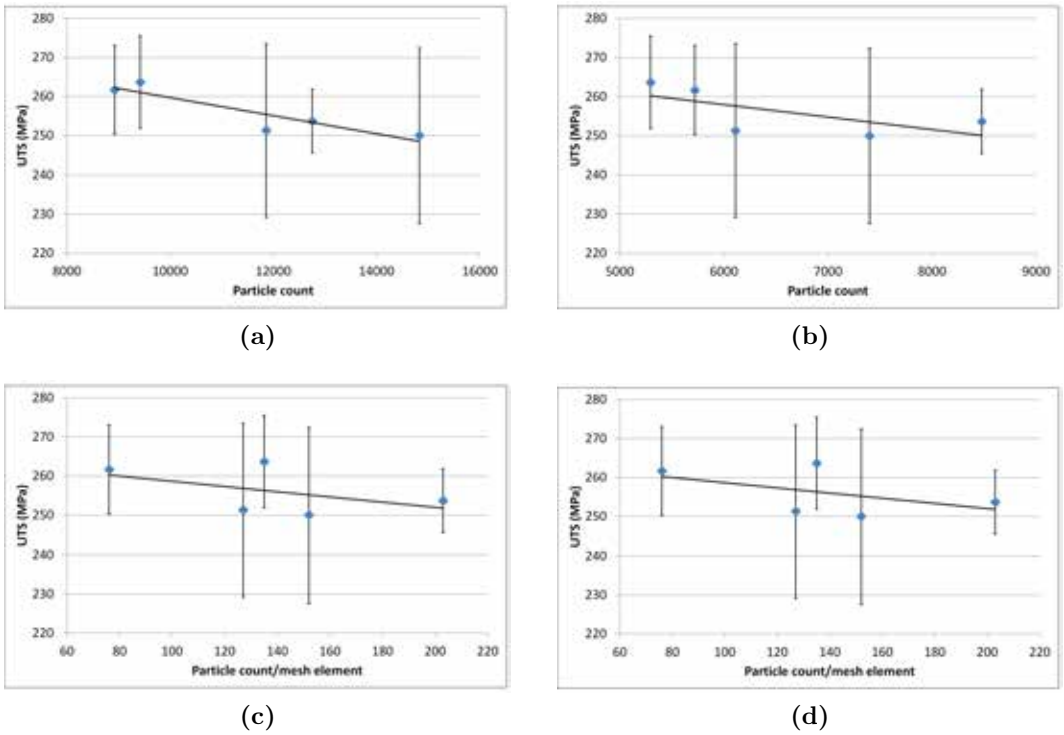

Figure 5.91: Plots of median UTS of the test bars vs. the predicted particle counts and maximum particle concentration obtained from the model using **non-sticky** particles. (the 1st group) The entrainment in the pouring basin **was not** considered. The error bars indicate the standard deviation of the UTS. (a). total particle count; (b). total particle count within the gauge length; (c). particle concentration; (d). particle concentration within the gauge length.

This general relationship agreed with the assumptions that greater particle counts or higher particle concentrations in test bars would adversely affect the mechanical properties of the test bars. However, it must be noted that the low reproducibility of the tensile strength of the test bars in different locations severely reduced the credibility of this relationship. Besides, the slopes of the trend lines for the sticky particles were

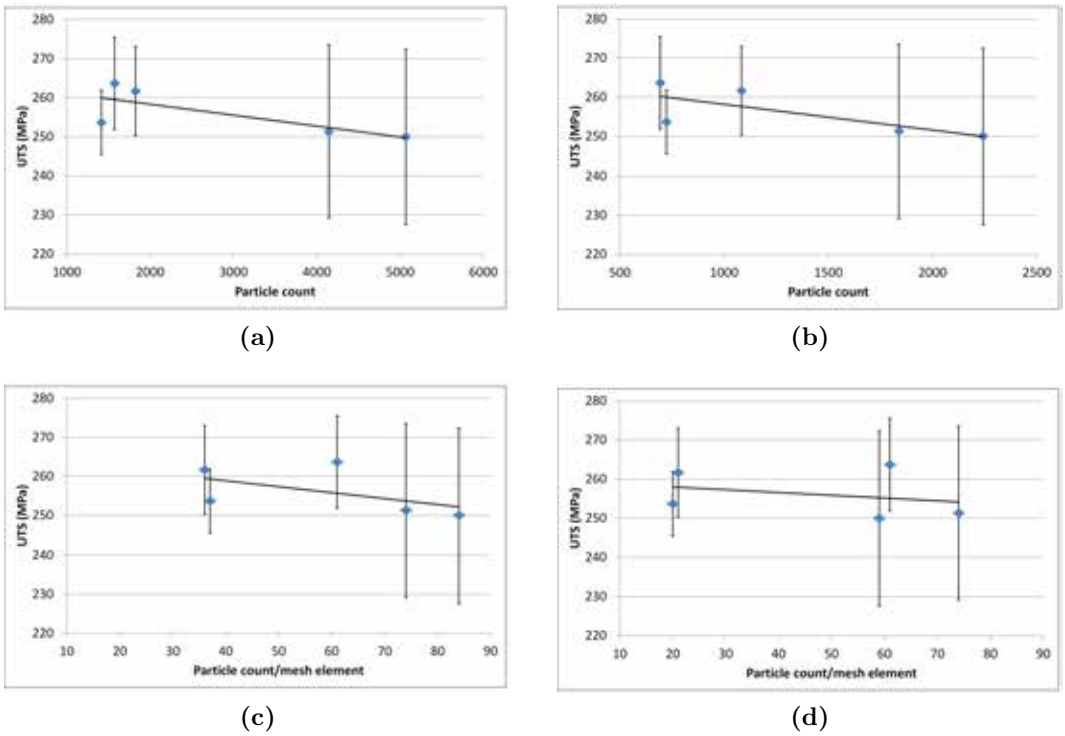

Figure 5.92: Plots of median UTS of the test bars vs. the predicted particle counts and maximum particle concentration obtained from the model using **sticky** particles. (the 1st group) The entrainment in the pouring basin **was not** considered. The error bars indicate the standard deviation of the UTS. (a). total particle count; (b). total particle count within the gauge length; (c). particle concentration; (d). particle concentration within the gauge length.

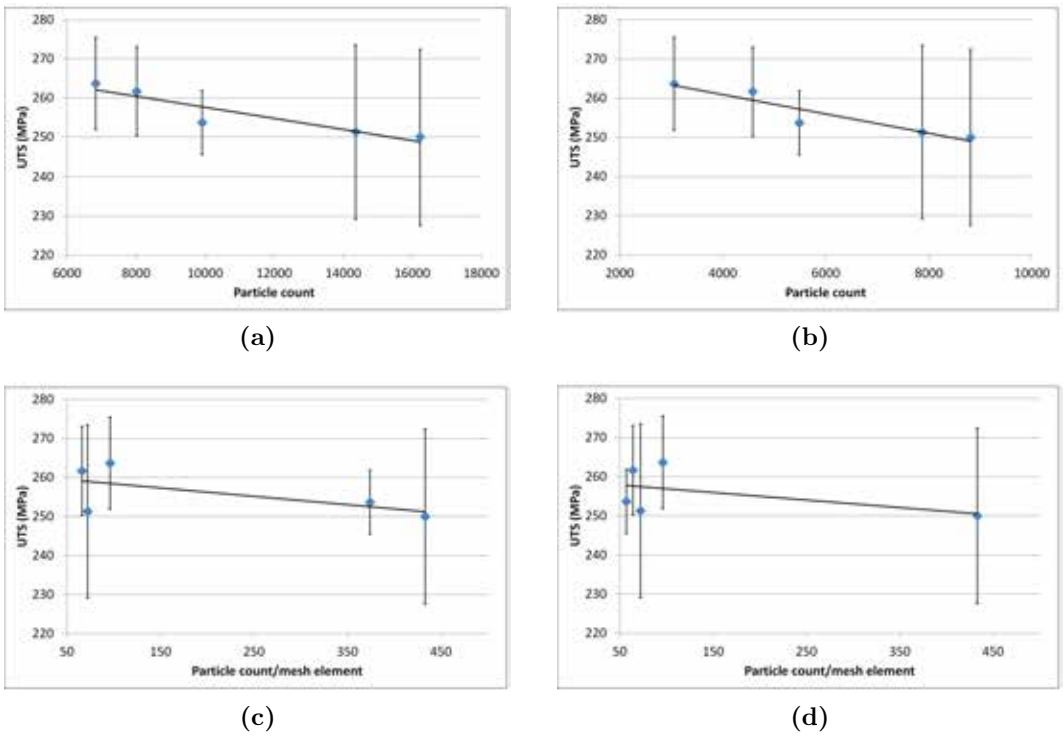

Figure 5.93: Plots of median UTS of the test bars vs. the predicted particle counts and maximum particle concentration obtained from the model using **non-sticky** particles. (the 1st group) The entrainment in the pouring basin **was** considered. The error bars indicate the standard deviation of the UTS. (a). total particle count; (b). total particle count within the gauge length; (c). particle concentration; (d). particle concentration within the gauge length.

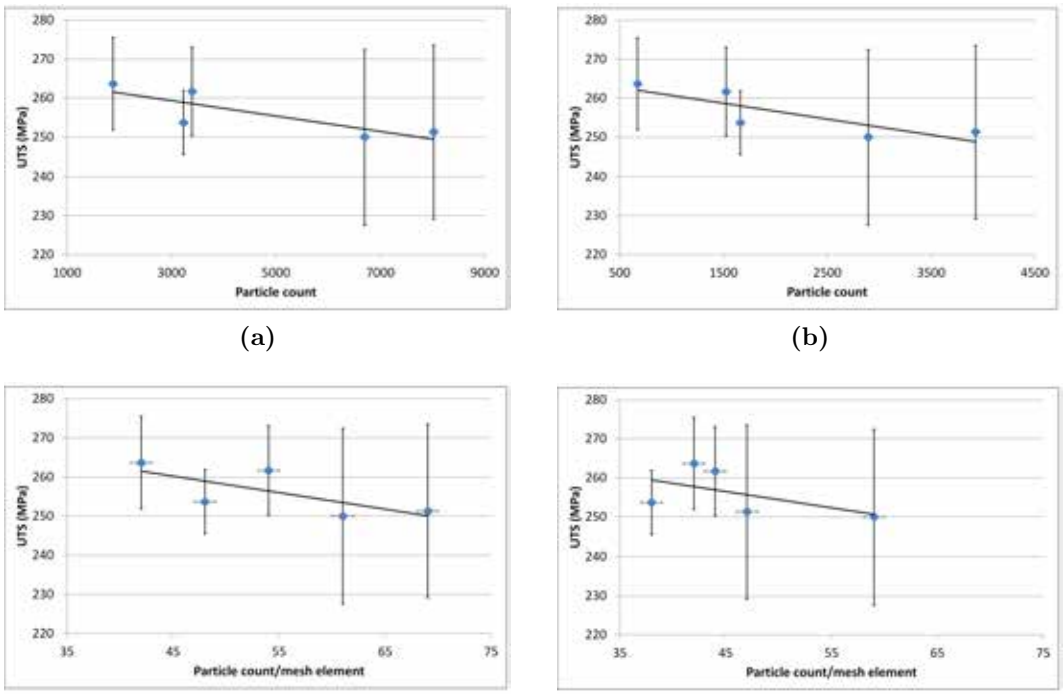

Figure 5.94: Plots of median UTS of the test bars vs. predicted particle counts and maximum particle concentration obtained from the model using **sticky** particles. (the 1st group) The entrainment in the pouring basin **was** considered. The error bars indicate the standard deviation of the UTS. (a). total particle count; (b). total particle count within the gauge length; (c). particle concentration; (d). particle concentration within the gauge length.

flatter than those for the non-sticky particles. The flatter slopes of the trend lines were gained from the results considering the maximum particle concentration, rather than the total particle counts in the test bars.

Figures 5.95 through to 5.98 show the correlation between the elongation of the test bars and the predicted particle counts and maximum particle concentration in test bars for different modelling conditions. The same vertical axis was applied in these figures, and the horizontal axes were the same as the corresponding axes that were used in Figures 5.91 to 5.94. Comparing the trend lines showing the relationship between UTS and predicted total particle counts or particle concentrations, the trend lines of the relationship between the elongation of the test bars and predicted total particle counts and particle concentrations are generally flatter, but also showing gently right downward slopes. The results of sticky particle concentration in the test bars in the models with and without consideration of the entrainment in the pouring basin show flat or even right upward slopes (see Figures 5.96d and 5.98d), contrary to the assumption that large number of defects would lead to low property. This result suggests that the sticky particle model may not be proper for prediction of particle distribution, especially when the filling of the mould was highly surface turbulent.

Comparing the relationships between the experimental results and the modelling results, the results obtained using UTS showed steeper slopes, *i.e.* more significant correlation between the test bar strength and the total particle counts and particle concentrations. Therefore, the UTS of test bars in the current experiment provided more appropriate data for validation of the modelling results, as they are clearer and easier to be compared with the model predictions.

A further analysis of tensile bar mould data was used to validate the predicted mechanical properties of the five test bars in each casting. The model assumed that the tensile strength and elongation of the test bars correlated with the reciprocal of the total particle count or the reciprocal of the maximum particle concentration in

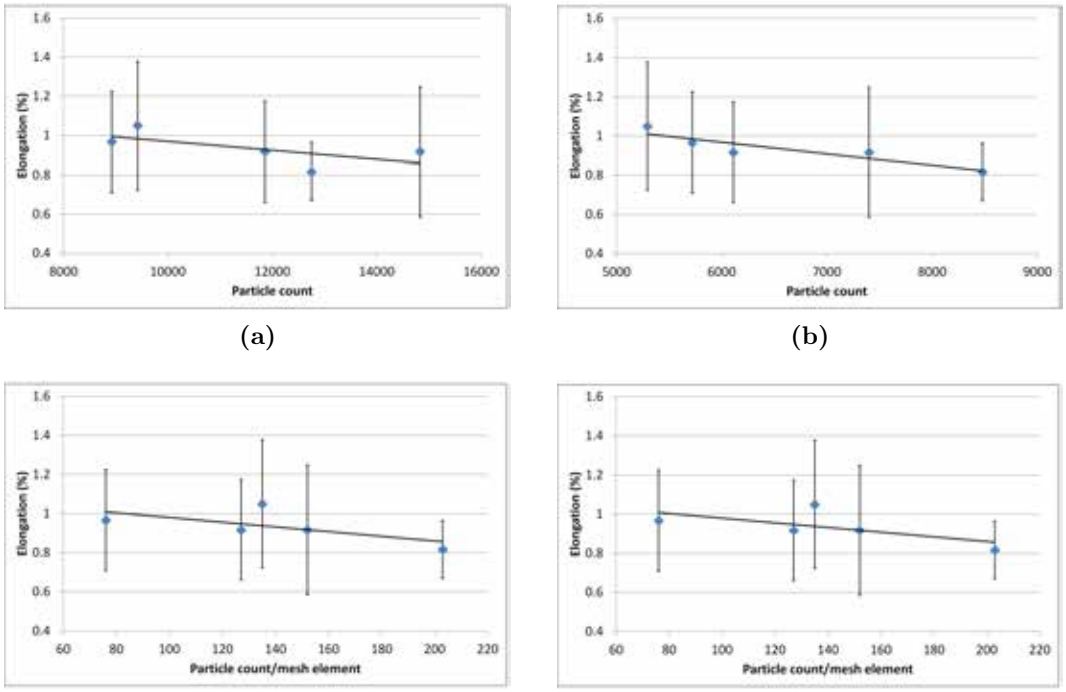

Figure 5.95: Plots of median elongation of the test bars vs. the predicted particle counts and maximum particle concentration obtained from the model using **non-sticky** particles. (the 1st group) The entrainment in the pouring basin **was not** considered. The error bars indicate the standard deviation of the elongation. (a). total particle count; (b). total particle count within the gauge length; (c). particle concentration; (d). particle concentration within the gauge length.

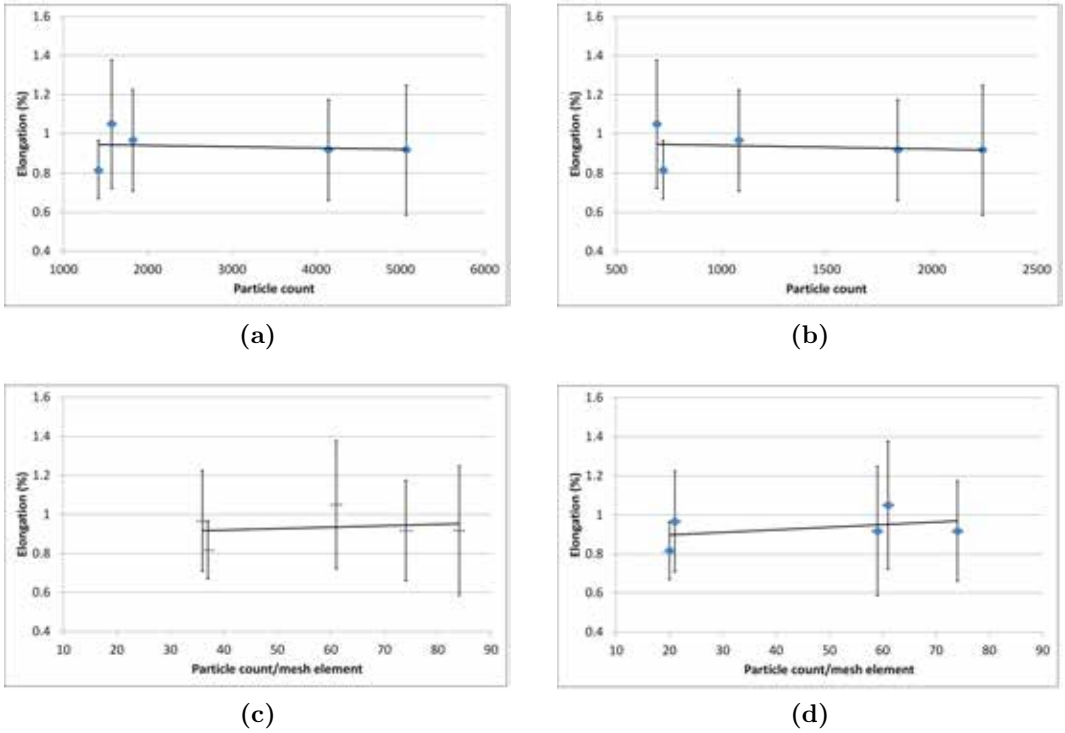

Figure 5.96: Plots of median elongation of the test bars vs. the predicted particle counts and maximum particle concentration obtained from the model using **sticky** particles. (the 1st group) The entrainment in the pouring basin **was not** considered. The error bars indicate the standard deviation of the elongation. (a). total particle count; (b). total particle count within the gauge length; (c). particle concentration; (d). particle concentration within the gauge length.

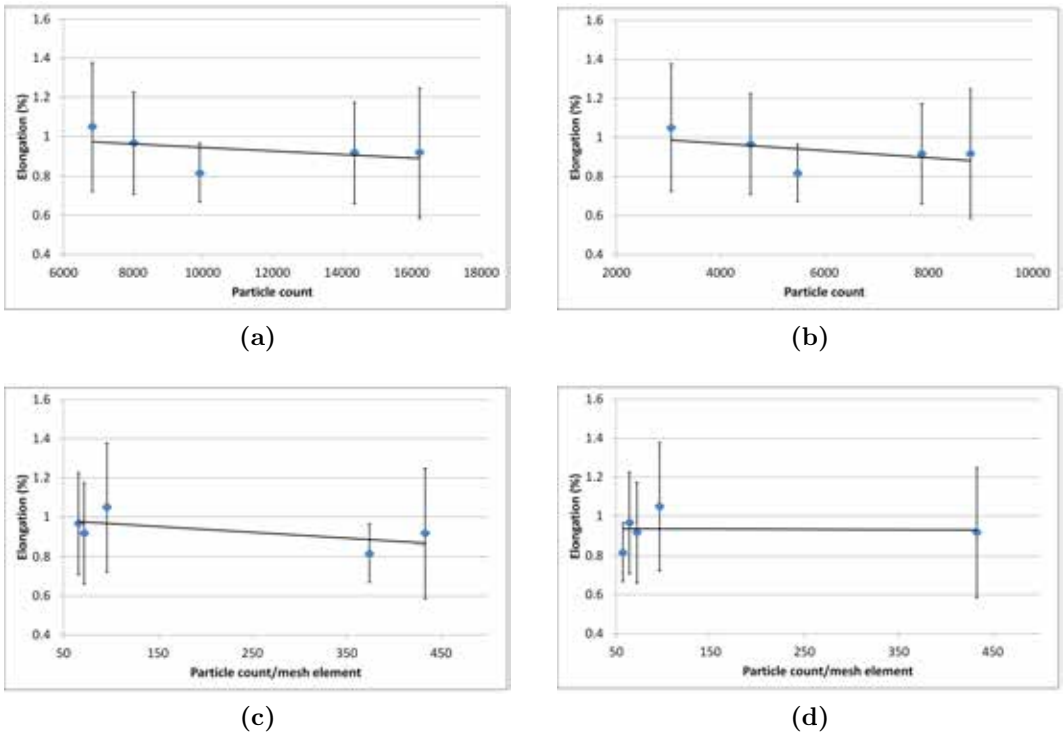

Figure 5.97: Plots of median elongation of the test bars vs. the predicted particle counts and maximum particle concentration obtained from the model using **non-sticky** particles. (the 1st group) The entrainment in the pouring basin **was** considered. The error bars indicate the standard deviation of the elongation. (a). total particle count; (b). total particle count within the gauge length; (c). particle concentration; (d). particle concentration within the gauge length.

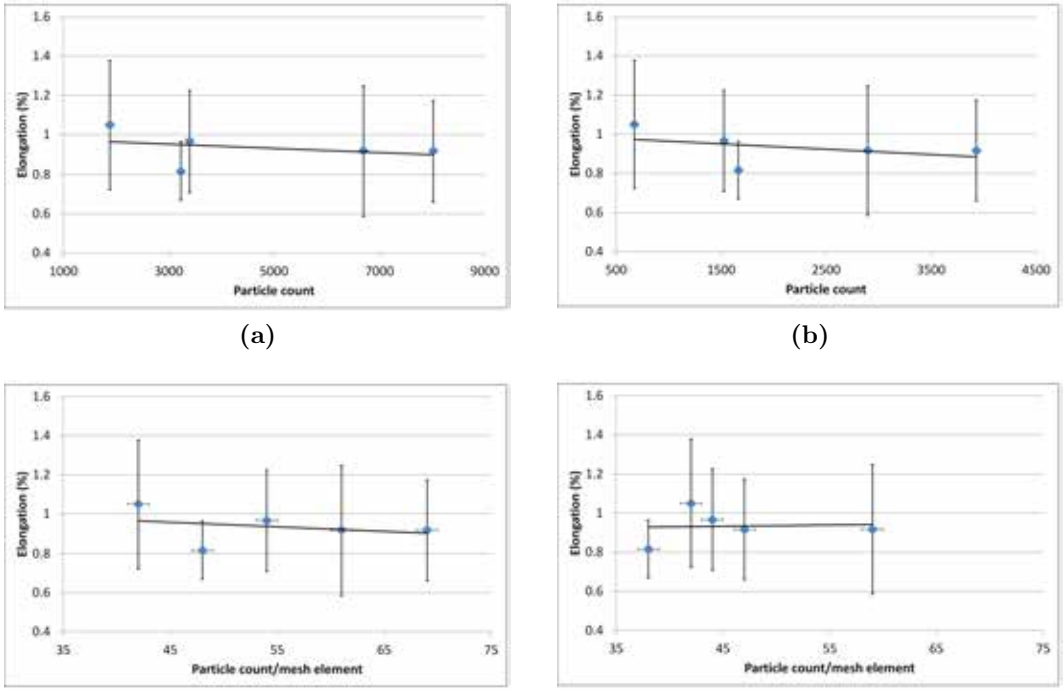

Figure 5.98: Plots of median elongation of the test bars vs. the predicted particle counts and maximum particle concentration obtained from the model using **sticky** particles. (the 1st group) The entrainment in the pouring basin **was** considered. The error bars indicate the standard deviation of the elongation. (a). total particle count; (b). total particle count within the gauge length; (c). particle concentration; (d). particle concentration within the gauge length.

the test bars. Figures 5.99 to 5.102 show predicted UTS and elongation trends for test bar positions 1 to 5. It should be noted that the reciprocal of the particle counts were normalised for a clearer demonstration of the trends in the figures. The absolute values of the reciprocal of the particle counts did not directly link to the mechanical properties of the test bars in the current models.

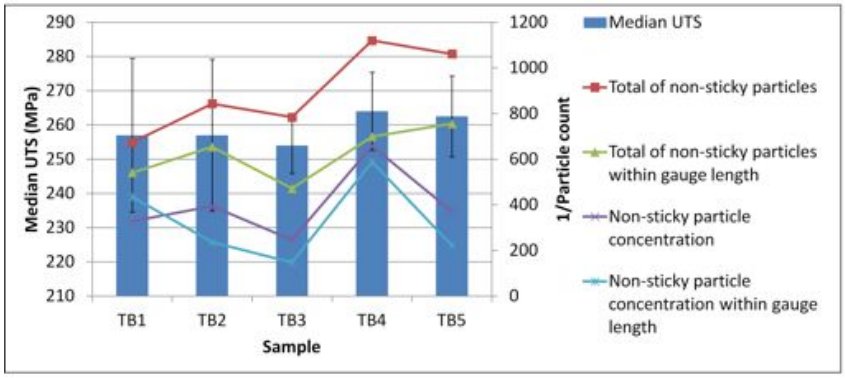

(a)

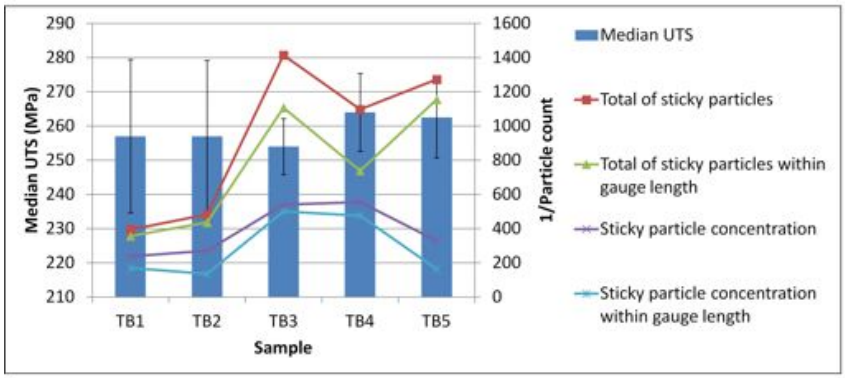

(b)

Figure 5.99: UTS variation of test bars vs. normalised reciprocal of predicted particle counts in the test bars. Entrainment in the pouring basin **was not** considered. (the 1st group) (a). Median UTS vs. normalised reciprocals of **non-sticky** particle counts; (b). Median UTS vs. normalised reciprocals of **sticky** particle counts.

It can be seen that the four models predicted four different trends. Further interpretation of each result, by considering the total particle counts and maximum particle concentration within each bar, also showed distinct trends, as the test bar with the highest particle concentration was not necessarily the one that contained the most particles. The predicted particle counts within the whole length of test bars were generally

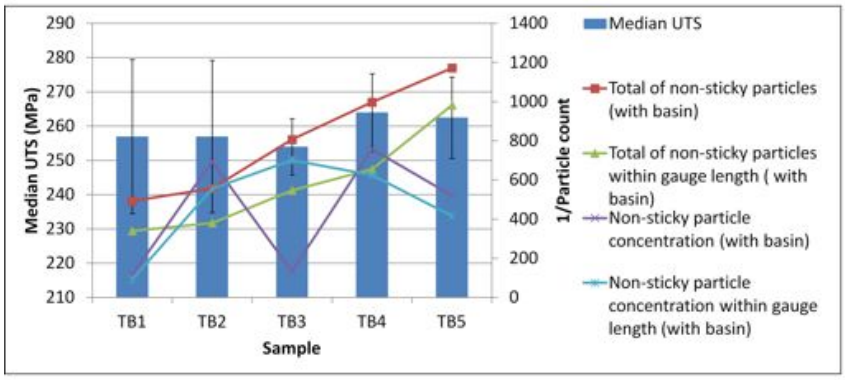

(a)

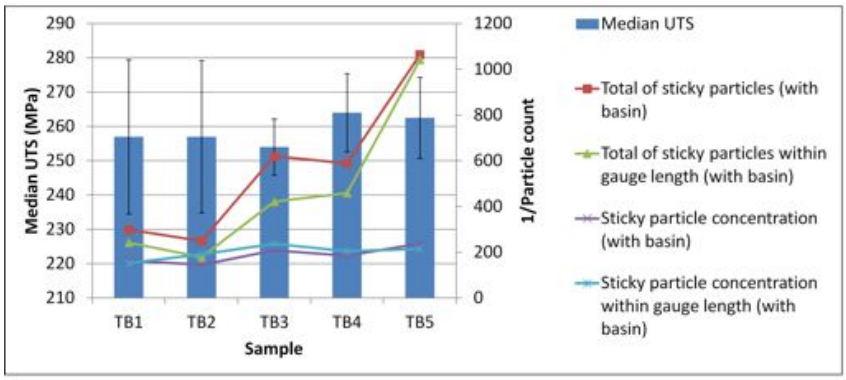

(b)

Figure 5.100: UTS variation of test bars vs. normalised reciprocal of predicted particle counts in the test bars. Entrainment in the pouring basin **was** considered. (the 1st group) (a). Median UTS vs. normalised reciprocals of **non-sticky** particle counts; (b). Median UTS vs. normalised reciprocals of **sticky** particle count.

in agreement with the trends that only considering particles within the gauge length. However, the trends for the maximum particle concentrations were easily affected by some clusters of particles outside the gauge length as mentioned before, as shown in Figures 5.100a and 5.102a.

The trend in Figure 5.99a roughly agrees with the variation in median UTS of the test bars. But other predicted UTS trends did not correlate the experimental results, and none of the trends correlated the elongation trends of test bars. Due to the inconsistent mechanical properties of test bars, it was difficult to provide a definite conclusion for the validity of the different models and their prediction of mechanical properties of castings.

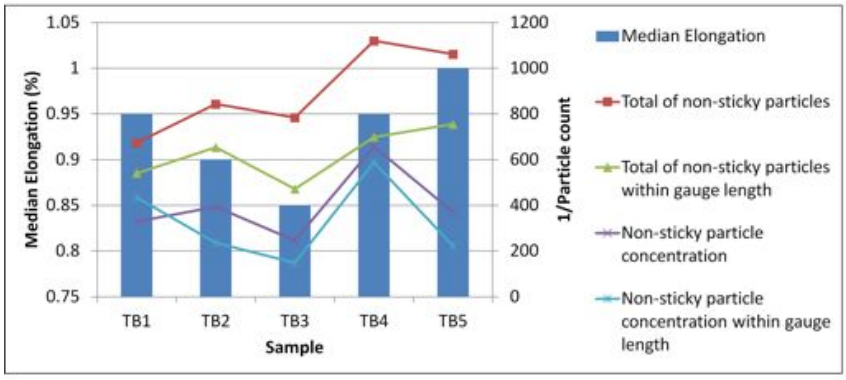

(a)

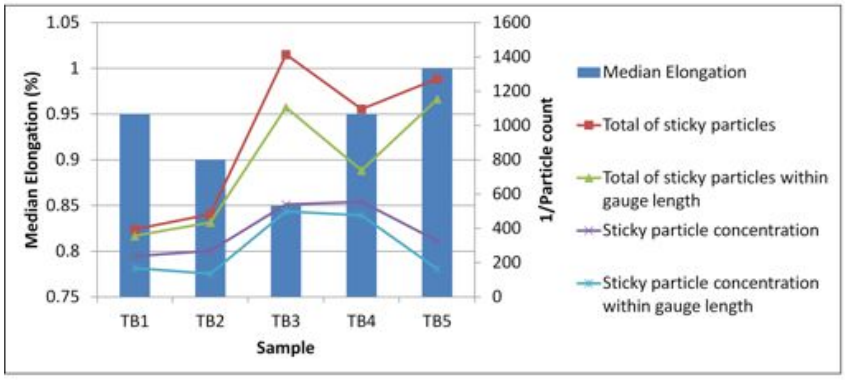

(b)

Figure 5.101: Elongation variation of test bars vs. normalised reciprocal of particle counts in the test bars. Entrainment in the pouring basin **was not** considered. (the 1st group) (a). Median elongation vs. normalised reciprocals of **non-sticky** particle counts; (b). Median elongation vs. normalised reciprocals of **sticky** particle counts.

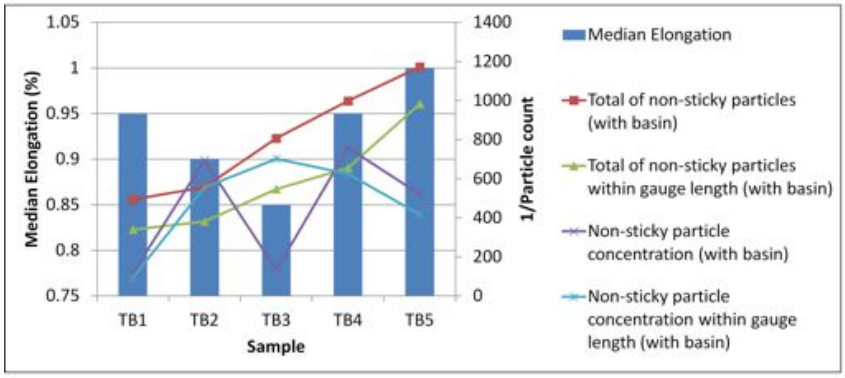

(a)

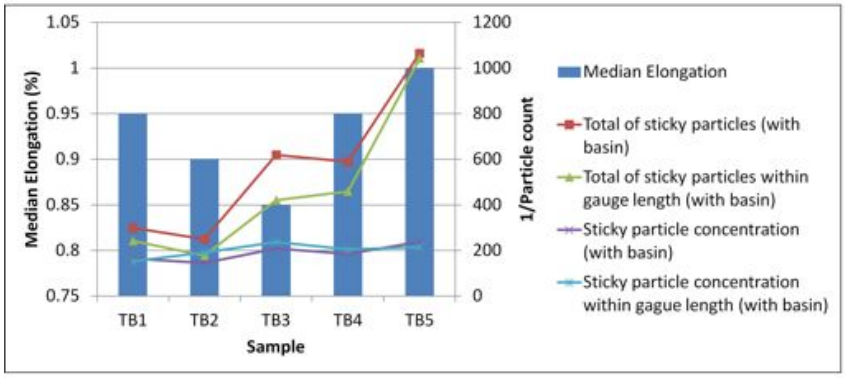

(b)

Figure 5.102: Elongation variation of test bars vs. normalised reciprocal of particle counts in the test bars. Entrainment in the pouring basin **was** considered. (the 1st group) (a). Median elongation vs. normalised reciprocals of **non-sticky** particle counts; (d). Median elongation vs. normalised reciprocals of **sticky** particle count.

5.5.6.2 Correlation between Modelling and Experimental Results (the 2nd Group)

As mentioned in the previous section, the results from the sticky particle model may not predict the mechanical properties of castings correctly, and the elongation results may not be reliable for model validation. Therefore, only the plots of non-sticky particles against UTS are shown in this section. Figures 5.103 and 5.104 show a correlation between median tensile strength of the test bars and the predicted particle counts and maximum particle concentration in test bars using the non-sticky particle model. The horizontal axes in these figures are the same as those used in Figures 5.91 through to 5.94, and the same range of scale of the vertical axes was used. Similar to the correlation of the 1st group of castings with the model, a slight right downward trend line could be plotted in each of the figures. This relationship indicates, firstly, a consistent distribution of UTS of the test bars achieved in the two different groups of castings; secondly, the particle counts or maximum particle concentration in the model could link to the mechanical properties of castings, although the relationship between the particle count and mechanical properties may not be simply inversely proportional.

This relationship observed in the plots considered the total particle count in the whole length and in the gauge length of the castings. But the slopes of the trend lines plotted by the particle counts within the whole length of the test bars were marginally steeper. This was also found in the plots of maximum particle concentration against UTS with consideration of particle in the whole test bar length or in the gauge length. This implies that the prediction of particle distribution may not yet be accurate. The slopes of trend lines obtained from models with or without consideration of particle entrainment in the pouring basin were nearly the same. The slopes of trend lines in the figures from the 2nd group of castings were similar to those in the 1st group of castings.

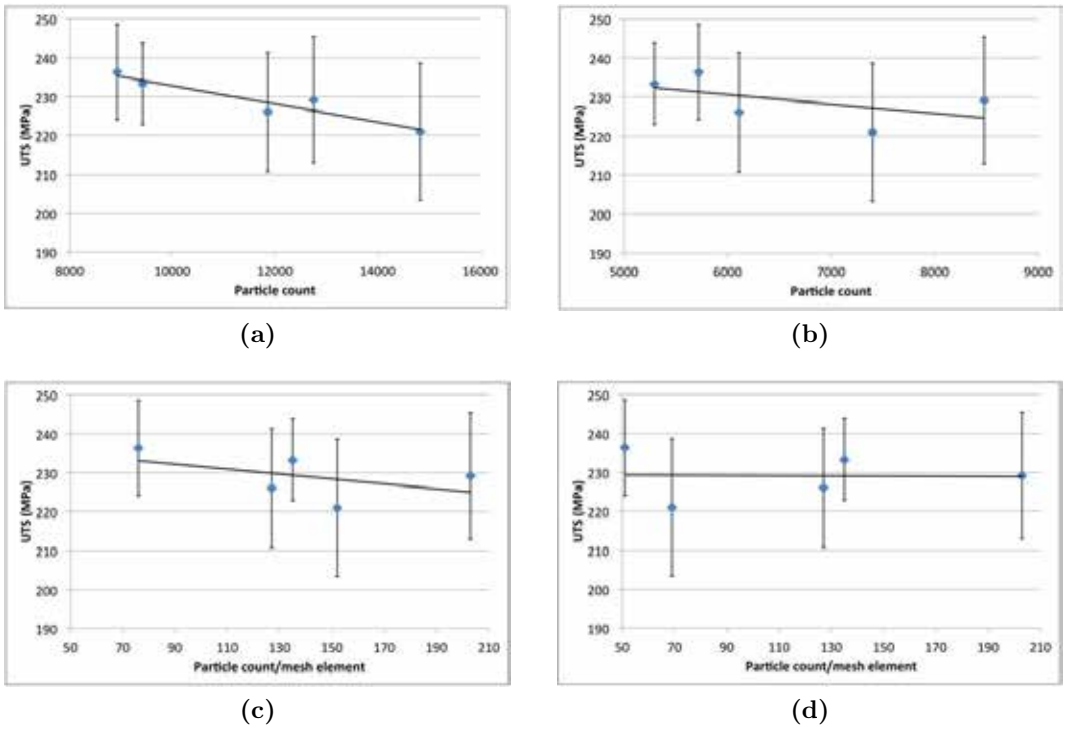

Figure 5.103: Plots of median UTS of the 2nd group test bars vs. the predicted particle counts and maximum particle concentration obtained from the model using **non-sticky** particles. The entrainment in the pouring basin **was not** considered. The error bars indicate the standard deviation of the UTS. (a). total particle count; (b). total particle count within the gauge length; (c). the maximum particle concentration; (d). the maximum particle concentration within the gauge length.

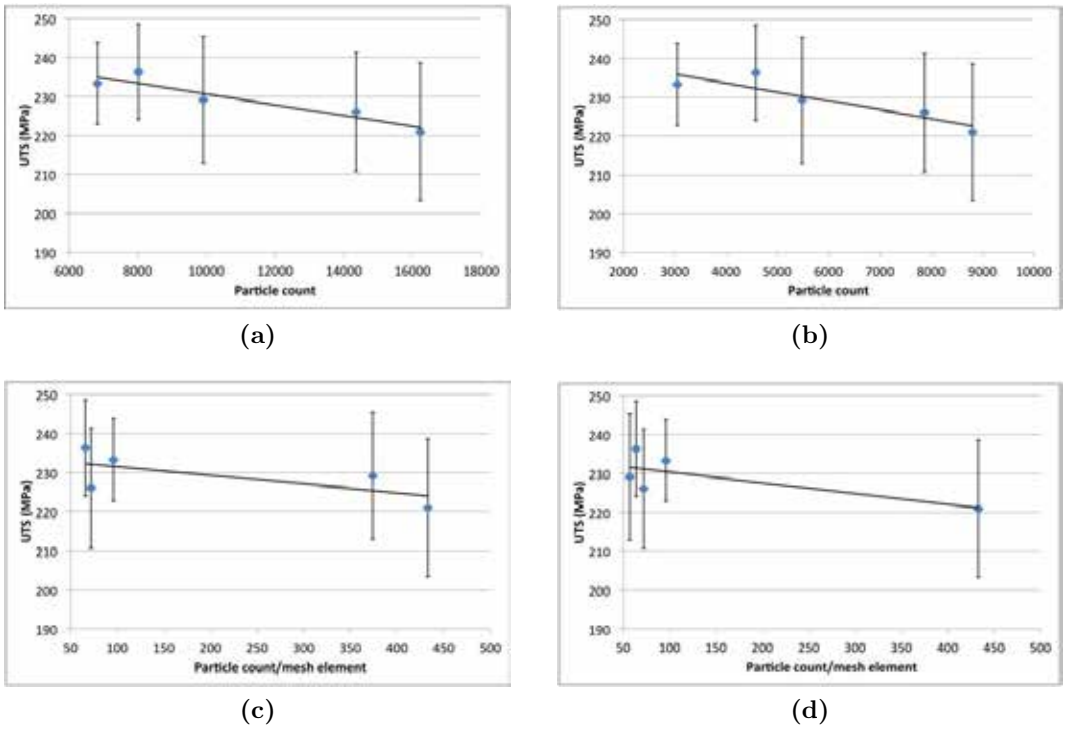

Figure 5.104: Plots of median UTS of the 2nd group test bars vs. the predicted particle counts and maximum particle concentration obtained from the model using **non-sticky** particles. The entrainment in the pouring basin **was** considered. The error bars indicate the standard deviation of the UTS. (a). total particle count; (b). total particle count within the gauge length; (c). the maximum particle concentration; (d). the maximum particle concentration within the gauge length.

Figure 5.105 compares the median UTS variation of test bars at different locations with predicted trends of mechanical properties. As mentioned before, the median UTS of the five test bars increased from TB1 to TB5. The trends of maximum particle concentration in the test bars did not show this tendency. On the contrary, considering the total particle counts in the whole length or within the gauge length of the test bars, shown in Figure 5.105a, models predicted that TB4 and TB5 had higher mechanical properties than TB1 and TB2, but the model predicted that TB3 had the lowest properties compared to the other four bars, which was not observed in the experimental results. The prediction of the model considering entrainment defects generated in the pouring basin, shown in Figure 5.105b, showed better correlation with the experimental results, which showed that the UTS of five test bars increased from left to right, though it did not reflect the higher strength of TB4 than TB5. Since the trends of the 1st and 2nd groups of castings were similar, but different in some locations, it is difficult to conclude that total particle counts in the test bars predicted by the model considering the entrainment in the pouring basin had the highest accuracy. Further validation experiments with a smaller scatter of properties are still required.

5.5.7 Pouring Position Sensitivity Study

The pouring position sensitivity study showed that different pouring positions of the crucible resulted in a similar quantity of particles generated, (approximately 230 000 in the mould), but distinct numbers of particles trapped in each test bar. Table 5.26 lists the particle counts and maximum particle concentrations in each test bar obtained from the different pouring positions models, and shows the total particle count in each bar was quite different, but of the same magnitude, *i.e.* approximately 12 000 to 17 000 particles in Test Bars 1 and 2, and several thousand of particles in Test Bars 3, 4 and 5. However, the magnitude of the maximum particle concentration form the models varied, from tens to thousands of particle trapped within one element. This led to distinct particle distribution patterns in the castings predicted by considering

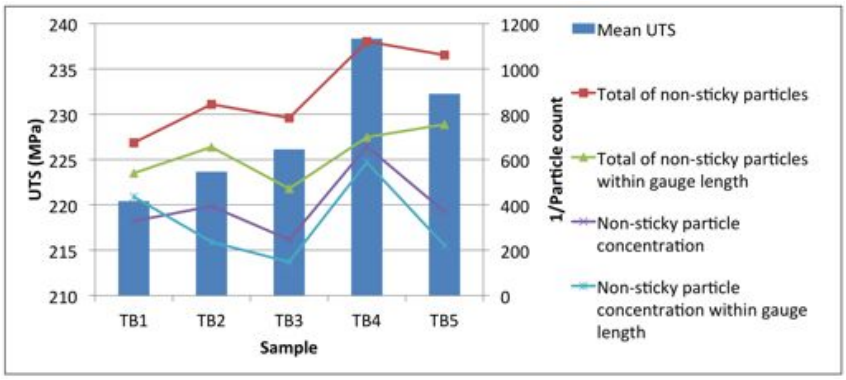

(a)

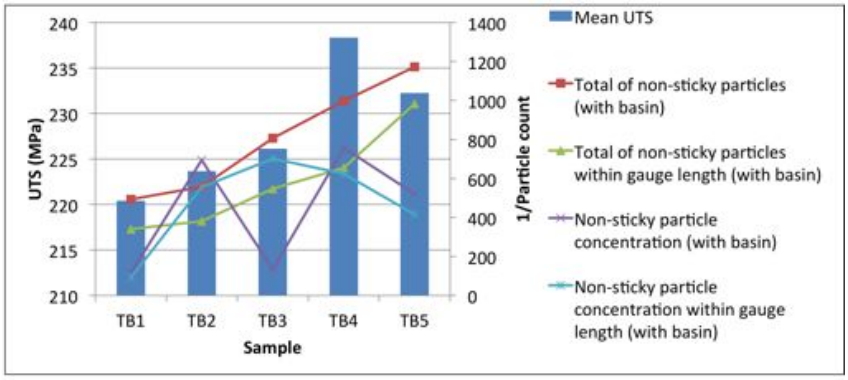

(b)

Figure 5.105: UTS variation of test bars vs. normalised reciprocal of particle counts in the test bars. (the 2nd Group). (a). UTS vs. normalised reciprocals of **non-sticky** particle counts; (b). UTS vs. normalised reciprocals of **non-sticky** particle counts with consideration of entrainment in basin.

particle concentration in each bar, as shown in Figure 5.106b, which showed a random variation of UTS in each test bar. The curves also showed two outliers of the particle concentration, 1380 and 1081 in Table 5.26, in the model with pouring position moved 10 mm in $x+$ direction.

Figure 5.106 shows the variation trends of predicted total defect quantities and maximum defect concentrations in each test bar from the models using different initial pouring positions. In terms of the trends predicted by the total particle counts, although there was some variation among individual trends, the general pattern shows that more particles were trapped in the test bars on the left (Test Bars 1 and 2) than in those on the right side (Test Bars 4 and 5), which is the same as the original modelling

Table 5.26: The particle counts and maximum particle concentration in the test bars from different pouring position.

ID	Total Particle Count	Total Particle Count in the Gauge Length	The Maximum Particle Concentration	The Maximum Particle Concentration in the Gauge Length
TB1 $x+$	13562	5976	755	95
TB2 $x+$	17840	8736	1380	526
TB3 $x+$	10773	6218	1081	1081
TB4 $x+$	5816	3133	82	77
TB5 $x+$	4296	2116	45	45
TB1 $x-$	14547	7617	266	93
TB2 $x-$	15039	7528	371	90
TB3 $x-$	8368	5369	107	107
TB4 $x-$	7753	3697	75	75
TB5 $x-$	5886	2661	137	137
TB1 $y+$	11173	5630	84	84
TB2 $y+$	13082	6866	90	79
TB3 $y+$	8130	4868	71	71
TB4 $y+$	6307	3319	80	80
TB5 $y+$	6717	3106	90	90
TB1 $y-$	12392	6342	81	57
TB2 $y-$	14669	8056	99	99
TB3 $y-$	6602	4231	118	69
TB4 $y-$	6569	4061	63	63
TB5 $y-$	5629	2856	52	52
TB1 $z+$	13634	7912	139	139
TB2 $z+$	12646	6995	54	54
TB3 $z+$	6167	3956	102	51
TB4 $z+$	5390	2942	81	45
TB5 $z+$	6880	3610	65	65

results from the model using non-sticky particles with consideration of entrainment in pouring basin, and correlated with the experiment results shown in Figure 5.87. In

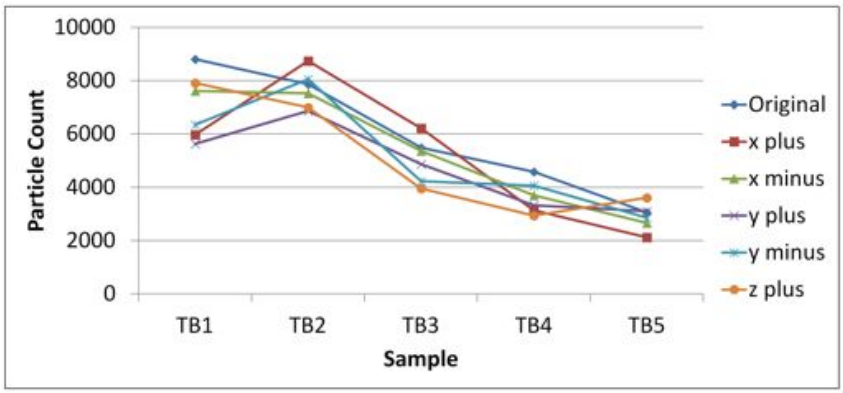

(a)

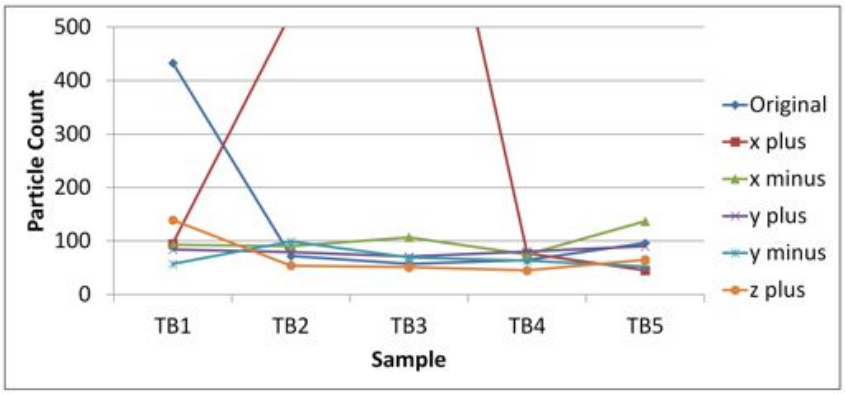

(b)

Figure 5.106: Different model predicted particle counts and particle concentrations in gauge length in each test bar. (a). the total particle count; (b). the maximum particle concentration.

the experimental results, the difference between the median UTS of test bars in the 1st and 2nd groups of experiments were around 15 MPa, which was about 6% of the strength of the bars. However, the predicted maximum particle count in the test bars was twice the number of the minimum particle count in bars. This has been observed in all models with different initial pouring positions. Weibull analysis confirmed the variation in particle quantity, as the Weibull modulus of the particle counts in the 30 test bars in the model (original position and five with varied pouring positions) was 2.9, much lower than 18, from the analysis of the experiments. The greater variation

of particle concentration in the test bars resulted in a even lower Weibull modulus of 1.3. This result suggests that currently the particle quantity in a test bar still cannot be linked to specific materials properties.

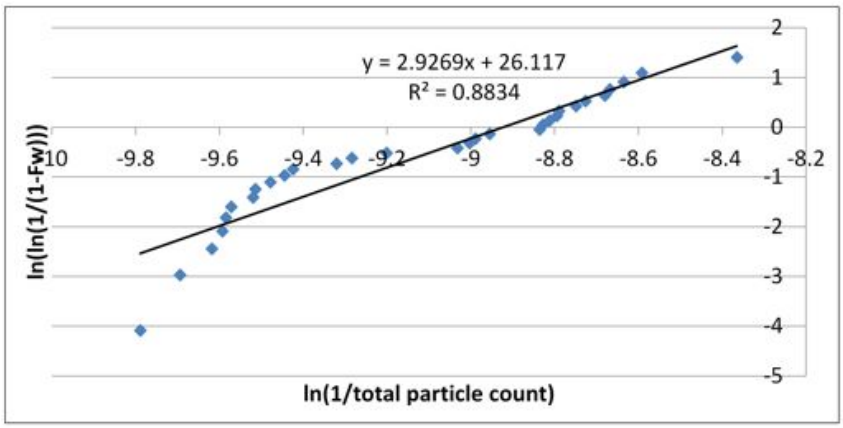

(a)

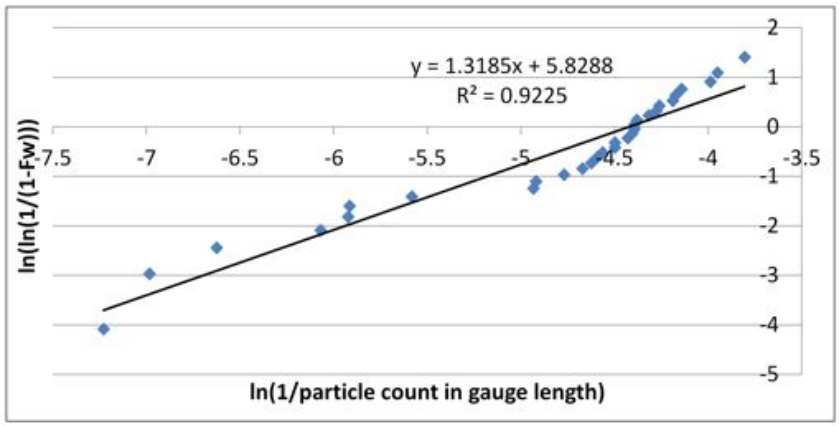

(b)

Figure 5.107: Different model predicted particle count and particle concentration in gauge length in each test bar. (a). total particle count; (b). maximum particle concentration.

Chapter 6

Discussions

Discussion of the results is divided into two parts: *i*). modelling of entrainment and associated defects and *ii*). characteristics of entrainment defects. The first part discusses entrainment during casting and the formation mechanisms of entrainment defects, then considers the entrainment criteria used in the model. The capability and accuracy of the oxide film entrainment model (OFEM) is discussed. The second part focuses on the characteristics of entrainment defects revealed through X-ray micro-tomography and image analysis. The driving force for change in morphology and size evolution of entrainment defects in the liquid alloy is discussed.

6.1 Entrainment in Casting Processing and Fluid Model

6.1.1 Formation Mechanisms of the Entrainment Defects

Entrainment in the casting process occurs during transfer of the liquid alloy from the crucible to the mould cavity, in which both gas bubble and solid particles (or debris of solid oxide films) are entrapped into the melt, forming micro-bubbles and inclusions respectively. Campbell proposed the concept of entrainment defects, and stated these defects are principally bubble and bubble trails, double oxide films and some entrained debris [7]. However, traditionally, entrainment defects mainly refer to double oxide film (bifilm) defects in most research, and the formation mechanism of entrainment

defects are accordingly associated with the folding of free surfaces owing to surface turbulence as reviewed in Section 2.1.1 [6]. The Weber number can be used to describe the breaking surface, in which some local melt rises above the general level of the liquid surface and falls back to entrap a portion of the surface film, as used in the definition of the "critical velocity" in the casting process by Runyoro *et al.* and Campbell [6, 82]. This description focuses on the uprising liquid jet. Bubble entrainment and other severe entraining scenarios may be underestimated, such as the plunging jet shown in Figure 2.4a. To fully consider entrainment in the casting process, it is necessary to consider bubble entrainment into the melt and its associated entraining mechanisms. Since the entrainment of air bubbles occurs at the interface between the two phases, while the free surface of liquid aluminium alloy is always covered by an oxide film, the entrainment of air bubbles also involves the entrapment of oxide film. In this process, the oxide film may be further broken into pieces instead of entraining in as folded large films.

Study of hydraulics has showed air bubbles can be entrained into bulk liquid flow by plunging jets, high speed flow in open channels, or by liquid jets discharging into the atmosphere [31]. The latter two mechanisms might be seen in high pressure die casting, while the commonly seen scenario in gravity casting is the plunging jet flow. In hydraulics, a plunging jet is defined as a liquid jet impacting or impinging into a receiving pool of liquid [31]. Therefore, although the three entrainment mechanisms studied in Sections 5.1.1 and 5.3 entered the mould cavities from different directions and showed different surface turbulence levels, they were similar in terms of the momentum of fluid and free surface, both in the running systems and in the mould cavities. This facilitates the simulation of air bubble entrainment in the model. Comparing with models that only considered folding mechanisms, *i.e.* Lin's and Dai's models (Section 2.2.3.2), and Ohnaka's model (Section 2.2.3.3), the additional consideration of the air entrainment obviously complicates the model, but meanwhile provides physically meaningful

information about entrainment of both oxide films and air bubbles in casting. In fact, the plunging jet flow scenarios have been considered by the OFEM algorithm in its entrainment criteria, which are defined as the 12 Impingement forms. The Impingement forms describe the plunging jet as that having both velocity directions and free surfaces in two mesh cells converging to one position, as shown in Figure 6.1, where a liquid jet impacts vertically on the liquid pool.

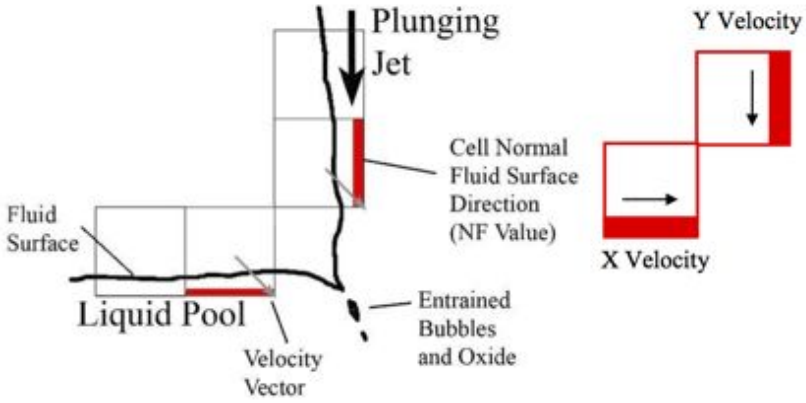

Figure 6.1: Example of a plunging jet and the description of its characteristics in the model (Entrainment Form 38) [8].

6.1.2 Entrainment Forms in OFEM

Preliminary modelling results in Section 5.1.1 showed that the majority of particles were placed by Impingement forms regardless of the moulds used and the filling patterns generated in the mould cavities. This highlighted the significance of the plunging jet type of flow in entraining surface film defects. The initial definitions of the three types of free surface interaction mechanisms in the model was aiming at simulating the formation of double oxide films, where Colliding Fronts and Shear Flow forms were supposed to capture the face-to-face encounter of two liquid fronts, while Impingement forms were used to catch the perpendicular impact of two free surfaces. However, the falling back of liquid fronts in the rising jet mould, which was believed to involve extensive collision of free surfaces, did not lead to more particles generated by the

Colliding Fronts forms in the OFEM algorithm. The returning back waves in the return wave moulds also did not show large amounts of particles entrained by the Shear Flows form in the model.

The decisive effect of Impingement forms in placing particles in the different models can be explained as the combination of two factors. Firstly, as mentioned before, different entrainment patterns bear similarity in terms of momentum of fluid. For example, a vertical dropping jet or plunging jet can be captured by the Impingement form in OFEM as described in Figure 6.1, while a horizontal returning back wave can also be captured in the similar way as demonstrated in Figure 6.2, where the velocity of flow in the horizontal plane towards the x-direction and the returning front moves downwards under gravity in the minus y direction, rolling the surface film into the bulk liquid pool. Since the orientation of free surfaces and velocity components in the flow correlated with the defined criteria in OFEM, the algorithm treats the return wave in Figure 6.2 without discrimination compared to the plunging jet shown in Figure 6.1. The explanation is also applicable if a coarse mesh is used in the same model, as the algorithm focuses on the direction of the velocity components rather than the absolute speed, and hence, the rolling pattern in Figure 6.2 in a coarse mesh can still be entraining.

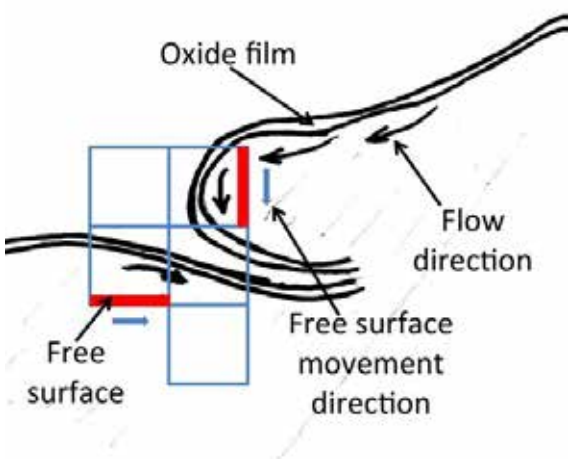

Figure 6.2: Sketch of the Impingement form capturing a return wave in model in 2D.

Secondly, the similarity of flow patterns was also reflected in similar Impingement forms in the algorithm. It is clear from Figure 5.1 that the Entrainment Forms 38, 39, 41 and 44 were dominant among all the Impingement forms in almost every model. As illustrated in Figure 6.3, these four forms show the same pattern, in that the vertical surface at a higher position moves downwards and the level surface in the orthogonal direction moves horizontally towards the vertical surface simultaneously. The two surfaces then converge at a corner cell in the next time step. The downwards movement of the vertical free surface was due to the effect of gravity in the minus y direction. Section 5.1.2 compared the results of models with the gravitational force set along the x direction, and the results in Figure 5.2 show there were another four forms that placed most of the particles. But these forms were comparable with previous ones, as they are inter-convertible. Figure 6.4 shows the transformation of Form 40 into Form 38 when the gravity direction changed from the minus y to the x direction. Both the flow and entrainment form similarities reveal that the plunging jet type of flows dominate the entrainment of surface films during mould filling.

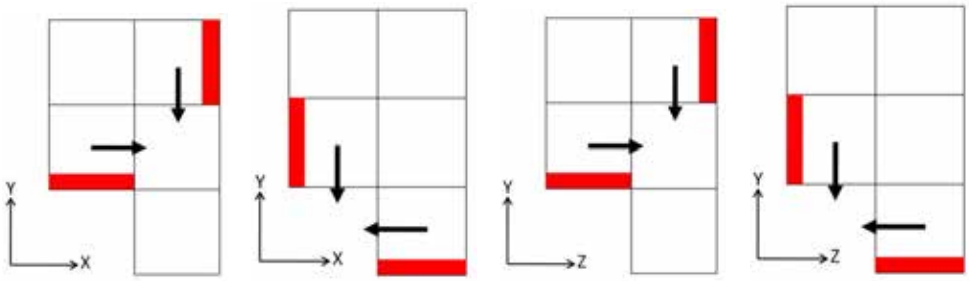

Figure 6.3: The definition of four important entrainment forms when the gravitational force set along y-axis in 2D view. Red strips represent free surfaces. (a). Form 38; (b). Form 39; (c). Form 41; (d). Form 44.

It should be noted that during mould filling each entrainment mechanism can not be strictly isolated from other mechanisms, especially in a mould with several ingates and complex geometries. In simple moulds as used in the study of OFEM, the application

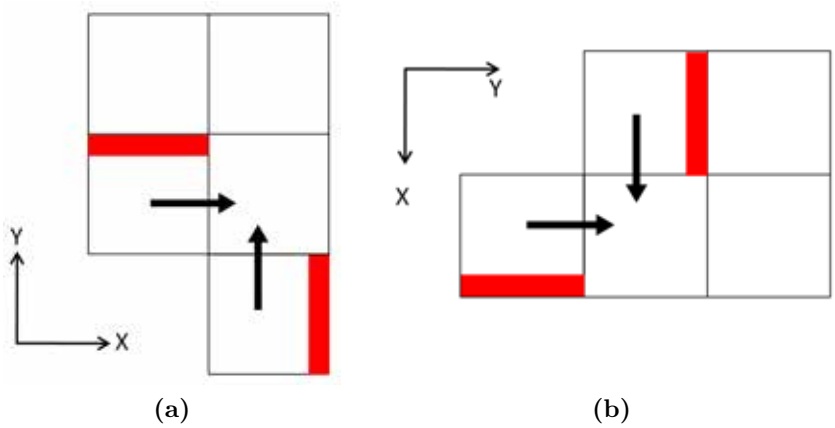

Figure 6.4: The definition of four important entrainment forms when the gravitational force set along y-axis in 2D view. Red strips represent free surfaces. (a). Form 40 (gravity along y-minus direction); (b). Form 40 (gravity along x direction).

of the down sprue in three moulds resulted in a plunging jet flow, the horizontal runner generated returning back wave when the liquid front collided with the far end of the mould wall and was reflected. The rising jet also resulted in return waves in the plate-shape mould cavity, when the fluid moved separately towards the two sides of the plate. As significant entrainment mechanisms, the general plunging jet types of flows are very common in the filling scenario. These flow patterns can be captured by the Impingement entrainment forms, and hence, most of the particles were placed by Impingement forms in the simulations.

In addition, the definition of Impingement forms in the algorithm is descriptive and only focuses on the velocity vector convergence of adjacent mesh cells, which is considered to be not as rigorous as those of the Colliding Fronts and Shear Flows forms. This is because of the difficulties in developing robust and accurate descriptions of the relative movements of free surfaces [8]. The definitions of Colliding Fronts and Shear Flow forms require two free surfaces positioned in parallel in adjacent mesh elements, which are rare in simulation. Simulation results reported in Section 5.1.3 showed that particles could be placed by these two types of entrainment forms, but are sparse and

may require an "ideal" flow pattern within the mesh. For example, the particle in the red circle in Figure 6.5b (Figure 5.5 reprint here), was placed by Shear Flow forms and could only be achieved when gravity forces were neglected in the model. This observation also explains why there were very limited number of particles placed in Ohnaka's model, as the entrainment forms defined in his model were quite similar to the definitions of Colliding Fronts forms in OFEM [102], and were the only mechanisms used to capture entrainment in the models. Compared with Impingement forms, the Colliding Fronts and Shear Flow forms are not necessarily linked with any macro flow patterns. Although particle placement by these forms are rare, they are important for full consideration of surface film entrainment during filling, as they describe the basic entrainment mechanisms, *i.e.* the folding of a surface film.

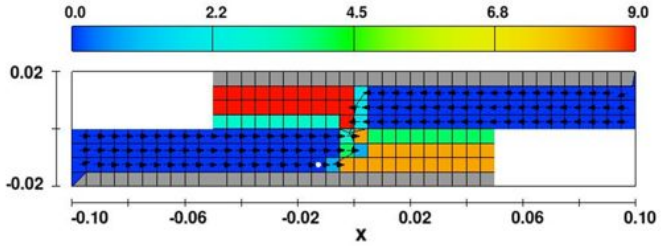

(a) t = 0.1209 s

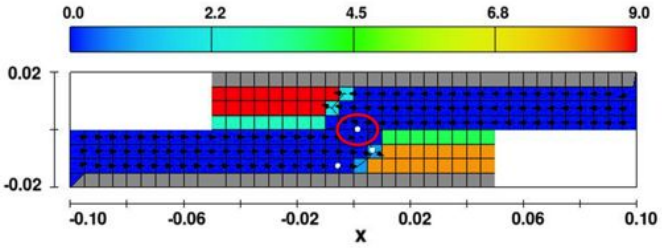

(b) t = 0.1297 s

Figure 6.5: Particle placement by shear flow form. (The colour shade indicates the Nf value of mesh cell. The white dots are the particles).

On the other hand, two free surfaces perpendicularly placed in two diagonally facing two cells are commonly found in the flow model, as plunging jet types of flow can easily lead to the arrangement of free surfaces in the cells as described in Figures 6.1 and 6.2. However, the potential problem remains, that these forms cannot differentiate

between a diagonally moving concave surface or a downwards moving plunging jet. The condition shown in Figure 6.6 has the same characteristics as the case shown in Figure 6.1 in terms of the velocity vectors and Nf value (the normal of free surface) in the model. This may cause some particles to be placed on the concave surface of the flow when very coarse mesh cells are used. But it is believed that this has limited influence on the accuracy of the final results, as flows with concave surfaces would drop down and the incorrectly placed particles (if any) on the surface will be merged into the fluid, representing entrapped surface films in the bulk flow. Therefore, the original definition of Impingement forms was still used in the rest of the study.

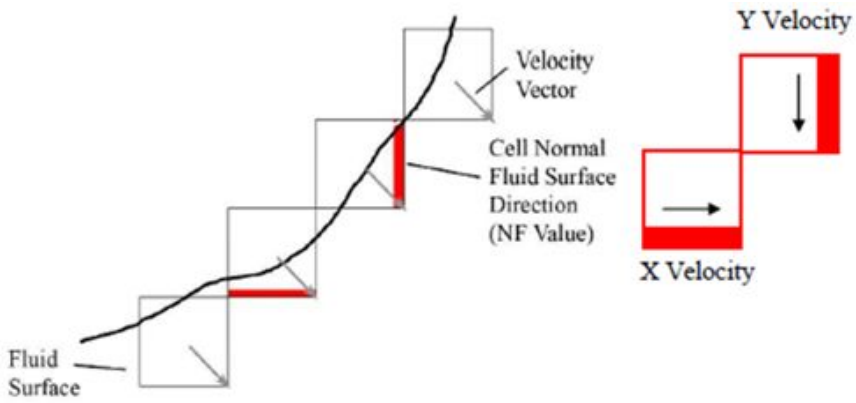

Figure 6.6: Example of a diagonally moving concave surface and its cell characteristics in the model (Entrainment Form 38) [8].

6.2 Entrainment Defect Distribution in Casting

6.2.1 The Effects of Mould Design and Flow Structures

The formation mechanisms of entrainment defects determined that the distribution of these defects in a casting would be closely related to the flow conditions, which in turn, would be determined by the filling method and mould design. Previous studies have proved that filling methods such as bottom filling or tilt-pouring, which can decrease surface turbulence during filling, lead to higher reproducibility of mechanical properties of castings [22,53,55,173], while poorly designed running systems or moulds

could generate highly entraining flow conditions [6, 174]. Flow simulation provides a tool to visualise the flow patterns in a mould and can generate animations of the filling conditions. The modelled filling patterns in different moulds in Chapter 5 have shown the capability of *FLOW-3D* to visualise flow conditions inside the mould. For example, Figures 5.21 and 5.20 illustrated the filling of two moulds. Through observation of the filling, the possible entrainment positions in the moulds were identified, as shown in Figure 5.22. But it must be noted that air or gas bubble entrainment cannot be directly reproduced in a single phase CFD software, and thus, some experience or "imagination" is still required in the analysis of the filling conditions.

A further example of linking filling behaviour with casting properties is from direct visualisation of the three entrainment mechanisms in the mould cavity and analysis of the flow patterns. Comparison between real-time X-ray observation and modelled filling scenarios in Figures 5.36 to 5.38 shows that the *FLOW-3D* flow model could relatively accurate capture the features of flow during mould filling. Obviously, three entrainment mechanisms of the liquid with highly surface turbulent flow structures all lead to surface films folded, broken and incorporated into the bulk liquid. However, different levels of entrainment were achieved. Observation showed that the Plunging Jet and Return Wave mechanisms could both entrain large volumes of gas with oxide films when high velocity liquid impacted on the slower moving liquid body at impingement points, but gas movement determined by the flow direction resulted in different levels of gas or defects entrapped. In the PJ mould the higher velocity of liquid led to more defects and gas entrained, and the gas pockets moved downwards, and which may take a longer time to float out. In the RW mould the jet moved horizontally and gas entrained was pushed only shallowly into the melt and could easily float to the surface. The velocity differences also led to volume differences in the entrained gas, *i.e.* large gas pockets in the PJ mould, but micro-bubbles in the RW mould. In the RJ mould the collapsed jets splashed onto the surface of the flow resulting in extensive surface

films being enfolded, but less gas entrapped due to the small relative velocity between the splashes and the main liquid body. The movement of bubbles left bubble trail damage in castings, which might cause more damage in the PJ and RW moulds than in the RJ moulds.

In addition, the evolution of flow patterns may have an impact on the entrainment level. As demonstrated in Figures 5.36 to 5.38, the chaotic turbulent level in the RJ and the RW moulds reduced dramatically when the moulds were filled gradually, but the gas could be constantly entrained by plunging jets and the momentum of the liquid severely affected bubble movement. These all would have some effects on the reliability of castings. The experimental data in Section 5.3.2.3 showed the variation of strength of samples from the three kinds of moulds and they followed different trends, while the sole difference in these castings was the flow pattern developed in the filling stage. This confirmed that the flow pattern played an important role in determination of entrainment defect distribution in casting.

Flow simulation only reveals the potential location of entrainment, while OFEM provides a quantitative measurement of the formation of entrainment defects and their distribution. The results in Table 5.16 in Section 5.3.2.2 clearly showed the responses of OFEM to three flow conditions, with a different number of particles placed in each sample in each mould. As discussed above, PJ flow entrained more gas bubbles and oxide films than RW and RJ flows, which in the models was reflected in much more particles being placed in the PJ model (7479 particles) than in the RW and RJ models (2741 and 5001 respectively). Weibull analysis of the reciprocal of particle counts in the samples could be potentially used to make a comparison of casting reliability between different mould designs. The Weibull modulus measures the variance of data: a high modulus represents low variance; while the position parameter measures the value of the data: here a low position parameter is associated with a low strength. Because of significant differences in particle counts, the Weibull analysis of the model data showed

variation not only in the moduli, but also in the position parameters. Figure 5.40 shows that samples from the PJ mould had the highest Weibull modulus, but lowest position parameter, which meant that the model predicted that the samples from the PJ mould had consistent low strength, compared with samples from the other two moulds. This did not correlate with experimental results. A possible reason is explained later in Section 6.2.2.

OFEM combined with a flow model also allows quantitative assessment of different mould designs. The comparison of particle quantity in the thick and thin runner moulds in Section 5.5.5 gives evidence of this capability. Figures 5.65 and 5.66 show the filling patterns of the two moulds. It can be seen that the thin section in the runner generated a hydraulic jump in the runner and had a plunging jet developed in the down sprue, and generally should have had a higher surface turbulence level. The particle quantities listed in Table 5.21 distinguished the difference in filling pattern between the two moulds, and at least 20% more particles were generated in the thin-runner mould during filling. The variation in quantity of particles generated suggested that the model could provide general indicators of entrainment levels in different running systems during mould filling when comparing different casting processes. However, currently there is no benchmark of particle quantity that can be applied to the model to measure the "poorness" of a mould design in terms of developing surface turbulence or air entrainment flow conditions. Therefore, 20% more particles in the thin runner mould did not necessarily mean that the thin runner mould was 20% worse than the thick runner mould.

6.2.2 Modelling and Validation of Defects Distribution

Physical properties of entrainment defects (both known and assumed) were assigned to particles in OFEM, and the motion of these particles coupled with the fluid movement in the simulations. Therefore, the distribution of particles can reflect the possible scatter of entrainment defects in a casting. On the other hand, since the time interval

of particle placement is governed by the model, this may not reflect the real generation rate of entrainment defects during casting. Comparing the number of entrainment defects observed in a casting with the quantity of particles in the models, the quantity of particles was higher than that of the defects. It is supposed that the quantity of particles in a specific region in a casting may not represents the real quantity, but a probability of the existence of entrainment defects, and a high particle count is related to high probability.

Predicted defect distribution can be directly viewed as profiles shown in Figure 5.88, or plotted as particle distribution contours as shown in Figure 5.8 to Figure 5.10. The latter illustrates particle number density information. However, direct visualisation of particle distribution can be difficult sometimes, especially when the mould geometry is complex, and analysis of the views does not quantify the entrainment severity and defect scatter. Special codes were written to count and export the number of particles trapped, and the particle concentration in each element in the moulds. These data were plotted against the properties of castings to study quantitative links between particle counts and the strength of castings or to investigate potential defect distributions inside castings, as shown in Chapter 5.

Current results show that there is a weak link between the particle quantity and the strength of a casting, as shown in Section 5.5.6.1, but the accuracy of predicted defect distribution requires further improvement. The credibility of the validation is subject to both the quality of experimental results and the accuracy of the model, here including the flow model and the OFEM algorithm. Sections 6.2.3 and 6.4 give more details about the effects of modelling conditions and factors in the OFEM.

As mentioned in Chapter 2, the study of entrainment defect distribution is experimentally difficult. In this work, the quality of experimental data severely restricted the validation of OFEM. The data on fatigue life and tensile strength of castings from the literature was used in preliminary validations of OFEM, but the pouring condition

in manufacturing the fatigue test bars and filling conditions within the mould cavity was not reported in Nyahumwa's work [156]. Although the modelled flow patterns in Figures 5.13 and 5.14 showed reasonable agreement with the real-time X-ray observation, the filling of the rest of the mould was unclear. In Nyahumwa's fatigue tests, the samples were randomly selected with different numbers of test bars chosen from each location, which means that the mean fatigue life of test bars at the specific location shown in Section 3.4.1, Table 3.6 might not be the proper value for validation. Reilly gave details of his Froude number validation experiments, and the modelled flow patterns in Figures 5.21 and 5.20 correlated with his real time X-ray observation. However, the high level of surface turbulence generated during filling resulted in a large number of air bubbles trapped in the castings, significantly reducing the UTS of test bars. This also affected the validation of OFEM, because of the low reproducibility of the mechanical properties of the test bars.

The pouring in three entrainment mechanism experiments was from the same position and controlled by robot arm, and hence good reproducibility was obtained. The pouring speed was recorded by datalogger and the information was imported as initial conditions in the simulations, and led to good agreement between the modelled flow patterns and experimental observation, as shown in Figures 5.36 to 5.38 in Section 5.3.2.1. However, the bend strength of samples was strongly influenced by shrinkage porosity formed in the centre of the plates. Besides, the rectangular mould cavity had less restriction on the momentum of fluid flow compared with other mould designs, which increased the difficulty of simulation. Without information about temperature gradients in the mould cavity, it was impossible to accurate estimate the flow field during solidification, and the particle distribution that was controlled by the flow conditions could not be correctly predicted. This may explain why a correlation between predicted particle count variation and the bend strength of samples was not achieved.

The design of the tensile test bar mould had more restriction on flow in the mould

cavity, and therefore, there would be less turbulence and convection in the test bars during cooling and solidification. It was felt that the potential inaccuracy of the heat transfer and solidification simulations might not alter the particle distribution pattern in this mould, or would alter it least compared to the other models. The application of a feeder helped to eliminate the shrinkage porosity, although the data from the tensile bar moulds still showed large variations. Nonetheless, a general UTS variation was achieved, which shows that UTS increased from Test Bar 1 to Test Bar 5, and this result was reproducible, as a second group of experiments showed a similar trend as shown in Figure 5.87. But the large standard deviation of the data reduced the credibility of the strength variation. It was unclear if the large scatter of UTS of the test bars was caused by the existence of entrainment defects or errors introduced during the experiment, though the same experimental procedure was carefully followed in making castings and subsequent tests.

In general, there were two main factors affecting the quality of the validation data: influences of other types of defects and the variance of the data. The characterisation of defects on the fracture surfaces of test bars in Sections 5.3.1.3 and 5.5.2 showed that the fracture of samples were not caused solely by double oxide film defects, but also gas and shrinkage porosity. Although Campbell claimed other types of defects are all associated with entrainment defects to some extent [6], it was felt that not isolating the effects of entrainment defects would still have an impact on the validation of OFEM. The mechanical properties of castings, *i.e.* fatigue life and UTS in the preliminary validation, bend strength in the three entrainment mechanisms experiment, and UTS in the tensile bar mould experiment, all used in validation attempts, all had low Weibull moduli (less than 20), which suggested a high variance of the data. Since the existence of entrainment defects in a casting reduces the reliability of the casting [58], the variance of data could be treated as a side effect of the large number of entrainment defects. However, in terms of justification of OFEM, it makes the data unclear and difficult to

interpret to validate the model. For example, the UTS of test bars ranged from 230 to 275 MPa in Figure 5.91 in Section 5.5.6.1. Although the fitted trend lines showed that the UTS was inversely proportional to the particle counts or maximum particle concentrations in the test bars, the confidence level of this conclusion was quite low. Besides, as mentioned in the beginning of this section, the large number of particles generated and widely distributed in the model resulted in very low Weibull moduli of the data (less than 10) as shown in Figures 5.40 and 5.107. This meant that the predicted reliability of castings could not be directly compared with the experimental data. Further work is still required to understand the relationship between the particle count or particle concentration in the model and the quantity of defects in a casting.

6.2.3 Particle Distribution in the Whole Length or Gauge Length of the Test Bar

Mechanical testing only tests the strength of materials within the machined gauge length of specimens. Therefore, using the number of predicted defects within the whole volume of the specimen to assess the properties of that material may introduce errors. Although it is possible to examine the defect quantities within the same region in the computational model, it would involve application of a very fine mesh and extend simulation times, and thus the current model considered the gauge length of a specimen, but not the reduction in diameter forming the waist of a specimen. Reilly modelled the filling and solidification of a casting similar to the one used in the fatigue life validation model shown in Section 3.4.1, and found the particle distribution in the round test bar was random [8]. He showed that, although not removing the excess volume of material from the test bars, as done by machining in a real experiment, would affect the predicted quantity of particles, it was unlikely to change the variation in properties of the results.

Similar results were found in the Froude number validation model and tensile bar model. An example from the unfiltered low mould shown in Figure 5.23 in Sec-

tion 5.2.2.2 illustrated the difference in quantity between the particles trapped in the whole length and the gauge length of the test bars, but showed almost the same distribution patterns of particles across the casting. Another example is from the comparison between Figures 5.89a and 5.89b, which showed either sticky or non-sticky particles being used in the model, the predicted particle distribution patterns in the moulds were the same, regardless whether particles in whole test bars or only in the gauge length of test bars were assessed. But the maximum particle concentration within an element in the models showed a different response when the two different volumes of materials were considered. This is discussed later in Section 6.4.1.

However, as mentioned before, the particle distribution is closely related to the mould geometry. Figure 5.42 to Figure 5.44 showed the variation in particle quantity in each sample within the cast plates used in the models of the three entrainment mechanisms. Although the gauge length only contained 22.2% of material in each sample, the results still showed quite similar distribution patterns within the two regions, but greater distinction within specific areas like in Samples 5 and 6 in the right part of the PJ mould in Figure 5.44 was also observed. In the Froude number validation and tensile test bar models, the round test bars confined the movement of the fluid and generally were filled smoothly, while the plate had much less restriction on the flow, and the specific flow pattern could greatly change the particle location. Hence, the particles were distributed according to the filling structures within the cast plate, and consequently there would be a difference between the particle distribution patterns predicted by assessing the whole length or just the gauge length of the samples.

In general, to simplify the model the particle count in the whole length of sample can be used to study the predicted particle distribution, but a comparison must be made between the particle quantities in the whole length or the gauge length of a sample that is cut from large bulk casting, to get a more accurate measurement.

6.3 Effects of Modelling Conditions in *FLOW-3D*

6.3.1 Effects of Particle Stickiness

Particle stickiness settings in *FLOW-3D* determine the interaction between a particle and the mould wall, *i.e.* if the particle will stay on the mould wall or be removed by the fluid during filling. The particle stickiness in *FLOW-3D* is defined by the coefficient of restitution (*PCRST*), which can be set to 1, 0, and -1. The particle can be reflected back specularly with no energy loss (non-sticky, *PCRST=1*), or lose its kinetic energy and stick to the wall, but is able to be scoured from it when the flow shears the mould wall (*PCRST=0*), or firmly sticks to the wall without further movement (sticky, *PCRST=-1*), when it contacts with a rigid object (the mould wall). This setting applies globally to all particles within the domain. Since the size of the particles used in the models were small, consequently, the kinetic energy of the particles in the flow was low. Therefore, the first two settings had almost the same output in simulations. Preliminary development and validation of the OFEM algorithm by Reilly used sticky particles, and later non-sticky particles, but did not study the difference in the results [8]. Since there is no experimental evidence on the adhesion of oxide films to a mould wall, the method in this project followed Reilly's setting initially during the preliminary validation of OFEM, and compared the difference in results between using sticky and non-sticky particles in the later simulations.

The potential problem of using sticky particles is that the model may not predict the location of particles accurately. The influence of particle stickiness might be underestimated in Reilly's simulations, and also in the preliminary validation models in this work. A straightforward example is shown in Figure 5.45 in Section 5.3.2.4, where snapshots of flow patterns during filling of the RJ mould using the sticky particle model, showed a "fountain" shape of particle distribution on the wall. The particles were adhered on the mould wall when they first contact the wall and did not move further until the end of filling. This implies that sticky particles can illustrate defect

distribution in early stages of filling, but not necessary the final location of defects if they become removed from the mould wall. Besides, sticky particles were inclined to stay at the location with the most severe surface turbulence in the mould, because particles have more chance to contact a mould wall, such as the vertical ingate in the Froude number validation mould and the horizontal runner behind the thin section in the tensile test bar mould. This would lead to less particles being delivered into the mould cavity, affecting the quantitative prediction of defects in the casting. For example, the results in Table 5.21 in Section 5.5.5 showed that a large amount of sticky particles were trapped in the running system of the tensile test bar mould.

Although the quantitative relationship between predicted particle counts and the defect number in a real casting has not been established, less particles were trapped in the mould cavity owing to using sticky particles may still result in an underestimation of entrainment severity or relative distribution of defects. The negative effects may be even worse when a mould with thin sections is employed, as thin sections in the mould can increase the probability of contact between the particles and the mould wall. Evidence may be seen in the comparison of plots of elongation of tensile test bars against particle counts using non-sticky and sticky particles in the models, as shown in Figure 5.95 to Figure 5.98 in Section 5.5.6.1. The expected relationship between the elongation of test bars and the number of particles trapped within the bars is that higher particles counts would be associated with lower elongation. However, modelling results in Figures 5.95 and 5.97 (non-sticky particles) showed slight downward trend lines, while the model using sticky particles, shown in Figures 5.96 and 5.98, showed relatively flat or even upward trend lines, indicating an opposite relationship to that expected. Furthermore, the variation in UTS and elongation of tensile bars according to their specific locations, shown in Figure 5.99 to 5.102, obtained from models with sticky particles, did not correlate with the trends obtained from the experiments.

Although there was a lack of evidence whether oxide film defects could be stuck on

the mould wall or removed in subsequent filling in reality, it is believed that the non-sticky particles give a better representation of the entrainment defect, and hence, more accurate results, especially when considering the layer of material in direct contacted with the mould wall that would be machined away for mechanical property testing.

6.3.2 Influence of Pouring Conditions on the Results

The pouring basin is an integral part of the mould in most cases in gravity casting. A previous modelling study on the filling of the mould conducted by Lai *et al.* showed that pouring liquid metal into the pouring basin generated the most surface turbulence during the whole filling process [73]. This observation demonstrated the significance of pouring conditions in generating entrainment defects in the early stage of filling. Because there was either no other results to compare the effects of different pouring conditions in his model, nor the effects of different mould designs on the entrainment levels reported, Lai's result cannot be applied to other moulds or casting process that involves different flow conditions in the pouring basin. Reilly studied the influence of different pouring positions in the pouring basin and showed through models, that although different pouring positions led to varied flow conditions within the pouring basin, the general flow patterns within the rest of the mould were negligibly different, which implied similar quantities of defects would be generated. This was confirmed by a quantitative comparison of entrainment events created in the mould [8].

Previous studies did not show the effect of the pouring basin on influencing the defect distribution within a casting. The fatigue life validation model in Figure 5.19, Section 3.4.1 compared the particle distributions in the models with and without consideration of the particle placement in the pouring basin. The results in Section 5.2.1.3 showed that three times more particles were generated in the model considering the entrainment in the pouring basin, again highlighting the severity of entrainment in the pouring basin. Similar to Lai and Reilly's models, this could be attributed to the flow condition: with the liquid impacting directly on the bottom of the pouring basin, and

later on the liquid pool, resulting in splashes and consequently, entrainment defects. However, Figure 5.18 showed that both conditions resulted in almost the same particle distribution pattern in the casting, and similar particle quantities were trapped in each test bar in the mould. These results agreed with Reilly's observation, and thus, the initial conclusion was that the influence of flow conditions in the pouring basin on the defect distribution was negligible. Therefore, the Froude number validation model and the initial validation models of the three entrainment mechanisms did not consider the particle placement in the pouring basin.

Since both Reilly's models and the fatigue life validation model used sticky particles in simulations, this may explain why three times more particles were generated when the entrainment in the pouring basin was considered, as shown in Table 5.8, but a similar number of particles was trapped within each bar, because part of the particles stuck on the mould wall. As later studies showed that non-sticky particle model provided better predictions of entrainment defect distributions, the effects of pouring conditions was reconsidered. Indeed, a later study using non-sticky particle in the models, reported in Section 5.5, revealed that the extra particles placed in the pouring basin did affect the predicted particle distribution in the castings, as shown in Figure 5.89. The pouring position sensitivity study results in Figure 5.106 further showed that small changes in the initial pouring position led to different predicted variation in the particle distribution. Therefore, the pouring condition should be considered into the model of entrainment defects, although the significance of the effects of the pouring conditions on the variation in mechanical properties of casting is not clear, due to a lack of comparison with experiment results.

6.3.3 The Application of a Filter in the Model

The application of ceramic foam filters for removal of inclusions from the melt has become a common procedure in casting. Generally the effects of a filter are, i). physical stopping of the solid inclusions passing through the pores within the porous media,

and/or *ii*). altering the filling behaviour of the casting by reducing the velocity of the incoming fluid. During filtration inclusions can be physically sieved or trapped by the filter, or attracted physicochemically to the filter wall by surface energy forces [175]. But the filtration mode for preventing entrainment defects from entering the mould cavity is not clearly understood, probably because of the difficulties of study of a defect of small size or convoluted morphology [174]. Din *et al.* studied the influences of using ceramic foam filters in a direct pour system on the tensile properties of aluminium alloy A356 and found that about 90% of the benefit of the application of a filter in the running system was derived from the improvement in the filling behaviour of the casting, as the reduced velocity of flow decreased the severity of surface turbulence, and hence, reduced the possibility of the formation of entrainment defects during filling [176]. Another possibility is that the filter fragmented the large film-like defects into smaller and less harmful oxide fragments, resulting in better mechanical properties of a casting.

Improvement of the properties of castings when a ceramic foam filter was used in the running system was also reported in the preliminary validation data in Sections 3.4.1.1 and 3.4.2. This has been reflected by the model as there were fewer particles placed in the moulds with filters, as shown in Figure 5.13. But limited by *FLOW-3D* model technique, the model could only consider the effect of reducing the velocity of flow during filtration. In the simulations, instead of embedding a solid component with the full internal microstructure of a ceramic foam filter into the model, the filter was replaced by a solid object with extra drag force applied within the domain using the Porous Media Model in *FLOW-3D*. This approach avoided using a very fine mesh in the model and saved computing time dramatically. However, as there was no consideration of the internal channels within a filter, details of the flow conditions when the liquid passed through the filter could not be reproduced. Examples are in Figures 5.13 and 5.14 in Section 5.2.1.1, which shows the filling condition in the filter region with real-time X-ray observation compared to modelled behaviour of fluid flow in filtered and unfiltered

conditions. Clearly, a correlation between the *FLOW-3D* model and the real filling scenario in the filling patterns was only found in the mould without filtration, as the filling could not be modelled accurately when the internal pores or pathways of a filter were neglected in the model. Consequently, the formation of double oxide films during this period could not be simulated, since the fronts of liquid from different pores may collide with each other and fold the surface oxide film into the bulk liquid. Besides, the blockage by the filter or attraction of entrainment defects to the filter wall cannot be modelled either. Both may introduce some errors in the estimation of defect number in the simulation. However, it must be mentioned that the modelled and real filling scenario showed very good agreement in filling velocity. This suggested the Porous Media Model in *FLOW-3D* is a good tool for study of the momentum of flow, but may not proper for validating the OFEM predicted particle quantities. Thus, a filter was not used in the later models and the corresponding validation experiments.

6.3.4 Effects of Different Particle Density

In the modelling studies, the models that integrated the entrainment defects as scalars did not consider the physical properties of the defects, while the discrete models of entrainment defects treated the defects as spherical particles, either without physical properties, *i.e.* marker particles for tracing the flow, or with specific physical properties, with the movement coupled with the flow. Ohnaka *et al.* mentioned setting the air density to the particles in their model [86]. Reilly used 2200 $kg \cdot m^{-3}$, which was slightly lower than the density of liquid A356 alloy [8], and this value was later used in Trejo's centrifugal models [177], which showed the particles moving towards the centre of the casting under centrifugal force during cooling and solidification, because of their lower density compared to the liquid. This proved that the particle density could affect the predicted defect distribution.

Results in Section 5.3.2.4 compared particle distributions in the models with varying particle densities used. Figure 5.48 demonstrated that denser particles tended to sink

to the bottom and resulted in higher reciprocals of particle counts in the samples in the top half of the plate. This figure also showed that the density of the particles was lower than that of the liquid, here lower than 2400 kg$\cdot$m^{-3}, had limited effects on the particle distribution, since different densities of particles led to similar tendencies in the curves. The trend predicted by a model with denser particles (3000 kg$\cdot$m^{-3}) was different from the other models and was distinct from experimental data. Due to the low quality of the experimental data, the correct density of particle that should be used in the model could not be derived from these results.

Previous experimental studies of entrainment defects did not report the influence of defect density on defect distribution in the casting, or flow condition in the mould during filling. Obviously, the density difference between the defects and the fluid could lead to relative movement between these two in a tranquil flow condition. The terminal velocity of the movement of a spherical object under gravity in a static viscous fluid flow can be calculated according to Stoke's law (Equation 6.1):

$$v_s = \frac{2}{9}\frac{\rho_p - \rho_f}{\mu} g R^2 \tag{6.1}$$

where v_s is the terminal velocity (m$\cdot$s^{-1}), ρ_p and ρ_f are the densities of the object and the fluid respectively (kg$\cdot$m^{-3}), μ is the dynamic viscosity of the fluid (N$\cdot$s$\cdot$m^{-2}), g is the gravitational acceleration (m$\cdot$s^{-2}) and R is the radius of the object (m). The equation is valid for small particles in laminar flow, with Reynolds number less than 10. This equation shows that the size (radius) of the defects is also an important factor in determination of the defect movement in tranquil flow.

The chemical reaction products of aluminium alloy A356 and oxygen are comprised of Al_2O_3, MgO and $MgAl_2O_4$. The densities of these oxides vary from 3580 to 3970 kg$\cdot$m^{-3} [170], which are higher than those of the liquid aluminium alloys. According to Equation 6.1, a solid Al_2O_3 particle (ρ_p=3970 kg$\cdot$m^{-3}) of diameter 0.5 mm, would sink in static liquid A356 alloy (ρ_f=2420 kg$\cdot$m^{-3}) and the terminal velocity achieved would be 0.18 m$\cdot$s^{-1}. However, *in situ* X-ray microtomography in Section 5.4.3 showed

that an entrainment defect of similar size could maintain its position in the tranquil liquid in the test period from several minutes to one hour. This implied that the density difference between the entrainment defects and the surrounding liquid alloy was smaller than that between solid Al_2O_3 and liquid A356. Considering the nature of folded-over double oxide film with a thin layer of gas trapped inside, or directly entrained micro-bubble that with a surrounding oxide film, the densities of defects are probably lower than that of solid alumina, magnesia, or spinel.

In both experiments and models the moulds were all turbulently filled, in which turbulent energy would dominate the particle distribution rather than their buoyancy, especially when considering a defect size of several μm. Besides, X-ray microtomography showed that the defects had a similar density to that of the surrounding liquid alloy, suggesting that for modelling, a value of particle density that was close to that of the fluid may give a better prediction of the particle distribution. Therefore, 2400 $\mathrm{kg}\cdot\mathrm{m}^{-3}$ was used for the particle density in later model. Furthermore, it should be noted, more experimental work on the characteristics of entrainment defects is still required to develop the particle model, and the individual uniqueness of entrainment defects implies that, potentially, a range of densities of particles should be applied in future models.

6.4 Oxide Film Entrainment Model

6.4.1 Total Particle Count vs. Maximum Particle Concentration

The total particle count in the mould cavity or a mesh block predicts the potential quantity of defects in a casting, while the particle concentration in a mesh element, *i.e.* the particle number density in the casting, describes the potential defect number density in a casting on a much smaller scale. Higher particle concentrations in specific regions suggest a greater possibility for the existence of significant entrainment

defects, possibly of larger size. Therefore, the analysis of total particle counts predicts the general distribution of defects, including both a large amount of small defects or several large defects, whereas an assessment of maximum particle concentration might reveal the distribution of the largest entrainment defect. Previous experimental research showed that the mechanical properties of cast Al-Si-Mg alloys are determined by the size distribution of defects, with the largest defect, *i.e.* the weakest link, causing premature failure [178]. This implies, from the modelling perspective, that the maximum particle concentration may be a better indicator for predicting mechanical properties of castings, since the effect of the largest defect can be covered up by a larger quantity of small defects when analysing the total particle count in a casting.

The results in Section 5.5 compared plots of the UTS of cast test bars against both the predicted total particle counts and maximum particle concentrations in the models. Figures 5.91 to 5.94 showed a similar tendency, whether considering the total particle counts or maximum particle concentrations in the bars from the 1st group of casting, in which the trend lines sloped slightly downwards to the right. The same results were observed in Figures 5.103 and 5.104 from the 2nd group of castings. The results from the two groups of experiments showed that in the models, either the higher total particle counts or the higher maximum particle concentration in the test bars, could be associated with the lower UTS of the test bars. However, the variation in UTS of the test bars in castings that predicted by assessing the maximum particle concentration in the test each bar were quite different from that predicted by assessing the total particle counts in the test bars. Compared with the latter, the strength variations obtained from the former could be flat, as shown in Figure 5.100b, or with large changes, as shown in Figures 5.99a and 5.100a. Further investigation showed that, in fact, the particle concentration in most of the mesh elements was quite similar, or at least in the same scale, suggesting relatively random distributions of particles in the test bars, which agrees with the discussion in Section 6.2.3. However, the maximum particle

concentration in each test bar was determined by the extreme value of the particle counts in the very small area in the castings, which may be significantly distinct from the rest. For example, Table 5.26 shows clearly that in most modelling conditions the maximum particle concentrations were in the same range, with the maximum concentration of several hundreds of particles being observed in Test Bars 1 and 2 and several tens of particles being observed in Test Bars 3, 4 and 5. However, the extreme values in the Test Bars 2 and 3 in the "$x+$" model, which were above one thousand, dramatically changed the predicted variation, as the curve of the model from "$x+$" position shown in Figure 5.106b was different from the others. The second highest particle concentration in Test Bars 2 and 3 in this model were 218 and 157 respectively, which were in a comparable scale with the maximum particle concentration in other test bars in different models.

Therefore, the results suggested that assessing maximum particle concentration in a casting did not necessarily provide a better prediction of casting properties. Since in the current model the size of the defects is defined by the size of particles, a higher particle concentration in a mesh cell may not directly link to the existence of a larger defect, but to a higher probability of greater defect quantities in that region. Although previous literature did not report the size distribution of entrainment defects in dynamic conditions, it is implied that a high quantity of defects in a specific region can be associated with a high probability of the existence of large defects, which means the particle concentration could be an index for predicting defect distribution. However, because of the sensitivity of maximum particle concentration in the element to the extreme value of particle counts within a small area in casting, the maximum particle concentration can only be used as a supplementary indicator, together with total particle count, for predicting properties. For example, the magnitude of particle concentration in the different test bars should be compared, instead of solely using the maximum particle concentration to predict the variation of properties of the castings.

6.4.2 Limitations of the Oxide Film Entrainment Model (OFEM)

The current OFEM model is limited by three main factors: *i*). the capability of the CFD package in which it runs, *ii*). a lack of knowledge about the subsequent behaviour of entrainment defects, and *iii*). the entrainment criteria.

As a customised subroutine integrated in a single phase CFD software *FLOW-3D*, the OFEM method does not include the entrainment of air in its entrainment criteria. Therefore, not only could the formation of folded oxide films be modelled, but neither could the gross entrained air bubbles or other inclusions. Besides, as a CFD software that focuses on the solution of fluid momentum, *FLOW-3D* seems incapable of modelling solidification and phase transformations properly. For example, the modelling conditions for the heating profile model shown in Section 3.6 did not consider the surface tension, because some test models crashed when the sample started to melt and form a curved free surface. In addition, the "critical solid fraction", which is used to define the temperature at which the drag force should be applied to the liquid phase in the *FLOW-3D* solidification model, is based on assumption and lacks experimental data support. Consequently, the formation of shrinkage and gas porosity cannot be included in the model, which makes it difficult to validate the OFEM, as in most cases the influence of entrainment defects cannot be simply isolated from other defects in the castings.

As mentioned in Section 6.3.4, the particle model in *FLOW-3D* considers either the variation in density or in the size of particles, and only uses spherical particles. Although adjustment of the particle density can be used to reflect the difference between several kinds of defects, this still limits the properties that can be given to particles, introducing a difficulty in mimicking the behaviour or morphology of varied film-like double oxide film defects, as shown in SEM figures in the metallographic characterisation.

Due to a lack of evidence of the behaviour of entrainment defects in the liquid

metal, including the interactions of defects and the surrounding environment, *i.e.* the mould wall, liquid metal, etc., and between defects, there could be some variation in simulation results compared with reality. The discussion in Section 6.3.1 suggested that using non-sticky particles in the model gave better results, but there is no experimental evidence to support this idea, while the interaction between defects, *i.e.* if the defects agglomerate to form larger defects, as used in Carlson and Beckermann's model [96], is still not clear and thus, is neglected in OFEM. Since the sizes of entrainment defects reported in a previous study are much smaller than the mesh cell size [19], the potential agglomeration or interaction of defects in adjacent mesh elements could be neglected, but this may not necessarily be true for the particles within one mesh element.

Current models still use an assumed density of defects with single value. This may not represent the properties of individual unique defects. In terms of morphology or size changes of the entrainment defects, the experiments involving the trapping of gas bubbles within liquid aluminium alloy in macro-scale demonstrated that the size of a double oxide film defect would be reduced in a casting, due to reaction between the trapped air and the surrounding alloy [28, 38], and this was confirmed further by the synchrotron X-ray microtomography study reported in Section 5.4. However, the morphology or size changes of the defects with time are not clear. The different initial morphology of entrainment defects also affect the changes of defects morphology or size. Therefore, the evolution of morphology and size of particles in the fluid is ignored.

The predefined entrainment forms in the OFEM capture plunging jet and other flow scenarios and model the formation of associated defects, namely young oxide films. However, it is clear from both literature and experiments that the adverse influence of entrainment defects involve both young and/or old oxide films [23]. Modelling work in Section 5.3.2.5 showed the possibility of considering the quantity of old oxide films in the simulation, but the method was not applied to later models. Without information about the quantity of old oxide films relative to young films, the assumed number

of old oxide films in the model may over- or under- estimate their effects on casting properties.

With regard to the quantity of young oxide films, as discussed in Section 6.1.2, the definitions of Impingement forms are descriptive and not rigorous as Colliding Fronts and Shear Flow forms. Therefore, this may result in excess placement of particles in simulations. A potential solution is to improve the definition of the Impingement forms through consideration of the momentum. For example, following the idea of "critical velocity" proposed by Runyoro *et al.* [82], a critical relative velocity of fluid in adjacent mesh elements can be defined, above which the surface oxide films would be entrained into the bulk liquid metal. Another idea is to define other criterion functions through some dimensionless numbers, to quantify the local turbulence level and link this to the quantity of particles generated in the model. This potential development model can be analogous to the air bubble entrainment in the free-surface flows, developed in the hydraulics study [31].

6.5 The Characteristics of Entrainment Defects

6.5.1 Morphology of Entrainment Defects

Entrainment defects are individually unique defects, which can have simple geometry such as the nearly spherical shape shown in Figure 5.53a, or a very complex shape such as the convoluted network as shown in Figure 5.53c. The morphology of each entrainment defect would be determined by the formation mechanism and/or the subsequent development of the defects. For example, a directly entrained gas bubble could remain in the liquid as a pore, while a convoluted surface oxide film might present as a folded network. Figures 5.61 and 5.62 showed a captured bubble that might further collapse to become a closed crack. This suggests the evolution of entrainment defects could alter the morphology of these defects.

The classification of entrainment defects in Section 5.4.1 was based solely on the morphological difference between defects. Although it is believed different types of entrainment defects should share similar characteristics as they all contain an amount of gas phase in their interior and have an oxide skin, they may have different influences on the mechanical properties of casting. This can be explained by considering the case of an entrainment defect in a round tensile test bar. An entrained bubble with nearly spheric morphology would reduce the loading area on the cross section, and this effect would be isotropic. On the contrary, a closed crack that has the same dimension in its length direction as the entrained bubble may not severely reduce the load-bearing area, if its orientation is parallel to the loading direction, but it could also be worse than a round bubble if its orientation was perpendicular to the loading direction. Also, the sharp edge of defect would lead to a higher stress concentration and dramatically reduce the propagation time of a crack. The tangled network of a convoluted double oxide film may have more complex effects, as its sharp edges do not show any preferential orientations, which may influence the mechanical properties of test bar differently when the force is loaded in different directions. Therefore, the current classification of entrainment defects is descriptive, and since the morphology of entrainment defects can change, the classification does not necessarily link to any conclusive adverse effects on casting properties.

6.5.2 Evolution of Entrainment Defects

Owing to the low quality of the images obtained from the experiment, quantitative measurement of volume and surface area changes of the defects were deemed inaccurate. Therefore, only the morphological evolution of entrainment defects is discussed.

Figures 5.61 and 5.62 show the morphological evolution of two entrained bubbles. Both bubbles underwent similar shape changes as they started as large pores, then collapsed and changed to irregular porosity in the images. Figure 5.62b was obtained at 560°C, slightly above the solidus temperature of A356 alloy, and demonstrated that

morphological change started when the sample started to melt. Figures 5.63 and 5.64 both show the morphological change of entrainment defects that contained less gas in the defect interior, and had limited shape and size changes during the holding period in the liquid state. Experimental observation showed these defects were all isolated in the liquid pool without connection to the ambient atmosphere. Thus, it is believed that the driving force of morphological evolution comes from the internal factors in the defects and the surrounding liquid metal.

As reviewed in Chapter 2, the morphology change (or healing) of double oxide film defects requires the two layers of films to come together, by application of an external force or by consumption of the internal atmosphere, or both [7]. In the experimental condition, the forces applied to the liquid pool were the metallostatic and atmospheric pressures. The former was small considering the size of the sample (3 mm in diameter, 6 mm in height) and the locations of defects (in the middle of the sample); the latter applied uniformly to the whole sample. Therefore, the morphological evolution of entrainment defects was believed to be determined by a combination of two factors: the reaction between any interior gases with the surrounding liquid metal and hydrogen diffusion into the defects as suggested by Raiszadeh and Griffiths [28,38,179,180]. The initial pore might contain a mixed atmosphere of entrained gas and hydrogen which diffused from the surrounding liquid alloy into the pore during solidification. When the sample was melted, the hydrogen would diffuse back into the melt while the entrained gas phase, which might be oxygen and nitrogen, would react with the melt and be consumed, resulting in a reduction in the volume of the defects.

During melting and holding, the volumes of defects in Figures 5.61, 5.62 and 5.64 were reduced to approximately 20%, 60% and 90% of their initial volumes respectively. These results show that the large pore that contained most gas, experienced the greatest change in both volume and shape, while the defects that had complex geometries and less trapped gas, maintained their general shape in the liquid state and after solid-

ification. This confirmed that the initial gas phase trapped in the void has a significant influence on the subsequent defect evolution. From the figures, it can also be seen that the defects did not close during the holding period and subsequent solidification. The remaining gas phase within the voids could be nitrogen, which needed a longer time to react with the surrounding liquid aluminium, or hydrogen, that had reached an equilibrium with the ambient atmosphere. Both may need a much longer time than the scanning time in the experiments to be consumed completely, and hence a small portion of gas remained in the voids in the figures.

Observation of morphological evolution of entrainment defects did not find the unfurling of oxide films suggested by Campbell [7], *i.e.* the reopening of a convoluted double oxide film in the liquid, was not observed in the experiments. As explained above, the driving force for morphological changes in entrainment defects could be due to internal gas consumption and diffusion of external hydrogen. Therefore, the unfurling of entrainment defects requires hydrogen to inflate the defects, which in turn demands a much higher hydrogen content in the liquid aluminium than in the gas phase trapped within. While during the holding period the hydrogen content in the interior and in the liquid metal would tend to reach equilibrium, so it may be impossible to diffuse excess hydrogen into the entrainment defects. Another explanation for the unfurling not being observed could be: *a*). the unfurling of entrainment defects requires longer holding times, *b*). the strength of the oxide film hinders shape changes in the defects, and *c*). the viscosity of the liquid metal obstructs the movement or deformation of the defects. It should be noted the morphological evolution of entrainment defects was investigated in a tranquil flow. In a real casting scenario, turbulence could affect the geometries of defects, as demonstrated in the model of Pita and Felicelli [107].

6.5.3 The Relationships between Entrainment Defects and Other Defects

As mentioned previously, the entrainment defects maintained their general morphology during solidification, but that morphology was affected by microporosity and solidification shrinkage to some extent. Figure 5.61(d to f) show that a spherical hydrogen pore nucleated near the entrainment defect and that shrinkage porosity originated nearly and on these voids (double oxide films and hydrogen pores). This shows that entrainment defects could provide heterogeneous sites for shrinkage porosity growth, possibly because the presence of the voids retarded heat transfer and changed the local solidification rate, as suggested by Lee and Gokhale [181]. However, the relationship between the entrainment defects and hydrogen porosity is still not clear. As shown in Figure 5.61e, hydrogen porosity did not originate with the large entrainment defect, as has been suggested should be the case [7]. Instead this occurred in an area where very small defects were present, which were difficult to see clearly in the images (circled in Figure 5.61d). Compared with the large defect, these small defects might be oxide films formed in the later stage of mould filling, which had less chance to react with their internal atmosphere, and hence, might be thinner and weaker, and might have already ruptured. Since the oxide layer formed on the surface of large defects could provide a barrier preventing hydrogen from penetrating into the void, as suggested by Griffiths and Raiszadeh [38], these small defects might be the preferred sites for nucleation and growth of hydrogen porosity.

6.6 Summary

Experimental results showed that the plunging jet type of flows directly entrainment air or surface film into the bulk liquid, and generate majority of entrainment defects. In the model, the Impingement forms defined in the OFEM algorithm captured most of the entrainment scenarios. This highlighted that the OFEM reproduced the similarity

of the flow conditions in different filling patterns, *i.e.* the plunging jet type of flow. The four entrainment forms defined in the codes captured the most of plunging jets, but also revealed the potential errors from the OFEM algorithm.

Owing to the formation mechanisms of entrainment defects, the distributions of these defects were affected by the flow conditions, which in turn were determined by the mould design. Results have shown that *FLOW-3D* could model the flow patterns within different moulds accurately, which implied that the OFEM based on the *FLOW-3D* software had the potential to predict the entrainment defect distribution. However, the current validations of the OFEM did not show high accuracy of the predictions. This could be attributed two factors: the difficulties in achieving high quality experimental data and the limitations of the OFEM.

Initial validation used the data that reported by other researchers, in which either the experimental conditions were not fully described, or the results were affected by other factors outside the reach of the OFEM algorithm. The consideration of the three different entrainment mechanisms showed the different entrainment severities in the moulds, and these were reflected by the simulations. However, the quantitative validations of the algorithm were adversely affected by the shrinkage porosity presented in the cast plates. Although a weak relationship was obtained from the validation using the tensile test bar mould, the results showed that the requirement of consistent results to validate the OFEM algorithm conflicted with the presence of entrainment defects in the castings, as a large number of entrainment defects would lead to highly variant results, shown as low Weibull moduli of the results in the experiments reported.

The main limitation of the OFEM was the properties that could be assigned to the particles in the model. The synchrotron-based X-ray tomography showed the different morphologies of the entrainment defects in 3D, and revealed the evolution of these defects in the fully liquid state, which obviously were very important work for the fundamental understanding of the behaviours of entrainment defects. However, these

properties could not be simply set to the particle model in the OFEM, which meant the model had to used with some assumed properties. There are also some unknown factors, such as the particle adhesion with the mould wall, affecting the modelling results. Another concern was the lack of the quantitative link between the number of particles in the models and the quantity of the entrainment defects in the castings. This sometimes limited the OFEM as a visualisation tool for the potential defect distribution in the castings, rather than a quantitative indicator of the properties of castings.

Modelling results have shown the adhesion of particles to the mould wall could affect the predicted defects distribution. The use of sticky particles in the model resulted in a biased estimation of the defect distributions in a casting, since the sticky particles were inclined to stay at the most entraining regions in the mould, and hence, the model could not predict the final location of defects in the mould cavity properly. Modelling work using sticky particles also underestimated the influence of pouring conditions on the defect distribution in a casting.

During the mould filling process, the plunging jet developed in the pouring basin generated a large number of entrainment defects. Although previous simulations and the models run in this research have demonstrated the pouring condition had limited effects on the fluid conditions in the rest of running system and mould cavity, the predicted defect distribution could be altered by the initial pouring condition in the basin, especially when the non-sticky particles were used.

Simulations showed the density of particles in the models did influence the predicted particle distribution in the castings. Although the densities of the oxides associated with the entrainment defects are heavier than the liquid aluminium alloy in this study, the X-ray tomographical observation showed the entrainment defects could maintain their positions in the static fluid, and this was proved by the calculation using Stokes' Law. Therefore, current results suggested using a density of particle that is similar to the liquid aluminium alloy, can provide reasonable predictions on the defect distribu-

tion.

The application of a ceramic foam filter in the model was avoided. This reduces ability to validate OFEM, since the current *FLOW-3D* Porous Media Model could not consider the internal flow condition in a porous object, although it could model the velocity reduction during the flow pass through a ceramic foam filter.

In summary, the current results suggested that, in a simulation without a ceramic foam filter, using non-sticky particles with a density of 2400 $kg \cdot m^{-3}$ in the model, with consideration of the entrainment in the pouring basin, would provide the best prediction of the entrainment defect distribution in a casting. Further potential work for the validation of the OFEM is suggested in Chapter 8.

Chapter 7

Conclusions

The OFEM algorithm has been investigated through a series of models, including: modelling of previously reported fatigue and tensile bar moulds, the three different entrainment mechanisms formed during filling of a plate-shaped mould, and filling of a tensile test bar mould with a specially designed runner section. The modelling results were used to predict the particle quantity and distribution in the castings. The estimated defect distributions within the castings and the predicted reliability of the castings were compared with the experimental results, to validate the OFEM algorithm. Currently, the validation experimental results have not correlated strongly with the model predictions. The characteristics of entrainment defects were investigated using synchrotron X-ray microtomography, and some previously unknown behaviour of oxide film defects in liquid aluminium alloy was revealed. Within the course of this research the following conclusions can be drawn:

1. During mould filling the plunging jet type of flows are the dominant mechanisms for surface film entrainment. Commonly defined entrainment mechanisms in the casting process, such as a rising jet, a plunging jet and a return wave, bear similarity in terms of flow momentum and energy dispersal, and can be broadly defined as plunging types of flow conditions.

2. Modelling results showed that the majority of particles were entrained by the

Impingement forms, which are used to describe the plunging jet types of flow, rather than Colliding Fronts or Shear Flows.

3. The particle quantity predicted by OFEM can be used as an quantitative indicator for measurement of entrainment severity, although the lack of a benchmark test of particle quantity made it impossible to directly link the particle count in the model to a specific entrainment severity in the mould.

4. A quantitative measurement method in the model was developed to determine the quantity or concentration of particles within the whole domain or in a specific area of a casting. The relationship between the predicted particle quantity/concentration and mechanical properties of casting showed that the predicted higher particle quantity/concentration could be linked to lower properties of the castings, although the trends were not distinct. Among the validation the simulations that used non-sticky particle model and considered entrainment during pouring and filling of all parts of mould showed highest correlation with experimental results.

5. The current validation attempt has not found very strong correlation between predicted particle distribution in specific area in models and strength variations in corresponding area of castings. The main challenges include: *a*). the obtaining of reliable experimental data, which requires the effects of entrainment defects to be isolated from those of other defects, and good reproducibility, *i.e.* high Weibull modulus, (however, large numbers of entrainment defects in the casting inevitably result in low Weibull modulus of the casting); *b*). the determination of the solidification time in the model, as the particles can move continuously by the momentum of fluid flow after the mould has been filled.

6. The particle "stickiness" setting in the model affects the modelling results. Although there is a lack of knowledge about the interaction between entrainment

defects and the mould wall, the comparison between the modelling and the experimental results has demonstrated that using non-sticky particles in the model provided more accurate predictions.

7. The pouring condition of the liquid alloy from the crucible to the pouring basin influenced the fluid flow within the mould, and hence the predicted defect distribution pattern. This implies that using a pressure boundary instead of simulation of pouring in the casting process would lead to inaccurate filling models.

8. The Porous Media Module in *FLOW-3D* can model the velocity reduction, but cannot accurate reproduce the flow structure that develops when the liquid metal passes through a porous ceramic filter. It is suggested to avoid the use and modelling of a filter in the validation of OFEM at the current stage.

9. Calculation shows the density of defects should have limited influence on their distribution. However, modelling results showed that the particle density setting has an effect on the modelled defect distribution in the casting. Current experimental observation suggests that the defects have a similar density to the surrounding liquid metal. Therefore, the density setting of 2400 $\mathrm{kg}\cdot\mathrm{m}^{-3}$ of particles in the model can give good estimation of the defect distribution.

10. The morphology of entrainment defects have been characterised by synchrotron X-ray tomography. The observation shows that the morphology of entrainment defects in 3D could be as simple as a spherical pore or very complex, with irregular branches.

11. The morphological evolution of entrainment defects in the liquid state are closely related to their initial shape and the amount of gas phase entrained. The defect with the most gas experienced the largest morphological change during holding in the liquid state, due to a reaction between the entrained gas phase and the surrounding liquid alloy.

12. The unfurling mechanism, or inflation of an oxide film defect during holding in the liquid state was not observed in the experiment. This is probably because: *a*). the unfurling or inflation of entrainment defects is impractical in casting condition,*e.g.* the rearrangement of the surface film in 3D space in the liquid metal may require much higher driving force; *b*). the experimental conditions could not initiate the process, *e.g.* the hydrogen content of the liquid alloy was too low; *c*). other factors hindered the unfurling process, such as the branches of defects resulting in a higher drag force applied to the defect surface.

Chapter 8

Future Work

The ultimate objective of this research was to develop an accurate model to predict the formation and distribution of entrainment defects and their associated defects, possibly gas and shrinkage porosity, in aluminium castings. The current model has demonstrated its capability and shown some useful results. However, obviously, the accuracy of the model still requires further improvement. Although the modelling approach used in *FLOW-3D* restricted the development of some important parameters in the algorithm, potential future work could include:

1. The entrainment criteria require further development. The current definition of the entrainment forms uses Boolean logical, considering the volume fraction of fluid, the free surface face normal and the velocity direction in adjacent mesh cells. More accurate definitions should consider the speed of fluid flow and link the quantity of particles generated during this process with this speed, as Ohnaka proposed [101].

2. Although a higher number of particles were generally associated with lower properties of castings, further experimental study is needed to understand the defect generation rate.

3. The method of interpretation of the particle quantity could be improved to better link the particle count in the model with the defect quantities in the casting. Since

the particle location could be interpreted to give the probability of existence of defects, there might be a linear relation between these two quantities.

4. The *FLOW-3D* particle model allows different particle densities to be defined. With further experimental evidence on defect density distribution, various particle densities could be used in the model, to predict defect distributions more accurately.

Experimental work to be conducted in the future to investigate the behaviour and influence of entrainment defects could include:

1. The creation of a mould with a running system that can generate different levels of entrainment during filling and deliver the liquid to different parts of a casting. The strength of samples from different parts of casting can then be used to establish a link between the local strength of a casting and the particle quantities in the model. For example, design a mould generates different levels of plunging jets in different parts and compare the strength of specimens from these locations and predicted particle quantities in these locations in the model.

2. Further X-ray microtomography studies with better prepared samples, with known hydrogen contents can be used to understand the effect of hydrogen content on the evolution of entrainment defects. A high performance computer should be employed to carry out the image analysis and 3D volume reconstruction to get quantitative measurements of the volumes and surface areas of entrainment defects to understand their evolution with time.

Chapter 9

Appendix

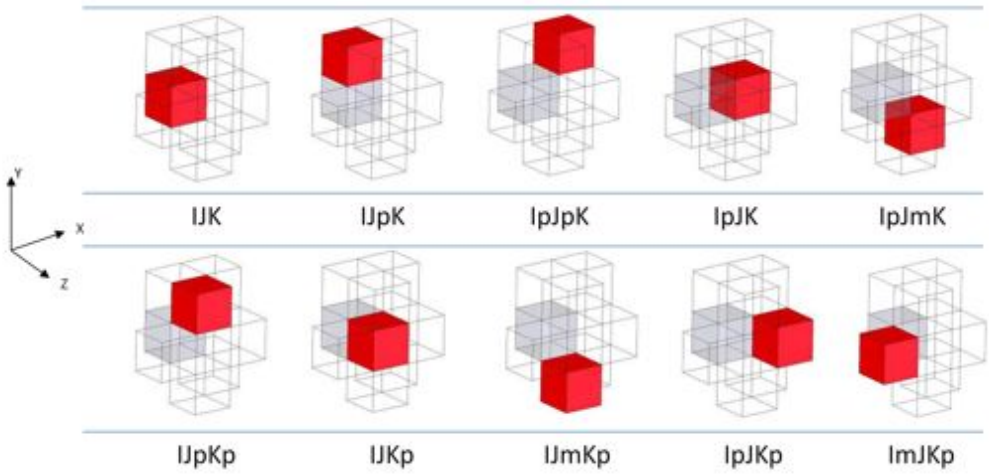

Figure 9.1: *FLOW-3D* cell indices. 'p' and 'm' indicate positive and negative in the direction by the preceding letter respectively.

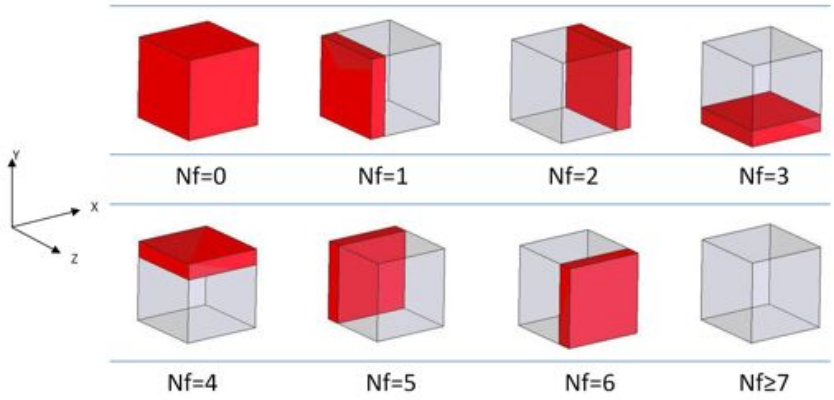

Figure 9.2: *FLOW-3D* cell surface normal orientations. (Nf values)

Entrainment Form	Description	Diagram	Logic
1	Colliding fronts x-plane		Nf(ijk)=0 arint(ijk).gt.zero fn(ijk).le.0.98 f(ijk).ge.1 nf(ipjk).ne.1 nf(ipjk).ne.2. nf(imjk).ne.1 nf(imjk).ne.2 nf(ijpk).ne.1 nf(ijpk).ne.2.
2	Colliding fronts y-plane		Nf(ijk)=.0 arint(ijk).gt.zero fn(ijk).le.0.98 f(ijk).ge.1 nf(ijpk).ne.3 nf(ijmk).ne nf(ijmk).ne.3 nf(ijmk).ne.4 nf(ipjk).ne.3 nf(ipjk).ne.4
3	Colliding fronts z-plane		Nf(ijk).=.0 arint(ijk).gt.zero fn(ijk).le.0.98 f(ijk).ge.1 nf(ipjk).ne.5 nf(ipjk).ne.6 nf(imjk).ne.5 nf(imjk).ne.6 nf(ijpk).ne.5 nf(ijpk).ne.6.

Figure 9.3: Boolean logic of entrainment types 1 to 3: Colliding fronts.

Entrainment Form	Description	Diagram	Logic	
4	Shear flow x-plane		Nf (ijk)= 1 u(ijk).ge.0 f(ijk)+f(ijpk).ge.1	Nf (ijpk)= 2 u(ijpk).le.0
5	Shear flow x-plane		Nf (ijk)= 2 u(ijk).le.0 f(ijk)+f(ijpk).ge.1	Nf (ijpk)= 1 u(ijpk).ge.0
6	Shear flow x-plane		Nf (ijk)= 2 u(ijk).le.0 f(ijk)+f(ijkp).ge.1	Nf (ijkp)= 1 u(ijkp).ge.0
7	Shear flow x-plane		Nf (ijk)= 1 u(ijk).ge.0 f(ijk)+f(ijkp).ge.1	Nf (ijkp)= 2 u(ijkp).le.0
8	Shear flow y-plane		Nf (ijk)= 3 v(ijk).ge.0 f(ijk)+f(ipjk).ge.1	Nf (ipjk)= 4 v(ipjk).le.0
9	Shear flow y-plane		Nf (ijk)= 4 v(ijk).le.0 f(ijk)+f(ipjk).ge.1	Nf (ipjk)= 3 v(ipjk).ge.0
10	Shear flow y-planes		Nf (ijk)= 4 v(ijk).le.0 f(ijk)+f(ijkp).ge.1	Nf (ijkp)= 3 v(ijkp).ge.0

Figure 9.4: Boolean logic of entrainment types 4 to 10: Shear flows.

Entrainment Form	Description	Diagram	Logic	
11	Shear flow y-plane		Nf (ijk)= 3 v(ijk).ge.0 f(ijk)+f(ijkp).ge.1	Nf (ijkp)= 4 v(ijkp).le.0
12	Shear flow z-plane		Nf (ijk)= 5 w(ijk).ge.0 f(ijk)+f(ipjk).ge.1	Nf (ipjk)= 6 w(ipjk).le.0
13	Shear flow z-plane		Nf (ijk)= 6 w(ijk).le.0 f(ijk)+f(ipjk).ge.1	Nf (ipjk)= 5 w(ipjk).ge.0
14	Shear flow z-plane		Nf (ijk)=6 w(ijk).le.0 f(ijk)+f(ijpk).ge.1	Nf (ijpk)= 5 w(ijpk).ge.0
15	Shear flow z-plane		Nf (ijk)= 5 w(ijk).ge.0 f(ijk)+f(ijpk).ge.1	Nf (ijpk)= 6 w(ijpk).le.0
16	Diagonal shear flow x-plane		Nf (ijk)= 1 u(ijk).ge.0 f(ijk).ge.0.95	Nf (ipjpk)= 2 u(ipjpk).le.0 f(ipjpk).ge.0.95
17	Diagonal shear flow x-plane	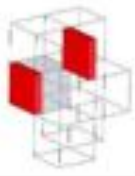	Nf (ijk)= 1 u(ijk).ge.0 f(ijk)+ f(ijpkp).ge.1	Nf (ijpkp)= 2 u(ijpkp).le.0

Figure 9.5: Boolean logic of entrainment types 11 to 17: Shear flows (continued).

Entrainment Form	Description	Diagram	Logic	
18	Diagonal shear flow x-plane		Nf (ijk)= 2 u(ijk).le.0 f(ijk)+ f(ijmkp).ge.1	Nf (ijmkp)=1 u(ijmkp).ge.0
19	Diagonal shear flow x-plane		Nf (ijk)= 2 u(ijk).le.0 f(ijk)+ f(ijpkp).ge.1	Nf (ijpkp)= 1 u(ijpkp).ge.0
20	Diagonal shear flow x-plane		Nf (ijk)=1 u(ijk).ge.0 f(ijk).ge.0.95	Nf (ipjkp)=2 u(ipjkp).le.0 f(ipjkp).ge.0.95
21	Diagonal shear flow x-plane		Nf (ijk)= 1 u(ijk).ge.0 f(ijk).ge.0.95	Nf (ipjmk)= 2 u(ipjmk).le.0 f(ipjmk).ge.0.95
22	Diagonal shear flow y-plane		Nf (ijk)= 3 v(ijk).ge.0 f(ijk)+ f(ijmkp).ge.1	Nf (ipjkp)=4 v(ipjkp).le.0
23	Diagonal shear flow y-plane		Nf (ijk)= 3 v(ijk).ge.0 f(ijk).ge.0.95	Nf (ipjpk)=4 v(ipjpk).le.0 f(ipjpk).ge.0.95
24	Diagonal shear flow y-plane		Nf (ijk)= 3 v(ijk).ge.0 f(ijk).ge.0.95	Nf (ijpkp)= 4 v(ijpkp).le.0 f(ijpkp).ge.0.95

Figure 9.6: Boolean logic of entrainment types 18 to 24: Shear flows (continued).

Entrainment Form	Description	Diagram	Logic	
25	Diagonal shear flow y-plane		Nf (ijk)= 4 v(ijk).le.0 f(ijk)+ f(ipjkp).ge.1	Nf (ipjkp)= 3 v(ipjkp).ge.0
26	Diagonal shear flow y-plane	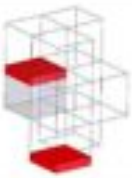	Nf (ijk)= 4 v(ijk).le.0 f(ijk).ge.0.95	Nf (ijmkp)=3 v(ijmkp).ge.0 f(ijmkp).ge.0.95
27	Diagonal shear flow y-plane		Nf (ijk)= 4 v(ijk).le.0 f(ijk).ge.0.95	Nf (ipjmk)=3 v(ipjmk).ge.0 f(ipjmk).ge.0.95
28	Diagonal shear flow y-plane		Nf (ijk)= 3 v(ijk).ge.0 f(ijk)+ f(imjkp).ge.1	Nf (imjkp)=4 v(imjkp).le.0
29	Diagonal shear flow y-plane	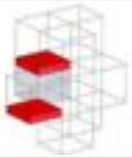	Nf (ijk)= 4 v(ijk).le.0 f(ijk)+ f(imjkp).ge.1	Nf (imjkp)=3 v(imjkp).ge.0
30	Diagonal shear flow z-plane	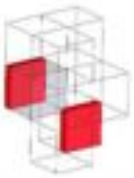	Nf (ijk)= 5 w(ijk).ge.0 f(ijk)+ f(ipjmk).ge.1	Nf (ipjmk)=6 w(ipjmk).le.0
31	Diagonal shear flow z-plane		Nf (ijk)= 5 w(ijk).ge.0 f(ijk)+ f(ijmkp).ge.1	Nf (ijmkp)= 6 w(ijmkp).le.0

Figure 9.7: Boolean logic of entrainment types 25 to 31: Shear flows (continued).

Table 9.1: Glossary of variables used in the entrainment form definitions

	Nf	primary normal to free surface
FLOW-3D variables	v	velocity in x- direction
	u	velocity in y- direction
	w	velocity in z- direction
	fn	fraction fluid at start of cycle
	f	fraction fluid at end of cycle
	arint	free surface area of cell
Fortran operators	.gt.	greater than
	.ge.	greater or equal to
	.eq.	equal to
	.lt.	less than
	.le.	less than or equal to

Entrainment Form	Description	Diagram	Logic	
32	Diagonal shear flow z-plane	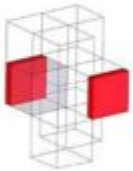	Nf (ijk)= 5 w(ijk).ge.0 f(ijk).ge.0.95	Nf (ipjkp)=6 w(ipjkp).le.0 f(ipjkp).ge.0.95
33	Diagonal shear flow z-plane		Nf (ijk)= 5 w(ijk).ge.0 f(ijk)+ f(ipjpk).ge.1	Nf (ipjpk)=6 w(ipjpk).le.0
34	Diagonal shear flow z-plane	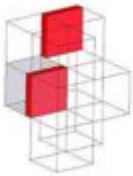	Nf (ijk)= 6 w(ijk).le.0 f(ijk)+ f(ipjpk).ge.1	Nf (ipjpk)= 5 w(ipjpk).ge.0
35	Diagonal shear flow z-plane	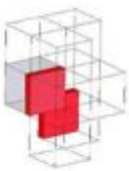	Nf (ijk)= 6 w(ijk).le.0 f(ijk)+ f(ipjmk).ge.1	Nf (ipjmk)= 5 w(ipjmk).ge.0
36	Diagonal shear flow z-plane		Nf (ijk)= 5 w(ijk).ge.0 f(ijk).ge.0.95	Nf (imjkp)= 6 w(imjkp).le.0 f(imjkp).ge.0.95

Figure 9.8: Boolean logic of entrainment types 32 to 36: Shear flows (continued).

Entrainment Form	Description	Diagram	Logic
37	Impingement around z-axis		Nf (ijk)= 1 Nf (ipjpk)=4 NOT(v(ijk).le.0.and.u(ipjpk).ge.0)
38	Impingement around z-axis		Nf (ijk)= 3 Nf (ipjpk)= 2 NOT (u(ijk).le.0.and.v(ipjpk).ge.0)
39	Impingement around z-axis		Nf (ijk)= 1 Nf (ipjmk)= 3 NOT (v(ijk).ge.0.and.u(ipjmk).ge.0)
40	Impingement around z-axis		Nf (ijk)= 4 Nf (ipjmk)= 2 NOT (u(ijk).le.0.and.v(ipjmk).le.0)
41	Impingement around x-axis		Nf (ijk)= 3 Nf (ijpkp)= 6 NOT(w(ijk).le.0.and.v(ijpkp).ge.0)
42	Impingement around x-axis		Nf (ijk)= 5 Nf (ijpkp)= 4 NOT(v(ijk).le.0.and.w(ijpkp).ge.0)

Figure 9.9: Boolean logic of entrainment types 37 to 42: Impingement.

Entrainment Form	Description	Diagram	Logic
43	Impingement around x-axis		Nf (ijk)= 4 Nf (ijmkp)= 6 NOT(w(ijk).le.0.and.v(ijmkp).le.0)
44	Impingement around x-axis		Nf (ijk)= 5 Nf (ijmkp)= 3 NOT(v(ijk).ge.0.and. w(ijmkp).ge.0)
45	Impingement around y-axis		Nf (ijk)= 5 Nf (ipjkp)= 2 NOT(u(ijk).le.0.and.w(ipjkp).ge.0)
46	Impingement around y-axis	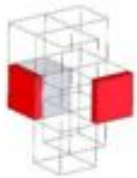	Nf (ijk)= 1 Nf (ipjkp)=6 NOT(w(ijk).le.0.and.u(ipjkp).ge.0)
47	Impingement around y-axis		Nf (ijk)= 2 Nf (imjkp)=6 NOT(w(ijk).le.0.and.u(imjkp).le.0)
48	Impingement around y-axis		Nf (ijk)= 5 Nf (imjkp)=1 NOT(u(ijk).ge.0.and.w(imjkp).ge.0)

Figure 9.10: Boolean logic of entrainment types 43 to 48: Impingement (continued).

Entrainment Form	Diagram	X Co-Ordinate	Y Co-Ordinate	Z Co-Ordinate	X-Vel	Y-Vel	Z-Vel
1		Centre	Centre	Centre	ImJK, IpJK linear interpellation	ImJK, IpJK linear interpellation	ImJK, IpJK linear interpellation
2		Centre	Centre	Centre	IJmK, IJpK linear interpellation	IJmK, IJpK linear interpellation	IJmK, IJpK linear interpellation
3		Centre	Centre	Centre	IJKm, IJKp linear interpellation	IJKm, IJKp linear interpellation	IJKm, IJKp linear interpellation

Figure 9.11: Particle initial position and velocity vectors in entrainment types 1 to 3: Colliding fronts.

Entrainment Form	Diagram	X Co-Ordinate	Y Co-Ordinate	Z Co-Ordinate	X-Vel	Y-Vel	Z-Vel
4		Below surface	Max	Centre	IJK, IJpK linear interpellation	IJK, IJpK linear interpellation	IJK, IJpK linear interpellation
5		Below surface	Max	Centre	IJK, IJpK linear interpellation	IJK, IJpK linear interpellation	IJK, IJpK linear interpellation
6		Below surface	Centre	Max	IJK, IJKp linear interpellation	IJK, IJKp linear interpellation	IJK, IJKp linear interpellation
7		Below surface	Centre	Max	IJK, IJKp linear interpellation	IJK, IJKp linear interpellation	IJK, IJKp linear interpellation
8		Max	Below surface	Centre	IJK, IpJK linear interpellation	IJK, IpJK linear interpellation	IJK, IpJK linear interpellation
9		Max	Below surface	Centre	IJK, IpJK linear interpellation	IJK, IpJK linear interpellation	IJK, IpJK linear interpellation
10		Centre	Below surface	Max	IJK, IJKp linear interpellation	IJK, IJKp linear interpellation	IJK, IJKp linear interpellation
11		Centre	Below surface	Max	IJK, IJKp linear interpellation	IJK, IJKp linear interpellation	IJK, IJKp linear interpellation

Figure 9.12: Particle initial position and velocity vectors in entrainment types 4 to 11: Shear flows.

Entrainment Form	Diagram	X Co-Ordinate	Y Co-Ordinate	Z Co-Ordinate	X-Vel	Y-Vel	Z-Vel
12		Max	Centre	Below surface	IJK, IpJK linear interpellation	IJK, IpJK linear interpellation	IJK, IpJK linear interpellation
13		Max	Centre	Below surface	IJK, IpJK linear interpellation	IJK, IpJK linear interpellation	IJK, IpJK linear interpellation
14		Centre	max	Below surface	IJK, IJpK linear interpellation	IJK, IJpK linear interpellation	IJK, IJpK linear interpellation
15		Centre	max	Below surface	IJK, IJpK linear interpellation	IJK, IJpK linear interpellation	IJK, IJpK linear interpellation
16		Below surface	max	Centre	IJK, IpJpK linear interpellation	IJK, IpJpK linear interpellation	IJK, IpJpK linear interpellation
17		Below surface	max	max	IJK, IJpKp linear interpellation	IJK, IJpKp linear interpellation	IJK, IJpKp linear interpellation
18		Below surface	max	max	IJK, IJmKp linear interpellation	IJK, IJmKp linear interpellation	IJK, IJmKp linear interpellation
19		Below surface	max	Max	IJK, IJpKp linear interpellation	IJK, IJpKp linear interpellation	IJK, IJpKp linear interpellation

Figure 9.13: Particle initial position and velocity vectors in entrainment types 12 to 19: Shear flows (continued).

Entrainment Form	Diagram	X Co-Ordinate	Y Co-Ordinate	Z Co-Ordinate	X-Vel	Y-Vel	Z-Vel
20		Below surface	Centre	max	IJK, IpJKp linear interpellation	IJK, IpJKp linear interpellation	IJK, IpJKp linear interpellation
21		Below surface	max	Centre	IJK, IpJmK linear interpellation	IJK, IpJmK linear interpellation	IJK, IpJmK linear interpellation
22		Max	Below surface	Max	IJK, IpJKp linear interpellation	IJK, IpJKp linear interpellation	IJK, IpJKp linear interpellation
23		Max	Below surface	Centre	IJK, IpJpK linear interpellation	IJK, IpJpK linear interpellation	IJK, IpJpK linear interpellation
24		Centre	Below surface	Max	IJK, IJpKp linear interpellation	IJK, IJpKp linear interpellation	IJK, IJpKp linear interpellation
25		max	Below surface	max	IJK, IpJKp linear interpellation	IJK, IpJKp linear interpellation	IJK, IpJKp linear interpellation
26		Centre	Below surface	max	IJK, IJmKp linear interpellation	IJK, IJmKp linear interpellation	IJK, IJmKp linear interpellation
27		max	Below surface	Centre	IJK, IpJmK linear interpellation	IJK, IpJmK linear interpellation	IJK, IpJmK linear interpellation

Figure 9.14: Particle initial position and velocity vectors in entrainment types 20 to 27: Shear flows (continued).

Entrainment Form	Diagram	X Co-Ordinate	Y Co-Ordinate	Z Co-Ordinate	X-Vel	Y-Vel	Z-Vel
28		min	Below surface	max	IJK, ImJKp linear interpellation	IJK, ImJKp linear interpellation	IJK, ImJKp linear interpellation
29		min	Below surface	max	IJK, ImJKp linear interpellation	IJK, ImJKp linear interpellation	IJK, ImJKp linear interpellation
30		max	min	Below surface	IJK, IpJmK linear interpellation	IJK, IpJmK linear interpellation	IJK, IpJmK linear interpellation
31		max	min	Below surface	IJK, IJmKp linear interpellation	IJK, IJmKp linear interpellation	IJK, IJmKp linear interpellation
32		max	Centre	Below surface	IJK, IpJKp linear interpellation	IJK, IpJKp linear interpellation	IJK, IpJKp linear interpellation
33		max	Max	Below surface	IJK, IpJpK linear interpellation	IJK, IpJpK linear interpellation	IJK, IpJpK linear interpellation
34		Max	max	Below surface	IJK, IpJpK linear interpellation	IJK, IpJpK linear interpellation	IJK, IpJpK linear interpellation
35		max	Min	Below surface	IJK, IpJmK linear interpellation	IJK, IpJmK linear interpellation	IJK, IpJmK linear interpellation
36		min	centre	Below surface	IJK, ImJKp linear interpellation	IJK, ImJKp linear interpellation	IJK, ImJKp linear interpellation

Figure 9.15: Particle initial position and velocity vectors in entrainment types 28 to 36: Shear flows (continued).

Entrainment Form	Diagram	X Co-Ordinate	Y Co-Ordinate	Z Co-Ordinate	X-Vel	Y-Vel	Z-Vel
37		Below surface	max	Centre	IJpK (Corner cell Velocity)	IJpK (Corner cell Velocity)	IJpK (Corner cell Velocity)
38		max	Below surface	Centre	IpJK (Corner cell Velocity)	IpJK (Corner cell Velocity)	IpJK (Corner cell Velocity)
39		Below surface	min	Centre	IJmK (Corner cell Velocity)	IJmK (Corner cell Velocity)	IJmK (Corner cell Velocity)
40		max	Below surface	Centre	IpJK (Corner cell Velocity)	IpJK (Corner cell Velocity)	IpJK (Corner cell Velocity)
41		Centre	Below surface	max	IJKp (Corner cell Velocity)	IJKp (Corner cell Velocity)	IJKp (Corner cell Velocity)
42		Centre	max	Below surface	IJpK (Corner cell Velocity)	IJpK (Corner cell Velocity)	IJpK (Corner cell Velocity)

Figure 9.16: Particle initial position and velocity vectors in entrainment types 37 to 42: Impingement.

Entrainment Form	Diagram	X Co-Ordinate	Y Co-Ordinate	Z Co-Ordinate	X-Vel	Y-Vel	Z-Vel
43		Centre	Below surface	max	IJKp (Corner cell Velocity)	IJKp (Corner cell Velocity)	IJKp (Corner cell Velocity)
44		Centre	min	Below surface	IJmK (Corner cell Velocity)	IJmK (Corner cell Velocity)	IJmK (Corner cell Velocity)
45		max	Centre	Below surface	IpJK (Corner cell Velocity)	IpJK (Corner cell Velocity)	IpJK (Corner cell Velocity)
46	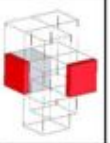	Below surface	Centre	max	IJKp (Corner cell Velocity)	IJKp (Corner cell Velocity)	IJKp (Corner cell Velocity)
47	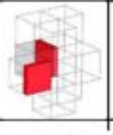	Below surface	Centre	max	IJKp (Corner cell Velocity)	IJKp (Corner cell Velocity)	IJKp (Corner cell Velocity)
48		Min	Centre	Below surface	ImJK (Corner cell Velocity)	ImJK (Corner cell Velocity)	ImJK (Corner cell Velocity)

Figure 9.17: Particle initial position and velocity vectors in entrainment types 43 to 48: Impingement (continued).

References

[1] U.S.Geological Survey. Mineral Commodity Summaries: 2012. Technical report, Reston, Virginia, USA, 2012.

[2] ASM International Handbook Committee. *Aluminium and Aluminium Alloys*. Asm Specialty Handbook. ASM International, The Materials Information Society, 5th edition, 1993.

[3] The Aluminum Association. Aluminum Industry Vision: Sustainable Solutions for a Dynamic World. Technical report, 2001.

[4] The Aluminum Association. Aluminum Industry Technology Roadmap. Technical report, 1997.

[5] I. Polmear. *Light Alloys: From Traditional Alloys to Nanocrystals*. Butterworth-Heinemann, 4th edition, 2006.

[6] J. Campbell. *Castings*. Butterworth-Heinemann, Oxford, 2nd ed edition, 2003.

[7] J. Campbell. Entrainment defects. *Materials Science and Technology*, 22(2):127–145, 2006.

[8] C. Reilly. *Development of Quantitative Casting Quality Assessment Criteria Using Process Modelling*. Thesis, University of Birmingham, 2010.

[9] S. Impey, D.M. Stephenson, and J.R. Nicholls. A study of the effect of magnesium additions on the oxide growth morphologies on liquid aluminium alloys. In *International Conference on the Microscopy of Oxidation*, pages 26–28, 1990.

[10] M.P. Silva and D.E.J Talbot. Oxidation of liquid aluminum-magnesium alloys. *Essential Readings in Light Metals, Cast Shop for Aluminum Production*, page 137, 2013.

[11] N. Birks, G.H. Meier, and F.S. Pettit. *Introduction to the High Temperature Oxidation of Metals*. Cambridge University Press, 2nd edition, 2006.

[12] G. Wightman and D.J. Fray. The dynamic oxidation of aluminum and its alloys. *Metallurgical Transactions B*, 14(4):625–631, 1983.

[13] C.N. Cochran, D.L. Belitskus, and D.L. Kinosz. Oxidation of aluminum-magnesium melts in air, oxygen, flue-gas, and carbon dioxide. *Metallurgical Transactions B*, 8(2):323–332, 1977.

[14] O. Ozdemir, J.E. Gruzleski, and R.A. Drew. Effect of low-levels of strontium on the oxidation behavior of selected molten aluminummagnesium alloys. *Oxidation of metals*, 72(5-6):241–257, 2009.

[15] W.W. Smeltzer. Oxidation of aluminum in the temperature range 400°-600°C. *Journal of The Electrochemical Society*, 103(4):209–214, 1956.

[16] W.C. Sleppy. Oxidation of molten high-purity aluminum in dry oxygen. *Journal of the Electrochemical Society*, 108(12):1097–1102, 1961.

[17] M. Syvertsen. Oxide skin strength on molten aluminum. *Metallurgical and Materials Transactions B*, 37(3):495–504, 2006.

[18] J. Weigel and E. Fromm. Determination of hydrogen absorption and desorption processes in aluminum melts by continuous hydrogen activity measurements. *Metallurgical Transactions B*, 21(5):855–860, 1990.

[19] S.A. Azarmehr, M. Divandari, and H. Arabi. Investigation on thickness of short time oxide films in Al-1Mg and Al-2Mg alloys. *Materials Science and ...*, 28(11):1295–1300, 2012.

[20] B. Nayebi and M. Divandari. Characteristics of dynamically formed oxide films on molten aluminium. *International Journal of Cast Metals Research*, 25(5):270–276, October 2012.

[21] M. Divandari and J. Campbell. Morphology of oxide films of Al5Mg alloy in dynamic conditions in casting. *International Journal of Cast Metals Research*, 18(3):187–192, March 2005.

[22] N.R. Green and J. Campbell. Influence of oxide film filling defects on the strength of Al-7Si-Mg alloy castings. *AFS Transactions*, 114(102):341–348, 1994.

[23] C. Nyahumwa, N.R. Green, and J. Campbell. Effect of mold-filling turbulence on fatigue properties of cast aluminum alloys. *AFS Transactions*, 106:215–224, 1998.

[24] D.W. Oxtoby, H.P. Gillis, and A. Campion. *Principles of Modern Chemistry.* Available Titles OWL Series. BROOKS COLE Publishing Company, 6 edition, 2007.

[25] Z. Fan, Y. Wang, Z.F. Zhang, and M. Xia. Shear enhanced heterogeneous nucleation in some Mg-and Al-alloys. *International Journal of Cast Metals Research*, 22(1-4):318–322, 2009.

[26] J. Campbell. Evidence for entrainment defects. *Materials Science and Technology*, 24(7):875–881, July 2008.

[27] X. Cao and J. Campbell. The nucleation of Fe-rich phases on oxide films in Al-11.5Si-0.4Mg cast alloys. *Metallurgical and Materials Transactions A*, 34(July):1409–1420, 2003.

[28] R. Raiszadeh and W.D. Griffiths. A method to study the history of a double oxide film defect in liquid aluminum alloys. *Metallurgical and Materials Transactions B*, 37(6):865–871, December 2006.

[29] S. Fox and J. Campbell. Visualisation of oxide film defects during solidification of aluminium alloys. *Scripta materialia*, 43(10):881–886, 2000.

[30] D.F. Young, B.R. Munson, T.H. Okiishi, and W.W. Huebsch. *A Brief Introduction to Fluid Mechanics*. John Wiley & Sons, 5 edition, 2010.

[31] Hubert Chanson. *Air Bubble Entrainment in Free-surface Turbulent Shear Flows*. ACADEMIC PRESS, 1st edition, 1996.

[32] F. Najafzadeh Bakhtiarani and R. Raiszadeh. Healing of double-oxide film defects in commercial purity aluminum melt. *Metallurgical and Materials Transactions B*, 42(2):331–340, February 2011.

[33] M. Aryafar, R. Raiszadeh, and A. Shalbafzadeh. Healing of double oxide film defects in A356 aluminium melt. *Journal of Materials Science*, 45(11):3041–3051, February 2010.

[34] Kittiphan Bangyikhan. *Effects of Oxide film, Fe-rich phase, Porosity and their Interactions on Tensile Properties of Cast Al-Si-Mg Alloys*. PhD thesis, University of Birmingham, 2005.

[35] J.G. Kaufman, E.L. Rooy, and American Foundry Society. *Aluminum Alloy Castings: Properties, Processes And Applications*. Asm International, 2004.

[36] K.D. Li and E. Chang. Mechanism of nucleation and growth of hydrogen porosity in solidifying A356 aluminum alloy: an analytical solution. *Acta materialia*, 52(1):219–231, 2004.

[37] J.C. Fisher. The fracture of liquids. *Journal of applied Physics*, 19(11):1062–1967, 1948.

[38] W.D. Griffiths and R. Raiszadeh. Hydrogen, porosity and oxide film defects in liquid Al. *Journal of Materials Science*, 44(November):3402–3407, 2009.

[39] M. Felberbaum and M. Rappaz. Curvature of micropores in AlCu alloys: An X-ray tomography study. *Acta Materialia*, 59(18):6849–6860, 2011.

[40] N.R. Green and J. Campbell. Statistical distributions of fracture strengths of cast Al-7Si-Mg alloy. *Materials Science and Engineering: A*, 173:261–266, 1993.

[41] X. Dai, X. Yang, J. Campbell, and J. Wood. Effects of runner system design on the mechanical strength of Al7SiMg alloy castings. *Materials Science and Engineering A*, 354(1-2):315–325, August 2003.

[42] X. Dai, X. Yang, J. Campbell, and J. Wood. Influence of oxide film defects generated in filling on mechanical strength of aluminium alloy castings. *Materials Science and Technology*, 20(April):505–513, 2004.

[43] C.H. Caceres and B.I. Selling. Casting defects and the tensile properties of an Al-Si-Mg alloy. *Materials Science and Engineering A*, 220(1-2):109–116, December 1996.

[44] J.A. Francis and G.M. Delphine Cantin. The role of defects in the fracture of an AlSiMg cast alloy. *Materials Science and Engineering A*, 407(July):322–329, 2005.

[45] J. Campbell. An overview of the effects of bifilms on the structure and properties of cast alloys. *Metallurgical and Materials Transactions B*, 37(6):857–863, December 2006.

[46] G. Eisaabadi, P. Davami, S.K. Kim, and N. Varahram. Effects of hydrogen and oxides on tensile properties of AlSiMg cast alloys. *Materials Science and Engineering: A*, 552:36–47, August 2012.

[47] J.F. Major. Porosity Control and Fatigue Behavior in A356-T61 Aluminum Alloy. *AFS Transactions*, pages 901–906, 1998.

[48] B. Zhang, D.R. Poirier, and W. Chen. Microstructural effects on high-cycle fatigue-crack initiation in A356.2 casting alloy. *Metallurgical and Materials Transactions A*, 30(10):2659–2666, October 1999.

[49] H. Jiang, P. Bowen, and J.F. Knott. Fatigue performance of a cast aluminium alloy Al-7Si-Mg with surface defects. *Journal of Materials Science*, 34:719 – 725, 1999.

[50] Q.G. Wang, D Apelian, and D.A. Lados. Fatigue behavior of A356-T6 aluminum cast alloys . Part I . Effect of casting defects. *Journal of Light Metals*, 1:73–84, 2001.

[51] Q.G. Wang, P.N. Crepeau, C.J. Davidson, and J.R. Griffiths. Oxide films, pores and the fatigue lives of cast aluminum alloys. *Metallurgical and Materials Transactions B*, 37(6):887–895, December 2006.

[52] A. Khalili and K. Kromp. Statistical properties of Weibull estimators. *Journal of materials science*, 26(24):6741–6752, 1991.

[53] M. Cox, M. Wickins, J.P. Kuang, R.A. Harding, and J. Campbell. Effect of top and bottom filling on reliability of investment castings in Al, Fe and Ni based alloys. *Materials Science and Technology*, 16(December):1445–1452, 2000.

[54] J. Mi, R.A. Harding, and J. Campbell. Effects of the entrained surface film on the reliability of castings. *Metallurgical and Materials Transactions A*, 35(9):2893–2902, September 2004.

[55] R.A. Harding. Towards more reliable investment castings. *International Journal of Cast Metals Research*, 19(5):289–301, 2006.

[56] A.M. Gokhale and G.R. Patel. Analysis of variability in tensile ductility of a semi-solid metal cast A356 Al-alloy. *Materials Science and Engineering A*, 392:184–190, 2005.

[57] A.M. Gokhale and G.R. Patel. Origins of variability in the fracture-related mechanical properties of a tilt-pour-permanent-mold cast Al-alloy. *Scripta Materialia*, 52(3):237–241, February 2005.

[58] M. Tiryakioglu and J. Campbell. Weibull analysis of mechanical data for castings: A guide to the interpretation of probability plots. *Metallurgical and Materials Transactions A*, 41A(December):3121–3129, 2010.

[59] J.T. Staley Jr., M. Tiryakioglu, and J. Campbell. The effect of hot isostatic pressing (HIP) on the fatigue life of A206-T71 aluminum castings. *Materials Science and Engineering: A*, 465(1-2):136–145, September 2007.

[60] C. Nyahumwa, N.R. Green, and J. Campbell. Influence of casting technique and hot isostatic pressing on the fatigue of an Al-7Si-Mg alloy. *Metallurgical and Materials Transactions A*, 32:349–358, 2001.

[61] R. Raiszadeh and W.D. Griffiths. A Semi-empirical mathematical model to estimate the duration of the atmosphere within a double oxide film defect in pure aluminum alloy. *Metallurgical and Materials Transactions B*, 39(2):298–303, April 2008.

[62] D.M. Stefanescu. Computer simulation of shrinkage related defects in metal castings a review. *International Journal of Cast Metals Research*, 18(3):129–143, March 2005.

[63] M.R. Jolly. Casting simulation: How well do reality and virtual casting match? State of the art review. *International Journal of Cast Metals Research*, 14:303–313, 2002.

[64] J.R. Welty, C.E. Wicks, G. Rorrer, and R.E. Wilson. *Fundamentals Of Momentum, Heat, And Mass Transfer*. Wiley India Pvt. Limited, 4th edition, 2009.

[65] J. Blazek. *Computational Fluid Dynamics: Principles and Applications*. Elsevier Science, 2nd edition, 2005.

[66] M. Cross, K. Pericleous, T.N. Croft, D. Mcbride, J.A. Lawrence, and A.J. Williams. Computational modeling of mold Filling and related free-surface flows in shape casting : An overview of the challenges involved. *Metallurgical and Materials Transactions B*, 37B(December):879–885, 2006.

[67] F.H. Harlow and J.E. Welch. Numerical calculation of time-dependent viscous incompressible flow of fluid with free surface. *Physics of fluids*, 8(12):2182–2189, 1965.

[68] C.W. Hirt and B.D. Nichols. Volume of fluid (VOF) method for the dynamics of free boundaries. *Journal of Computational Physics*, 39(1):201–225, January 1981.

[69] C.W. Hirt, B.D. Nichols, and N.C. Romero. SOLA-A Numerical Solution Algorithm for Transient FLuid Flows. Technical report, Los Alamos Scientific Laboratory, 1975.

[70] P. Cleary, J. Ha, V. Alguine, and T. Nguyen. Flow modelling in casting processes. *Applied Mathematical Modelling*, 26(2):171–190, February 2002.

[71] I. Ginzburg and K. Steiner. Lattice Boltzmann model for free-surface flow and its application to filling process in casting. *Journal of Computational Physics*, 185:61–99, 2003.

[72] W. Sun, P. Scarber, H. Li, and Charles E Bates. Modeling, Model Verification, and Defect Formation in Iron Castings. In *Ductile Iron Society 2003 Millis Symposium*, volume 11, 2003.

[73] N.W. Lai, W.D. Griffiths, and J. Campbell. Modelling of the potential for oxide film entrainment in light metal alloy castings. In D.M. Stefanescu, J.A. Warren, M.R. Jolly, and J. Campbell, editors, *Modeling of Casting, Welding and Advanced Solidification Processes- X*, pages 415–422, Destin, FL, 2003. TMS (The Minerals, Metals & Materials Society).

[74] J. Campbell. The modeling of entrainment defects during casting. *Simulation of Aluminum Shape Casting Processing: From Alloy Design to Mechanical Properties*, pages 123–132, 2006.

[75] M.R. Barkhudarov and C.W. Hirt. Tracking defects. Technical report, Flow Science, Inc., 1999.

[76] P. Cleary, M. Prakash, J. Ha, M. Sinnott, T. Nguyen, and J. Grandfield. Modeling of cast systems using smoothed-particle hydrodynamics. *JOM*, 56(3):67–70, March 2004.

[77] M. Prakash, P. Cleary, and J. Grandfield. Modelling of metal flow and oxidation during furnace emptying using smoothed particle hydrodynamics. *Journal of Materials Processing Technology*, 209(7):3396–3407, April 2009.

[78] P. Cleary. Extension of SPH to predict feeding, freezing and defect creation in low pressure die casting. *Applied Mathematical Modelling*, 34(11):3189–3201, November 2010.

[79] C.W. Hirt. Modeling turbulent entrainment of air at a free surface. Technical report, Flow Science, Inc, 1998.

[80] C. Pozrikidis. *Fluid Dynamics: Theory, Computation, and Numerical Simulation*. Springer London, Limited, 2nd edition, 2009.

[81] R. Cuesta, A. Delgado, A. Maroto, and D. Mozo. Numerically modeling oxide entrainment in the filling of castings : The effect of the Webber number. *Journal of the Minerals, Metals and Materials Society*, 58(11):62–65, 2006.

[82] J. Runyoro, S.M.A. Boutorabi, and J. Campbell. Critical gate velocities for film-forming casting alloys. *AFS Transactions*, 100:225–234, 1992.

[83] C. Reilly, N.R. Green, and M.R. Jolly. Surface oxide film entrainment mechanisms in shape casting running systems. *Metallurgical and Materials Transactions B*, 40B, 2009.

[84] J.J. Hernandez-Ortega, R. Zamora, J. Palacios, J. Lopez, and F. Faura. An experimental and numerical study of flow patterns and air entrapment phenomena during the filling of a vertical die cavity. *Journal of Manufacturing Science and Engineering*, 132(5):1–9, 2010.

[85] M. Divandari and J. Campbell. Mechanisms of bubble damage in castings. In *1st Int. Conf. on Gating, Filling and Feeding of Aluminum Castings*, pages 11–13, 2001.

[86] A. Kimatsuka, I. Ohnaka, J.D. Zhu, and T. Ohmichi. Mold filling simulation with consideration of gas escape through sand mold. *International Journal of Cast Metals Research*, 15(3):149–152, 2002.

[87] A. Kimatsuka, I. Ohnaka, J.D. Zhu, A. Sugiyama, and Y. Kuroki. Mold filling simulation for predicting gas porosity. In *Modeling of Casting, Welding and Advanced Solidification Processes XI, TMS*, pages 603–610, 2006.

[88] B.G. Thomas and L. Zhang. Mathematical modeling of fluid flow in continuous casting. *ISIJ international*, 41(10):1181–1193, 2001.

[89] H. Wang, G. Djambazov, K.A. Pericleous, R.A. Harding, and M. Wickins. Modelling the tilt-casting process for the tranquil filling of titanium alloy turbine blades, 2009.

[90] H. Wang, G. Djambazov, and K.A. Pericleous. Modelling the dynamics of the tilt-casting process and the effect of the mould design on the casting quality. *Computers & ...*, 42(1):92–101, 2011.

[91] D.L. McBride, N.J. Humphreys, T.N. Croft, P. Whitey, N.R. Green, and M. Cross. Complex free surface flows for mould filling using centrifugal casting. In S.L. Cockcroft and D.M. Maijer, editors, *Modeling of Casting, Welding and Advanced Solidification Processes-XII*, pages 77–84, Vancouver, Canada, 2009. TMS (The Minerals, Metals & Materials Society).

[92] S. Bounds, G. Moran, K. Pericleous, M. Cross, and T.N. Croft. A computational model for defect prediction in shape castings based on the interaction of free surface flow, heat transfer, and solidification phenomena. *Metallurgical and Materials Transactions B*, 31B(June):515, 2000.

[93] S. Pang, L. Chen, M. Zhang, Y. Yin, T. Chen, J. Zhou, and D. Liao. Numerical simulation two phase flows of casting filling process using SOLA particle level set method. *Applied Mathematical Modelling*, 34(12):4106–4122, 2010.

[94] C.T. Crowe, T.R. Troutt, and J.N. Chung. Numerical models for two-phase turbulent flows. *Annual Review of Fluid Mechanics*, 28:11–43, 1996.

[95] H.P. Zhu, Z.Y. Zhou, R.Y. Yang, and A.B. Yu. Discrete particle simulation of particulate systems: A review of major applications and findings. *Chemical Engineering Science*, 63(23):5728–5770, 2008.

[96] K.D. Carlson and C. Beckermann. Modeling of reoxidation inclusion formation during filling of steel castings. In *Defect Formation, Detection, and Elimination During Casting, Welding, and Solidification*, pages 35–46. Materials Science & Technology, 2005.

[97] A.J. Melendez, K.D. Carlson, C. Beckermann, and M.C. Schneider. Modeling of reoxidation inclusion formation in steel sand casting. In DM Cockcroft, SL and Maijer, editor, *Modeling of Casting, Welding and Advanced Solidification Processes-XII*, pages 393–400, 184 THORN HILL RD, WARRENDALE, PA 15086-7514 USA, 2009. AnyCasting; ESI Grp; MAGMA; Qualica; JSCAST; METSOC, MINERALS, METALS & MATERIALS SOC.

[98] A.J. Melendez, K.D. Carlson, and C. Beckermann. Modelling of reoxidation inclusion formation in steel sand casting. *International Journal of Cast Metals Research*, 23(5):278–288, October 2010.

[99] J.T. Lin, M.R.A Sharif, and J.L. Hill. Numerical simulation of the movement, breakup and entrapment of oxide films during aluminum casting. *Aluminum transactions*, 1(1):71–78, 1999.

[100] X. Yang, X. Huang, X. Dai, J. Campbell, and J. Tatler. Numerical modelling of entrainment of oxide film defects in filling of aluminium alloy castings. *International Journal of Casting Metals Research*, 17(6):321–331, 2004.

[101] Y. Sako, I. Ohnaka, J.D. Zhu, and H. Yasuda. Modelling of oxide entrapment during mold filling of Al-alloy castings. In *the 7th Asian Foundry Congress*, pages 363–369, Taipei, Taiwan, 2001.

[102] I. Ohnaka, J. Iwane, Y. Sako, H. Yasuda, and H.D. Zhao. Estimation of porosity defects in Al-alloy and spheroidal-graphite iron castings. In *the 65th World Foundry Congress*, Gyeongju, Korea, 2002.

[103] H.D. Zhao, I. Ohnaka, Y. Sako, H. Onda, J. Zhu, and H. Yasuda. Estimation of porosity defects with consideration of oxide entrapment. In *the 65th World Foundry Congress*, Gyeongju, Korea, 2002.

[104] C. Reilly, M.R. Jolly, N.R. Green, and J-C. Gebelin. Assessment of casting filling by modeling surface entrainment events using CFD. In *2010 TMS Annual Meeting & Exhibition*, 2010.

[105] C. Reilly, N.R. Green, M.R. Jolly, and J-C Gebelin. The modelling of oxide film entrainment in casting systems using computational modelling. *Applied Mathematical Modelling*, page in press, 2013.

[106] J. Jakumeit, S. Jana, T. Waclawczyk, A. Mehdizadeh, A. Sadiki, and J. Jouani. Four-phase fully-coupled mold-filling and solidification simulation for gas porosity prediction in aluminum sand casting. *IOP Conference Series: Materials Science and Engineering*, 33:012074, 2012.

[107] C.M. Pita and S.D. Felicelli. A fluidstructure interaction method for highly deformable solids. *Computers & Structures*, 88(3-4):255–262, February 2010.

[108] B. Sirrell, M. Holliday, and J. Campbell. Benchmark testing the flow and solidification modeling of AI castings. *JOM*, 48(3):20–23, 1996.

[109] H.D. Zhao, I. Ohnaka, and J.D. Zhu. Modeling of mold filling of Al gravity casting and validation with X-ray in-situ observation. *Applied Mathematical Modelling*, 32:185–194, 2008.

[110] S. Kashiwai, I. Ohnaka, A. Kimatsuka, T. Kaneyoshi, T. Ohmichi, and J.D. Zhu. Numerical simulation and X-ray direct observation of mould filling during vacuum suction casting. *International Journal of Cast Metals Research*, 18(3):144–148, 2005.

[111] W.D. Griffiths, Y. Beshay, D.J. Parker, and X. Fan. The determination of inclusion movement in steel castings by positron emission particle tracking (PEPT). *Journal of Materials Science*, 43(21):6853–6856, October 2008.

[112] W.D. Griffiths, D.J. Parker, X. Fan, and M.N. Hausard. Tracking inclusions in aluminium alloy castings using positron emission particle tracking (PEPT). *Materials Science and Technology*, 26(5):528–533, 2010.

[113] Y.K. Beshay. *The application of positron emission particle tracking to study non-metallic inclusions in metal castings*. PhD thesis, 2010.

[114] D. Burnard, J. Gargiuli, T.W. Leadbeater, D.J. Parker, and W.D. Griffiths. The application of positron emission particle tracking (PEPT) to study inclusions in the casting process. In *Materials Science Forum*, volume 690, pages 25–28. Trans Tech Publ, 2011.

[115] W.D. Griffiths, Y. Beshay, A.J. Caden, X. Fan, J. Gargiuli, T.W. Leadbeater, and D.J. Parker. The use of positron emission particle tracking (PEPT) to study the movement of inclusions in low-melting-point alloy castings. *Metallurgical and Materials Transactions B*, 43(2):370–378, 2012.

[116] X. Yang, X. Huang, X. Dai, J. Campbell, and R.J. Grant. Quantitative characterisation of correlations between casting defects and mechanical strength of Al7SiMg alloy castings. *Materials Science and Technology*, 22(5):561–570, 2006.

[117] S.R. Stock. X-ray microtomography of materials. *International Materials Reviews*, 44(4):141–164, April 1999.

[118] L. Salvo, P. Cloetens, E. Maire, S. Zabler, J.J. Blandin, J.Y. Buffiere, W. Ludwig, E. Boller, D. Bellet, and C. Josserond. X-ray micro-tomography an attractive characterisation technique in materials science. *Nuclear Instruments and Methods*

in Physics Research Section B: Beam Interactions with Materials and Atoms, 200:273–286, January 2003.

[119] O. Betz, U. Wegst, D. Weide, M. Heethoff, L. Helfen, W-K. Lee, and P. Cloetens. Imaging applications of synchrotron X-ray phase-contrast microtomography in biological morphology and biomaterials science. I. General aspects of the technique and its advantages in the analysis of millimetre-sized arthropod structure. *Journal of Microscopy*, 227(1):51–71, 2007.

[120] G.T. Herman. *Fundamentals of Computerized Tomography: Image Reconstruction from Projections*. Advances in Pattern Recognition. Springer London, 2nd edition, 2009.

[121] D. Xia, X. Xiao, J. Bian, X. Han, E.Y. Sidky, F. De Carlo, and X. Pan. Image reconstruction from sparse data in synchrotron-radiation-based microtomography. *The Review of scientific instruments*, 82(4):043706, April 2011.

[122] Insight Segmentation and Registration Toolkit (ITK). http://www.itk.org/.

[123] NiftyRec Open Source Tomography Toolbox. http://niftyrec.scienceontheweb.net/wordpress/.

[124] Amira. http://www.vsg3d.com/amira/overview.

[125] D. Cooper, A. Turinsky, C. Sensen, and B. Hallgrimsson. Effect of voxel size on 3D micro-CT analysis of cortical bone porosity. *Calcified tissue international*, 80(3):211–219, 2007.

[126] S.R. Stock. Recent advances in X-ray microtomography applied to materials. *International Materials Reviews*, 3:129–181, May 2008.

[127] D. Fuloria and P.D. Lee. An X-ray microtomographic and finite element modeling approach for the prediction of semi-solid deformation behaviour in AlCu alloys. *Acta Materialia*, 57(18):5554–5562, October 2009.

[128] J.R. Jones, R.C. Atwood, G. Poologasundarampillai, S. Yue, and P.D. Lee. Quantifying the 3D macrostructure of tissue scaffolds. *Journal of materials science. Materials in medicine*, 20(2):463–71, February 2009.

[129] A.B. Phillion, P.D. Lee, E. Maire, and S.L. Cockcroft. Quantitative assessment of deformation-induced damage in a semisolid aluminum Alloy via X-ray microtomography. *Metallurgical and Materials Transactions A*, 39A(October):2459–2469, 2008.

[130] Light sources of the world. http://www.lightsources.org/regions.

[131] G.R. Davis and J.C. Elliott. Artefacts in X-ray microtomography of materials. *Materials Science and Technology*, 22(9):1011–1018, September 2006.

[132] M. Boin and A. Haibel. Compensation of ring artefacts in synchrotron tomographic images. *Optics express*, 14(25):12071–5, December 2006.

[133] P. Weiss, L. Obadia, D. Magne, X. Bourges, C. Rau, T. Weitkamp, I. Khairoun, J.M. Bouler, D. Chappard, O. Gauthier, and G. Daculsi. Synchrotron X-ray microtomography (on a micron scale) provides three-dimensional imaging representation of bone ingrowth in calcium phosphate biomaterials. *Biomaterials*, 24(25):4591–4601, November 2003.

[134] Aphelion Imaging Software Suite. http://www.adcis.net/en/Products/Aphelion-Imaging-Software-Suite.html.

[135] Volume Graphics. http://www.volumegraphics.com/en/.

[136] Avizo. http://www.vsg3d.com/avizo/overview.

[137] ImageJ. http://rsbweb.nih.gov/ij/.

[138] Fiji. http://fiji.sc/wiki/index.php/Fiji.

[139] E. Maire, J.Y. Buffière, L. Salvo, J.J. Blandin, W. Ludwig, and J.M. Létang. On the application of X-ray microtomography in the field of materials science. *Advanced Engineering Materials*, 3(8):539–546, August 2001.

[140] E. Maire, J.C. Grenier, D. Daniel, A. Baldacci, H. Klocker, and A. Bigot. Quantitative 3D characterization of intermetallic phases in an AlMg industrial alloy by X-ray microtomography. *Scripta Materialia*, 55(2):123–126, July 2006.

[141] P. Li, P.D. Lee, D.M. Maijer, and T.C. Lindley. Quantification of the interaction within defect populations on fatigue behavior in an aluminum alloy. *Acta Materialia*, 57(12):3539–3548, 2009.

[142] J-Y. Buffière, E. Maire, P. Cloetens, G. Lormand, and R. Fougeres. Characterization of internal damage in a MMC p using X-ray synchrotron phase contrast microtomography. *Acta materialia*, 47(5):1613–1625, 1999.

[143] A.B. Phillion, R.W. Hamilton, D. Fuloria, A.C.L. Leung, P. Rockett, T. Connolley, and P.D. Lee. In situ X-ray observation of semi-solid deformation and failure in AlCu alloys. *Acta Materialia*, 59(4):1436–1444, February 2011.

[144] C. Puncreobutr, P.D. Lee, R.W. Hamilton, and A.B. Phillion. Quantitative 3D Characterization of Solidification Structure and Defect Evolution in Al Alloys. *JOM*, 64(1):89–95, 2012.

[145] C. Puncreobutr, P.D. Lee, R.W. Hamilton, B. Cai, and T. Connolley. Synchrotron tomographic characterization of damage evolution during aluminum alloy solidification. *Metallurgical and Materials Transactions A*, pages 1–7, 2012.

[146] H. Toda, I. Sinclair, J.Y. Buffière, E. Maire, K.H. Khor, P. Gregson, and T. Kobayashi. A 3D measurement procedure for internal local crack driving forces via synchrotron X-ray microtomography. *Acta Materialia*, 52(5):1305–1317, March 2004.

[147] H. Zhang, H. Toda, H. Hara, M. Kobayashi, T. Kobayashi, D. Sugiyama, N. Kuroda, and K. Uesugi. Three-dimensional visualization of the interaction between fatigue crack and micropores in an aluminum alloy using synchrotron X-ray microtomography. *Metallurgical and Materials Transactions A*, 38(8):1774–1785, 2007.

[148] A. Chaijaruwanich, R.J. Dashwood, P.D. Lee, and H. Nagaumi. Pore evolution in a direct chill cast Al6wt.% Mg alloy during hot rolling. *Acta Materialia*, 54(19):5185–5194, November 2006.

[149] A. Chaijaruwanich, P.D. Lee, R.J. Dashwood, Y.M. Youssef, and H. Nagaumi. Evolution of pore morphology and distribution during the homogenization of direct chill cast AlMg alloys. *Acta Materialia*, 55(1):285–293, January 2007.

[150] S. Youssef, E. Maire, and R. Gaertner. Finite element modelling of the actual structure of cellular materials determined by X-ray tomography. *Acta Materialia*, 53(3):719–730, February 2005.

[151] I.G. Watson, P.D. Lee, R.J. Dashwood, and P. Young. Simulation of the mechanical properties of an aluminum matrix composite using X-ray microtomography. *Metallurgical and Materials Transactions A*, 37(3):551–558, March 2006.

[152] J.M. Park. *Behaviours of bifilms in A356 alloy during solidification: developing observation techniques with 3D micro X-ray tomography.* Master thesis, University of Birmingham, 2009.

[153] FLOW-3D official website. http://www.flow3d.com/.

[154] C.W. Hirt and J.M. Sicilian. A porosity technique for the definition obstacles in rectangular cell meshes. Technical report, Flow Science, Los Alamos, New Mexico, 1985.

[155] Flow-3D. *FLOW-3D V9.3 User Manual*. 1 edition, 2009.

[156] C.W.M. Nyahumwa. *Influence of Oxide Film Filling Defects on Fatigue Properties of Cast A1-7Si-Mg Alloy*. PhD thesis, University of Birmingham, 1997.

[157] M.R. Barkhudarov and C.W. Hirt. Casting simulation: Mold filling and solidification: Benchmark calculations using FLOW-3D. *Modeling of Casting, Welding and Advanced Solidification Processes (MCWASP VII), London*, pages 935–946, 1995.

[158] J.L. Fife, M. Rappaz, M. Pistone, T. Celcer, G. Mikuljan, and M. Stampanoni. Development of a laser-based heating system for in situ synchrotron-based X-ray tomographic microscopy. *Journal of synchrotron radiation*, 19(Pt 3):352–8, May 2012.

[159] Pyrex 7740 Borosilicate Glass. http://www.matweb.com/search/datasheettext.aspx?matguid=5bb651ca58524e79a503011b2cd8083d.

[160] ASTM Standard E290: Bend Testing of Material for Ductility. Technical report, ASTM International, West Conshohocken, PA, 2009.

[161] J.M. Hodgkinson, editor. *Mechanical Testing of Advanced Fibre Composites*. CRC Press, 2000.

[162] R. Mokso, F. Marone, M. Stampanoni, R. Garrett, I. Gentle, K. Nugent, and S. Wilkins. Real Time Tomography at the Swiss Light Source. In *AIP Conference Proceedings*, volume 87, pages 87–90, 2010.

[163] M. Stampanoni, A. Groso, A. Isenegger, G. Mikuljan, Q. Chen, A. Bertrand, S. Henein, R. Betemps, U. Frommherz, P. Böhler, D. Meister, M. Lange, and R. Abela. Trends in synchrotron-based tomographic imaging: the SLS experience. *Proceedings of SPIE*, 6318:63180M–63180M–14, 2006.

[164] F. Marone, R. Mokso, P. Modregger, J.L. Fife, B. Pinzer, T. Thuering, K. Mader, G. Mikuljan, A. Isenegger, and M. Stampanoni. Present and future X-ray tomographic microscopy at TOMCAT. In *10th International Conference on X-ray Microscopy: AIP Conference Proceedings*, 2011.

[165] J. Schindelin. Fiji is just ImageJ-Batteries included. In *ImageJ User and Developer Conference*, Luxembourg, 2008.

[166] P.A. Yushkevich, J. Piven, H.C. Hazlett, R.G. Smith, S. Ho, J.C. Gee, and G. Gerig. User-guided 3D active contour segmentation of anatomical structures: significantly improved efficiency and reliability. *NeuroImage*, 31(3):1116–28, July 2006.

[167] E.P. DeGarmo, J.T. Black, and R.A. Kohser. *Materials and processes in manufacturing*. J. Wiley & Sons, Chichester, 11th edition, 2011.

[168] ASTM Standard B557M: Standard test methods for tensile testing: wrought and cast aluminium-and-magnesium-alloy products. Technical report, ASTM International, West Conshohocken, PA, 2007.

[169] M.R. Barkhudarov. Additions to the Particle Transport and Diffusion Model for FLOW-3D.pdf. Technical report, Flow Science, Inc, 1995.

[170] S. Makarov, D. Apelian, and R. Ludwig. Inclusion removal and detection in molten aluminum: mechanical, electromagnetic and acoustic techniques. In *AFS Transaction, vol 107*, volume 107 of *Transactions of the American foundymen's society*, pages 727–735. AMER FOUNDRYMENS SOC, 1999.

[171] A.V. Getling. *Rayleigh-Bénard Convection: Structures and Dynamics*. Advanced Series in Nonlinear Dynamics Series. World Scientific Publishing Company, Incorporated, 1998.

[172] Mahmoud ElSayed. *Double Oxide Film Defects and Mechanical Properties in Aluminium Alloys*. PhD thesis, University of Birmingham, 2012.

[173] R.A. Harding, M. Wickins, and H. Wang. Development of a turbulence-free casting technique for titanium aluminides. *Intermetallics*, 19:805–813, 2011.

[174] J. Campbell. *Castings Practice: The Ten Rules of Castings*. Elsevier Science, 2004.

[175] H. Nomura, Y. Yang, and M. Takita. Inclusion removal using ceramic foam filters and filter size estimation. *International Journal of Cast Metals Research*, 9(1):27–35, 1996.

[176] T. Din, R. Kendrick, and J. Campbell. Direct Filtration of A 356 Al Alloy. *Transactions of the American Foundry Society*, 111(17):91–100, 2003.

[177] Eduardo Trejo. *Centrifugal Casting of an Aluminium Alloy*. PhD thesis, University of Birmingham, 2011.

[178] M. Tiryakioglu. Fracture toughness potential of cast Al7% SiMg alloys. *Materials Science and Engineering: A*, 497(1-2):512–514, 2008.

[179] R. Raiszadeh and W.D. Griffiths. The Effect of Holding Liquid Aluminum Alloys on Oxide Film Content. *Metallurgical and Materials Transactions B*, 42(1):133–143, October 2010.

[180] R. Raiszadeh and W.D. Griffiths. The behaviour of double oxide film defects in liquid Al alloys under atmospheric and reduced pressures. *Journal of Alloys and Compounds*, 491:575–580, 2010.

[181] S.G. Lee and A.M. Gokhale. Formation of gas induced shrinkage porosity in Mg-alloy high-pressure die-castings. *Scripta Materialia*, 55(4):387–390, August 2006.